

ASSESSING THE VIABILITY OF PEGOGENIC GIBBSITE AS A PROXY FOR PALEO-PCO₂

by

JASON CHARLES AUSTIN

(Under the Direction of Paul A. Schroeder)

ABSTRACT

Field test of gibbsite as a proxy for paleo-PCO₂ indicates that the current one-dimensional Fickian diffusion model in use does not adequately account for physical and biological processes in the upper portion of the soil (above the B horizon). Cycling of nutrients and non-uniform input of organic material at all depths result in stable isotope compositions of CO₂ trapped in pedogenic gibbsite that is not well represented by a simple diffusive mixing model. As a proxy for paleo-PCO₂, differences in results between this and previous studies indicate that differences in the conditions of soil formation such as parent material, may also affect the preservation of carbon in ways that are not accounted for by the model.

INDEX WORDS: Gibbsite, Stable Carbon Isotopes, Soil, Paleosol, Paleo-PCO₂, Proxy

ASSESSING THE VIABILITY OF PEDOGENIC GIBBSITE AS A PROXY FOR PALEO-PCO₂

by

JASON CHARLES AUSTIN

BS, Southern Connecticut State University, 2004

A Dissertation Submitted to the Graduate Faculty of The University of Georgia in Partial Fulfillment of
the Requirements for the Degree

DOCTOR OF PHILOSOPHY

ATHENS, GEORGIA

2012

© 2012

Jason Charles Austin

All Rights Reserved

ASSESSING THE VIABILITY OF PEDOGENIC GIBBSITE AS A PROXY FOR PALEO-PCO₂

by

JASON CHARLES AUSTIN

Major Professor: Paul A. Schroeder

Committee: John F. Dowd

Douglas E. Crowe

Daniel Markewitz

Electronic Version Approved:

Maureen Grasso

Dean of the Graduate School

The University of Georgia

August 2012

DEDICATION

For Kim, the realization of our walk in the wood

ACKNOWLEDGEMENTS

In the course of this dissertation I have caught a glimpse the most important truth in both life and science. This would not have been possible without the guidance of Dr. Paul A. Schroeder, the support of Kim, and the inspiration of Amelia and example of my parents.

Dr. Paul Schroeder provided the perfect mix of guidance, encouragement, and freedom that allowed me to find my way successfully through this process. He was always eager to discuss ideas, put me in the position to have life-enriching and career-advancing opportunities, and display the patience required to allow me to experience life and develop as a person and scientist.

Dr. John Dowd was an invaluable resource in planting the seed and nurturing the growth of my programming and modeling abilities, without which this would not have been possible.

Dr. Doug Crowe's method of running the Stable Isotope Lab, requiring thought about what would happen next, as opposed to knowing what step comes next, is something I will never forget and has served me well outside the lab.

Dr. Dan Markewitz provided thoughtful feedback and discussion from the perspective of a soil scientist and helped me to consider multiple points of view when considering my data.

The office staff of the Geology department, including Patty Gary, Ashley Moore, Rachael Ashton, and especially Beatrice Stephens was invaluable in the navigation of the graduate school administration.

Julie Cox in the isotope lab was extremely patient and helpful with all of the isotope work.

I am very thankful for these specific contributions and all of those that were unmentioned due to negligence on my part. There was not a member of the Geology faculty that did not inspire and encourage me in some way; either as a teacher in the classroom or by their example as a scientist.

TABLE OF CONTENTS

| | Page |
|--|------|
| ACKNOWLEDGEMENTS | v |
| LIST OF TABLES | ix |
| LIST OF FIGURES | x |
| CHAPTER | |
| 1 INTRODUCTION AND LITERATURE REVIEW | 1 |
| 1.1 STATEMENT OF PROBLEM..... | 1 |
| 1.2 PROPOSAL FOR A NEW PROXY UTILIZING PEDOGENIC GIBBSITE..... | 22 |
| 2 NUMERICAL MODELING OF SOIL PHYSICAL CHARACTERISTICS..... | 46 |
| 2.1 INTRODUCTION..... | 46 |
| 2.2 METHODS | 48 |
| 2.3 RESULTS | 53 |
| 2.4 DISCUSSION | 54 |
| 2.5 CONCLUSIONS..... | 58 |

| | | |
|-----|---|-----|
| 3 | SOIL CO ₂ EFFLUX SIMULATIONS USING MONTE CARLO METHOD AND IMPLICATIONS FOR RECORDING PALEO-PCO ₂ IN PEDOGENIC GIBBSITE | 78 |
| 3.1 | ABSTRACT..... | 79 |
| 3.2 | INTRODUCTION | 79 |
| 3.3 | METHODS | 83 |
| 3.4 | RESULTS | 84 |
| 3.5 | DISCUSSION | 85 |
| 3.6 | CONCLUSIONS..... | 90 |
| 3.7 | ACKNOWLEDGEMENTS | 91 |
| 4 | FIELD TEST OF THE GIBBSITE PALEO-PCO ₂ PROXY | 98 |
| 4.1 | INTRODUCTION..... | 98 |
| 4.2 | SITE DESCRIPTION AND METHODS..... | 100 |
| 4.3 | RESULTS | 105 |
| 4.4 | DISCUSSION | 110 |
| 4.5 | CONCLUSIONS..... | 117 |
| 5 | ASSESSING THE VIABILITY OF GIBBSITE AS A PROXY FOR PALEO-PCO ₂ | 139 |
| 5.1 | MODEL CONSIDERATIONS | 139 |

| | |
|--|-----|
| 5.2 APPLICATION TO PALEOSOLS | 141 |
| 5.3 FINAL ASSESSMENT | 143 |
| REFERENCES..... | 145 |
| APPENDICES | |
| A C++ CODE FOR SOLVING MODEL | 153 |
| A1 RUNNING MODEL | 153 |
| A2 CLASS CIPHER | 168 |
| A3 UNITS CLASS | 183 |
| A4 BOWEN CLASS | 185 |
| B SUPPLEMENTAL DATA AND FIGURES FOR FIELD TEST | 1 |

LIST OF TABLES

| | Page |
|---|------|
| Table 2.1: Constant parameters used in modeling schemes | 74 |
| Table 2.2: Variable parameters used in modeling schemes..... | 75 |
| Table 3.1: Model Assumptions and Coefficients | 97 |
| Table 4.1: % Organic Carbon and $\delta^{13}\text{C}$ of Soil Organic Carbon..... | 137 |
| Table 4.2: Model Assumptions and Coefficients | 138 |
| Table B1: Gibbsite Dehydration CO_2 and H_2O Yields and Isotope Compositions | 195 |

LIST OF FIGURES

| | Page |
|---|------|
| Figure 1.1: Temperature anomaly calculated after the trend of increasing $\delta^{18}\text{O}$ in seawater is removed. Labels 10/20 and 20/50 indicate a 10 or 20 million year running mean with a 20 or 50 million year window. These best fit the periodicity of the Paleolatitude of Ice-Rafted debris (PIRD) data. EBM anomalies are calculated using an energy balance model to predict expected temperatures using PCO_2 of the atmosphere as determined by proxies and mass balance modeling. Histograms of PIRD and OGD are also shown to indicate periods of cool and warm temperatures (also noted by the dark and light grey bars across the top of the plot). Modified from Veizer et al., (2000)..... | 25 |
| Figure 1.2: Phanerozoic $\delta^{18}\text{O}$ trend based on belemnites and brachiopods. Running average is based on 20Ma window and 5Ma forward step. Cold and glacial periods after Frakes et al., (1992) modified from Veizer et al., 1999, dark grey band represents 1σ , and light grey band represents 2σ | 26 |
| Figure 1.3: Compilation of proxy CO_2 concentrations for paleosol carbonate $\delta^{13}\text{C}$, stomatal indices, phytoplankton $\delta^{13}\text{C}$, marine boron, and liverwort $\delta^{13}\text{C}$ (Royer, 2006)..... | 27 |
| Figure 1.4: Box model showing the reservoirs and fluxes considered by the GEOCARB III model (modified from Berner, 2004). | 28 |
| Figure 1.5: General solution of GEOCARB III. Squares represent calculated PCO_2 and solid lines indicate uncertainty (Berner, 2004). | 29 |

| | |
|--|----|
| Figure 1.6: Phytoplankton paleo-pCO ₂ estimates compared to the general solution for GEOCARB III. (modified from Berner, 2004 and Royer, 2006) | 30 |
| Figure 1.7: Boron Isotope paleo-pCO ₂ estimates compared to the general solution for GEOCARB III (Modified from Berner, 2004 and Royer, 2006) | 31 |
| Figure 1.8: Response of Stomatal Index (SI) to changing CO ₂ pressure. (Royer, 2001) | 32 |
| Figure 1.9: Stomatal Density and Stomatal Index paleo-pCO ₂ estimates compared to the general solution for GEOCARB III (Modified from Berner, 2004 and Royer, 2006) | 33 |
| Figure 1.10: Relationship between the PCO ₂ of the atmosphere and the δ ¹³ C value of five species of bryophytes (Fletcher et al., 2005) | 34 |
| Figure 1.11: Paleo-PCO ₂ estimates based on liverwort δ ¹³ C values compared to the general solution for GEOCARB III (Modified from Royer, 2001) | 35 |
| Figure 1.12: Box model describing the fractionation of stable carbon isotopes by the C ₃ and C ₄ photosynthetic pathways; the center box shows the theoretical fractionation factor for each step compared to the measured values for each plant type (Modified from O'Leary, 1986)..... | 36 |
| Figure 1.13: Histograms of δ ¹³ C values of C ₃ and C ₄ plants (Bender, 1968; Bender, 1971; Hattersley, 1982; Smith and Epstein, 1971)..... | 37 |
| Figure 1.14: Sensitivity of the pedogenic carbonate –PCO ₂ model to variations in the fraction of C ₃ /C ₄ plants as inputs to soil CO ₂ (Cerling, 1991)..... | 38 |
| Figure 1.15: Sensitivity of the pedogenic carbonate-PCO ₂ model to variations in soil respiration rate (Cerling, 1991) | 39 |

| | |
|--|----|
| Figure 1.16: Sensitivity of the pedogenic carbonate-PCO ₂ model to variations in the value assumed for S(z) (equation 1.19) (Cerling, 1991)..... | 40 |
| Figure 1.17: Paleo-PCO ₂ estimates based on pedogenic carbonates (closed circles) and pedogenic goethites (open squares) compared to the general solution of the GEOCARB III model (Modified from Royer, 2001) | 41 |
| Figure 1.18: HRTEM images showing the stages of growth of goethite crystals from (b) nanodots, and (a) some elongate nanorods, to (d) micro goethite particles shown in TEM image. (c) HTREM image of nanorod showing that is made of aggregated nanodots (highlighted) and the elongate character of the nanorod (Guyodo et al., 2003) | 42 |
| Figure 1.19: Expected response from a hypothetical goethite dehydration. Top graph shows the expected linear trend in $\delta^{13}\text{C}$ values if all carbon is from the same trapped source of CO ₂ . The bottom graph shows the expected slope of X _s (CO ₂) vs. X _s (H ₂) depending on the fraction of goethite CO ₂ that is trapped. The y intercept gives the fraction of CO ₂ that is not trapped in the goethite structure (Yapp and Poths, 1991)..... | 43 |
| Figure 1.20: Compilation of all paleo-PCO ₂ estimates from the discussed proxies compared to the general solution of the GOECARB III model (modified from Royer, 2001)..... | 44 |
| Figure 1.21: Summary of the time range and amount of uncertainty associated with pedogenic carbonates, stomatal index, and phytoplankton $\delta^{13}\text{C}$ values; maximum effective PCO ₂ shown in parentheses for stomatal index and phytoplankton | 45 |
| Figure 2.1: Crystal structures of goethite. Note the open channel along the <i>c</i> axis in the goethite structure..... | 60 |

| | |
|--|----|
| Figure 2.2: Schematic representation of the finite difference notation showing the change in time as opposed to the change in depth..... | 61 |
| Figure 2.3: Box model showing the transfer of carbon between the fast, slow, and stable reservoirs, and soil pore gas for the Bowen and Beerling model (Bowen and Beerling, 2004) ... | 62 |
| Figure 2.4: Step-wise functions for D_s^* calculated using data and parameters in table 2.1 for the South Plot (dotted line), Pedon 8, (dashed line) and the exponential function in equation 2.3 | 63 |
| Figure 2.5: Model solutions for changes in D_s^* as a function of depth using parameters in table 2.1. Q = Soil respiration rate in $\text{gC m}^{-2} \text{y}^{-1}$. Data points are from the Panola Mountain soil profile with error bars showing maximum variation between replicate samples | 64 |
| Figure 2.6: Distributions of soil CO_2 production with depth based on equation 1.19 | 65 |
| Figure 2.7: Model solutions for changes in the characteristic depth (Z) of soil CO_2 production using parameters in table 2.1. Q = Soil respiration rate in $\text{gC m}^{-2} \text{y}^{-1}$. Data points are from the Panola Mountain soil profile as described in Figure 2.5 | 66 |
| Figure 2.8: Calculated concentration of CO_2 vs. depth for the distributions of CO_2 production vs. depth shown in Figure 2.6. Q = soil respiration rate in $\text{gC m}^{-2} \text{y}^{-1}$ | 67 |
| Figure 2.9: Model solutions for incorporation of the model by Bowen & Beerling (2004) for CO_2 production. Models solved using parameters in table 2.2. Q = Soil respiration rate in $\text{gC m}^{-2} \text{y}^{-1}$. Data points are from the Panola Mountain soil profile as described in Figure 2.5..... | 68 |
| Figure 2.10: Soil CO_2 production rate vs. depth for models using eqn. 1.18 (M0031 & M0027) and the Bowen and Beerling model (2004) (M0034 & M0035)..... | 69 |

| | |
|--|----|
| Figure 2.11: Concentrations of CO ₂ vs. depth calculated by models used in Figures 2.10 and 2.9 | 70 |
| Figure 2.12: Calculated model solutions using bulk density data (M0038 & M0036) and D _s [*] (z) (M0040) using eqn. 2.3 and φ [*] as a function of depth using eqn. 1.19 plotted for comparison to Panola Mountain. Measured data. Z is the characteristic depth of CO ₂ production used in equation 1.19; all model parameters listed in tables 2.1 and 2.2..... | 71 |
| Figure 2.13: Calculated model solutions using bulk density data (M0039 & M0037) and D _s [*] (z) (M0041) using eqn. 2.3 and φ [*] as a function of depth using eqn. 1.19 plotted for comparison to Panola Mountain. Measured data. Z is the characteristic depth of CO ₂ production used in equation 1.19; all model parameters listed in tables 2.1 and 2.2..... | 72 |
| Figure 2.14: Dominant monovalent species of aluminum determined by pH..... | 73 |
| Figure 3.1: Histograms and Normal probability density functions for porosity (A) and inverse tortuosity (B) based on the values calculated from bulk density data (eqn. 3.2 & 3.3) (Perkins, 1987)..... | 92 |
| Figure 3.2: Histograms and Normal probability density functions for stable carbon isotope composition of CO ₂ produced in soil by C ₄ (A) and C ₃ (B) plants (Bender, 1968, 1971; Hattersley, 1982; Smith and Epstein, 1971)..... | 93 |
| Figure 3.3: Results of fast literature (FL) (A) and slow literature (SL) (B) Monte Carlo simulations using parameters listed for model numbers 013 and 015 in table 3.1. Data points represent measured δ ¹³ C measurements of the carbonate associated with pedogenic gibbsite (Schroeder et al., 2006)..... | 94 |

| | |
|--|-----|
| Figure 3.4: Results of FL (A) and SL (B) Monte Carlo simulations using parameters listed for run numbers 013 and 015 in table 1. Data points represent measured $\delta^{13}\text{C}$ measurements of the carbonate associated with pedogenic gibbsite (Schroeder et al., 2006) | 95 |
| Figure 3.5: Results of FL (A) and SL (B) Monte Carlo simulations using parameters listed for model numbers 021 and 023 in table 3.1. Data points represent measured $\delta^{13}\text{C}$ measurements of the carbonate associated with pedogenic gibbsite (Schroeder et al., 2006)..... | 96 |
| Figure 4.1: Topographic map showing location of the field site, Watkinsville Quadrangle, 7.5 minute series, 2011 | 119 |
| Figure 4.2: Aerial photographs of the field site from 1938 to 2007 showing the presence of wooded area through at least 75 years | 120 |
| Figure 4.3: Physical and chemical treatments used to prepare samples for carbon extraction during dehydration/decarbonation procedure..... | 121 |
| Figure 4.4: Dehydration/decarbonation heating times and sample extractions | 122 |
| Figure 4.5: Schematic of the CO_2 extraction line. Sample is separated and collected using one cryogenic trap while the next sample is frozen in the other trap..... | 123 |
| Figure 4.6: %Clay for the three cores extracted around the sides of the soil pit. Error bars represent one standard deviation of three replicate analyses | 124 |
| Figure 4.7: X-ray diffraction pattern of $<2\mu\text{m}$ size fraction of soil material (after chemical treatment)..... | 125 |
| Figure 4.8: X-ray diffraction pattern of powdered bulk soil material | 126 |

| | |
|---|-----|
| Figure 4.9: Dehydration/decarbonation steps for replicates of sample 0005. $X_v(\text{CO}_2)$ is the fraction of the total CO_2 yield in a given step. Average plateau $\delta^{13}\text{C}$ values are labeled on arrows representing the plateau region | 127 |
| Figure 4.10: Amount of CO_2 yield ($\mu\text{mol/g}$) for each depth. Data points are the average for all replicates at each depth and error bars represent one standard deviation | 128 |
| Figure 4.11: Dehydration/decarbonation steps for replicates of samples 3545 and 4555. $X_v(\text{CO}_2)$ is the fraction of the total CO_2 yield in a given step. Average plateau $\delta^{13}\text{C}$ values are labeled on arrows representing the plateau region | 129 |
| Figure 4.12: $\delta^{13}\text{C}$ values of CO_2 trapped in pedogenic gibbsite vs. depth. Data points represent the average plateau value of replicates at each depth and the error bars represent one standard deviation of variability between replicates..... | 130 |
| Figure 4.13: $\delta^{13}\text{C}$ vs. $\delta^{18}\text{O}$ of the plateau samples for each sample depth. Organic CO_2 value is the average of all samples collected during the 850°C step in the dehydration procedure. Atmosphere is an average value for atmospheric CO_2 . The line between atmosphere and organic matter is arbitrary and represents linear mixing between the two reservoirs | 131 |
| Figure 4.14: Monte Carlo simulation of soil CO_2 stable isotopic composition. Dashed line is the finite difference solution calculated using a gamma distribution for CO_2 production with depth, see table 4.2 for all parameters used | 132 |
| Figure 4.15: F ratio vs. $\delta^{13}\text{C}$ CO_2 trapped in pedogenic gibbsite..... | 133 |
| Figure 4.16: $\delta^{13}\text{C}$ values for carbon in bulk soil samples (open circles) and the 850°C step of the dehydration process..... | 134 |

Figure 4.17: Compilation of all data collected at field site. (A) reproduction of figure 4.6, open squares – core 1, open circles – core 2, hexagons – core 3. (B) % carbon from core 3 (squares) and core 1 (hexagons), (C) Mineral index defined as XRD peak height of gibbsite peak (open squares) and goethite peak (open circles) as a ratio with kaolinite peak heights. (D) $\delta^{13}\text{C}$ of organic carbon from bulk soil (circles) and 850C step of dehydration process (squares). (E) $\delta^{13}\text{C}$ of plateau values from dehydration process, (F) $\delta^{18}\text{O}$ of plateau values from dehydration. 135

Figure 5.1 Standard deviation of F factor at each depth (see Figure 4.15 for data at each depth). 144

Figure B1: Dehydration/decarbonation steps for replicates of samples 0515 and 1020. $X_v(\text{CO}_2)$ is the fraction of the total CO_2 yield in a given step. Average plateau $\delta^{13}\text{C}$ values are labeled on arrows representing the plateau region 200

Figure B2: Dehydration/decarbonation steps for replicates of samples 2025 and 2535. $X_v(\text{CO}_2)$ is the fraction of the total CO_2 yield in a given step. Average plateau $\delta^{13}\text{C}$ values are labeled on arrows representing the plateau region 201

Figure B3: Dehydration/decarbonation steps for replicates of samples 5575, 7595, and 95105. $X_v(\text{CO}_2)$ is the fraction of the total CO_2 yield in a given step. Average plateau $\delta^{13}\text{C}$ values are labeled on arrows representing the plateau region 202

Figure B4: Dehydration/decarbonation steps for replicates of samples 2535Fe51 and 2535Al2. $X_v(\text{CO}_2)$ is the fraction of the total CO_2 yield in a given step. Average plateau $\delta^{13}\text{C}$ values are labeled on arrows representing the plateau region 203

CHAPTER 1

INTRODUCTION AND LITERATURE REVIEW

1.1 STATEMENT OF THE PROBLEM

1.1.1 THE ROLE OF CARBON DIOXIDE AS A DRIVER OF CLIMATE

In light of the fact that the concentration of CO₂ in the atmosphere has increased from 280ppm to 380ppm since 1860 (Royer, 2006), and it is generally agreed that this increase is partially responsible for the concurrent increase in near surface temperatures of 0.6 K (Barnett et al., 2001; Crowley, 2000; Karoly et al., 2003; Parker et al., 1994; Tett et al., 2001) it is important politically and ecologically to attempt to quantify the magnitude of forcing the concentration of CO₂ in the atmosphere exerts on global surface temperatures.

A qualitative record of past climate exists in the stratigraphic record in the form of striated pavements, tillites, erratic boulders, and ice-rafted dropstones that indicate cold climates and the distribution of carbonate deposition and fossil evidence of tropical flora and fauna at high latitudes that indicate warm climates (Figure 1.1) (Frakes et al., 1992). A quantitative record of the temperature of the shallow sea exists in the stable oxygen isotope composition of calcite skeletons of brachiopods, belemnites, and foraminifera. This record relies on the difference between the $\delta^{18}\text{O}$ value of calcite and aragonite and seawater, a relationship that is dependent on the temperature of seawater (Epstein et al., 1951; Savin, 1977; Urey et al., 1951). It should be noted that there is a discrepancy in the record of seawater $\delta^{18}\text{O}$ value through time in

that it has a linear trend increasing from -8.0‰ Standard Mean Ocean Water (SMOW) in the early Phanerozoic to 0‰ SMOW at present (Figure 1.2) (Veizer, 1999). Three explanations for this trend have been proposed including: warmer sea water temperatures, a stratified ocean resulting from sinking of saline water created by excess evaporation, or a change in the $\delta^{18}\text{O}$ of seawater through time (Karhu and Epstein, 1986; Perry and Tan, 1972; Railsback, 1990). Veizer et al., (2000) concluded that based on the correlation between the $^{87}\text{Sr}/^{86}\text{Sr}$ composition and the $\delta^{18}\text{O}$ value of the seawater, that this trend was tectonically controlled. By removing the trend they were able to align the excursions in the $\delta^{18}\text{O}$ record to variations in temperature that coincided well with evidence of cold climates based on the paleo-latitude distribution of ice-rafted debris and other glacial deposits (Figure 1.1) (Frakes et al., 1992).

Comparison of these temperature excursions to the proxy and geochemical modeling records of PCO_2 through time has revealed discrepancies. Namely, periods that were expected to have warm climates, based on high estimations of PCO_2 matched up with periods of oxygen isotope depletion, which indicate lower temperatures. This result lead Veizer et al., (2000) to conclude that in the Earth's history climate was not coupled to CO_2 concentration the way it is believed to be at present. Several attempts have been made to resolve this discrepancy, including using a new method to measure $\delta^{18}\text{O}$ value of carbonates used for paleo-thermometry (Came et al., 2007), using the carbon isotope composition of liverwort gametophyte fossils to estimate paleo- PCO_2 (Fletcher et al., 2008), compiling a detailed and comprehensive collection of plant stomatal index data (Retallack, 2002), and attempting to resolve the issue of the completeness of the proxy record by compiling a comprehensive list of all proxy data and attempting to align them in time (Royer, 2006). Ultimately, while these four methods appear to

solve this issue, there is still considerable disagreement between the different proxies for paleo- PCO_2 .

The PCO_2 estimates of these proxies are often compared to the mass balance model GEOCARB III, which attempts to calculate the change in atmospheric CO_2 concentration through time using a box model to account for the sources and sinks of carbon over geologic time scales (Berner, 2004). The fact remains while the proxies and the models appear to generally follow the same trends, the only way to be sure that the proxies are or the model is correct is to find proxies that are independent of, and in agreement with, each other.

1.1.2 PROXIES AND MASS BALANCE MODELING

Figure 1.3 shows a compilation of proxy CO_2 concentrations reported in the literature using different proxies, including $\delta^{13}\text{C}$ value of paleosol carbonates, $\delta^{13}\text{C}$ value of phytoplankton and foraminifera, $\delta^{11}\text{B}$ value of marine boron, stomatal indices, and $\delta^{13}\text{C}$ value of liverworts (Royer, 2006). Each of these will be reviewed, noting the particular benefits and limitations of each and a new proxy will be proposed. The purpose of this dissertation is to investigate and test various aspects of this new proxy.

1.1.3 GEOCARB III

GEOCARB III is one of several mass balance models that incorporate geologic data to determine the rate of change of the amount of carbon stored in various pools to calculate the concentration of CO_2 in the atmosphere (Berner, 2004; Tajika, 1998; Wallmann, 2001). The basis for this model is the long-term carbon cycle wherein CO_2 is transferred into and out of rock reservoirs by various processes on geologic time scales. The major pathways of carbon into the atmosphere, biosphere, and oceans include volcanic degassing, CO_2 released during metamorphism and diagenesis on the seafloor, and the weathering of organic carbon in sediments. CO_2 is returned

to the rock reservoirs by dissolving of CO₂ in precipitation and transportation to the sea in rivers where it is used for calcite production and ultimately buried after deposition (Berner, 2004). The model calculates the weathering rate of Ca and Mg silicates as the method through which CO₂ is removed from the atmosphere and transferred to the ocean for burial. This is shown by the equation (Berner, 2004; Urey, 1952):



Fluxes are assigned to the different processes in the long term carbon cycle including the weathering of silicates, the burial of organic and carbonate carbon in sediments, and the degassing of volcanism, diagenesis, and metamorphosis of organic and carbonate carbon (Figure 1.4). Weathering of silicates does not appear on figure 1.4 because it is the difference between carbonate carbon burial and weathering. To give the model some basis in fact, each flux shown has rate functions defined that are constrained by some data on geological processes.

Parameters affecting the rate of Ca and Mg silicate weathering are also given some function through time based on data for each feedback. These include the rates of erosion and uplift as well as the presence of plants. Additionally, the amount of CO₂ in the atmosphere and the solar irradiance affects temperature, which in turn affects the weathering rate. Each of these parameters is assigned a value at each time period for which the model is to be solved as a feedback to the flux of silicate weathering. Because this is ultimately the flux that is being solved for, these factors are calculated through time and applied to the model as it solves for the silicate weathering flux at each step to calculate the RCO₂; which is defined as the ratio of CO₂ in the atmosphere at time (t) to a preindustrial concentration of 280 ppm (Berner, 2004). The best model solution with the error bands are shown in figure 1.5. This model has been the basis that most proxies are compared against verify to that their predictions are plausible.

1.1.4 $\delta^{13}\text{C}$ OF PHYTOPLANKTON AND FORAMINIFERA

All proxies for CO_2 concentration in the atmosphere that use stable isotopes rely on identifying a modern process that causes fractionation of isotopes in a predictable way, and is dependent on the concentration of CO_2 . The results of this process must then be preserved during burial and lithification of the material. In the case of phytoplankton and foraminifera, the stable carbon isotope composition of carbon used by the cell depends on the internal and external PCO_2 of the seawater and the fractionation associated with fixation (Farquhar and Richards, 1984; Pagani et al., 1999). The PCO_2 of the surrounding seawater is calculated using equation 1.2.

$$p\text{CO}_2 = [\text{CO}_{2(aq)}]/K_H \quad (1.2)$$

Where K_H is the solubility constant of CO_2 in seawater and is dependent on the salinity and temperature of the seawater. Generally, the salinity is assumed to be 35 and the temperature of the seawater is determined by the oxygen isotope method described in section 1.1 (Hinga et al., 1994). Aqueous CO_2 (C_e) is related to ϵ_p , which is the fractionation factor between the organic carbon of the cell and the inorganic carbon which is fixed by the cell, and is defined as

$$\epsilon_p = (\alpha - 1) \times 1000 \quad (1.3)$$

$$\alpha = \frac{R_p}{R_s} = \text{fractionation factor} = \frac{R_{\text{product (organic carbon)}}}{R_{\text{source (inorganic carbon)}}} \quad (1.4)$$

where R_p is the $^{13}\text{C}/^{12}\text{C}$ ratio of the organic carbon and R_s is the $^{13}\text{C}/^{12}\text{C}$ ratio of the inorganic carbon. The relationship between ϵ_p and C_e is:

$$\epsilon_p = \epsilon_f \frac{b}{C_e} \quad (1.5)$$

where b is a factor that accounts for the growth rate and geometry of the cell and ϵ_f is the fractionation associated with fixation (Hinga et al., 1994; Pagani et al., 1999; Pagani et al., 2002).

There are two important assumptions that must be met for this method to be valid. First, the carbon that is being fixed must be inorganic carbon; and second, the carbon must arrive at the area around the cell wall by simple diffusion. Any process that the cell uses to actively increase the pressure of $\text{CO}_{2(\text{aq})}$ near the cell will make the method invalid (Pagani et al., 2002). Additionally, the b term in equation 1.5 is specific to individual species of plankton and is empirically derived for different species (Hinga et al., 1994). This b term has been shown to be correlated with the concentration of $[\text{PO}_4^{-3}]$ (Bidigare et al., 1999).

Other difficulties with this method include knowing the $\delta^{13}\text{C}$ value of the seawater DIC and the temperature of the seawater. These values are obtained from the carbon and oxygen isotopic compositions of foraminifera. The uncertainties associated with the $\delta^{18}\text{O}$ temperature reconstructions discussed in section 1.1.1 apply to these values. Nevertheless, this proxy provides good resolution through time, as continuous cores of marine deposits can be measured and the uncertainty of PCO_2 estimates is relatively low when compared to soil carbonates (Figure 1.21). Figure 1.6 plots the estimated values of paleo- pCO_2 for all the data compiled by Royer (2006) compared to the general solution of GEOCARB III (Berner, 2004).

1.1.5 $\delta^{10}\text{B}$ OF MARINE BORON

This proxy takes advantage of the fact that the ratio of $\text{B}(\text{OH})_4^-$ to $\text{B}(\text{OH})_3$ in seawater is dependent on pH. Additionally, the $^{11}\text{B}/^{10}\text{B}$ ratio of $\text{B}(\text{OH})_4^-$ is also dependent on pH. Therefore, by estimating the temperature, $\delta^{11}\text{B}$ value, and amount of DIC in the ocean, you can reconstruct the pH of the ocean through time (Sanyal et al., 1996; Spivack et al., 1993). The pH

of the ocean is dependent on the amount of CO₂ that is dissolved in the seawater, and this will change as equilibrium between the atmosphere and seawater is disturbed by changes in the concentration of CO₂ in the atmosphere (Pearson and Palmer, 1999; Pearson and Palmer, 2000).

As with other proxies there are some assumptions that must be considered. First, the method assumes that the δ¹¹B value of seawater has remained constant through time. Modeling the input of boron to the sea from rivers and uptake in the sea by carbonate precipitation indicates that it is likely that the δ¹¹B value of the oceans has varied between 42 and 36 ‰ over the past 120 Myr (Lemarchand et al., 2000). Similar to the phytoplankton proxy, there is also a temperature dependence that relies on the record of paleo-temperatures derived from the δ¹⁸O value of marine carbonates. Figure 1.7 shows paleo-PCO₂ values that have been predicted using this method; though until the understanding of the changes in δ¹¹B values of seawater through time is improved, this proxy is suspect.

1.1.6 STOMATAL INDEX

It has been noted that plant leaves change their morphology in response to the partial pressure of CO₂ in the atmosphere; specifically, there is an inverse relationship between the number of stomata and the PCO₂ of the atmosphere (Woodward, 1987; Woodward and Bazzaz, 1988). The stomata on the leaves are the openings where CO₂ required for photosynthesis is allowed to enter the plant; the number and the amount that are open are controlled by the plant to optimize water use efficiency (Stanhill, 1986). The relationship between stomata density (SD), defined as the number of stomata per mm², or the stomatal index (SI), defined as:

$$SI\% = \frac{SD}{SD + ED} \times 100 \quad (1.6)$$

where ED is the density of epidermal cells, and PCO_2 is applied to fossil cells in order to estimate the PCO_2 of the atmosphere through time (e.g. (Beerling and Royer, 2002; McElwain and Chaloner, 1995; Retallack, 2002)).

The response of SD and SI to changes in PCO_2 is specific to the plant species (Beerling, 1999; Royer et al., 2001) (Figure 1.8) and in the case of SD can be affected by various environmental factors independent of PCO_2 (Bazzaz and Williams, 1991; Beerling and Chaloner, 1992; Buchmann et al., 1997). For example, the SD response is related to insolation, water stress, and shade leaves vs. sun leaves in addition to the PCO_2 (Retallack, 2002). Because of these considerations, if possible it is preferred to use the SI, rather than the SD.

The response in the number or density of stomata on plant leaves is to the partial pressure of CO_2 in the atmosphere, not the concentration of CO_2 . Therefore, the environment of the plant must be taken into consideration, for example, a plant under heavy canopy may experience a higher PCO_2 than the atmosphere and may also be protected from changes in PCO_2 that affect the rest of the atmosphere. Additionally, as the PCO_2 is affected by altitude compensation must be made for the paleo-altitude at which the plant grew (Beerling, 1999).

Figure 1.9 shows a compilation of data for PCO_2 based on this proxy. This proxy also has relatively low error estimates, but it has been shown in green house experiments that the response tends to decrease for PCO_2 greater than 350ppm (Woodward and Bazzaz, 1988).

1.1.7 $\delta^{13}C$ OF LIVERWORTS

Another plant based proxy uses the same relationship between the concentration of CO_2 in the atmosphere and the fractionation of carbon isotopes associated with photosynthesis in marine phytoplankton. In this case however, the proxy uses bryophytes which are terrestrial plants that lack stomata. Similar to the marine phytoplankton proxy described in section 1.2.2,

the fractionation of carbon isotopes depends on the ratio of the concentration of CO₂ inside the cell (C_i) and outside the cell (C_a) (eqn. 1.7) (Farquhar et al., 1989; Fletcher et al., 2006). The internal concentration is maintained by the plant at some value below the external concentration depending on the rate of photosynthesis and the resistance of diffusion (r) (Fletcher et al., 2005; Fletcher et al., 2006). The rate of photosynthesis is determined in large part by the concentration of CO₂ in the atmosphere; therefore, if the response of photosynthesis to C_a and the resistance are known, the ratio C_i/C_a can be calculated by:

$$C_i/C_a = A \cdot r \quad (1.7)$$

This simplistic model does not accurately describe the influence of environmental factors, such as temperature and water availability, on the rate of photosynthesis (Fletcher et al., 2006). Fletcher et al., (2005) experimentally determined the response of bryophyte δ¹³C value to variations in PCO₂, water availability, and temperature (Figure 1.10); and noted that the response of moss was influenced by water availability while the response of liverworts only responded to changes in CO₂ concentration.

In order to more accurately account for variations in the response of the kinetics of photosynthesis (A), a new model, BRYOCARB was developed that combined the existing model describing the fractionation of carbon isotopes in the C₃ photosynthetic pathway and a model that describes the assimilation of carbon by C₃ plants. The model accounts for changes in O₂, irradiance, and temperature (Fletcher et al., 2006). Rearranging eqn. 7 to solve for C_i and combining it with the model describing the fractionation of carbon isotopes results in:

$$\delta^{13}C_p = \delta^{13}C_a - a - (b - a) \left(1 - \frac{r \cdot A}{C_a}\right) + \frac{f \cdot \Gamma_* + e \cdot \frac{r_d}{\left(\frac{A + r_d}{C_a - r \cdot A - \Gamma_*}\right)}}{C_a} \quad (1.8)$$

Where:

$\delta^{13}\text{C}_a$ = stable carbon isotope composition of atmospheric CO_2

$\delta^{13}\text{C}_p$ = stable carbon isotope composition of plant organic carbon

a = ^{13}C fractionation due to molecular diffusion effects (4.4‰)

b = ^{13}C fractionation due to photosynthesis effects (30‰)

f = ^{13}C fractionation due to photorespiration effects (2‰)

Γ^* = CO_2 compensation point for photorespiration vs. carboxylation (Brooks and Farquhar, 1985)

e = ^{13}C fractionation due to dark respiration effects (7‰)

r_d = rate of dark respiration (0.06A)

This model has been used to reconstruct PCO_2 of the atmosphere in the Mesozoic and Cenozoic to try to resolve the issue of uncoupled CO_2 and temperature demonstrated by Veizer et al., (2000) (Fletcher et al., 2008). This is a relatively new proxy but it seems to have promise. The limited results are plotted compared to the general solution for GEOCARB III in figure 1.11.

1.1.8 $\delta^{13}\text{C}$ OF PALEOSOL CARBONATES, INCLUDING GOETHITE

As the interface between the Earth's surface and the atmosphere, it stands to reason that it is likely that soil will record information about the composition of the atmosphere, especially during periods when the concentration of CO_2 in the atmosphere is high. In arid environments, the evaporation of soil water causes the formation of soil carbonates at rates of 1×10^{-6} to 1×10^{-5} mole cm^{-2} yr^{-1} ; quite slow when compared to the typical respiration rates of 5×10^{-3} mol cm^{-2} yr^{-1} for grasslands soil respiration (Raich and Schlesinger, 1992; Singh and Gupta, 1977). Therefore, the $\delta^{13}\text{C}$ value of soil carbonates is controlled by the isotopic composition of the soil respired CO_2 (Cerling, 1984; Cerling, 1991; Cerling et al., 1989). CO_2 production in soil by

microbes and plant respiration causes the PCO_2 at depth to increase, resulting in a diffusion gradient upward through the soil (Buyanovsky and Wagner, 1983; Dorr and Munnich, 1980; Reardon et al., 1979); which can be described using a one dimensional Fickian diffusion equation (eqn. 1.10). A variation of this method has been applied to goethite using a different method of calculating PCO_2 of the atmosphere which is described in section 1.1.8.2.

1.1.8.1 PEDOGENIC CARBONATES

Because of the difference in mass between $^{13}\text{CO}_2$ (44) and $^{12}\text{CO}_2$ (45) (M^β and M^γ respectively), the diffusion rates of $^{13}\text{CO}_2$ are slower than that for $^{12}\text{CO}_2$ (D^{45} and D^{44} respectively) in a ratio related to the mass of the air (M_a) by equation 1.9 (Cerling, 1984).

$$\frac{D^\beta}{D^\gamma} = \left[\frac{(M^\gamma + M_a)}{M^\gamma M_a} \times \frac{M^\beta M_a}{(M^\beta + M_a)} \right]^{1/2} = 1.0044 \quad (1.9)$$

This difference in diffusion rates results in $\delta^{13}\text{C}$ values of soil CO_2 4.4 ‰ more enriched in ^{13}C than the $\delta^{13}\text{C}$ value of the soil respired CO_2 (Cerling, 1999). For the purposes of this discussion, soil CO_2 refers to the CO_2 in the soil produced by microbes and plant respiration and soil respired CO_2 is defined as the CO_2 that exits the soil and enters the atmosphere. The $\delta^{13}\text{C}$ value of soil CO_2 varies with depth based on the rate of soil respiration; which, in turn depends on the concentrations of CO_2 in the soil and the atmosphere, and the diffusion coefficient of CO_2 through the soil. The concentration of CO_2 in the soil can be described by the diffusion equation

$$\frac{\partial C^*}{\partial t} = D_s^* \frac{\partial^2 C_s^*}{\partial z^2} + \phi_s^* \quad (1.10)$$

with the boundary conditions

$$z = 0 : C_s^* = C_a^* \quad (1.11)$$

$$z = L : \frac{\partial C_s^*}{\partial z} = 0 \quad (1.12)$$

where the superscript * indicates bulk composition and subscripts *s* and *a* indicate soil and atmosphere respectively. *L* represents the characteristic depth of the soil below which CO₂ concentration does not change with depth and ϕ represents the soil CO₂ production rate. Traditionally, the depth of *L* has been assumed to be 150 cm. It has been argued that the depth of active CO₂ production is much deeper than that, especially in highly weathered and relatively wet environments. The implications of this are discussed in chapter 2 (Richter and Markewitz, 1995). The solution for eqn. 1.10 is written, for bulk soil CO₂ as:

$$C_s^* = \frac{\phi^*}{D_s^*} \left(LZ - \frac{z^2}{2} \right) + C_a^* \quad (1.13)$$

The diffusion coefficient are defined as

$$D_s^* = D_{air} \epsilon \tau \quad (1.14)$$

where D_{air} is the diffusion coefficient of CO₂ in free air, ϵ is the free air porosity of the soil, and τ is a tortuosity factor which ranges from 0 to 1 (i.e. $\tau = 1/\text{Tortuosity}$). The model used by Cerling assumes that the diffusion coefficient, and thus the porosity of the soil, does not vary with depth.

Porosity of the soil can be related to bulk density by

$$\epsilon = 1 - \frac{\rho_s}{\rho_r} \quad (1.15)$$

where ρ_s and ρ_r are the bulk density of the soil and parent material respectively. The free air porosity also depends on the moisture content of the soil as increased water content results in decreased porosity.

The CO₂ production rate in the soil can be considered constant with depth, decreasing linearly with depth, or decreasing exponentially with depth. In the case where the production rate is assumed to be a constant value to depth L; as in the solution shown in eqn. 1.13, the soil respiration rate (Q), measuring the flux of CO₂ through the soil surface, can be related to the soil production rate by

$$\phi^* = \frac{Q}{L} \quad (1.16)$$

If describing the soil CO₂ production as a linear or exponential function with depth, the solution is modified to

$$C_s^*(z) = S(z) + C_a^* \quad (1.17)$$

and S(z) is the solution to the specific function for changing CO₂ production with depth. In the case of exponential decrease of CO₂ production with depth described by,

$$\phi_s^*(z) = \phi_s^*(0)e^{-(z/\bar{z})} \quad (1.18)$$

the solution is

$$S(z) = \frac{\phi_s^*(0)\bar{z}^2}{D_s^*} (1 - e^{-(z/\bar{z})}) \quad (1.19)$$

where \bar{z} is the characteristic depth of soil CO₂ production.

Solving this diffusion equation for ¹³C and ¹²C independently, using the appropriate D for each case as determined by equation 9 and substituting into equation 11 results in

$$\delta_s(z) = \left(\frac{1}{R_{PDB}} \left[\frac{S(z) \frac{D_s^*}{D_s^{13}} \hat{\delta}_\phi + C_a^* \hat{\delta}_a}{S(z) \left(1 - \frac{D_s^*}{D_s^{13}} \hat{\delta}_\phi \right) + C_a^* (1 - \hat{\delta}_a)} \right] \right) \times 1000 \quad (1.20)$$

where δ_s is the $\delta^{13}\text{C}$ value of the soil CO_2 and, $\hat{\delta}_i$ represents

$$\hat{\delta}_i = \left[\frac{R_{PDB} \left(\frac{\delta_i}{1000} + 1 \right)}{1 + R_{PDB} \left(\frac{\delta_i}{1000} + 1 \right)} \right] \quad (1.21)$$

for the soil produced CO_2 , and atmosphere. The result of this is that the equation (from eqn. 1.20)

$$\frac{S(z) \frac{D_s^*}{D_s^{13}} \hat{\delta}_\varphi + C_a^* \hat{\delta}_a}{S(z) \left(1 - \frac{D_s^*}{D_s^{13}} \hat{\delta}_\varphi \right) + C_a^* (1 - \hat{\delta}_a)} = \frac{^{13}\text{C}}{^{12}\text{C}} \quad (1.22)$$

can be solved for the $^{13}\text{C}/^{12}\text{C}$ of the soil CO_2 .

Therefore, the stable isotope composition of the pedogenic carbonate can be used with equation 1.22, and assumed values for the isotopic composition of the atmosphere, the porosity of the soil, the soil CO_2 production rate, and the stable isotope composition of the soil respired CO_2 at the time of soil formation, to calculate the concentration of CO_2 in the atmosphere at the time of mineral production in the soil.

There are some characteristics of the stable isotope composition of soil CO_2 that are important to understand for the application of this method and that will have important implications for the utility of pedogenic gibbsite as a similar proxy for CO_2 concentration. As seen by equation 1.22, the stable carbon isotope composition of the soil CO_2 is determined by the diffusive mixing of soil produced CO_2 and atmospheric CO_2 . Therefore, the $\delta^{13}\text{C}$ value of the soil CO_2 will be largely determined by the $\delta^{13}\text{C}$ value of the soil produced CO_2 , especially during periods when the PCO_2 of the atmosphere is low. During periods where the PCO_2 of the atmosphere is higher, the contribution of atmospheric CO_2 will result in less negative $\delta^{13}\text{C}$ value of the soil CO_2 .

The main control of $\delta^{13}\text{C}$ value of the soil produced CO_2 is the photosynthetic pathway used by the plants that are respiring in the soil. This also affects the CO_2 contributed by the microbial decomposition of the organic material in the soil because the plant organic material will have the same $\delta^{13}\text{C}$ value as the soil respired CO_2 . The $\delta^{13}\text{C}$ of the plant organic matter is determined by the method of photosynthesis used by the plant. The fractionation of carbon isotopes occurs during this process because ^{12}C is preferentially used by plants during photosynthesis. $^{13}\text{CO}_2$ is heavier, forms stronger bonds, and diffuses slower than $^{12}\text{CO}_2$. Therefore, during the various steps required during photosynthesis, diffusion of CO_2 into the cell, and carboxylation of the CO_2 result in some amount of fractionation. The overall fractionation of the process is controlled by the rate limiting step in the process.

In C_3 plants, CO_2 diffuses into the plant, is dissolved into sap, and diffuses to the chlorophyll where it is carboxylized by ribulose biphosphate (RuBP) (Figure 1.12). The expected amount of fractionation is shown on figure 1.12 depending on which step is rate limiting. The difference in the observed and calculated $\delta^{13}\text{C}$ values indicates that there are some other processes that control the final $\delta^{13}\text{C}$ of the leaf organic material, such as efficiency of CO_2 uptake and water-use (O'Leary, 1988). C_4 plants are typically found in more arid settings and include most grasses. These plants concentrate CO_2 inside their leaves by reacting phosphoenolpyruvate carboxylase with CO_2 in the leaf interior to produce malate or aspartate. This is transported to the sheath cells where the CO_2 is removed and carboxylation by RuBP occurs. In this case the $\delta^{13}\text{C}$ of the leaf is controlled by the fractionation of the first step. The end result of this is that there are two distinct fractionations for the different plant types, and thus two distinct $\delta^{13}\text{C}$ values for soil produced CO_2 (fig 1.13) (O'Leary, 1988).

Equation 1.21 assumes that the $\delta^{13}\text{C}$ value of the organic material in the soil is known. The fraction of C_4/C_3 biomass in the soil must therefore be known during the time the soil minerals were formed. The fraction of C_4/C_3 plants can change through time as the type of vegetation, for example grasslands (C_4) or forest (C_3), changes due to climate, or more recently, land use changes (Fox and Koch, 2004). The fraction of C_4/C_3 plants directly affects the stable carbon isotope signature of the soil CO_2 (fig 1.13). Cerling determined the sensitivity of this model to variations in the various factors that must be assumed in order to solve the model (Cerling, 1991); with the $\delta^{13}\text{C}$ value of the biomass as one of the most important variables accounting for a variation of up to 14‰ for low atmospheric PCO_2 (fig 1.14).

The other variable that accounts for a large amount of variation is the soil respiration rate. The importance of this factor is related to the concentration of CO_2 in the atmosphere; having the most variation on the $\delta^{13}\text{C}$ value of the soil CO_2 when the concentration of CO_2 in the atmosphere is high (Figure 1.15). This relationship implies that the $\delta^{13}\text{C}$ value of soil carbonates, which does not vary much below 20 cm in arid soils (Cerling et al., 1989), is a proxy for PCO_2 during periods of high PCO_2 and soil respiration rate during periods of low PCO_2 . Other variables that are important to consider are the diffusion coefficient of the soil, which is a function of the air-filled porosity and inverse tortuosity; and the characteristic depth of soil CO_2 production. These factors show greater variability when the PCO_2 of the atmosphere is high, and account for about 10‰ variation in the $\delta^{13}\text{C}$ value of soil CO_2 under high PCO_2 conditions.

Generally, the value for $S(z)$ is estimated based on the soil type and environmental conditions that it is believed the minerals formed under and the $\delta^{13}\text{C}$ value of the soil carbonates are plotted on a plot similar to figure 1.16 to determine the PCO_2 of the atmosphere. The range of $\delta^{13}\text{C}$ values for the data from a paleosol give a range of likely PCO_2 values. Because the model is

more sensitive to the atmospheric component only during periods of high CO₂ concentration, this proxy is generally more reliable when the PCO₂ is greater than ca. 1000-1500 ppm (Royer et al., 2001). Figure 1.17 shows all of the estimates for PCO₂ made using this model (closed circles) as compiled by Royer, 2001 compared to the solution for GEOCARB III.

1.1.8.2 Goethite

While conducting experiments to describe oxygen and hydrogen isotope systematics during the dehydration of goethite (FeOOH), Yapp (1983) described CO₂ as an impurity collected during the dehydration process. He determined the CO₂ was likely coming from an unknown FeCO₃ phase that was contributing to the gas evolved during dehydration. He determined that the loss of hydrogen and CO₂ was diffusion controlled and could be shown to be related to the dehydration of the mineral structure.

Yapp and Poths (1986) concluded that there are two distinct pools of carbon in natural goethites, carbon trapped in the mineral structure and organic carbon. The $\delta^{13}\text{C}$ values for CO₂ extracted from goethite ranged from -27.2‰ to -8.1‰; values that are indicative of a possible organic source, as they match relatively well with carbon isotope ratios found in C₃ and C₄ plants. This observation led to the hypothesis that the carbon in goethite could be used to determine something about the environment, specifically the PCO₂ of the atmosphere using a method similar to that described by Cerling (Section 1.1.8.1).

Five possible sources of CO₂ in goethite are surface adsorbed carbon, discrete carbonate phases in the sample, organic acids that are oxidized when heated to 230C, fluid inclusions in the minerals, and a solid solution of Fe(CO₃, O)OH in goethite. Some of these possibilities are ruled out by the procedure that is used to dehydrate the goethite and collect the CO₂.

The samples are ground and sieved to less than 63 μ m and then treated with HCl and H₂O₂ (30%). These chemical treatments are designed to remove any discrete carbonate phases and to remove any labile organic carbon from the mineral surfaces (Yapp and Poths, 1986; Yapp and Poths, 1993). Data presented by Yapp and Poths (1986) and Yapp (1987) demonstrate that these treatments result in an increase in the contribution of carbon enriched in ¹³C, indicating that the source of labile organic carbon was removed. Additionally, it has been shown that surface adsorbed CO₂ will desorb under vacuum at room temperature (Russell et al., 1975). While treatment with HCl serves to dissolve any discrete carbonate phase in the sample, the possibility of contamination by such a phase is unlikely because CO₂ is not collected from carbonate phases heated to 230C (Yapp and Poths, 1986).

These considerations leave the two options of fluid inclusions and a solid solution of an iron carbonate phase; fluid inclusions are ruled out by comparing the ratio of non-stoichiometric water collected during dehydration to CO₂. The ratio is much lower than the expected 7300 to 18000 from fluid inclusions in carbonates and can only account for 0.4% of the carbon that is collected during dehydration; leaving only the option that the CO₂ exists in solid solution with goethite (Yapp, 1987). There is some evidence that CO₂ is commonly adsorbed to the goethite surface and that the amount of CO₂ adsorbed is related to the concentration of CO₂ in the environment (Russell et al., 1975). Additionally, an unstable Fe(III) carbonate phase has been shown to exist, allowing for the possibility that it may form under the conditions present at the mineral surface during mineral crystal growth (Dvorak et al., 1969). Finally, high resolution transmission electron microscope (HRTEM) images of goethite crystals show that they grow as round nanodots (ca. 3.5 nm), which later combine to form long groups and eventually elongate crystals. This method of aggregation allows for carbonate ions adsorbed to the surface of a

nanodot to be trapped and incorporated in the goethite structure (Figure 1.18) (Guyodo et al., 2003). These facts, combined with the $\delta^{13}\text{C}$ values of the trapped carbon collected in previous studies indicate that the amount of CO_2 that is trapped in the goethite structure, or incorporated in solid solution, can be used as a proxy for the CO_2 concentration of the atmosphere for goethite that formed in surface environments like soils (Yapp, 1987).

The carbonate component is assumed to be incorporated into the goethite structure in the *c*-axis channel by reacting with an O^{2-} in the structure as the mineral grows around it. Infrared spectral analysis of goethite supports this assumption with absorption peaks at 1345cm^{-1} and 1515cm^{-1} , which indicate the expected split in the carbonate ion resulting from unidentate bonding in the goethite structure (Yapp and Poths, 1990). The PCO_2 of the atmosphere can be calculated using the equation:

$$\log \text{PCO}_2 = \log X + 6.04 - 1570/T \quad (1.23)$$

where X is the mole fraction of FeCO_3OH as determined by stepwise dehydration reactions and T is the temperature in Kelvins as determined by oxygen and hydrogen isotopes (Yapp, 1993; Yapp, 2001; Yapp and Poths, 1986; Yapp and Poths, 1992; Yapp and Poths, 1993).

$\delta^{13}\text{C}$ values of the carbon evolved during the dehydration steps are used to determine when the CO_2 that is released is part of the FeCO_3OH component. When the evolved carbon is from the dehydration of the goethite structure, the expectation is that the $\delta^{13}\text{C}$ value of the carbon will be constant. Therefore, a plateau value is identified in the data (Figure 1.19) which is used to calculate the mole fraction of the carbonate component of the goethite (Yapp, 2001). In addition, plotting the mole fraction of CO_2 remaining in the sample after a dehydration step ($X_s(\text{CO}_2)$) against the mole fraction of hydrogen remaining in the mineral after the dehydration step ($X_s(\text{H}_2)$) should result in a straight line that is described by the equation

$$X_s(\text{CO}_2) = [1 - X_s(\text{CO}_2)^*]X_s(\text{H}_2) + X_s(\text{CO}_2)^* \quad (1.24)$$

where $X_s(\text{CO}_2)^*$ is the value of $X_s(\text{CO}_2)$ when $X_s(\text{H}_2) = 0$ (Yapp and Poths, 1991).

Specifically, when determining the PCO_2 of the atmosphere, using the same one-dimensional Fickian diffusion model for CO_2 transport in the soil, the PCO_2 is related to the mole fraction of the carbonate component of CO_2 incorporated in goethite by the equation:

$$\delta^{13}\text{C}_m = (\delta^{13}\text{C}_A - \delta^{13}\text{C}_O)X_A \left(\frac{1}{X_m} \right) + \delta^{13}\text{C}_O \quad (1.25)$$

where:

$\delta^{13}\text{C}_m$ = the measured $\delta^{13}\text{C}$ value for the plateau portion of the dehydration

X_m = the measured mole fraction of the $\text{Fe}(\text{CO}_3)\text{OH}$ component

$\delta^{13}\text{C}_A$ = the expected $\delta^{13}\text{C}$ of the goethite CO_2 assuming it is in equilibrium with the atmosphere

X_A = the expected mole fraction of the goethite CO_2 assuming it is in equilibrium with the atmosphere.

$$\delta^{13}\text{C}_O = [\alpha_k \delta^{13}\text{C}_B + 1000(\alpha_k - 1)] \quad (1.26)$$

where $\delta^{13}\text{C}_B$ is the expected $\delta^{13}\text{C}$ value of the goethite CO_2 assuming it is in equilibrium with the soil CO_2 and α_k is the ratio of $^{44}\text{D}/^{45}\text{D}$ (1.0044). Equation 1.25 shows that, if $\delta^{13}\text{C}_A$ and $\delta^{13}\text{C}_O$ are assumed to be constant, the relationship between X_m and $\delta^{13}\text{C}_m$ should be a straight line, the slope of which will allow the calculation of X_A . X_A can then be used with equation 1.23 to calculate the PCO_2 of the atmosphere (Yapp, 2001). Estimates of paleo- PCO_2 that have been made using this proxy are shown as open squares on figure 1.17 compared to the general solution for GEOCARB III (Royer, 2001).

1.1.9 SUMMARY OF PROXY DATA

If all paleo-PCO₂ estimates are plotted and compared to the solution to the GEOCARB III model, it appears that the proxies confirm in a general sense the trend of the prediction made by the model (Figure 1.20). That is to say that there are times of high proxy PCO₂ that occur during times of high model PCO₂; and the lows in both model and proxy PCO₂ occur from about 350-250Ma and again starting around the Miocene. Closer inspection shows that the proxy CO₂ values are greater than the model PCO₂ during the period between the Triassic and the Miocene. It is important to note during discussions comparing the model solution to the proxy data that neither can be assumed to be correct; the proxy data can be used as a check to see if the model data is reasonable and therefore doing an adequate job of estimating the processes and fluxes that regulate the concentration of CO₂ in the atmosphere. As a result, it is important to consider the different proxies in light of each other to see if independent methods result in similar results.

When comparing proxies, it is important to consider the amount of uncertainty associated with each and the age-range that each is useful for. Figure 1.21 is a summary of the useful range of each proxy and the uncertainty of each. Marine phytoplankton and stomatal density have relatively small error but they are both limited to low concentrations of carbon dioxide, less than 350 ppmv for stomatal density, and less than 1250 ppmv for marine carbonates (Kump and Arthur, 1999; Woodward and Bazzaz, 1988). Both of these proxies are also limited in time to earlier than the Cretaceous leaving pedogenic carbonates, which has relatively large error estimates, as the sole proxy for periods older than about 145 million years. Therefore, it is important to find another proxy that is useful over a large age range that can be compared to the proxy CO₂ estimates using the paleosol carbonate method.

1.2 PROPOSAL FOR A NEW PROXY UTILIZING PEDOGENIC GIBBSITE

1.2.1 BACKGROUND

It has been shown that if gibbsite is dehydrated following a procedure similar to that used for goethite dehydration, some amount of carbon dioxide is released that appears to be related to the structural breakdown of the mineral as it is collected (Schroeder and Melear, 1999; Tabor and Yapp, 2005a). Therefore, it has been proposed that the $\delta^{13}\text{C}$ value of this gibbsite occluded CO_2 is a possible proxy for paleo- PCO_2 in the same way as goethite. This would provide a proxy that is useful over the same age range and forms in a different environment than pedogenic carbonates; allowing for comparison of proxy PCO_2 estimates through time and across different climates, and thus eliminating local variables and providing a broader look at global PCO_2 .

In order for this to be a viable proxy, it is necessary to test if the models currently used for either pedogenic carbonates or goethite apply, or if a new model must be developed. The model used for pedogenic goethite assumes that the carbonate ion is incorporated into the goethite structure and is accommodated in the *c*-axis channel in the goethite structure. A carbonate component of goethite can be shown to be chemically possible by the reaction



Because of this structural and chemical compatibility, and the infrared spectral evidence for a stretched carbonate ion in goethite allows for the assumption that the CO_3^{-2} is part of the structure of goethite; it is possible to determine the Henry's law constant and the fractionation factor required for this model to work.

Unlike goethite, the mineral structure of gibbsite does not have an open channel available to accommodate the carbonate ion that is adhered to the surface. Additionally, there is a charge imbalance as the chemical formula for gibbsite is $\text{Al}(\text{OH})_3$ and the CO_3^{-2} ion would have to

displace two OH⁻ ions to remain balanced. Therefore, Schroeder and Melear (1999) proposed that the carbonate ion was located in an edge defect, which becomes trapped in the mineral structure as it is precipitated. This model allows for the carbonate to be trapped in place and to be released only when the gibbsite structure breaks down without actually being part of the gibbsite structure. Because of this, the diffusion model for pedogenic carbonates is used assuming that the fractionation factor (α) = 1.00 and the carbon isotopes are in equilibrium with the soil CO₂ as described in the soil carbonate model (Schroeder and Melear, 1999). When the model developed by Cerling was applied to data for $\delta^{13}\text{C}$ values for carbon extracted from a modern soil located at Panola Mountain, Georgia, USA, the results were promising and indicated that the carbonate trapped in the gibbsite structure may record information about the environmental conditions under which the gibbsite formed.

1.2.2 HYPOTHESES

The goal of this research is to develop a model that describes the stable carbon isotope composition of soil CO₂ and compare it to the $\delta^{13}\text{C}$ values of carbon extracted from a modern soil to attempt to discern the utility of carbon occluded in pedogenic gibbsite as a proxy for paleo-PCO₂. Schroeder and Melear (1999) attempted to model the respiration rate of the soil using the model developed by Cerling, the PCO₂ of the atmosphere was known for the modern soil, and the results were 30-60% less than the measured average value. This discrepancy indicates an error in the model assumptions; either the model does not accurately describe the physical processes, or the assumed values of the various coefficients are not correct. This project attempts to falsify the following hypotheses:

1. A more accurate description of the soil physical parameters, including variations with depth will result in a better model fit of the stable isotope composition of carbon collected from the thermal decomposition of pedogenic gibbsite from a modern soil.
2. The assumption that the stable carbon isotope composition of carbon occluded in gibbsite is in equilibrium with the soil CO₂ at the average growing season respiration rate is correct, and the discrepancy between measured and modeled respiration rates can be accounted for by the natural variability of the various model factors.
3. A new data set collected from a modern soil will confirm the presence of CO₂ in the gibbsite structure, and the $\delta^{13}\text{C}$ values of the trapped CO₂ will be similar to those measured by Schroeder and Melear (1999); and will prove useful as a proxy for PCO₂ of the atmosphere using the model established in sections 2 and 3.

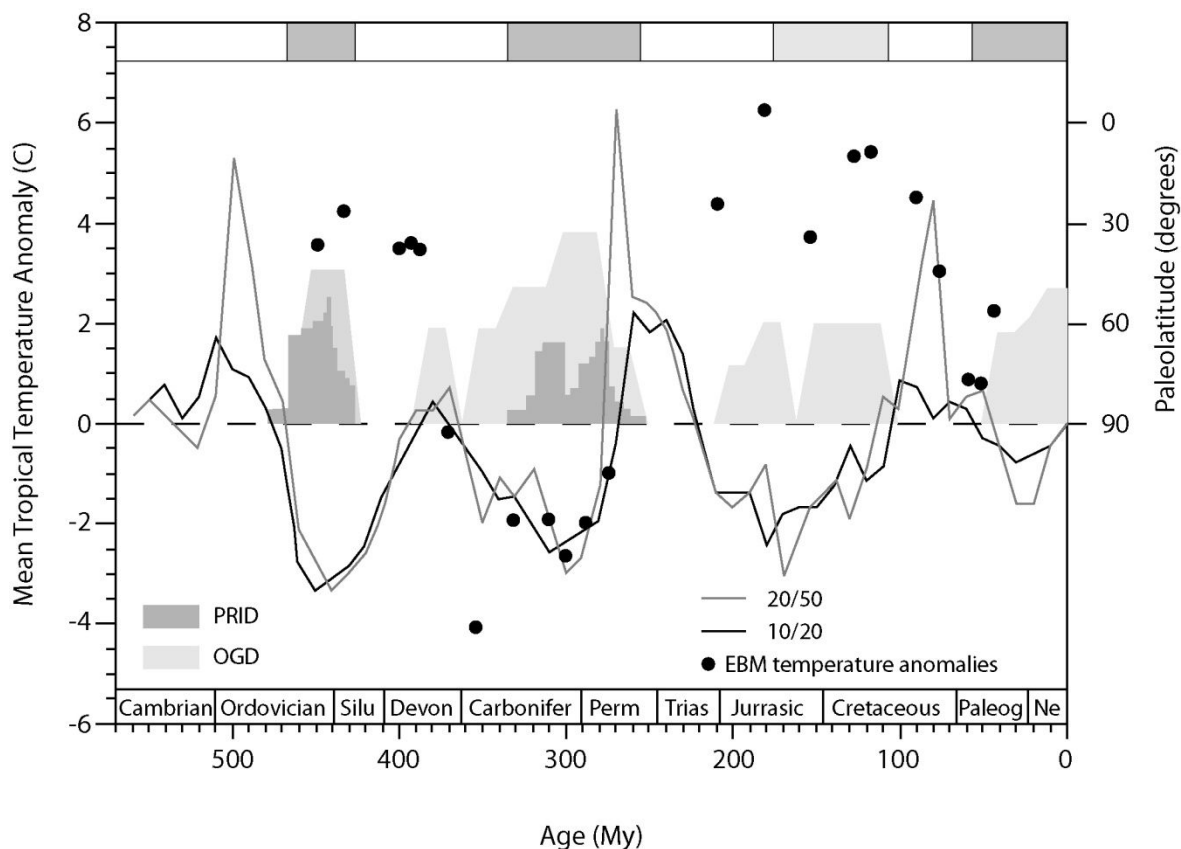


Figure 1.1: Temperature anomaly calculated after the trend of increasing $\delta^{18}\text{O}$ in seawater is removed. Labels 10/20 and 20/50 indicate a 10 or 20 million year running mean with a 20 or 50 million year window. These best fit the periodicity of the Paleolatitude of Ice-rafted debris (PIRD) data. EBM anomalies are calculated using an energy balance model to predict expected temperatures using pCO_2 of the atmosphere as determined by proxies and mass balance modeling. Histograms of PIRD and OGD are also shown to indicate periods of cool and warm temperatures (also noted by the dark and light grey bars across the top of the plot) (modified from Veizer et al. (2000)).

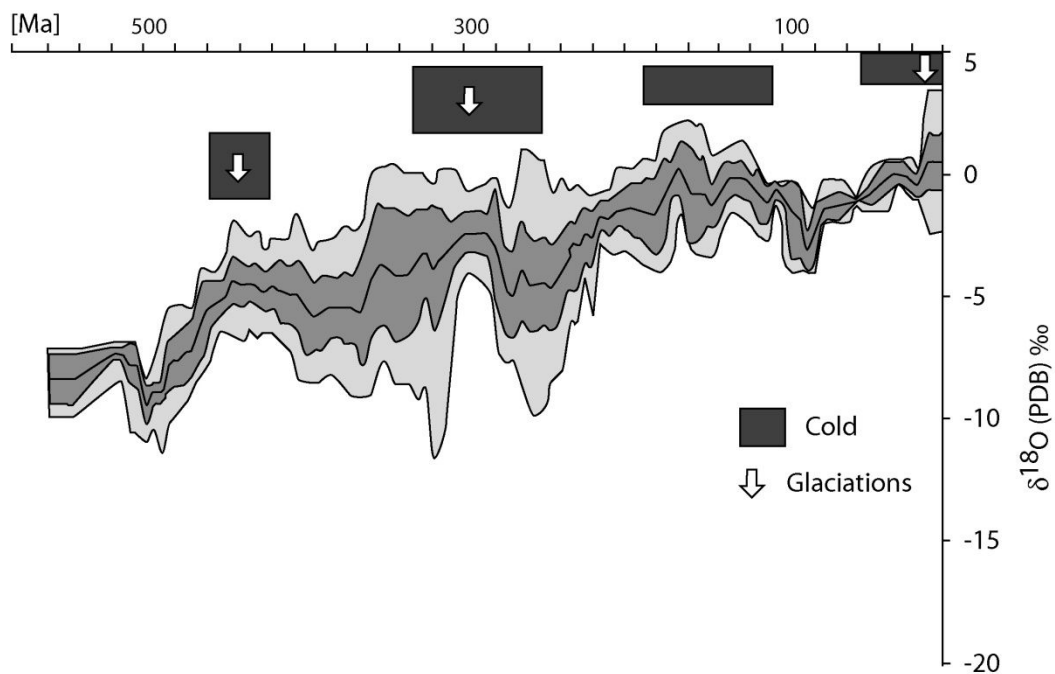


Figure 1.2: Phanerozoic $\delta^{18}\text{O}$ trend based on belemnites and brachiopods. Running average is based on 20Ma window and 5Ma forward step. Cold and glacial periods after Frakes et al., (1992) modified from Veizer et al. (1999), dark grey band represents 1σ , and light grey band represents 2σ

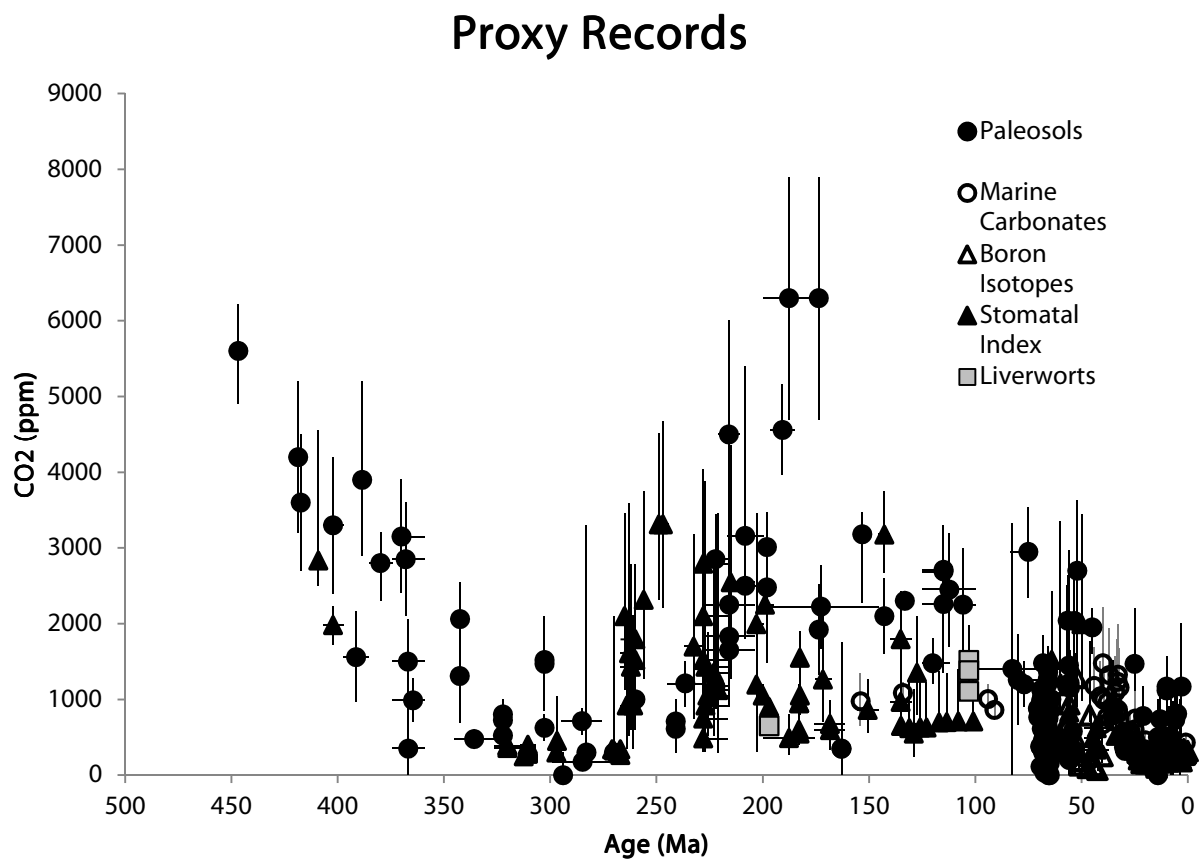


Figure 1.3: Compilation of proxy CO₂ concentrations for paleosol carbonate $\delta^{13}\text{C}$, stomatal indices, phytoplankton $\delta^{13}\text{C}$, marine boron, and liverwort $\delta^{13}\text{C}$ (Royer, 2006).

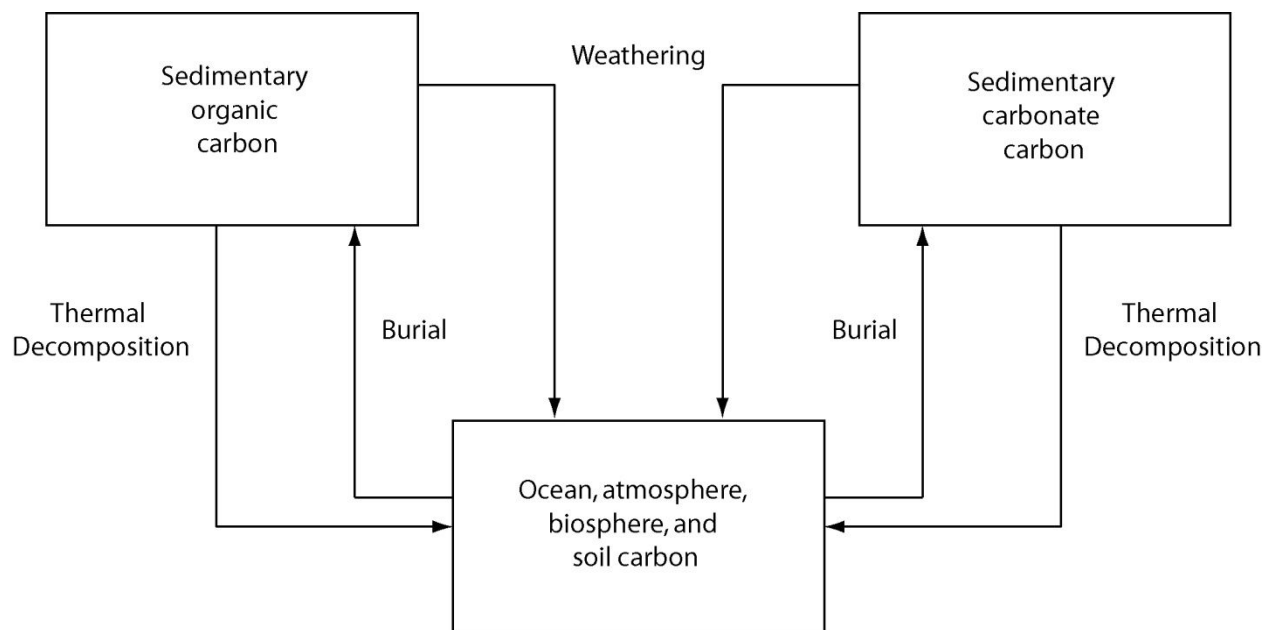


Figure 1.4: Box model showing the reservoirs and fluxes considered by the GEOCARB III model (modified from Berner, 2004)

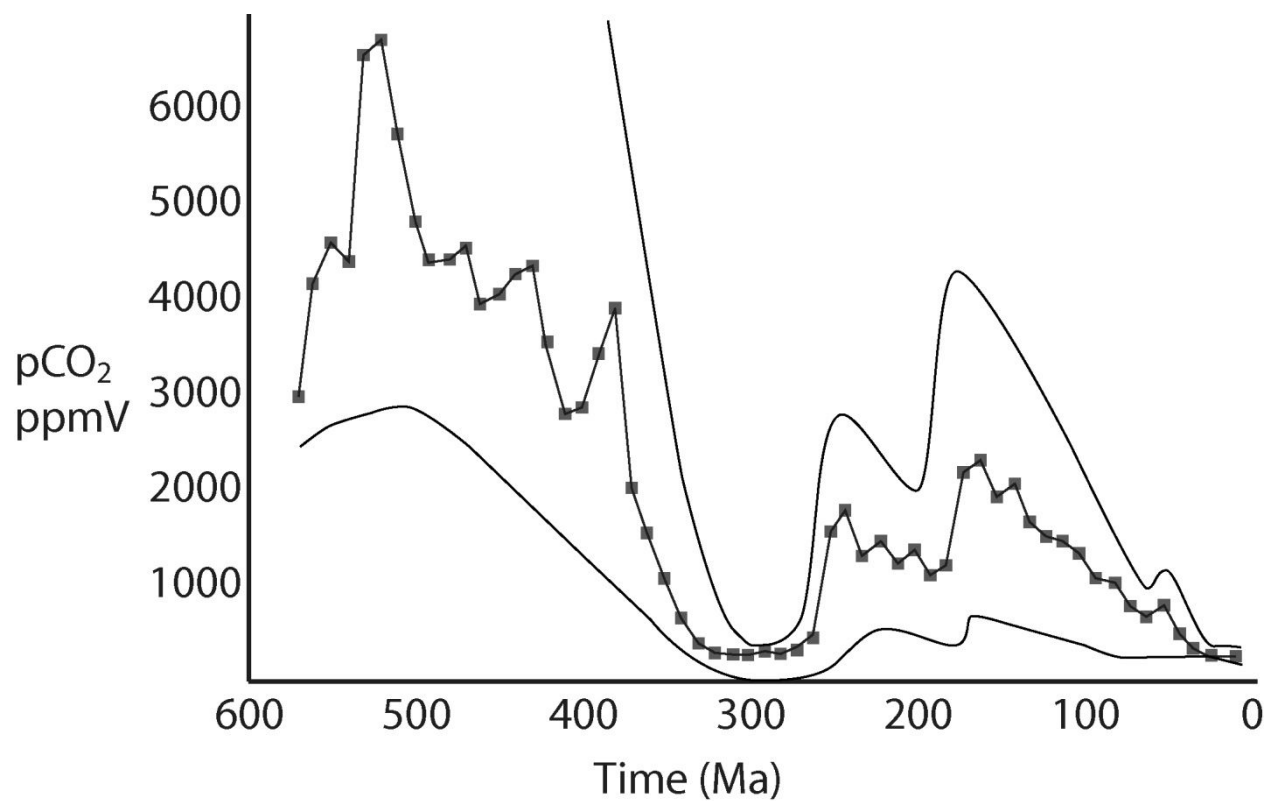


Figure 1.5: General solution of GEOCARB III. Squares represent calculated PCO₂ and solid lines indicate uncertainty (Berner, 2004).

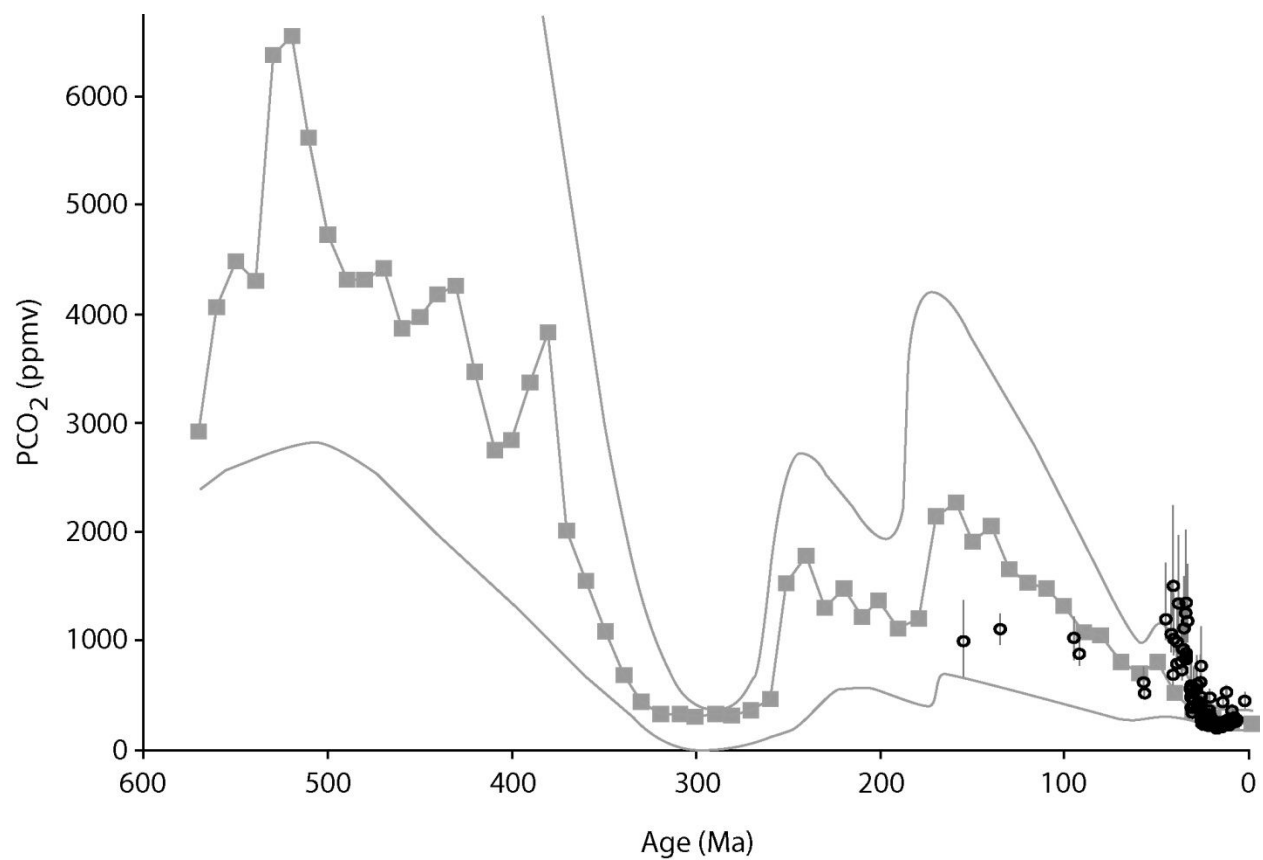


Figure 1.6: Phytoplankton paleo-pCO₂ estimates compared to the general solution for GEOCARB III. (modified from Berner, 2004 and Royer, 2006)

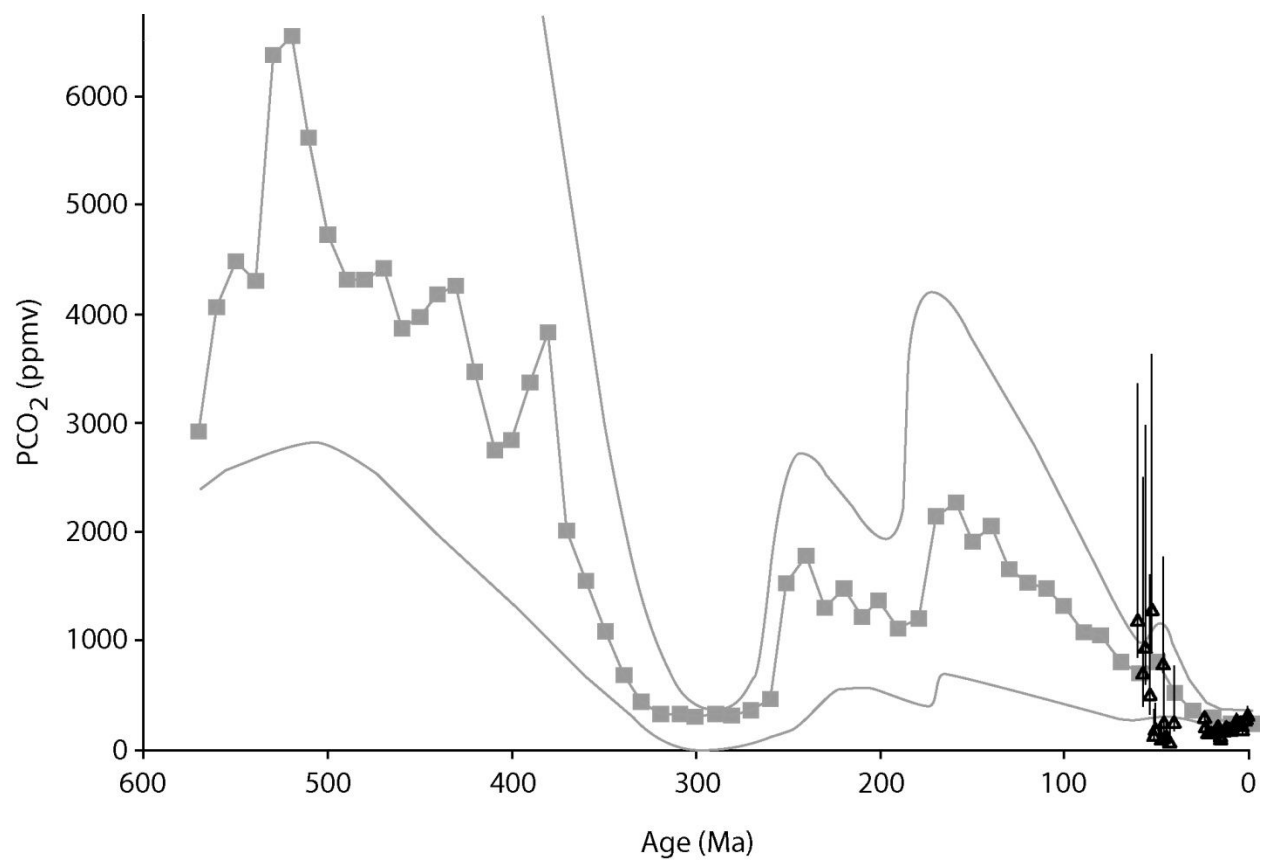


Figure 1.7: Boron Isotope paleo-pCO₂ estimates compared to the general solution for GEOCARB III (Modified from Berner, 2004 and Royer, 2006)

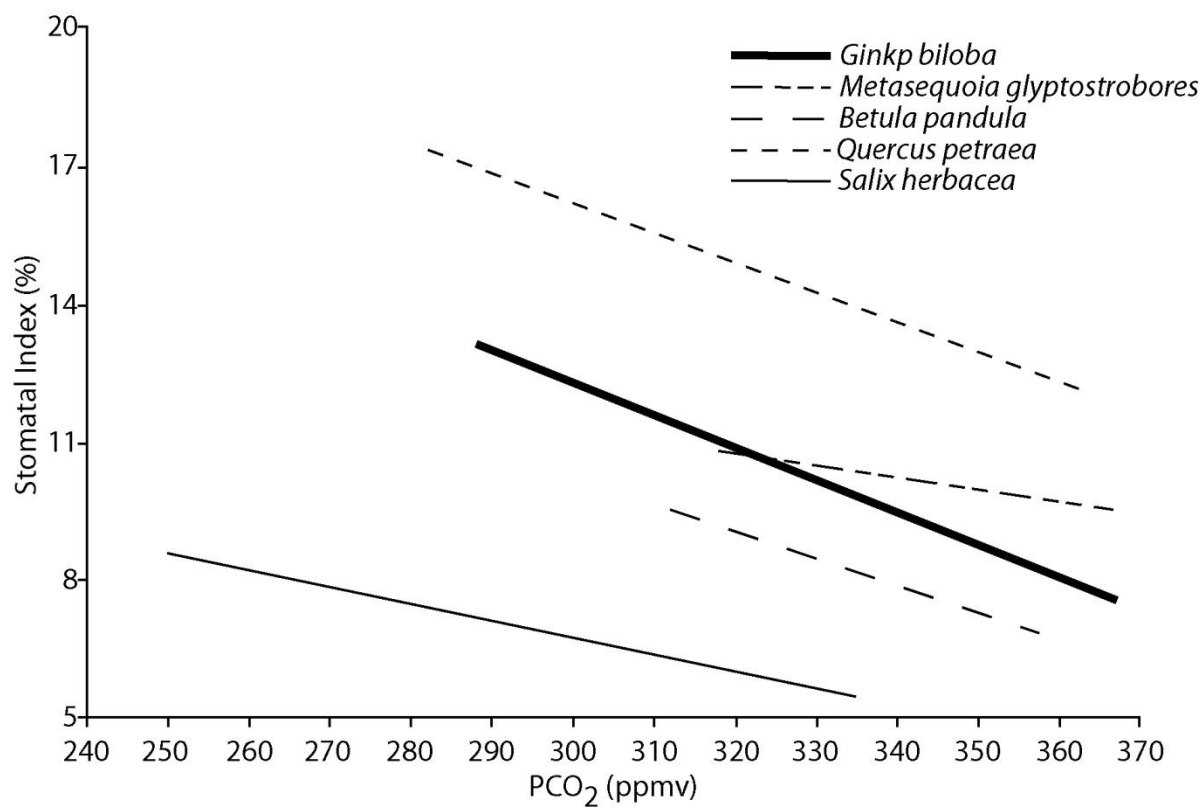


Figure 1.8: Response of SI to changing CO₂ pressure. (Royer, 2001)

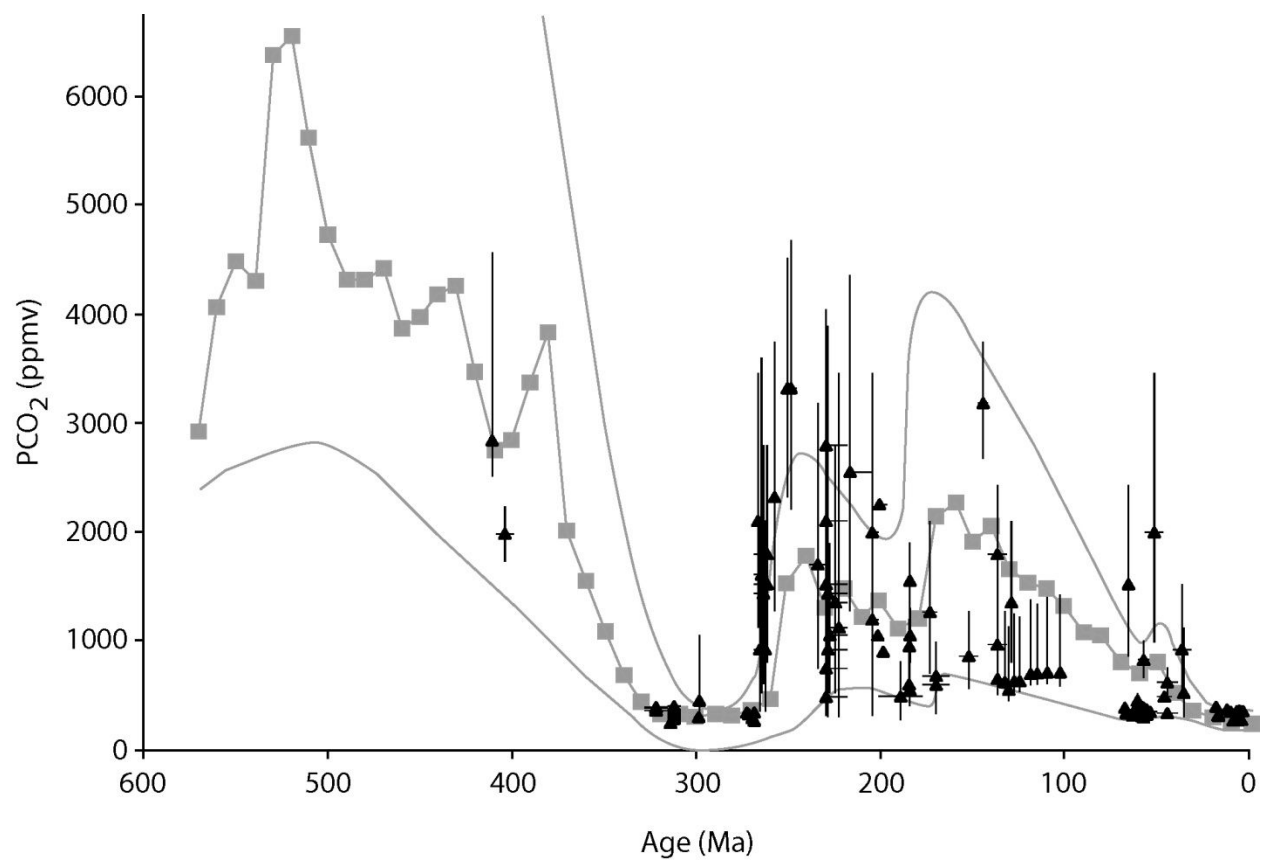


Figure 1.9: Stomatal Density and Stomatal Index paleo-pCO₂ estimates compared to the general solution for GEOCARB III (Modified from Berner, 2004 and Royer, 2006)

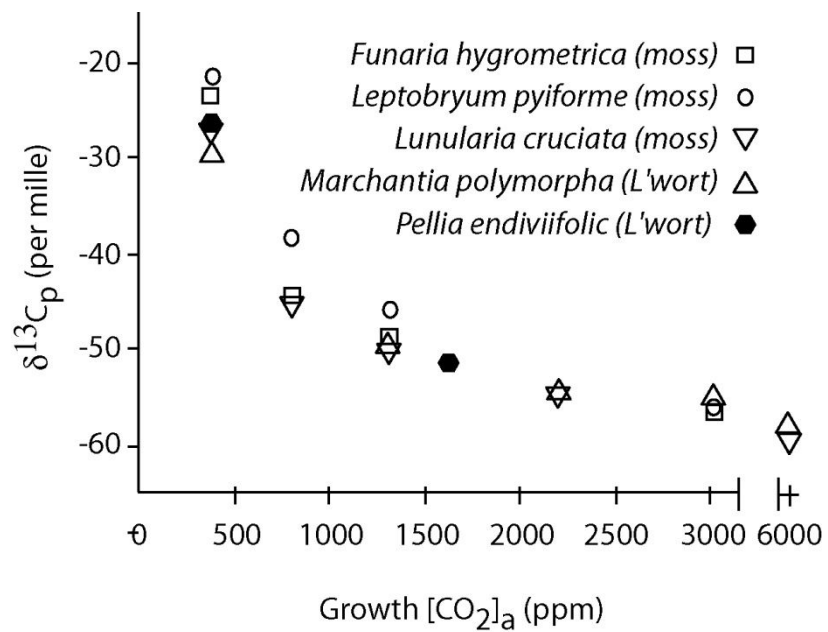


Figure 1.10: Relationship between the PCO₂ of the atmosphere and the δ¹³C value of 5 species of bryophytes (Fletcher et al., 2005)

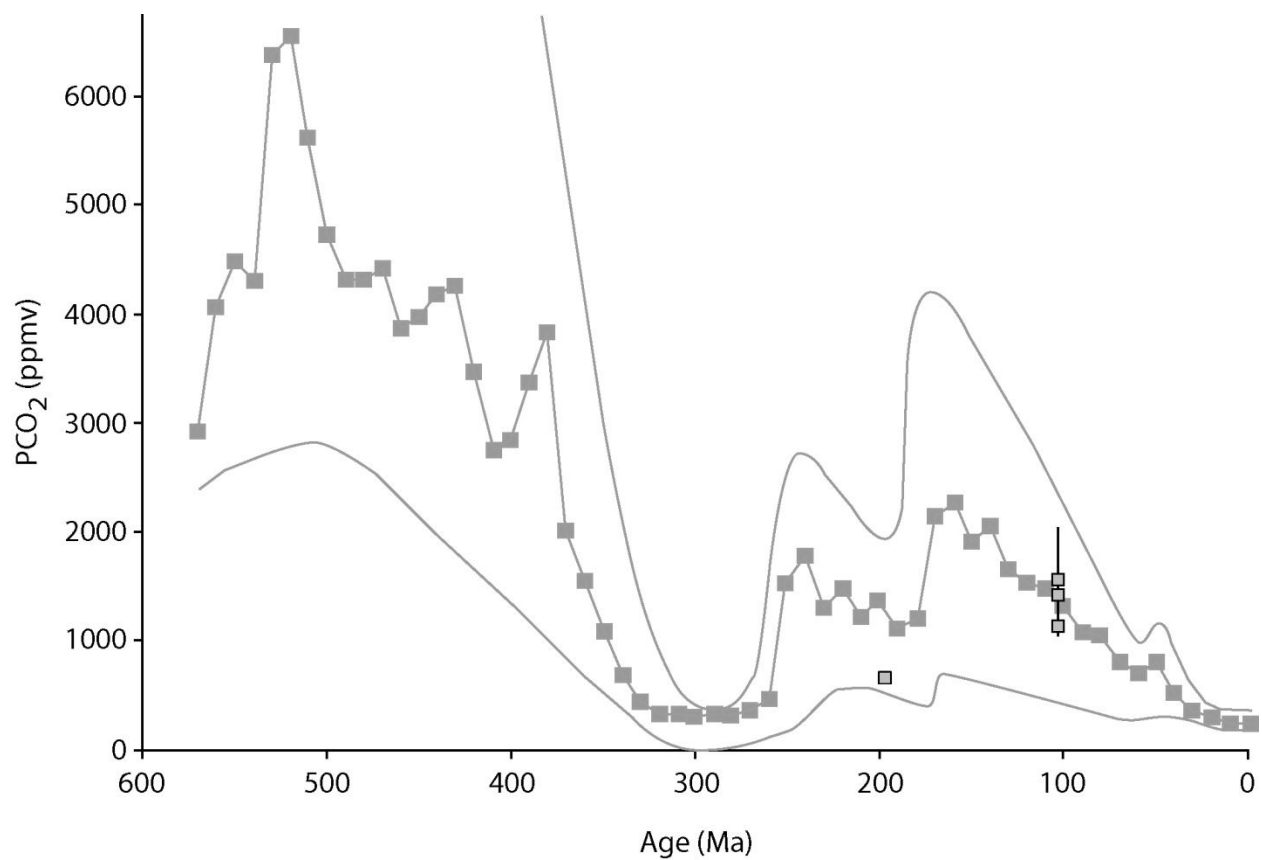


Figure 1.11: Paleo-PCO₂ estimates based on liverwort $\delta^{13}\text{C}$ values compared to the general solution for GEOCARB III (Modified from Royer, 2001)

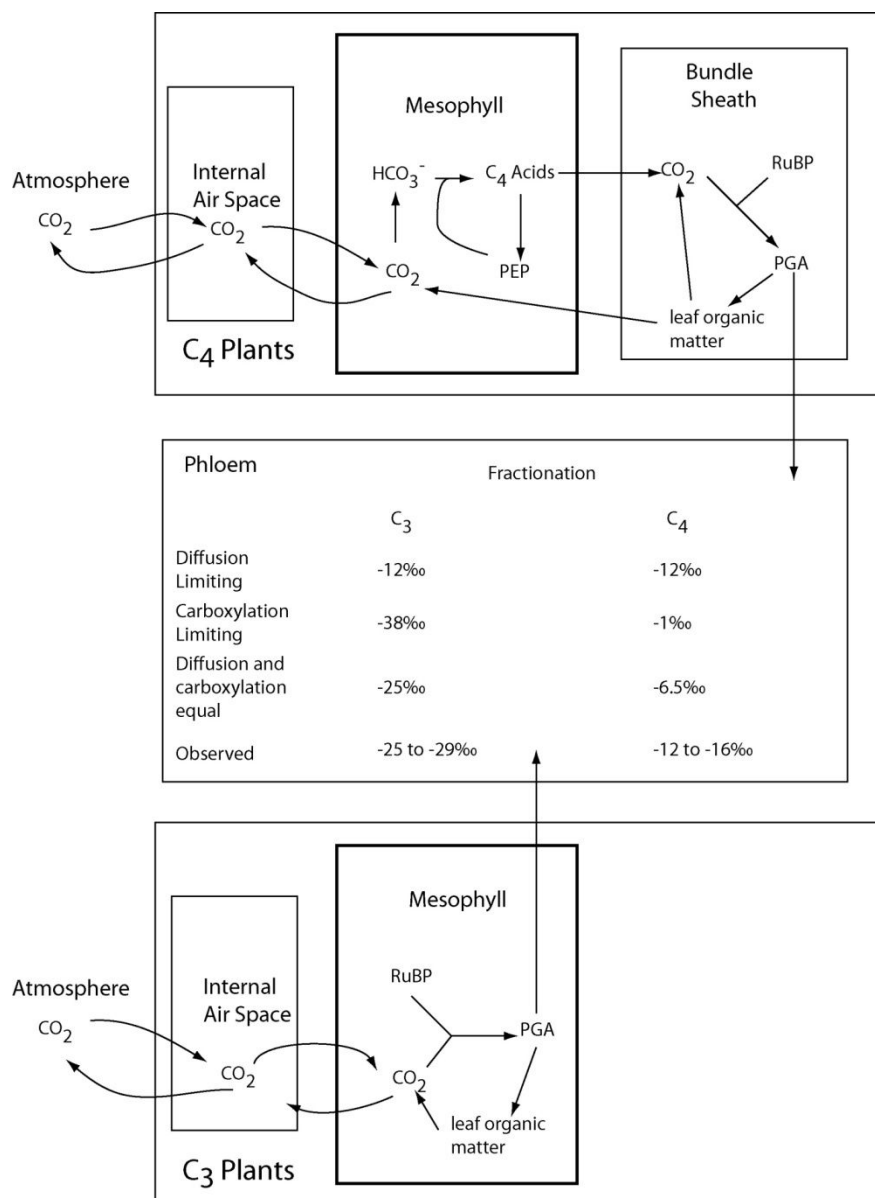


Figure 1.12: Box model describing the fractionation of stable carbon isotopes by the C_3 and C_4 photosynthetic pathways; the center box shows the theoretical fractionation factor for each step compared to the measured values for each plant type (Modified from O'Leary, 1988)

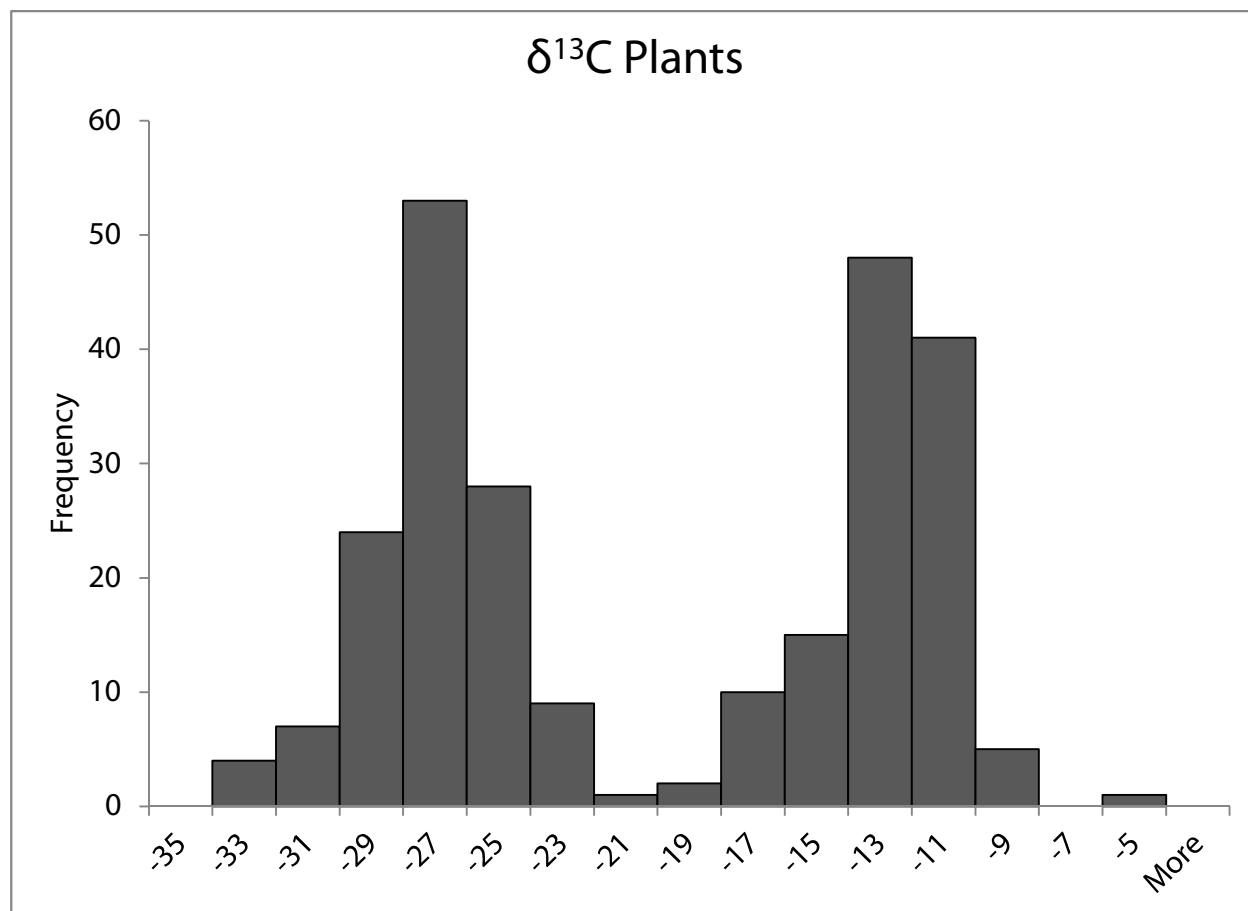


Figure 1.13: Histograms of $\delta^{13}\text{C}$ values of C_3 and C_4 plants (Bender, 1968; Bender, 1971; Hattersley, 1982; Smith and Epstein, 1971)

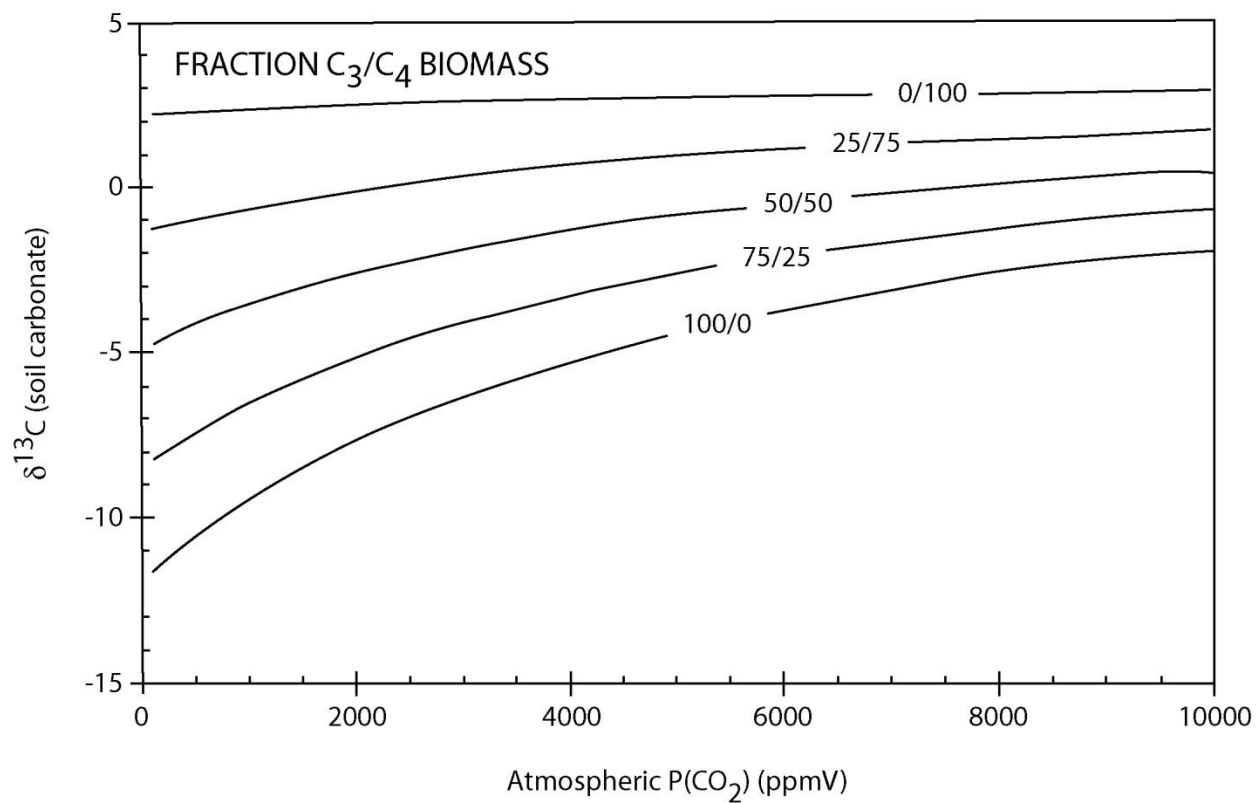


Figure 1.14: Sensitivity of the pedogenic carbonate – $\text{P}(\text{CO}_2)$ model to variations in the fraction of C_3/C_4 plants as inputs to soil CO_2 (Cerling, 1991)

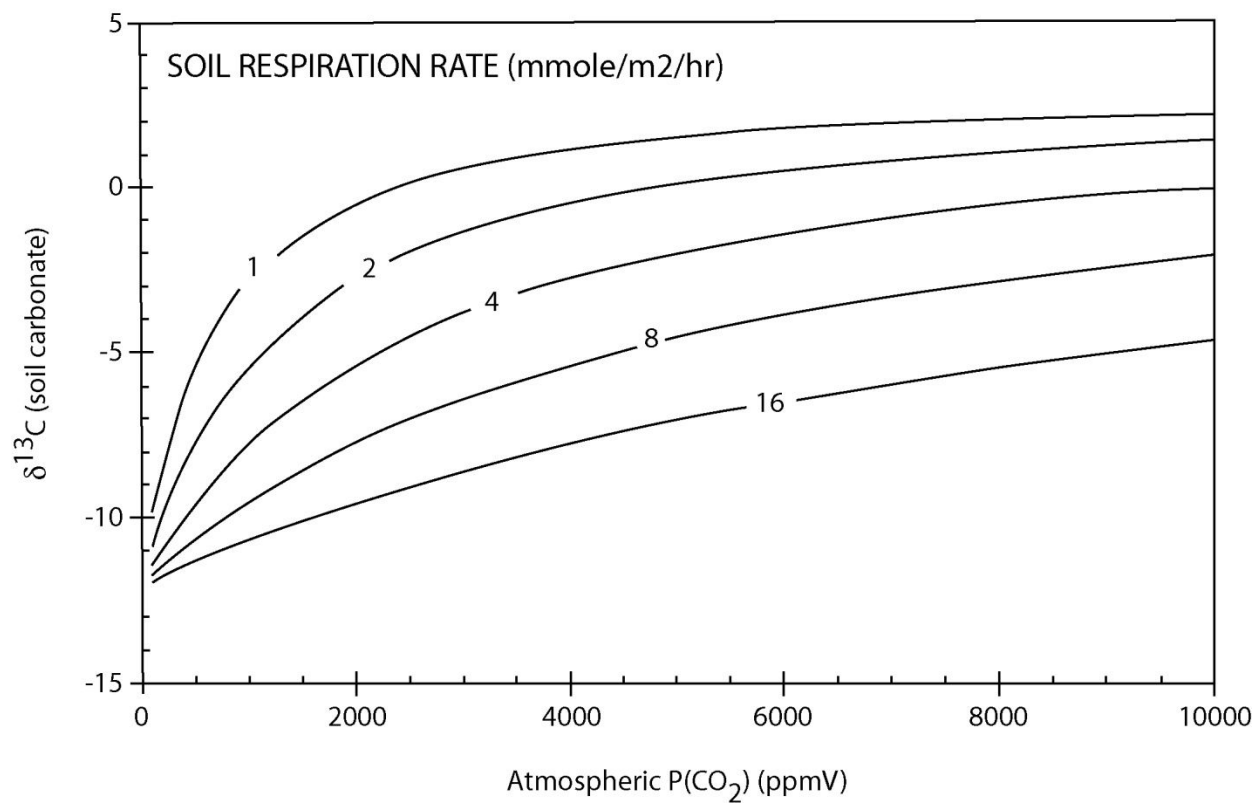


Figure 1.15: Sensitivity of the pedogenic carbonate- $\text{P}(\text{CO}_2)$ model to variations in soil respiration rate (Cerling, 1991)

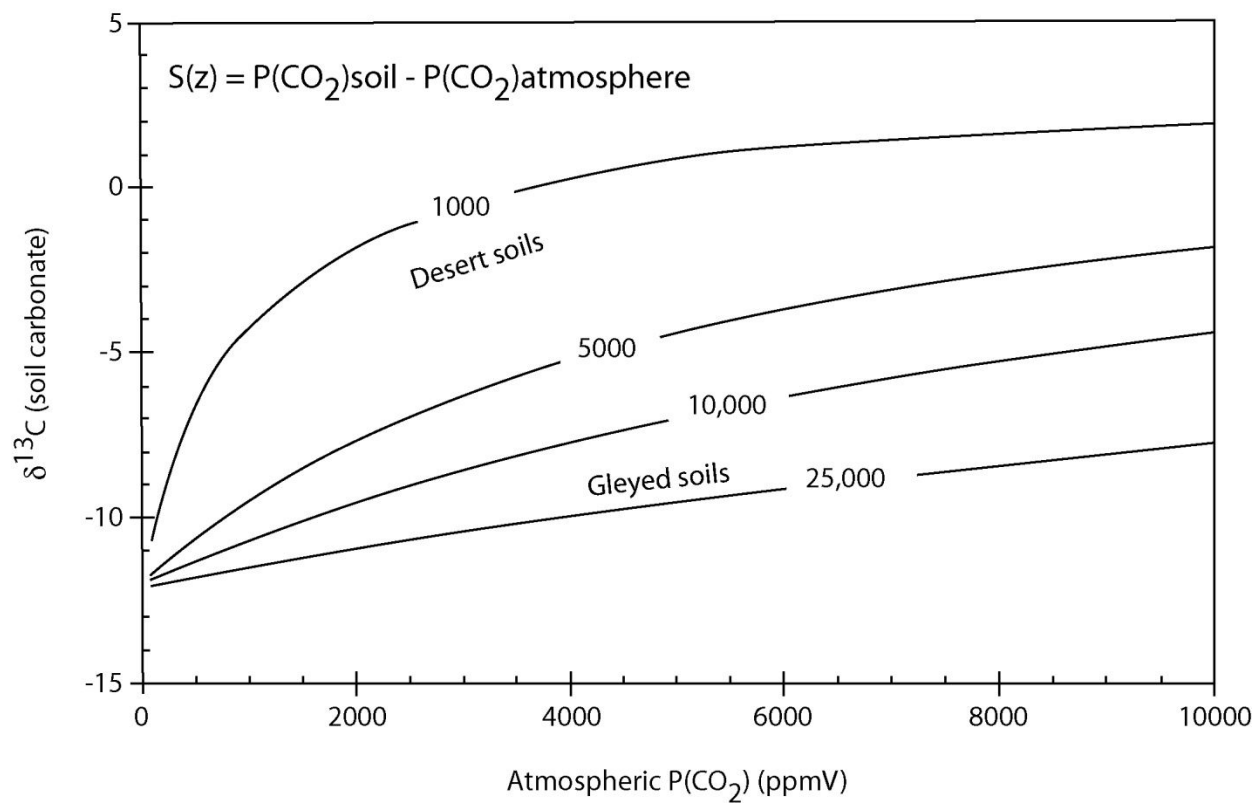


Figure 1.16: Sensitivity of the pedogenic carbonate- $\text{P}(\text{CO}_2)$ model to variations in the value assumed for $S(z)$ (Cerling, 1991)

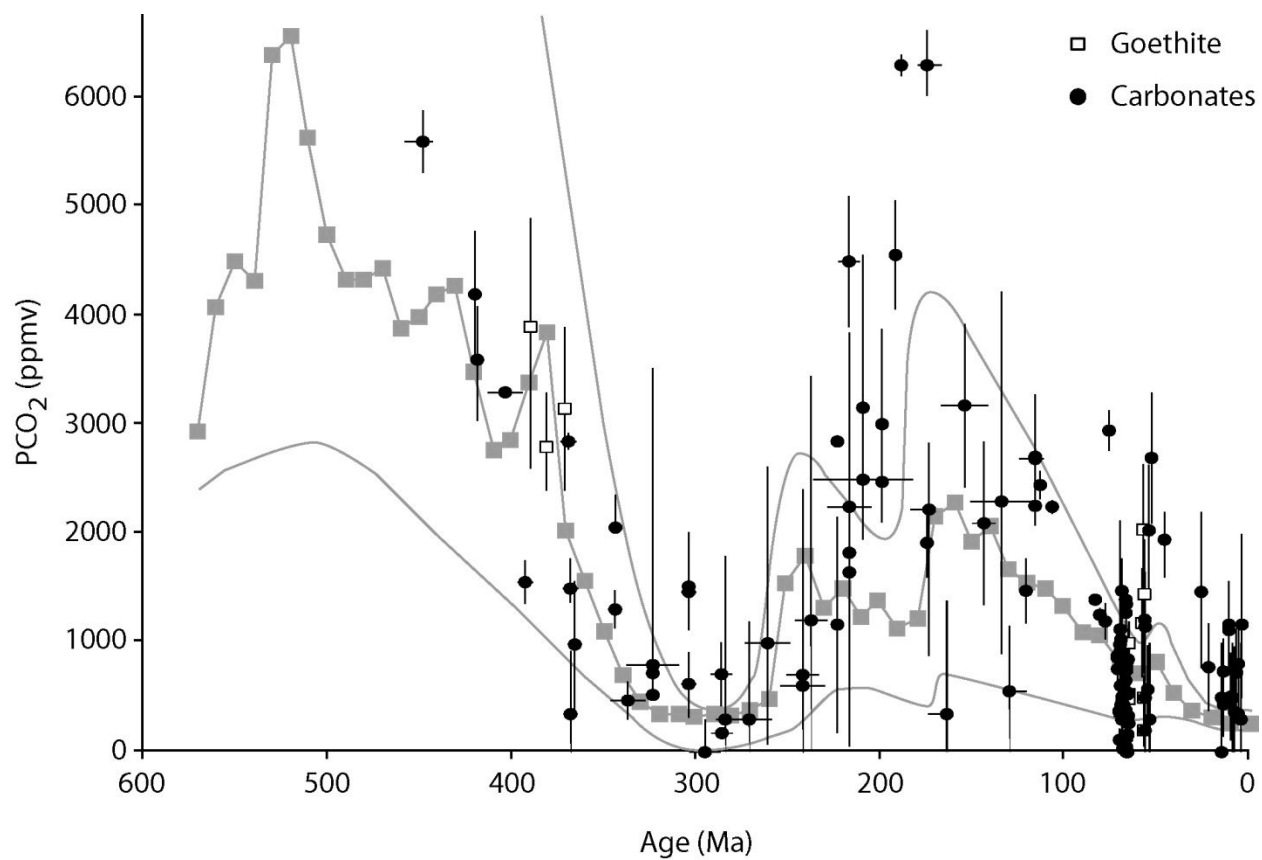


Figure 1.17: Paleo-PCO₂ estimates based on pedogenic carbonates (closed circles) and pedogenic goethites (open squares) compared to the general solution of the GEOCARB III model (Modified from Royer, 2001)

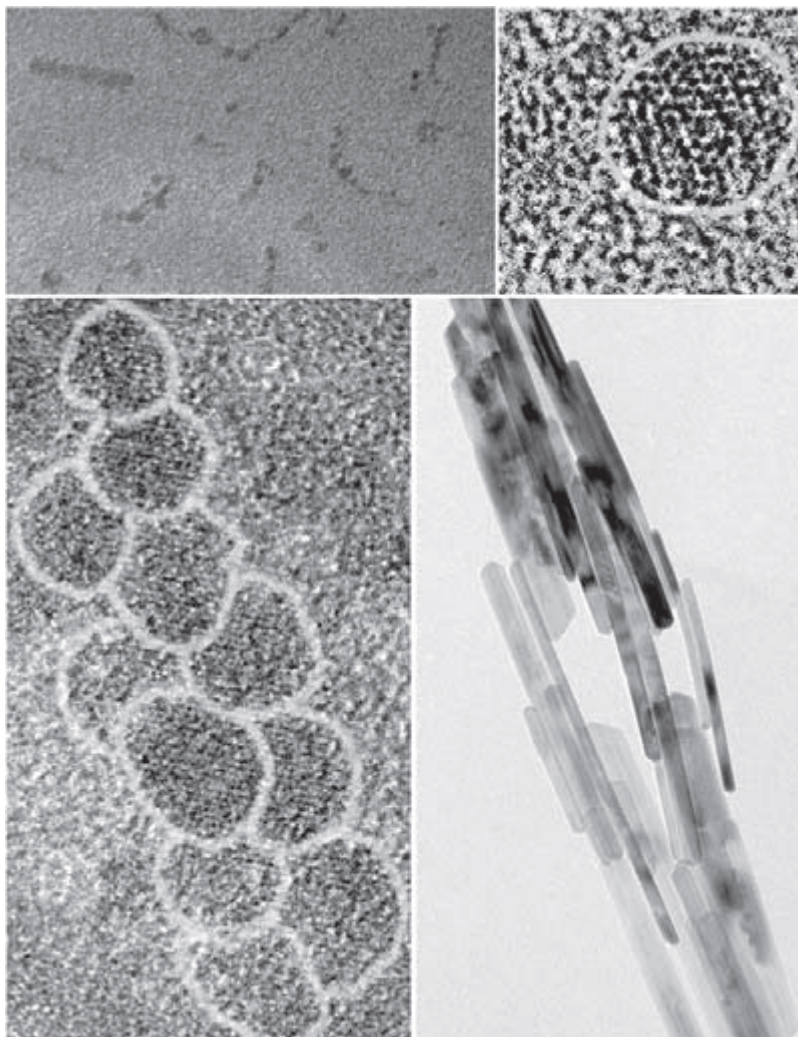


Figure 1.18: HRTEM images showing the stages of growth of goethite crystals from (b) nanodots, and (a) some elongate nanorods, to (d) micro goethite particles shown in TEM image. (c) HTREM image of nanorod showing that is made of aggregated nanodots (highlighted) and the elongate character of the nanorod (Guyodo et al., 2003)

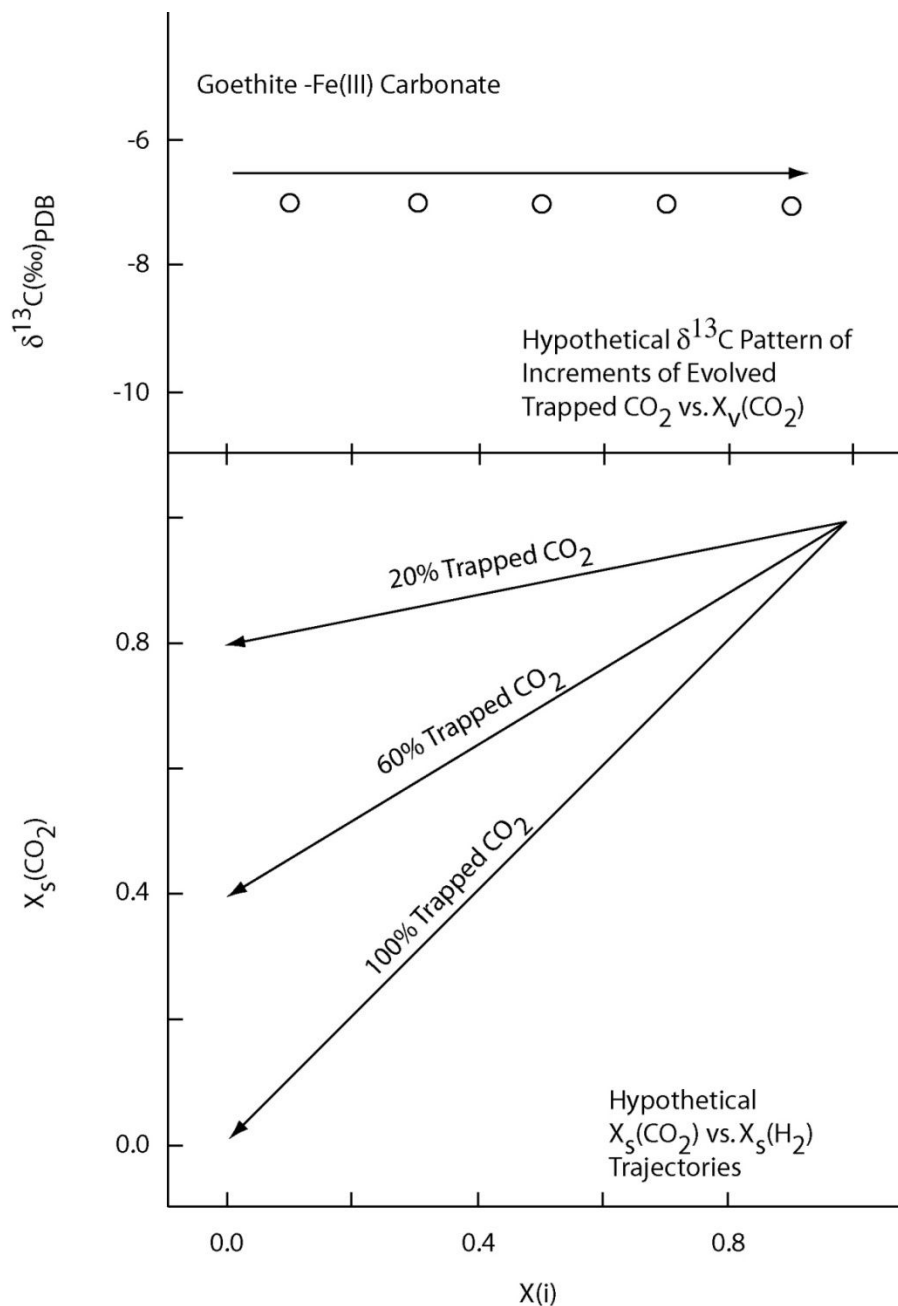


Figure 1.19: Expected response from a hypothetical goethite dehydration. Top graph shows the expected linear trend in $\delta^{13}\text{C}$ values if all carbon is from the same trapped source of CO_2 . The bottom graph shows the expected slope of $X_s(\text{CO}_2)$ vs. $X_s(\text{H}_2)$ depending on the fraction of goethite CO_2 that is trapped. The y intercept gives the fraction of CO_2 that is not trapped in the goethite structure (Yapp and Poths, 1991)

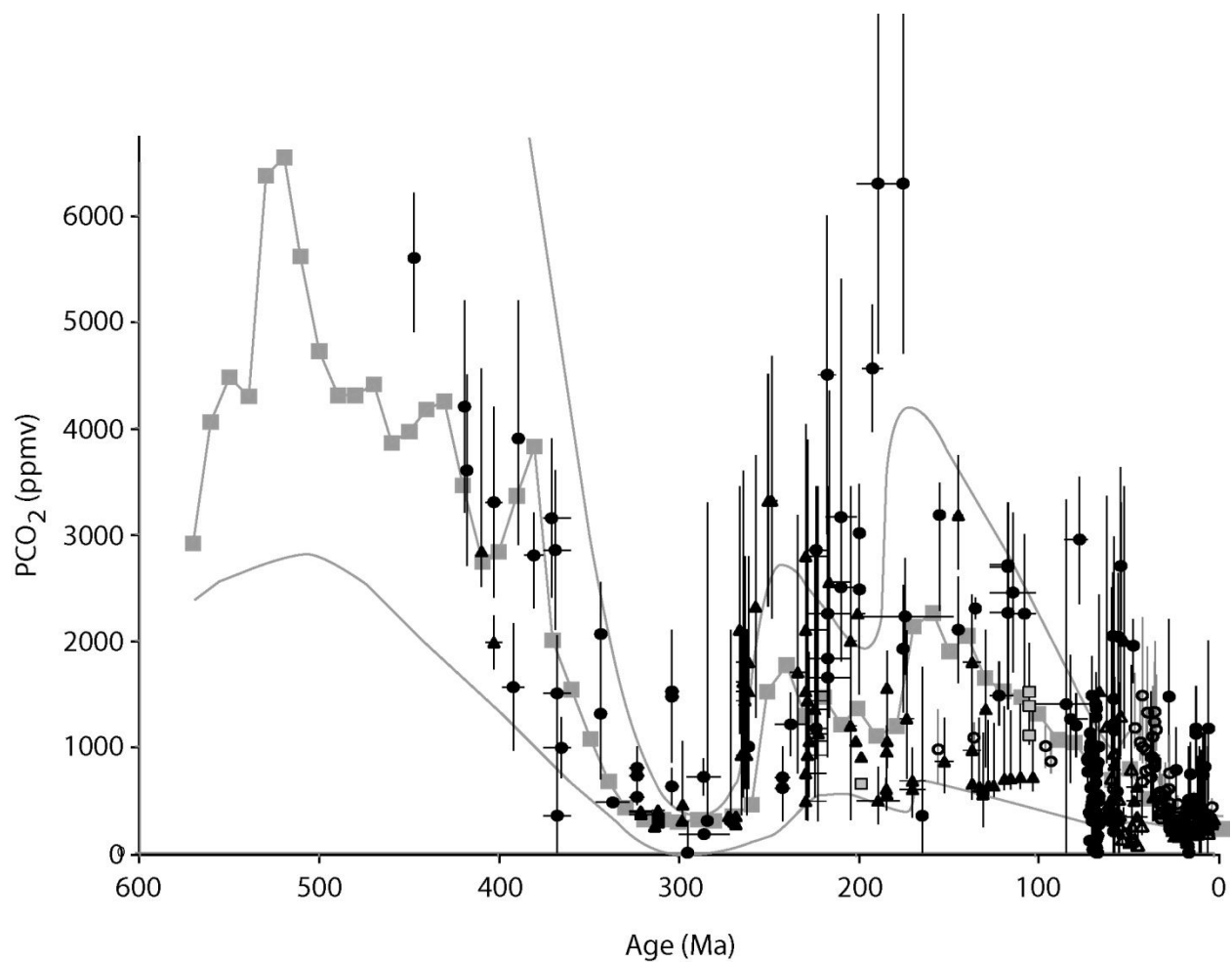


Figure 1.20: Compilation of all paleo-PCO₂ estimates from the discussed proxies compared to the general solution of the GOECARB III model (modified from Royer, 2001)

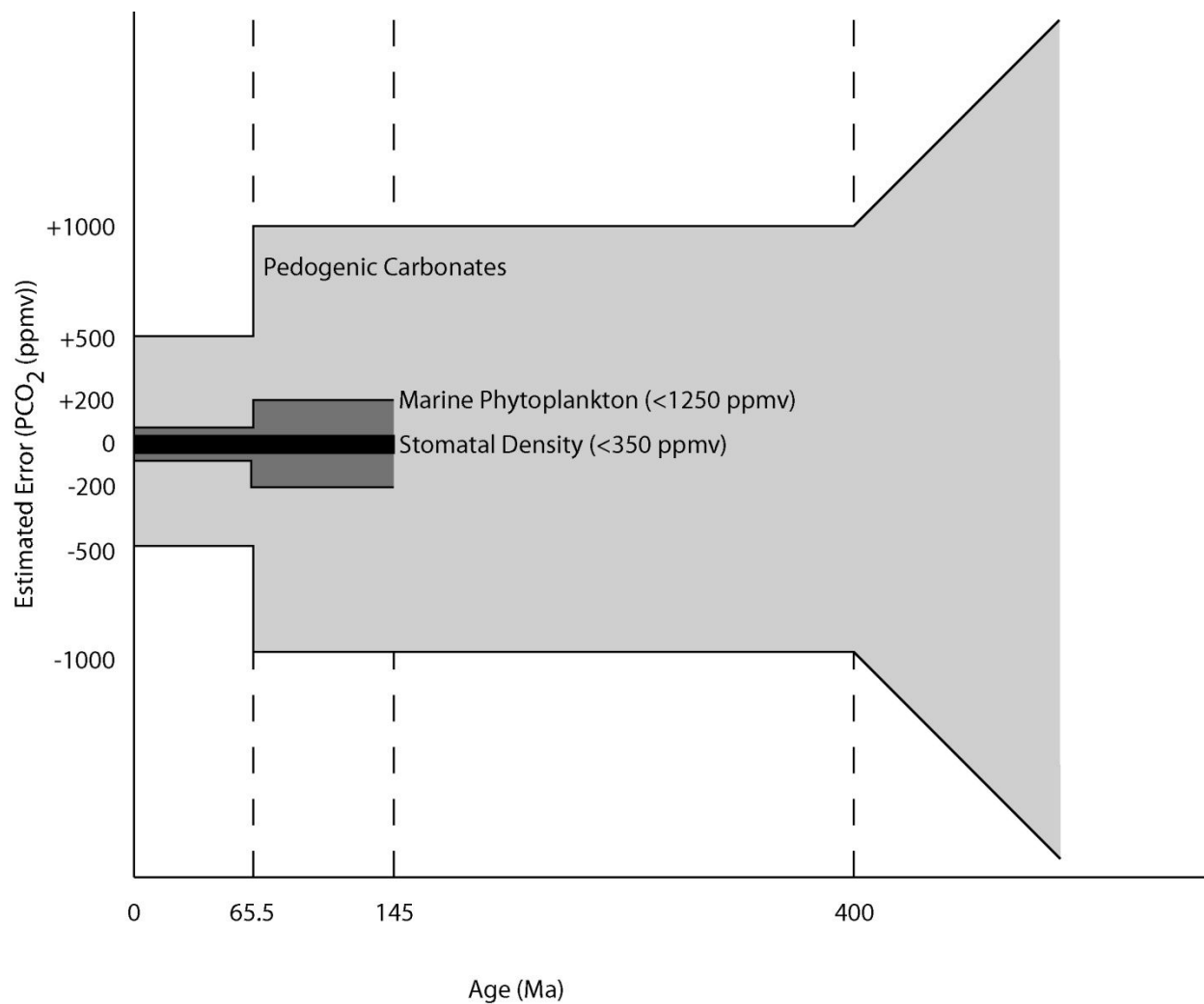


Figure 1.21: Summary of the time range and amount of uncertainty associated with pedogenic carbonates, stomatal index, and phytoplankton $\delta^{13}\text{C}$ values; maximum effective PCO₂ shown in parentheses for stomatal index and phytoplankton

CHAPTER 2

NUMERICAL MODELING OF SOIL PHYSICAL CHARACTERISTICS

2.1 INTRODUCTION

In the model described by Cerling (1991), the physical properties of the soil that affect the diffusion rate of CO₂ through soil are grouped into the term $S(z)$ (eqn. 1.19). This allows for the analytical solution of the differential equation used to describe one-dimensional Fickian diffusion (eqn. 1.10). While this term allows for variation in the amount of CO₂ produced in the soil with depth, there is no allowing for changes in the bulk density and air-filled porosity with depth, characteristics that determine the diffusion coefficient (D_s^*) of bulk CO₂ in soil (eqn. 1.14). In order to test the hypothesis that a more accurate description of the physical properties of the soil, as well as adding the ability to model the $\delta^{13}\text{C}$ value of the soil CO₂ (Bowen and Beerling, 2004), will result in a more accurately modeled solution, a finite difference solution of eqn. 1.10 was developed.

The finite difference model will allow either a continuous or step-wise function for bulk density with depth, which can be related to the porosity by the equation 1.15. Cerling (1991, Figure 5) shows the variation in the expected $\delta^{13}\text{C}$ value of the soil carbonate of -12.00 ‰ to 0.00 ‰ for a change in porosity from 0.1 to 0.5. If this variability is applied to the solutions for soil respiration rate plotted in figure 6 of Schroeder and Melear (1999), the higher respiration rate solutions should come closer to fitting the plotted data. Bulk density of the soil is not constant with depth (Perkins, 1987; Wilkinson et al., 2009; Wilson et al., 2011), and the implication is that increasing bulk density with depth following a minimum in the clay rich B

horizon will result in a decrease in porosity and therefore a decrease in the contribution of the atmospheric CO₂ to soil CO₂ during periods of high concentrations in the atmosphere; or increased soil respiration rates during periods of low atmospheric PCO₂. When considering the diffusion of CO₂ out of the soil, it is important to classify the effectiveness of the pore space as either effective, i.e. connected to the surface, or ineffective. There is evidence that as the bulk density of the soil increases, the ineffective pore spaces are collapsed first, so that there may be an increase in D_s^* even as soil bulk density increases (Arthur et al., 2012; Dorner et al., 2010).

In addition to D_s^* , the $S(z)$ term includes a function to describe an exponential decrease in soil CO₂ production (ϕ^*) with increasing depth (eqn. 1.18). This equation depends on the characteristic depth of CO₂ production, with shallow production depths allowing for more enrichment of soil carbonates, indicating an increase in the atmospheric component (Cerling, 1991, Figure 4). The characteristic soil depth that Cerling used for arid soils was 10 cm; Schroeder and Melear (1999) showed more enriched carbon isotopes in the bulk soil in the top 40 cm of the Panola Mountain soil, possibly indicating more active turnover in this portion of the soil and suggesting that the characteristic depth of CO₂ production was within the top 40 cm.

While the majority of soil CO₂ production takes place in the top 20-40 cm of the soil, the bulk of that CO₂ moves rapidly through the soil surface to the atmosphere. There is also CO₂ produced in the soil at greater depths, up to 1.5 meters, and in some cases much deeper, that is not as easily able to diffuse to the surface, resulting in the increased concentration of CO₂ in the soil at depth. While this CO₂ at depth is slow to diffuse through the soil, it does respond to changes in CO₂ production tending to increase to the maximum value during the growing season and decrease to the minimum during the winter months (Richter and Markewitz, 1995). The implication of this is that while the mean production depth is shallow in the soil, the production

depth that is relevant to the timescales that mineral growth occurs on would be better represented with a deeper characteristic depth.

This difference in source, between the surface where the CO₂ produced is dominated by the $\delta^{13}\text{C}$ value of the plants that are actively respiring, and the CO₂ at depth which is for the most part produced by the decomposition of organic material by soil microbes, can also result in a change in the $\delta^{13}\text{C}$ value of soil CO₂ with depth, Bowen and Beerling (2004) have developed a model to account for changes in the source of soil CO₂ with depth and soil pore space CO₂ concentrations with depth. The finite difference model has been modified so that this effect can be accounted for. This model divides the contributions to the soil CO₂ reservoir into three groups; rapid, slow, and stable, and then describes the inputs to each pool as well as the consumption, assimilation, and transformation of carbon from one pool to the next, including the contribution of the soil CO₂ (Figure 2.3).

The numerical model presented here will incorporate each of these refinements in an attempt to prove that they will result in a predicted soil CO₂ $\delta^{13}\text{C}$ values that more closely matches observed $\delta^{13}\text{C}$ values for CO₂ extracted from pedogenic gibbsite. The model results are compared to the data provided in Schroeder and Melear (1999) in an attempt to get a better fit for the data using the average growing season soil respiration rate.

2.2 METHODS

2.2.1 NUMERICAL MODELING

In order to solve eqn. 1.10 while allowing for the variation of parameters with depth, a numerical solution must be used; in this case a finite difference method is used. Equation 1.10 is recast as:

$$\frac{C_i^{k+1} - C_i^k}{\Delta t} = D_s^*(z) \left(\frac{(C_{i+1}^k - C_i^k) - (C_i^k - C_{i-1}^k)}{\Delta z^2} \right) + \phi^*(z) \quad (2.1)$$

where the variables are as listed in section 1.2.6.1 and the subscripts i and k are used to denote changes in depth and time respectively (Figure 2.2). Solving for C_i^{k+1} results in:

$$C_i^{k+1} = \Delta t \left[D_s^*(z) \left(\frac{C_{i+1}^k - 2C_i^k + C_{i-1}^k}{\Delta z^2} \right) + \phi^*(z) \right] + C_i^k \quad (2.2)$$

This equation is solved using code written in C++ that iterates the solution through time and runs until the total sum of squares of the difference between the last two iterations is less than 1×10^{-24} . All code for the model functions can be found in Appendix A. Using the finite difference solution allows for the independent solving of $D_s^*(z)$ and $\phi^*(z)$; the form of these functions is not restricted by the ability to easily solve them analytically, allowing for more detailed mathematical representations of these properties.

The physical properties of the soil were modeled in two ways. The first was using a continuous function which describes increasing bulk density or decreasing diffusion coefficient with depth (eqn. 2.3).

$$D_s^* = D_{air}^* (a + bz^2) \left(\frac{e}{d} \right) \quad (2.3)$$

where a , b , c , d , and e are coefficients used to adjust the shape of the curve. The values used in modeling are listed in table 1 and the curve shape can be seen in figure 2.4. Coefficients were adjusted in this equation to achieve a reasonably close fit by visual inspection to soil bulk density

data for a Cecil type soil (Pedon 9 from (Perkins, 1987)) and to allow for a gradual increase in D_s^* with depth. Values for all variables used in model runs are listed in table 1. The model was also run using stepwise functions of bulk density based on data for Cecil soil pedon 9 described by Perkins (1987) and using the difference between the 0 and -300 cm soil water pressure as described by Schroeder et al., (2006) based on a the south plot described by Bruce et al., (1983) (Figure 2.3 below).

The variation in soil CO₂ production is modeled in two ways; an exponential decrease described by equation 1.18 and using the model developed by Bowen and Beerling (Bowen and Beerling, 2004) . Figure 2.6 shows how the function of equation 1.18 responds to changes in the characteristic depth of CO₂ production. The model was run with characteristic depths of 20cm, the value typically used for pedogenic carbonates and 60cm to represent the possibility that while most of the production of CO₂ takes place in the top 20-40cm, that carbon is quickly removed to the atmosphere. As a result, the carbon that is in the pore space at depth may be more representative of the CO₂ that is occluded in soil minerals.

In order to effectively estimate the PCO₂ of the atmosphere, it is important to have a reliable estimate of the organic matter that was contributing CO₂ to the soil. Usually, this is obtained by measuring the $\delta^{13}\text{C}$ value of some organic material that is in place with the soil carbonate. In paleosols, especially those from arid environments where soil carbonates are common, it is likely that there is not enough organic material remaining to measure, or the organic material that is there has been altered. As seen in figure 1.14, the estimation of the $\delta^{13}\text{C}$ value of the organic matter in the soil can have a large effect on the estimation of PCO₂ in the atmosphere. In addition to this difficulty, there are processes that take place in the soil that alter the $\delta^{13}\text{C}$ value of the soil organic material (SOM) and result in variation in the $\delta^{13}\text{C}$ value with

depth. The decomposition of SOM tends to enrich the residual in ^{13}C . This enrichment is believed to be related to the selective decomposition of organic matter (Bowen and Beerling, 2004; Buchmann et al., 1997; Krull and Skjemstad, 2003; Nadelhoffer and Fry, 1988 ; Schweizer et al., 1999).

The model of Bowen and Beerling divides the SOM into three compartments, rapid (r), slow (sl), and stable (st). Organic material is added to the fast and slow compartments through the surface and at depth through root inputs. Root inputs are assumed to have an exponential decrease with depth as described by the equation

$$\zeta_{i,z} = \frac{\zeta_i}{Z} e^{-(z/Z)} \quad (2.4)$$

where ζ is the root input with subscripts i and z representing the pool and depth respectively. Z represents the scaling depth. This model assumes that the organic material in the soil move vertically by advection and the material at depth in the soil is more restricted in motion than the material at the surface. The advection function is linear with depth and is represented by the equation:

$$a_z = a_0(1 - z\tau) \quad (2.5)$$

Where a_0 is the advection constant at the surface and τ is the scaling term. As carbon is consumed by microbes (k), it is released as CO_2 , assimilated into microbes (e), transformed to a more stable pool (t), or returned to the pool it originated in (Figure 2.3). The equations that describe the change in concentration in each pool over time are

$$\frac{\partial C_{r,z}}{\partial t} = -a_z \frac{\partial C_r}{\partial z} + \zeta_{r,z} - k_r C_{r,z} [1 - e_r(1 - t_r)] \quad (2.6)$$

$$\frac{\partial C_{sl,z}}{\partial t} = -a_z \frac{\partial C_{sl}}{\partial z} + \zeta_{sl,z} - k_{sl} C_{sl,z} [1 - e_{sl}(1 - t_r)] + k_r C_{r,z} e_r t_r \quad (2.7)$$

$$\frac{\partial C_{st,z}}{\partial t} = -a_z \frac{\partial C_{st}}{\partial z} - k_{st} C_{st,z} (1 - e_{st}) + k_{sl} C_{sl,z} e_{sl} t_{sl} \quad (2.8)$$

These equations are used to calculate the concentration of ^{12}C in the soil, using a kinetic isotope fractionation factor (α) for microbial respiration (eqn. 2.9), it is possible to calculate the concentration of ^{13}C (C^*) in the soil using equations 2.10 – 2.12.

$$\alpha = \frac{R_{product}}{R_{reactant}} \quad (2.9)$$

$$\frac{\partial C_{r,z}^*}{\partial t} = -a_z \frac{\partial C_{r,z}^*}{\partial z} + \zeta_{r,z}^* - k_r C_{r,z}^* [1 - (1 - [1 - e_r]\alpha)(1 - t_r)] \quad (2.10)$$

$$\begin{aligned} \frac{\partial C_{sl,z}^*}{\partial t} = & -a_z \frac{\partial C_{sl,z}^*}{\partial z} + \zeta_{sl,z}^* - k_{sl} C_{sl,z}^* [1 - (1 - [1 - e_{sl}]\alpha)(1 - t_{sl})] \\ & + k_r C_{r,z}^* (1 - [1 - e_r]\alpha) t_r \end{aligned} \quad (2.11)$$

$$\frac{\partial C_{st,z}^*}{\partial t} = -a_z \frac{\partial C_{st,z}^*}{\partial z} - k_{st} C_{st,z}^* (1 - e_{st}) \alpha + k_{sl} C_{sl,z}^* (1 - [1 - e_{sl}]\alpha) t_{sl} \quad (2.12)$$

The CO_2 production of ^{12}C and ^{13}C are calculated by the equations:

$$\omega_z = k_r C_{r,z} (1 - e_r) + k_{sl} C_{sl,z} (1 - e_{sl}) + k_{st} C_{st,z} (1 - e_{st}) + (\zeta_{r,z} + \zeta_{sl,z}) \quad (2.13)$$

$$\begin{aligned} \omega_z^* = & k_r C_{r,z}^* (1 - e_r) \alpha + k_{sl} C_{sl,z}^* (1 - e_{sl}) \alpha + k_{st} C_{st,z}^* (1 - e_{st}) \alpha \\ & + [(\zeta_{r,z} + \zeta_{sl,z}) \times R_{veg}] \end{aligned} \quad (2.14)$$

The code for solving this model can be found in section A1.4. This production term is divided by the porosity to volumetrically normalize the pore space and is substituted into equation 1.10 in the place of ϕ (Bowen and Beerling, 2004).

Model run solutions were compared to stable isotope composition data from the Panola Mountain site (Schroeder and Melear, 1999).

2.3 RESULTS

2.3.1 VARIATIONS IN BULK DENSITY AS A FUNCTION OF DEPTH

The model was solved using three different inputs for varying bulk density of the soil with depth. Two of the profiles were constructed using data from Cecil type soils in Georgia. The first soil is identified as the south plot and is described by Bruce et al. (1983) and the second is identified as Pedon 9 and is described by Perkins (1987). These soils were chosen because they showed opposite trends in bulk density with depth; the bulk density of the South Plot increases to a maximum between 30 and 60 cm depth and then decreases slightly with a small increase between 70 and 90 cm. Conversely, the bulk density of Pedon 9 decreases with depth to a minimum between 69 and 110 cm (Figure 2.4). In addition to the data from the soil profiles, the function described in equation 2.3 was used to try to match the same change in bulk density with depth as the South Plot, shifted to lower bulk density values. The values for bulk density were shifted because the model solutions using the South Plot data were shifted toward slightly more ^{13}C depleted $\delta^{13}\text{C}$ values compared to the data points for the model solution with the South Plot data. Decreasing the bulk density serves to increase the porosity which shifts the solution to more ^{13}C enriched $\delta^{13}\text{C}$ values (Figure 2.5). In this case the best fit for the model solution comes with a soil respiration rate of $75 \text{ gC m}^{-2} \text{ yr}^{-1}$ using the exponentially decreasing function to

describe bulk density with depth. Compared to the analytical solution using the average bulk density of the exponential function, the solution using the function is a closer match to the data at 30 cm depth. The parameters for all model solutions plotted in figure 2.5 are listed in table 2.1.

2.3.2 VARIATIONS IN CO₂ PRODUCTION AS A FUNCTION OF DEPTH

The model was solved using two values for the characteristic depth term (Z) in equation 1.19 and two different values of soil respiration rate of the soil (Figure 2.6). The characteristic depths were chosen as 20 cm, which is the typical depth of maximum CO₂ production and a deeper depth of 60 cm to address the possibility that it is the CO₂ produced at depth that controls the $\delta^{13}\text{C}$ value of the soil CO₂ as most of the CO₂ produced at shallower depths immediately fluxes through the surface to the atmosphere.

The solution for $Z = 20$ never matches the Panola Mountain data for any reasonable soil respiration rate; even at $900 \text{ gC cm}^{-2} \text{ y}^{-1}$, the calculated $\delta^{13}\text{C}$ value of soil CO₂ is enriched in ¹³C compared to the measured values (Figure 2.7). The model solution for $Z = 60$ cm is a good match to the measured data for $Q = 300 \text{ gC m}^{-2} \text{ y}^{-1}$. Neither the deep nor the shallow depths chosen for the characteristic depth of soil CO₂ production are good matches if the average growing season soil respirations rates are used; in the case of deep soil CO₂ production, the modeled soil CO₂ is too depleted in ¹³C (not shown), while the shallow CO₂ production depths results in enriched. It should be noted that using a shallow depth results in approximately fifty percent decrease in the concentration of CO₂ at depth in the soil relative to the concentration calculated using the deep depth (Figure 2.8).

2.3.3 BOWEN AND BEERLING MODEL OF SOIL CO₂ $\delta^{13}\text{C}$

Model results using the Bowen & Beerling model described in section 2.2.1 show that when the model parameters are adjusted to similar functions of soil CO₂ production with depth

(Figure 2.11), the calculated $\delta^{13}\text{C}$ value of is more depleted in ^{13}C than the standard model using a function of soil CO_2 production with depth. As a result, in the case of the shallow characteristic depth model ($Z = 20\text{cm}$), the solution was a slightly better fit; while the deeper characteristic depth model ($Z = 60\text{cm}$) was too depleted compared to the measured data. Therefore, assuming that the shallow characteristic depth of CO_2 production is correct, this model is useful in that the soil respiration rate that is required to produce a reasonable model solution is closer to values that are measured in the field. If, on the other hand, the deeper Z value is correct, this model implies that a slower respiration rate is appropriate for modeling the $\delta^{13}\text{C}$ value of soil CO_2 that is relevant to the CO_2 preserved in pedogenic gibbsite. In both cases the concentration of CO_2 in the soil profile is different compared to values calculated for the models solved using equation 1.19 (Figure 2.11). The fact that the concentration of CO_2 in the soil for the $Z=20\text{cm}$ model using the Bowen & Beerling method is less than the $Z = 20$ model using equation 1.19, and the solution is more depleted indicates that the reason for the shift in the solution is not simply a result of the change in concentration with depth.

2.3.4 COMBINED VARIATIONS IN D_s^* AND ϕ^*

Models were run using both the variation in D_s^* in the form of data from the South Plot, Pedon 9, and $D_s^*(z)$ (section 2.3.1) and the exponential change in CO_2 production with depth (figs. 2.12 and 2.13). $\delta^{13}\text{C}$ values calculated using the shallow characteristic depth (20cm) in general were more depleted than models using the same function for CO_2 production with constant D_s^* . Comparing these solutions to those that had a constant soil CO_2 production rate with depth, the fit to the data is comparable, but the soil respiration rates for the models are much different (Figure 2.5). In the case of constant ϕ , the soil respiration rate is very low ($75 \text{ gC m}^{-2} \text{ y}^{-1}$); while the respiration rate for models using $\phi(z)$ is $900 \text{ gC m}^{-2} \text{ y}^{-1}$. The models that used the

deep characteristic depth ($Z=60\text{cm}$) show a similar increase in the soil respiration rate ($300\text{ gC m}^{-2}\text{ y}^{-1}$).

2.4 DISCUSSION

In this study, the diffusion model was used to predict the soil respiration rate of the soil because the PCO_2 of the atmosphere was assumed to be constant at 250 ppm. When using this model to predict PCO_2 , the soil respiration rate will be assumed and the PCO_2 will be modeled. Therefore, these models could also be solved to predict the PCO_2 of the atmosphere. Based on all model solutions except for models where soil CO_2 production is allowed to vary with depth (M0027, M0031, and M0034-M0041) the predicted soil respiration rate is 8 to 9 times less than the typical soil respiration rate for a deciduous forest of $647\text{ gC m}^{-2}\text{ y}^{-1}$. This corresponds to a prediction of PCO_2 of the atmosphere that is 8 to 9 times greater than the assumed value, or 2000 to 2250ppmv. Therefore, the conclusion must be either this model is not able to predict PCO_2 of the atmosphere during soil formation, the PCO_2 of the atmosphere was 2000 – 2250 ppmv, or the soil respiration rate was slower.

^{14}C ages of CO_2 trapped in the gibbsite structure from the Panola Mountain soil profile show at least two distinct populations of soil mineral age. Near the surface the model ^{14}C ages are ca. 3000 years, while deeper in the profile the ages are much older (ca. 8000 years) (Schroeder et al., 2001). One implication of this is that the minerals deep in the soil have trapped CO_2 that was in equilibrium with soil conditions that are different than the surface minerals. As the soil weathering front moves downward, into the parent material, there appears to be at least three zones of mineral formation. At the surface, where the high concentration of organic acids promotes mineral weathering, the minerals are cycled and perhaps on long time scales continuously dissolving and precipitating in the zone of rapid carbon turnover, which in the

Panola Mountain data would correspond with the depth of the youngest age, about 40 cm (Schroeder et al., 2001). As the soil profile thickens, the newly formed gibbsite at the weathering front retains the age of its initial formation while the gibbsite closer to the surface begins to be dissolved and precipitated, and therefore the $\delta^{13}\text{C}$ values of the trapped CO_2 are more likely to be in equilibrium with current conditions.

Following from this, the assumption that the mean growing season soil respiration rate is appropriate should be questioned. If in fact, the soil minerals show evidence of representing discrete periods of time on long time scales, perhaps they are also representative of discrete intervals on short-time scales as well. Because of the rapid rates of change of CO_2 efflux and storage change on the same time scales, the soil CO_2 can be said to be in steady state as conditions change (Jassal et al., 2005). As discussed in section 3.4, there is evidence of seasonal variation in the $\delta^{13}\text{C}$ value of pedogenic carbonates (Breecker et al., 2009), the implication of this is that mineral precipitation is episodic rather than continuous and the conditions that favor mineral precipitation are the conditions that are recorded in the $\delta^{13}\text{C}$ of pedogenic gibbsite. Therefore, identification of conditions where gibbsite is most likely to form should give some indications of the conditions that are preferentially recorded. A plot of aluminum species activity vs. pH (Figure 2.14) shows that gibbsite ($\text{Al}(\text{OH})_3$) is the dominant monovalent species of Al between pH 6 and 8. Soil pH is generally acidic due to CO_2 dissolved in rainwater and organic acids produced in the soil. Increased soil PCO_2 results in more HCO_3^- in the soil water and higher acidity which is responsible for increasing the rate of chemical weathering of silicate minerals (Berner and Ji-Long, 1997). If on the other hand, the soil PCO_2 is reduced, due to reduced production, which can be correlated to precipitation and temperature (Jassal et al., 2005) (Raich and Schlesinger, 1992), the alkalinity of the soil will be increased (Norton et al., 2001).

Based on this discussion, I propose that the low respiration rate of CO₂ predicted by the model may be accurately recording periods of low CO₂ production, which are characterized by low soil PCO₂ and thus soil water pH that is higher, and approaching the range required for gibbsite precipitation.

A third possibility is that there is a discontinuity between the soil CO₂ produced at depth in the soil and the CO₂ produced near the surface. In a typical soil profile, the PCO₂ of the soil gas increases with depth because as depth increases the connectivity of the pore spaces with the surface decreases and the CO₂ concentration builds up over time. Most of the CO₂ that is respired through the surface is produced in the shallow portion of the soil (Jassal et al., 2005). The difference between modeled and measured respiration rates may be explained by this difference in diffusion between the surface and the samples at depth. This consideration is especially important for the utility of pedogenic gibbsite as a proxy for paleo-PCO₂ because generally in a paleosol the deep samples are more likely to be preserved and sampled.

Finally, Schroeder et al., (2006) introduced the idea that the $\delta^{13}\text{C}$ values of pedogenic gibbsite may be representative of a long-term respiration rate. Briefly, the idea is that the soil respiration rate recorded in the soil minerals is distinct from the instant soil respiration rate that is measured at the surface, a phenomenon that is known to occur in other geologic processes. The extension of this idea is that the process of gibbsite precipitation appears to happen slowly and continuously through time over long time scales, while in reality the process progresses in episodic events that occur under conditions favorable for mineral formation. As in the discussion above, it seems likely that gibbsite formation would occur more often during times of low soil CO₂ concentration, low water content, and therefore low soil respiration rates such as might be expected during a summer drought or in areas with dry winter climates.

2.5 CONCLUSIONS

The discrepancies between modeled and measured soil respiration rates using the $\delta^{13}\text{C}$ value of CO_2 trapped in pedogenic gibbsite seem to indicate that there is a disconnect between the model and the reality of the natural system. Before this system can be used effectively as a proxy for paleo- PCO_2 these issues need to be resolved. In order to discriminate between the possible errors, the sensitivity of the model to natural variations in the factors that are estimated will be assessed using the Monte Carlo method in Chapter 3. The data that was collected at Panola Mountain will be replicated at a different site in an attempt to determine whether the model can be used under different conditions and to see if the same discrepancies are repeated. The remaining sections will attempt to determine which of the explanations offered above are correct. Ultimately it is hoped that these additional refinements will allow for a useful proxy for paleo- PCO_2 that is comparable to the current model using pedogenic carbonates, to allow verification of the results obtained by this method and to refine the mass balance models.

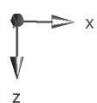
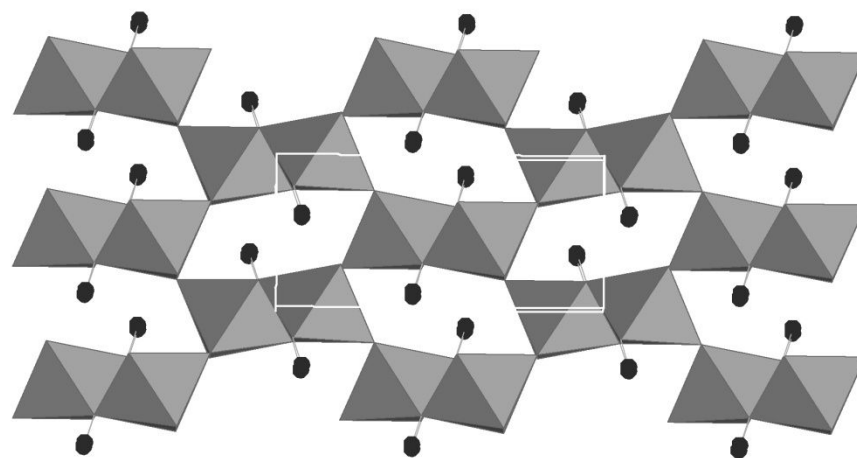


Figure 2.1 Crystal structures of goethite. Note the open channel along the c axis in the goethite structure.

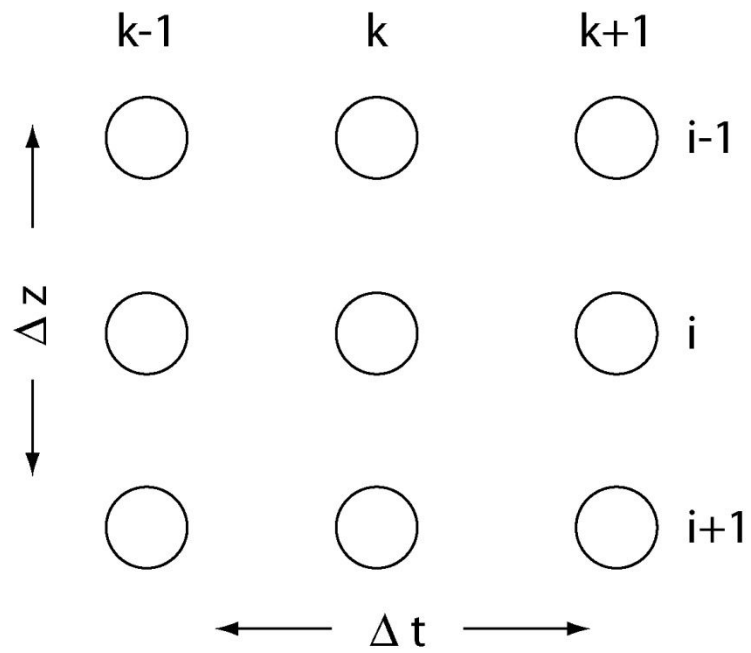


Figure 2.2: Schematic representation of the finite difference notation showing the change in time as opposed to the change in depth

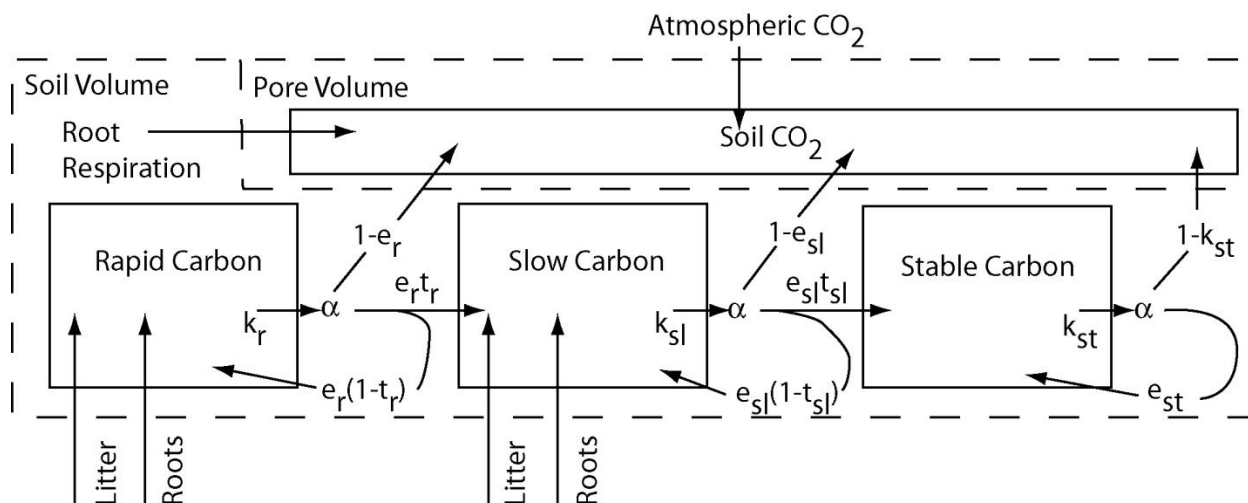


Figure 2.3: Box model showing the transfer of carbon between the fast, slow, and stable reservoirs, and the soil pore gas for the Bowen and Beerling model (Bowen and Beerling, 2004)

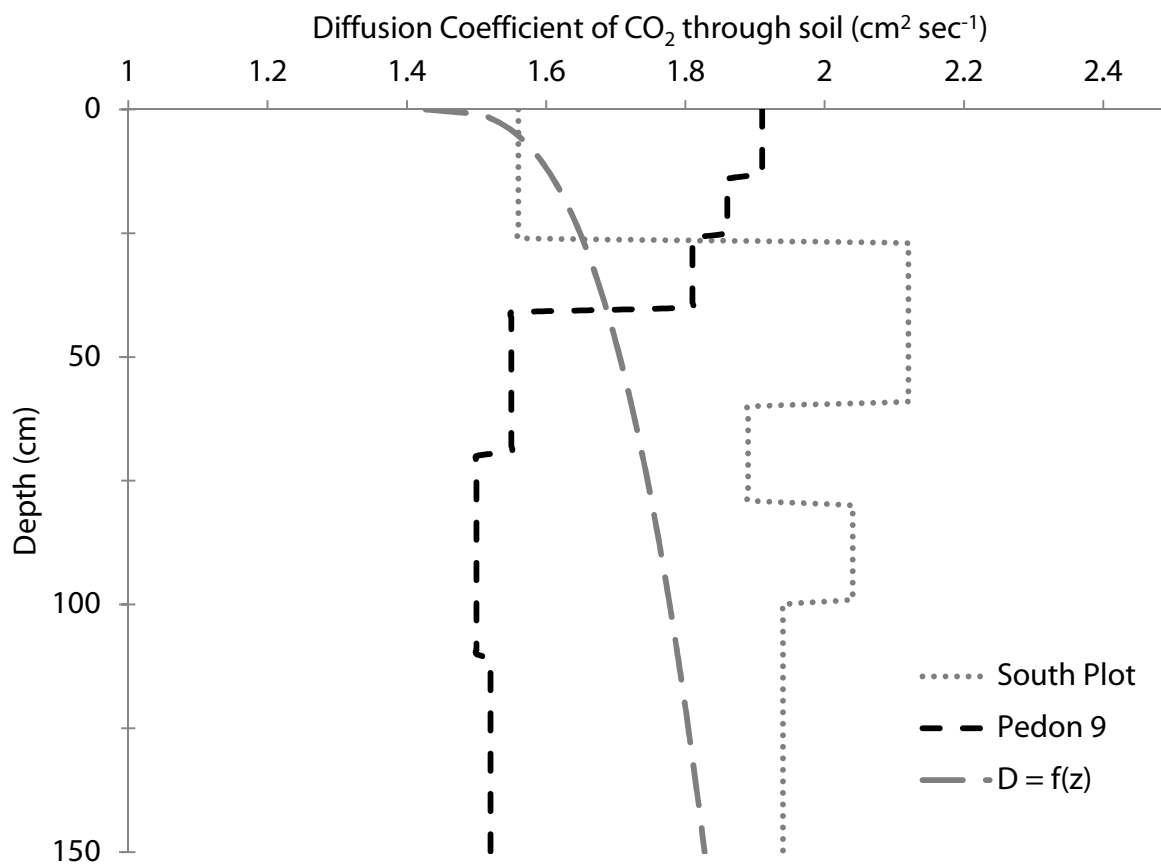


Figure 2.4: Step-wise functions for D_s^* calculated using data and parameters in table 2.2 for the South Plot (dotted line), Pedon 8, (dashed line) and the exponential function in equation 2.3.

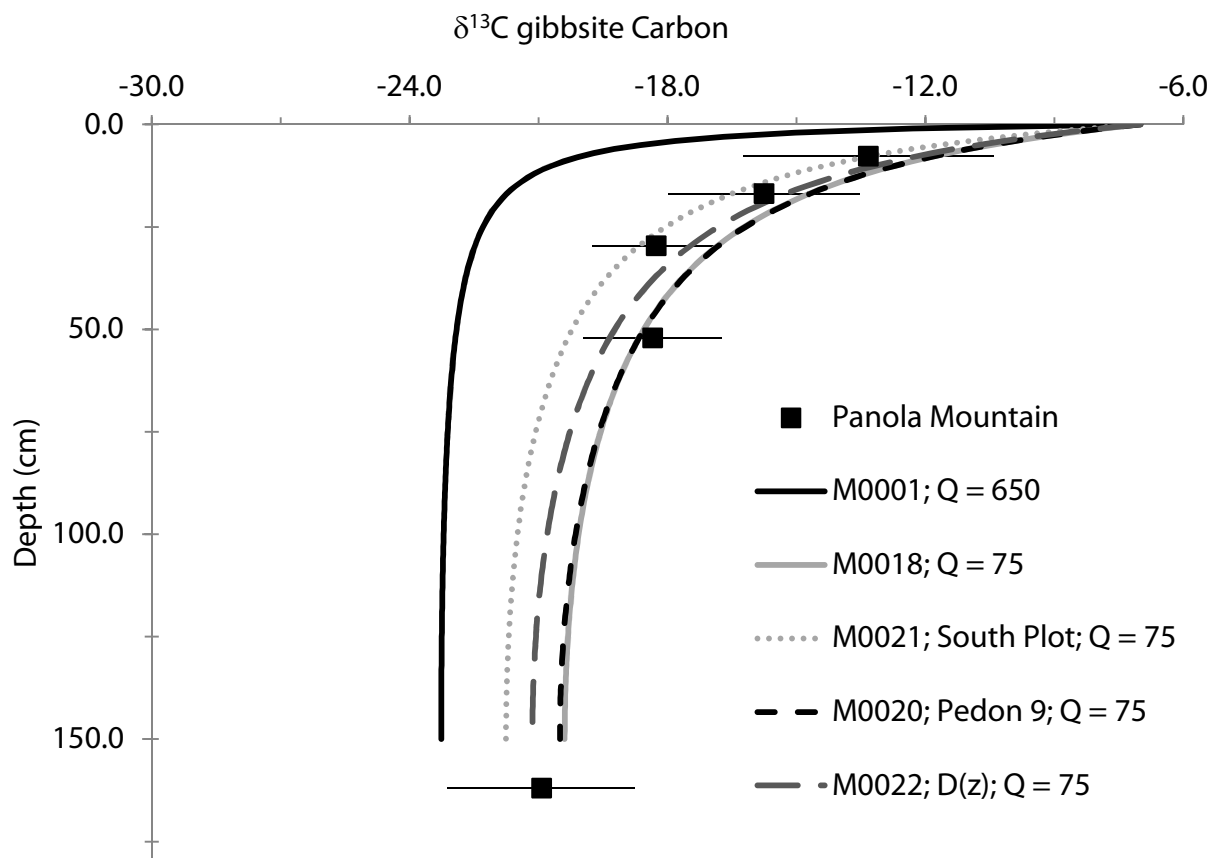


Figure 2.5: Model solutions for changes in D_s^* as a function of depth using parameters in tables 2.1 and 2.2. Q = Soil respiration rate in $\text{gC m}^{-2} \text{y}^{-1}$. Data points are from the Panola Mountain soil profile with error bars showing maximum variation between replicate samples.

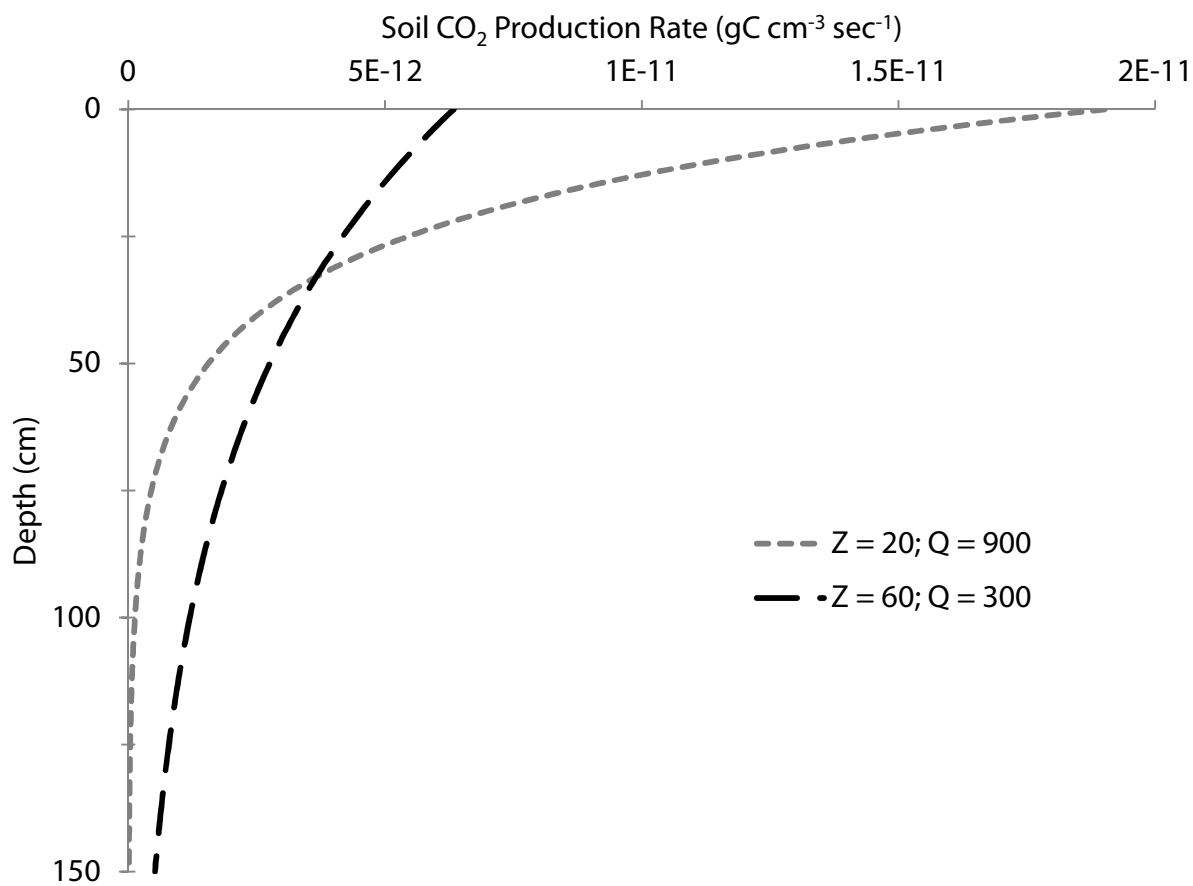


Figure 2.6: Distributions of soil CO₂ production with depth based on equation 1.18.

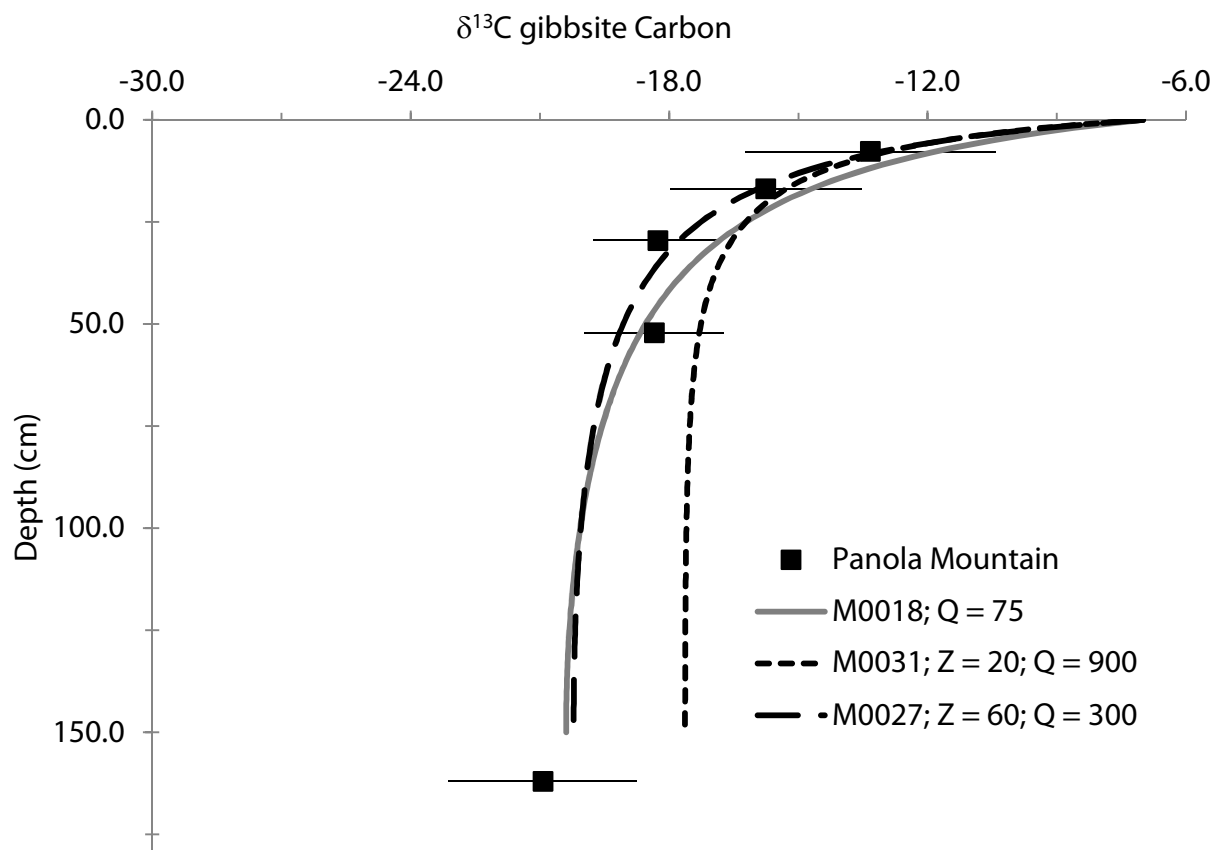


Figure 2.7: Model solutions for changes in the characteristic depth (Z) of soil CO_2 production using parameters in table 2.2. Q = Soil respiration rate in $\text{gC m}^{-2} \text{y}^{-1}$. Data points are from the Panola Mountain soil profile as described in Figure 2.5

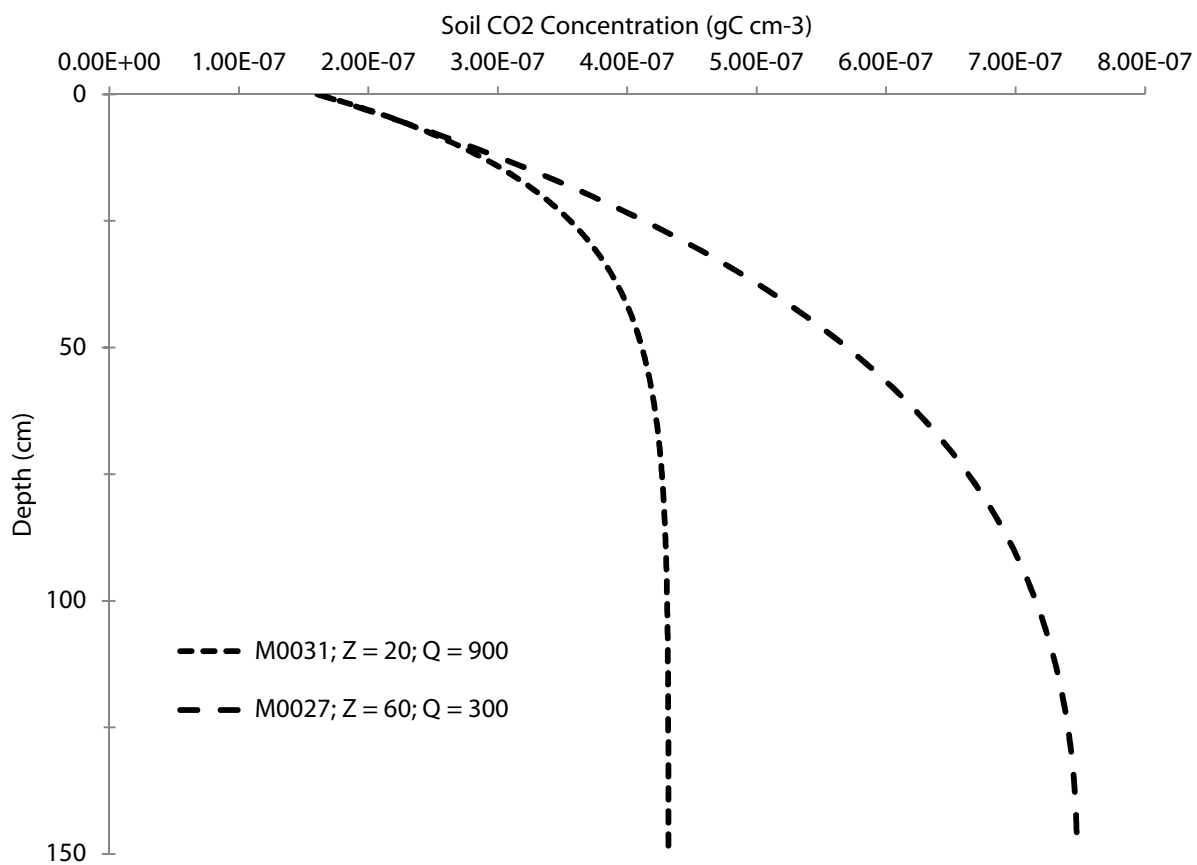


Figure 2.8: Calculated concentration of CO₂ vs. depth for the distributions of CO₂ production vs. depth shown in Figure 2.6. Q = soil respiration rate in gC m⁻² y⁻¹.

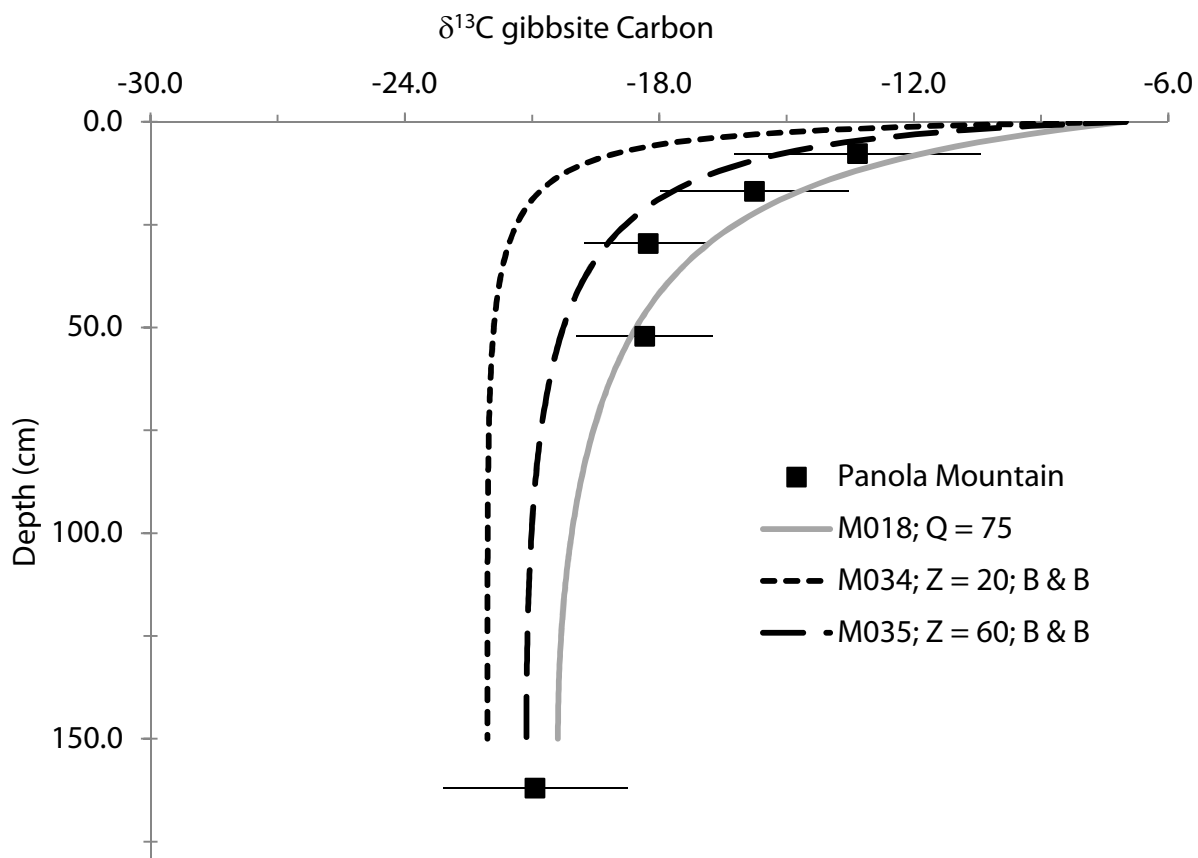


Figure 2.9: Model solutions for incorporation of the model by Bowen & Beerling (2004) for CO_2 production. Models solved using parameters in table 2.2. Q = Soil respiration rate in $\text{gC m}^{-2} \text{y}^{-1}$. Data points are from the Panola Mountain soil profile as described in Figure 2.5

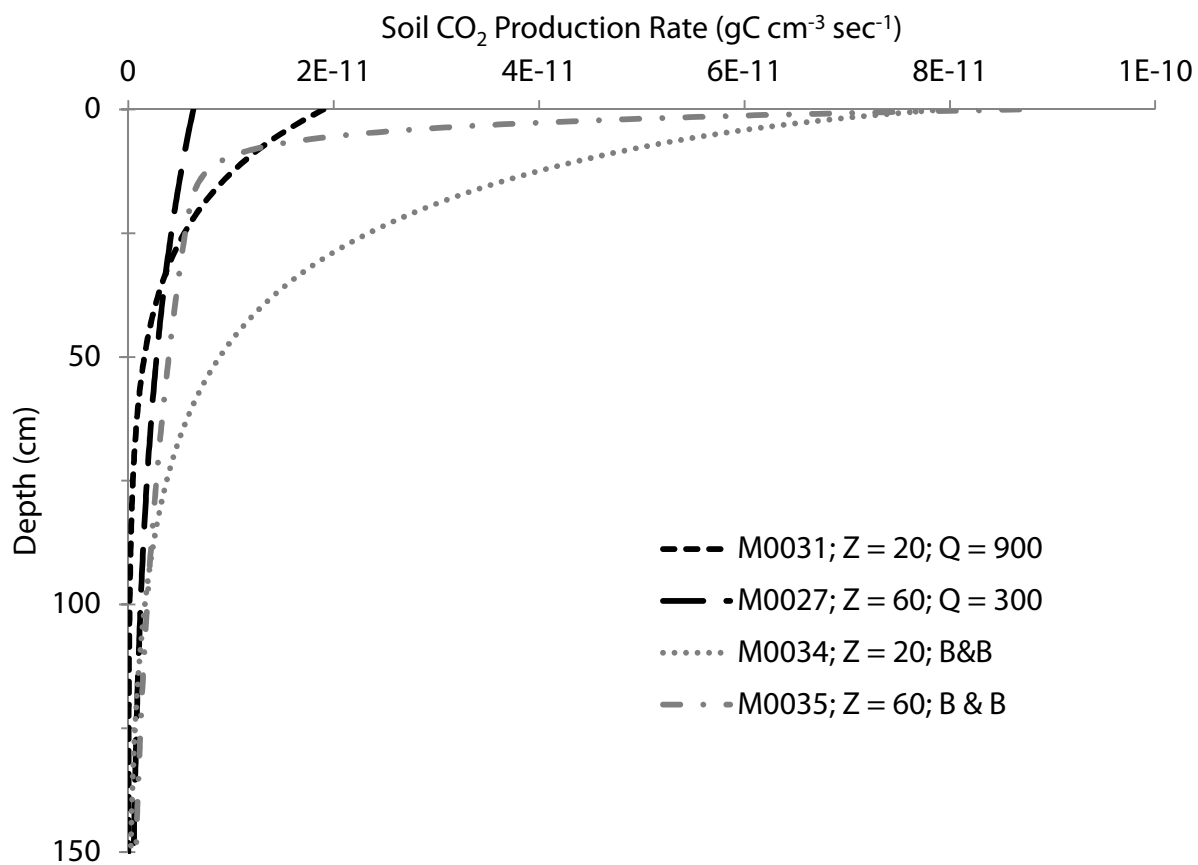


Figure 2.10 Soil CO₂ production rate vs. depth for models using eqn. 1.18 (M0031 & M0027) and the Bowen and Beerling model (2004) (M0034 & M0035).

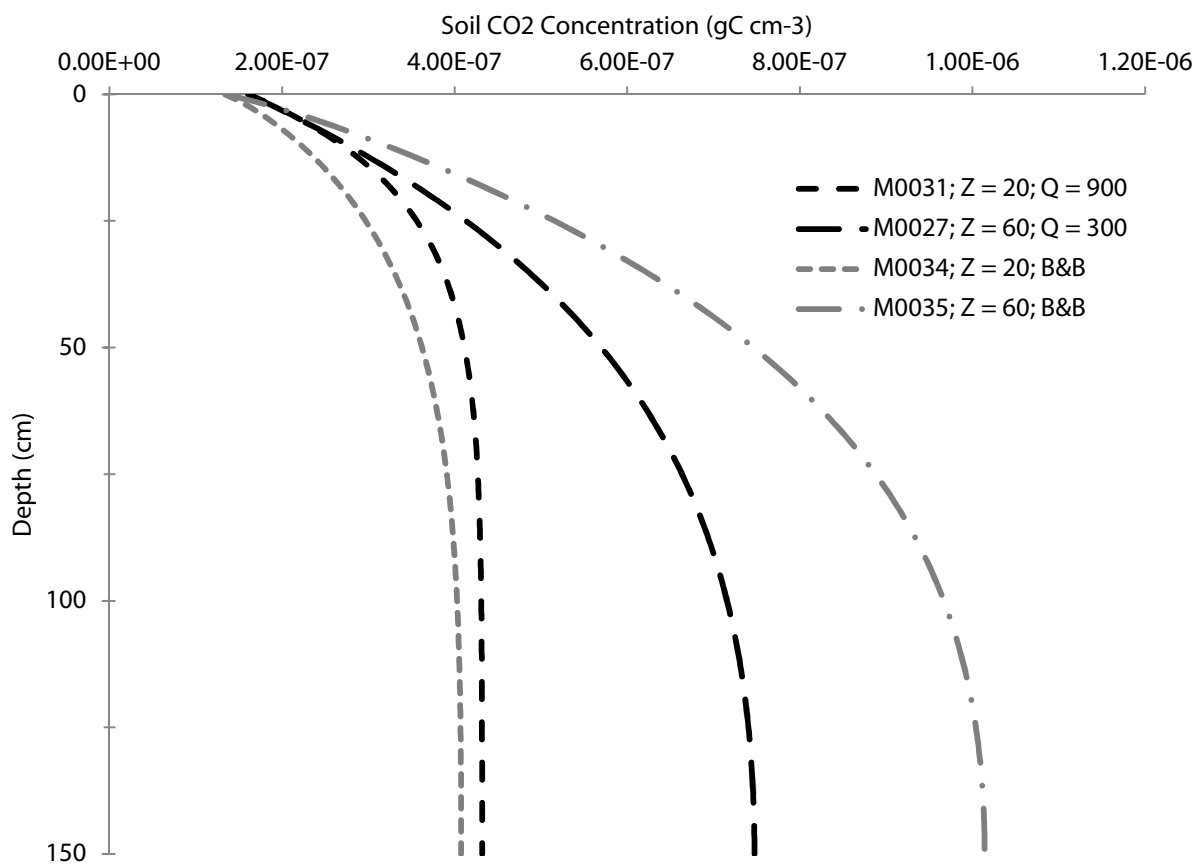


Figure 2.11 Concentrations of CO₂ vs. depth calculated by models used in figs. 2.10 and 2.9.

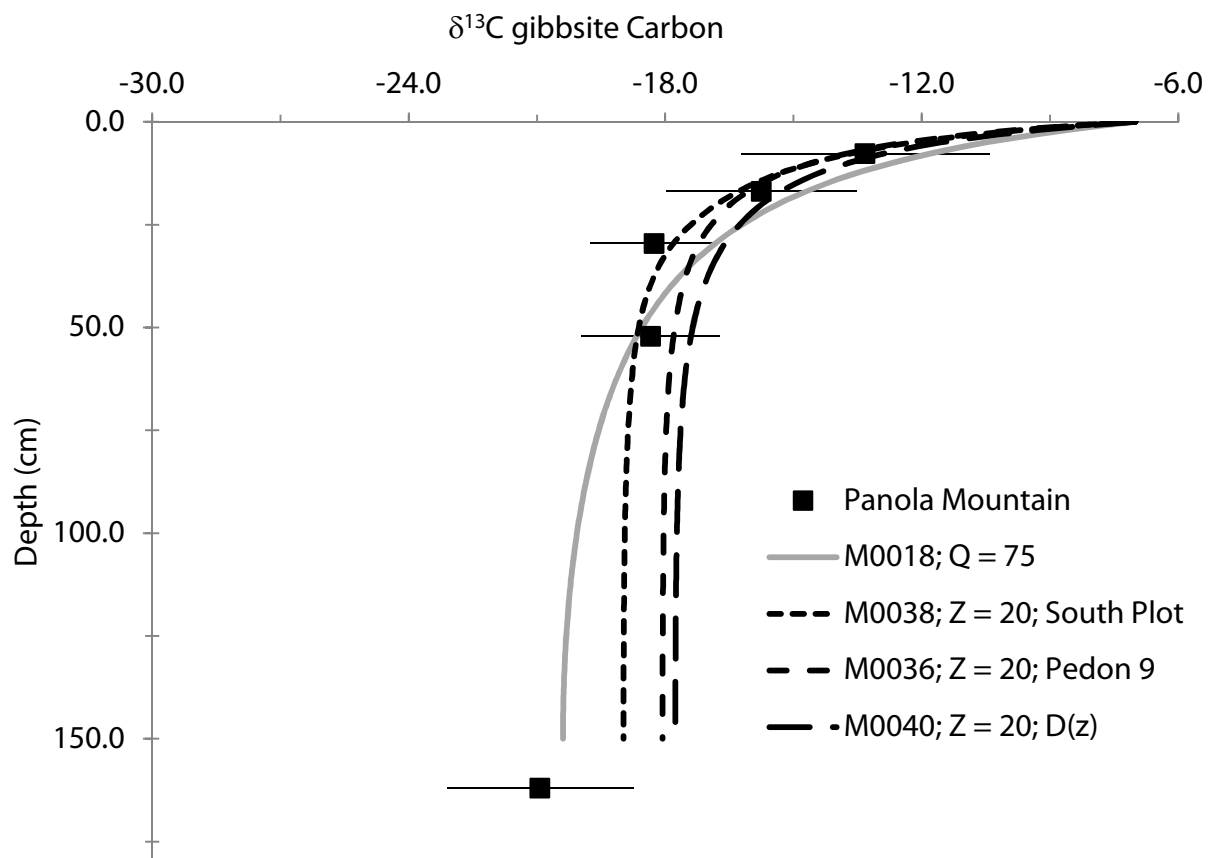


Figure 2.12. Calculated model solutions using bulk density data (M0038 & M0036) and $D_s^*(z)$ (M0040) using eqn. 2.3 and ϕ^* as a function of depth using eqn. 1.19 plotted for comparison to Panola Mountain Measured data. Z is the characteristic depth of CO_2 production used in equation 1.19; all model parameters listed in tables 2.1 and 2.2.

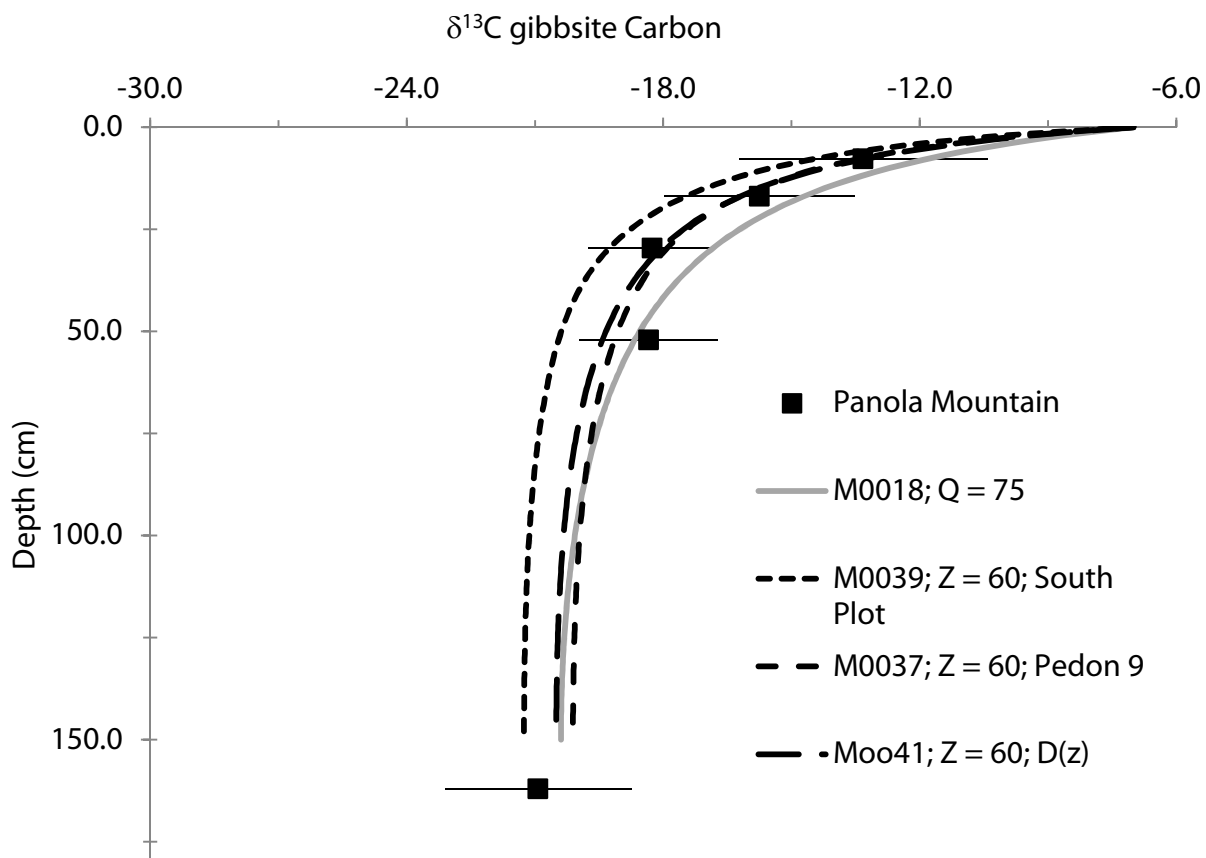


Figure 2.13. Calculated model solutions using bulk density data (M0039 & M0037) and $D_s^*(z)$ (M0041) using eqn. 2.3 and ϕ^* as a function of depth using eqn. 1.19 plotted for comparison to Panola Mountain Measured data. Z is the characteristic depth of CO_2 production used in equation 1.19; all model parameters listed in tables 2.1 and 2.2.

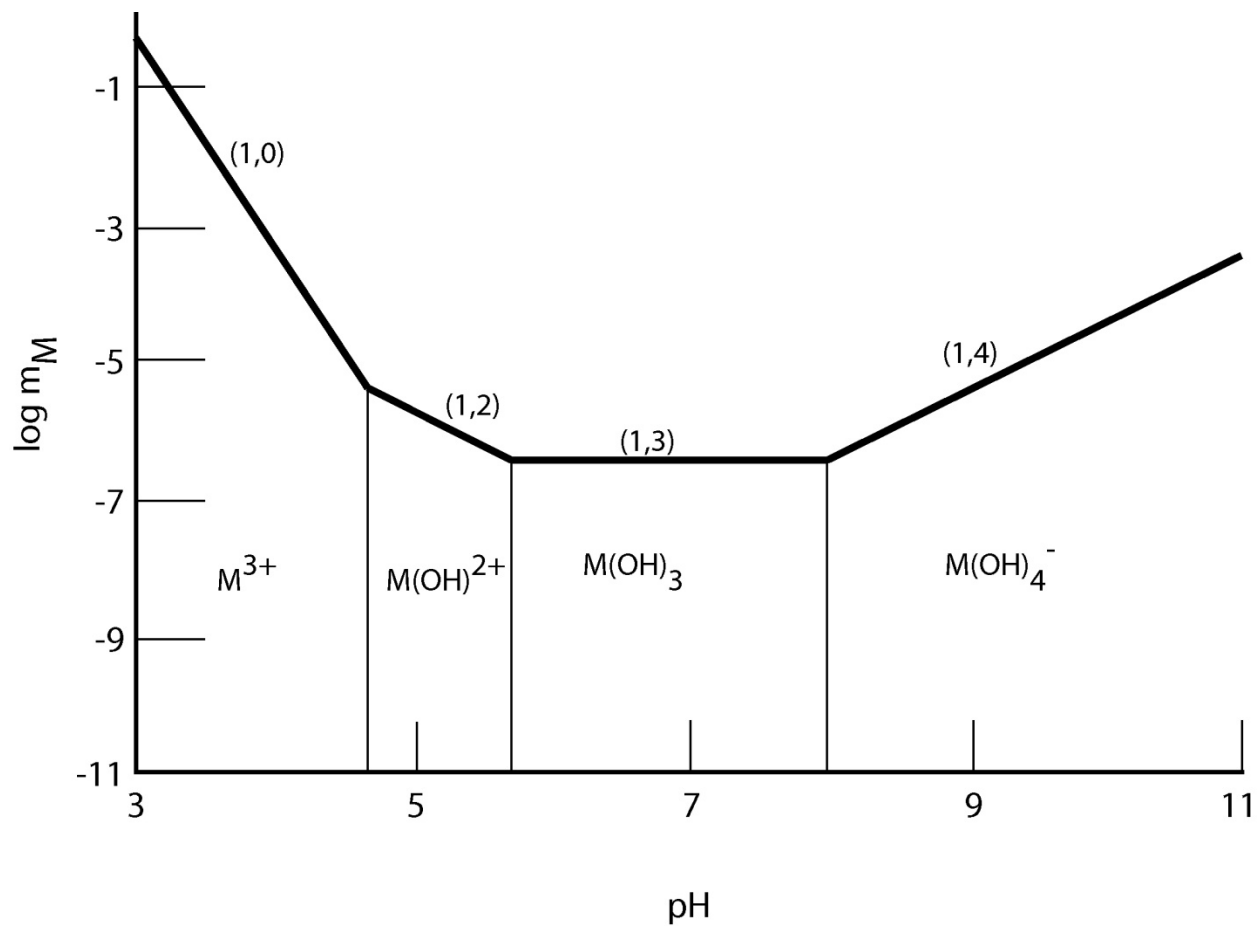


Figure 2.14 Dominant monovalent species of aluminum based on pH.

Table 2.1 Constant parameters used in modeling schemes

| Variable | Description | Units | Value |
|---|------------------------------|---------------------------------|----------------|
| Max. Depth (Z) | | cm | 150 |
| [CO ₂]atm (C _{atm}) | | gC cm ⁻³ / ppm | 1.61E-07 / 300 |
| dz | Change in depth per step | cm | 1 |
| $\delta^{13}\text{C}_{\text{atm}}$ | | ‰ (PDB) | -7.00 |
| $\delta^{13}\text{C C}_3$ | | ‰ (PDB) | -28.05 |
| dt | Change in time per step | s | 10 |
| D _{air} | Diffusion Coefficient in air | cm ² s ⁻¹ | 0.14 |
| k _r | Fast Consumption | y ⁻¹ | 0.2 |
| k _{sl} | Slow Consumption | y ⁻¹ | 0.01 |
| k _{st} | Stable Consumption | y ⁻¹ | 0.001 |
| e _r | Fast Assimilation | | 0.4 |
| e _{sl} | Slow Assimilation | | 0.4 |
| e _{st} | Stable Assimilation | | 0.2 |
| t _r | Fast Transformation | | 0.45 |
| t _{sl} | Slow Transformation | | 0.15 |
| a ₀ | Advection Coefficient at z=0 | | 0.999 |
| τ | Advection scaling term | | 0.5 |
| α | Fractionation factor | | 0.004 |

Table 2.2. Variable parameters used in modeling schemes

| Model Number | Q (gC cm ⁻² s ⁻¹) | porosity | tortuosity ⁻¹ | D _s [*] | Z (cm) |
|--------------|---|----------|--------------------------|--|---|
| M0001 | 2.06E-09 | 0.38 | 0.52 | eqn. 1.14 | NA |
| M0018 | 2.38E-10 | 0.38 | 0.52 | eqn 1.14 | NA |
| M0021 | 2.38E-10 | | | depth (cm) | Bulk Density (g cm ⁻³) NA |
| | | 0.6 | 0.3 | 5 | 1.56 |
| | | 0.6 | 0.3 | 50 | 2.12 |
| | | 0.6 | 0.3 | 70 | 1.89 |
| | | 0.6 | 0.3 | 91 | 2.04 |
| | | 0.6 | 0.3 | 109 | 1.94 |
| | | 0.6 | 0.3 | 146 | 1.37 |
| M0020 | 2.38E-10 | | | depth (cm) | Bulk Density (g cm ⁻³) NA |
| | | 0.28 | 0.29 | 7 | 1.91 |
| | | 0.3 | 0.25 | 21 | 1.86 |
| | | 0.32 | 0.22 | 32 | 1.81 |
| | | 0.42 | 0.13 | 51 | 1.55 |
| | | 0.46 | 0.11 | 90 | 1.43 |
| | | 0.43 | 0.12 | 133 | 1.52 |
| M0022 | 2.38E-10 | 0.38 | 0.52 | factor | value NA |
| | | | | a | 0.67 |
| | | | | b | -0.042 |
| | | | | c | 0.33 |
| | | | | d | 0.67 |
| | | | | e | 0.24 |
| M0031 | 2.85E-09 | 0.38 | 0.52 | eqn. 1.14 | 20 |
| M0027 | 9.51E-10 | 0.38 | 0.52 | eqn 1.14 | 60 |
| M0034 | NA | 0.38 | 0.52 | factor | value 20 |
| | | | | ζ _r (mol m ⁻² y ⁻¹) | 0.013 |
| | | | | ζ _{sl} (mol m ⁻² y ⁻¹) | 0.00325 |
| | | | | Cr (mol m ⁻² y ⁻¹) | 0.0065 |
| | | | | Csl (mol m ⁻² y ⁻¹) | 0.00433 |

Table 2.2 Variable parameters used in modeling schemes (cont.)

| Model Number | Q (gC cm ⁻² s ⁻¹) | porosity | tortuosity ⁻¹ | D _s * | | Z (cm) |
|--------------|---|----------|--------------------------|--|---------|-----------|
| M0035 | NA | 0.38 | 0.52 | factor | | 60 |
| | | | | value | | |
| | | | | ζ _r (mol m ⁻² y ⁻¹) | 0.027 | |
| | | | | ζ _{sl} (mol m ⁻² y ⁻¹) | 0.00675 | |
| | | | | Cr (mol m ⁻² y ⁻¹) | 0.0135 | |
| | | | | Csl (mol m ⁻² y ⁻¹) | 0.009 | |
| M0036 | 2.05E-09 | 0.28 | 0.29 | Bulk Density | | 20 |
| | | | | depth (cm) | | |
| | | | | (g cm ⁻³) | | |
| | | | | 7 | 1.91 | |
| | | | | 21 | 1.86 | |
| | | | | 32 | 1.81 | |
| | | | | 51 | 1.55 | |
| 90 | 1.43 | | | | | |
| M0038 | 2.05E-09 | 0.43 | 0.12 | Bulk Density | | 20 |
| | | | | depth (cm) | | |
| | | | | (g cm ⁻³) | | |
| | | | | 5 | 1.56 | |
| | | | | 50 | 2.12 | |
| | | | | 70 | 1.89 | |
| | | | | 91 | 2.04 | |
| 109 | 1.94 | | | | | |
| M0040 | 2.05E-09 | 0.38 | 0.52 | factor | | 20 |
| | | | | value | | |
| | | | | a | 0.67 | |
| | | | | b | -0.042 | |
| | | | | c | 0.33 | |
| | | | | d | 0.67 | |
| e | 0.24 | | | | | |
| M0037 | 2.05E-09 | 0.28 | 0.29 | Bulk Density | | 60 |
| | | | | depth (cm) | | |
| | | | | (g cm ⁻³) | | |
| | | | | 7 | 1.91 | |
| | | | | 21 | 1.86 | |
| | | | | 32 | 1.81 | |
| | | | | 51 | 1.55 | |
| 90 | 1.43 | | | | | |
| | | | | 133 | 1.52 | |

Table 2.2 Variable parameters used in modeling schemes (cont.)

| Model Number | Q (gC cm ⁻² s ⁻¹) | porosity | tortuosity ⁻¹ | D _s [*] | Z (cm) | |
|--------------|---|----------|--------------------------|-----------------------------|-----------------------|----|
| M0039 | 2.05E-09 | 0.38 | 0.52 | depth | Bulk Density | 60 |
| | | | | (cm) | (g cm ⁻³) | |
| | | | | 5 | 1.56 | |
| | | | | 50 | 2.12 | |
| | | | | 70 | 1.89 | |
| | | | | 91 | 2.04 | |
| | | | | 109 | 1.94 | |
| M0041 | 2.05E-09 | 0.38 | 0.52 | factor | value | 60 |
| | | | | a | 0.67 | |
| | | | | b | -0.042 | |
| | | | | c | 0.33 | |
| | | | | d | 0.67 | |
| | | | | e | 0.24 | |

CHAPTER 3

SOIL CO₂ EFFLUX SIMULATIONS USING MONTE CARLO METHOD AND IMPLICATIONS FOR
RECORDING PALEO-ATMOSPHERIC PCO₂ IN PEDOGENIC GIBBSITE¹

¹ Austin, J. C – Accepted by *Palaeogeography, Palaeoclimatology, Palaeoecology*. Reprinted here with permission of the publisher.

3.1 ABSTRACT

Monte Carlo simulation testing of the sensitivity of the Fickian diffusion model used for paleo-PCO₂ proxies indicates assuming annual average soil respiration rate results in over-estimation of PCO₂. In all cases, the natural variability of the factors of the model, including soil porosity and inverse tortuosity and the $\delta^{13}\text{C}$ value of the soil produced CO₂ were not able to account for discrepancies between measured $\delta^{13}\text{C}$ values from a modern soil and modeled results using established assumptions. Assuming that there is negligible carbon isotope fractionation during the occlusion of CO₂ in pedogenic gibbsite, the flaw in the model appears to be the assumed value of soil respiration rate. If correct, there are implications for its use.

3.2 INTRODUCTION

Increased concern about the link between changing atmospheric greenhouse gas concentrations and climate makes precise knowledge of atmospheric CO₂ concentrations throughout Earth's history useful for anticipating future extents and rates of change. The relationship between atmospheric CO₂ concentration and climate has been documented for times younger than 740 kya in the Dome C ice core record (Augustin et al., 2004), whose gas bubble CO₂ signal and ice O and H isotope pattern serve as credible recorders of coupled climate and atmospheric CO₂ change. The stable carbon isotope composition of pedogenic oxyhydroxides and carbonates are two proxies that have been commonly used as a record of atmospheric CO₂ on millennia to million year time scales (Cerling, 1991; Ekart et al., 1999; Royer et al., 2001; Tabor et al., 2004; Yapp and Poths, 1996). Use of these proxies gives insight into the potential range of climate response to changing atmospheric CO₂ concentration because they occurred during periods of earth's history that were either much warmer or much cooler than today (Royer et al., 2007). One of the key assumptions used to assess the changing concentration of CO₂ in the

atmosphere is the concentration of CO₂ in the soil, which is related to the rate of CO₂ efflux from the soil reservoir to the atmosphere. CO₂ efflux is the net transport of gas out of the earth's surface due to changes in atmospheric pressures and gradients caused by thermal and biological oxidation of carbon. The latter is collectively referred to as soil respiration which is mediated by the rate of microbial and plant root metabolism.

One potential proxy that has yet to be implemented is the carbon dioxide occluded on or incorporated in pedogenic gibbsite during mineral formation. Using a method similar to that of Yapp and Poths (1992), carbon dioxide was extracted from pedogenic gibbsite by Schroeder and Melear (1999). Because this carbon is thought to be occluded on the surface of the gibbsite in site defects rather than part of a solid solution as is suspected for goethite, it is not possible to use the same model for calculating the pCO₂ of the ancient atmosphere that is used for the goethite method (Schroeder and Melear, 1999; Yapp and Poths, 1990; Yapp and Poths, 1996). Therefore, a model based on that developed by Cerling (1989), with some important differences, was tested to verify the utility of this mineral as a proxy for paleo-pCO₂. Two significant differences stand out: (1) this model does not use the term $S(z)$ to include parameters such as the porosity, inverse tortuosity, and soil respiration rate into an estimation of soil CO₂ concentration; and (2) because the soil column in use is an active soil the top 50 cm that are typically not available in paleosols is used. This second difference takes advantage of the shape of the top part of the diffusion curve to more stringently confine the solution. In the study by Schroeder et al. (2006) the measured $\delta^{13}\text{C}$ values of carbonate evolved during the dehydration-decarbonation of gibbsite were compared to modeled solutions to assess the utility of carbon occluded on gibbsite as a proxy for paleo-pCO₂. Finite difference methods were used to allow for the variation of soil properties that are included in the $S(z)$ term with depth. The workers concluded that the soil

respiration rate that corresponded to the best fit solution of the stable carbon isotope ratio versus depth in the soil curve was an order of magnitude lower than the measured rate using a static chamber method. Possible implications proposed for this difference include the possibility that the stable isotope values of the occluded carbon is representative of a long term average and some period of cool monsoonal climate skewed the results to favor a low soil respiration rate. Or, it is possible that the implicit assumptions of the model are not correct, resulting in a solution that has no utility. This paper will attempt to determine if the assumptions used in the model are correct in order to eliminate this as a source of uncertainty.

Assuming the theory underlying paleosol oxyhydroxide and carbonate proxies for paleo- PCO_2 is sound, the discrepancy between the modeled soil respiration rate and measured respiration rate lies within the model. Assumptions can be classified as either process assumptions or factor assumptions. Process assumptions involve our understanding of the process by which the isotope composition of the soil CO_2 signal is generated and how that signal is preserved in the mineral record. Factor assumptions involve the accuracy of the equation forms used in the model and the accompanying coefficient values. The purpose of this study is to use Monte Carlo analysis to determine the sensitivity of the model to each factor and to minimize the uncertainty of the outcome. More accurately describing the soil processes and constraining the values will lead to improved assignments of model factors. Additionally, assessing the sensitivity of the model to these factors will reveal whether factor uncertainty or the underlying model process assumptions are incorrect.

Previous work relies on the analytical solution of the one-dimensional Fickian diffusion model of the form:

$$\frac{\partial C}{\partial t} = 0 = D_s^* \frac{\partial^2 C}{\partial z^2} + \varphi^* \quad (3.1)$$

(Cerling, 1984), where C is the concentration of CO_2 in the soil, D_s^* is the diffusion coefficient of bulk CO_2 through the soil, and φ^* is the bulk production rate of CO_2 in the soil. The difference in $^{12}\text{CO}_2$ and $^{13}\text{CO}_2$ diffusion rates results in a distinct profile of $\delta^{13}\text{C}$ values with depth in the soil. $\delta^{13}\text{C}$ is the standard notation established using the Cretaceous Pee Dee Belemnite (PDB) from the Pee Dee Formation in South Carolina. The model used to relate the stable carbon isotope value of pedogenic carbonate includes the diffusion coefficient and the bulk production rate of soil into a concentration term $S(z)$ (eqn. 3.3)

$$C_s^*(z) = S(z) + C_a^* \quad (3.2)$$

$$S(z) = \frac{\varphi_s^*(0)\bar{z}^2}{D_s^*} (1 - e^{-(z/\bar{z})}) \quad (3.3)$$

(Cerling, 1991), where the variables are as stated and \bar{z} is the characteristic depth of soil CO_2 production. Typically, values used are representative of the mean growing season. These estimates are not well constrained and one of the goals of this research is to attempt to constrain these variables.

The bulk rate of soil efflux and the stable carbon isotope composition of the soil CO_2 is determined by the physical characteristics; air-filled porosity and inverse tortuosity, and the biological characteristics; plant photosynthetic pathway (i.e. Calvin-Benson cycle CO_2 fixing into 3-carbon sugar versus 4-carbon sugar; or C3 vs. C4, respectively), the rate of plant and microbial respiration, of the soil, as well as the characteristics of the atmosphere, PCO_2 and $\delta^{13}\text{C}$ value of the atmosphere.

The analytical model assumes the rate of CO_2 production and flow through the soil is several orders of magnitude faster than the rate of mineral growth. Under this scenario, carbon

occluded onto the gibbsite mineral surfaces is likely to be in equilibrium with the soil carbon isotope composition (Cerling, 1984; Schlesinger, 1977). In attempting to develop this model, the soil respiration rate was assumed to be the annual average rate measured at the field site. Soil respiration rates however, are known to vary widely depending on the immediate temperature and water content of the soil (Camporese et al., 2008; Irvine et al., 2008). The precipitation of clay sized minerals goethite (FeOOH) and gibbsite ($\text{Al}(\text{OH})_3$) is largely controlled by the saturation of iron and aluminum in the soil solution. It then stands to reason that there is a bias toward the isotope signal that dominates during periods of fast mineral growth rates, which may not necessarily correspond to average annual soil respiration rates.

3.3 METHODS

Each parameter in the numerical diffusion model was described as either a physical property of the soil, porosity and inverse tortuosity, or a property of soil respiration, the stable carbon isotope composition of soil respired CO_2 . The natural variability as determined from literature values of each factor was assigned a Normal probability density function which was used during the Monte Carlo simulation to randomly choose realistic inputs for the model and establish the range of variability of calculated $\delta^{13}\text{C}$ values of soil CO_2 . This range of model results was compared to the measured $\delta^{13}\text{C}$ values from the Panola Mountain site by Schroeder and Melear(1999) to assess whether the natural variability of any or all of these parameters accounted for the disparity between the model and measured values. All calculations were made using algorithms written in the C++ programming language; the source code is available for download as a text file or Borland 2006 Studio Project file at

<<<http://austinj1.myweb.uga.edu/>>>.

Values for porosity of soils typically found in Georgia, USA, were calculated from bulk density data using the equation:

$$\varepsilon = 1 - \frac{\rho_{bulk}}{\rho_{parent}} \quad (3.4)$$

(Perkins, 1987) where ε is the air-filled porosity, ρ_{bulk} is the bulk density of the soil, and ρ_{parent} is the bulk density of the parent material with an assumed value of 2.65 g cm^{-3} (Figure 3.1A).

Inverse tortuosity (τ^{-1}) values were calculated from the porosity values using the relationship:

$$\tau^{-1} = \frac{(\varepsilon - \theta_w)^{7/3}}{\varepsilon^2} \quad (3.5)$$

(Millington and Quirk, 1961) where θ_w is the volumetric water content of the soil with an assumed value of 0.2 (Davidson et al., 2000; Millington and Quirk, 1961). The data for typical soils from Georgia was used because of their similarity to the study site and could be applied to paleosols that are identified as ultisols. The porosity and inverse tortuosity are incorporated into the diffusion coefficient in eqn. 1 by the relationship:

$$D_s^* = D_{air} \varepsilon \tau^{-1} \quad (3.6)$$

The Monte Carlo simulation was set up to calculate the inverse tortuosity related to random porosity value using the relationship in eqn. 5. Similar distributions were established for the stable carbon isotope composition of C3 and C4 plants using data from the literature (Figure 3.2) (Bender, 1968; Bender, 1971; Hattersley, 1982; Smith and Epstein, 1971).

The normal probability distributions were used to randomly seed the model, solving the analytical solution in the Monte Carlo simulation with boundary conditions:

$$C(0) = C_{atm} \quad (3.7)$$

$$\frac{\partial C}{\partial z} = 0 \text{ at } z = L \quad (3.8)$$

where L is the maximum depth represented by an impermeable barrier. The results of ten thousand model runs were plotted and compared to field measured values in order to determine if the natural variability of one or all of these parameters could account for the discrepancy between modeled and measured values. An attempt was made to establish a normal probability distribution for soil respiration rate, however the large variation of this parameter, daily, seasonally, and in response to precipitation, made it impossible to get useful results from the Monte Carlo Simulation (Jia and Zhou, 2009). In order to account for respiration rate variability, the model was solved assuming different values for soil respiration rate, a fast measured value (FM), a fast literature value (FL), and slow rates for each of these (SM & SL), equivalent to one-tenth the fast values. The fast measured rate is $0.10 \text{ gC m}^{-3} \text{ y}^{-1}$, the average soil respiration rate measured at Panola Mountain, Georgia from September 1, 1994 to December 1, 1996 (Huntington, 1995). The fast literature rate is $0.07 \text{ gC m}^{-3} \text{ h}^{-1}$, a rate typical for the vegetation type found at the Panola Mountain site, temperate deciduous forest (Raich and Schlesinger, 1992). The corresponding slow rates were $0.010 \text{ gC m}^{-3} \text{ h}^{-1}$ (SM) and $0.007 \text{ gC m}^{-3} \text{ h}^{-1}$ (SL). Solving the model also requires assumptions for the maximum depth, the stable carbon isotope composition of the atmosphere, and the concentration of CO_2 in the atmosphere. Boundary soil depth was assumed to be 150 cm and the pre-industrial values of -6.5 ‰ (PDB) and 250 ppm were chosen for the stable carbon isotope composition of the atmosphere and concentration of CO_2 in the atmosphere respectively (table 3.1) (Schroeder and Melear, 1999).

3.4 RESULTS

The calculated $\delta^{13}\text{C}$ values of the models run (table 3.1) are compared to the measured $\delta^{13}\text{C}$ values reported by Schroeder and others (2006). These data are plotted with error bars representing the maximum amount of variability ($\pm 1.5\text{‰}$) of multiple measurements. The model solution is considered successful if the data error bars overlap the range of possible solutions. Each simulation was conducted in pairs using the above mentioned FL and SL values for soil respiration rate. The run number corresponding to the run number in table 1 will be listed in parentheses.

The variability of the soil parameters, porosity and the resulting inverse tortuosity calculated using eqn. 5; results in a relatively small amount of variation in possible solutions (Figure 3.3). There is not enough variability to cause the data to overlap the solutions at any depth in the profile. Changing the respiration rate from the FM (009) to SM (011) makes the range of possible solutions closer to the measured values but the chosen respiration rate is still too high. Adding the variability of the stable carbon isotope composition of the soil produced CO_2 , assuming 100% C3 plants with a $\delta^{13}\text{C}$ value of -28.05‰ PDB , the mean of the C3 data (Figure 3.2B), results in a much wider range in the possible solutions (Figure 3.4). In this case the data points at greater depth in the profile, 28 cm and 51 cm, overlap the range of the solution representing 5% probability for FL (013) soil respiration rate. If the SL (015) soil respiration rate is used, the data overlaps at all depths with at least 20% probability of including all data points. The bulk soil carbon $\delta^{13}\text{C}$ value of the Panola mountain sample site ranged from -18.9 to -24.9‰ . This indicates that the most likely scenario is 100% C3 plants with a $\delta^{13}\text{C}$ value of -24.9‰ which is the value lowest in the soil profile (Schroeder et al., 2006).

Because there is no evidence of C4 plants at the Panola Mountain site, the model was run using -24.9 ‰, the $\delta^{13}\text{C}$ value of the bulk soil at 140 cm measured by Schroeder and Melear (1999), was used for model runs 037(SL) and 038(FL). In this case, the SL(037) solution appears to be the best fit of all the models run with all data points falling within at least 25% probability, while the FL(038) model results in at best 5% probability (Figure 3.5). In this case the model solution is acceptable with a 100% C3 source with a respiration rate that is 10% the amount typical for the vegetation at the site.

3.5 DISCUSSION

The utility of this model relies ultimately on predicting the concentration of CO_2 in the atmosphere based on the profile of the $\delta^{13}\text{C}$ value of CO_2 occluded in soil minerals. When used for this purpose, conditions under which those minerals formed in the soil need to be assumed. The more sensitive the model is to the physical properties of the soil and the CO_2 in the soil, the more imperative it is that the assumptions be accurate. The results of these Monte Carlo simulations identify two important facts about this model and the utility of pedogenic gibbsite as a proxy for paleo- pCO_2 .

The results of simulations 009 and 011 (Figure 3.3) indicate the model is not sensitive enough to the natural variability of physical properties of the soil to account for the discrepancy between the measured $\delta^{13}\text{C}$ values of the CO_2 associated with pedogenic gibbsite and the predicted values of $\delta^{13}\text{C}$ for soil respired CO_2 . This agrees with the fact that using a finite difference model to more accurately represent changes in soil properties with depth did not improve the fit of the model without simultaneously choosing a lower respiration rate (Schroeder et al., 2006). Likewise, the natural variability of $\delta^{13}\text{C}$ values of the soil produced CO_2 , assuming the photosynthetic pathway of the dominant biomass is known, is not able to account for the

difference. While the possibility of mixing C3 and C4 sources can account for the difference between measured and modeled $\delta^{13}\text{C}$ value profiles, C4 plants are generally restricted by climate, preferring dry and warm climates typical of grasslands and deserts and are therefore not a factor in this case (Cerling, 1991).

Therefore, if the $\delta^{13}\text{C}$ of soil produced CO_2 can be determined based on the likely climate during formation, age of the sample, or some organic material preserved in the paleosol, it can be stated that the failure of the model to correctly predict the $\delta^{13}\text{C}$ value of the CO_2 occluded in pedogenic gibbsite is not caused by the factor assumptions of the model; leaving only the process assumptions. The two process assumptions that should be considered involve the way the CO_2 becomes associated with pedogenic gibbsite. This proxy was developed after the methods of Yapp (1996) which used the carbonate component of goethite as a proxy for paleo- CO_2 . Based on the availability of space in the *c*-axis channel of the goethite structure to accommodate the carbonate molecule and infrared spectral evidence for a carbonate component in solid solution in goethite, Yapp and Poths (1990) determined that the carbonate was incorporated into the goethite structure. In the gibbsite structure, there is no channel that will accommodate the carbonate molecule; a fact which led Schroeder and Melear (1999) to propose that the carbonate was occluded in site defects during mineral formation. In both cases, it was assumed that there was no fractionation of the carbon isotopes in the process of incorporating the carbonate in or on the mineral structure. Molecular dynamics modeling indicates fractionation factors of between +3.9 and +12.3 ‰ if the carbonate component is incorporated into the gibbsite structure, depending on where in the structure the CO_2 is located (Rosso and Rustad, 2001). All of the simulations in this study assume that the carbonate is occluded on the mineral surface in edge defects during mineral formation and therefore, it was assumed that there was no fractionation of carbon

isotopes. The effect of fractionation would be to over-estimate the PCO_2 of the atmosphere. If you compare the solutions of two models where one uses the $\delta^{13}\text{C}$ value of the soil organic material, and one used +4.00 ‰ enrichment, the solution of the fractionated model would be shifted towards more positive values. If the fractionation was incorrectly assumed to be zero, it would appear that there was a larger contribution from the atmosphere. This can be seen graphically by comparing the solutions to models 015 and 036 (Figures 4B and 6B).

The remaining process assumption that the $\delta^{13}\text{C}$ value of the carbonate occluded in soil minerals is representative of a profile resulting from the average annual respiration rate. This assumes that mineral formation is a constant process that is integrating the entire range of soil respiration rates throughout the year. In all of the simulations run, assuming a respiration rate one-tenth the annual average resulted in a solution closer to the measured $\delta^{13}\text{C}$ values. This has been seen to be the case for pedogenic carbonates, where the solubility of calcite resulted in mineral formation only during warm, dry periods. As a result of this the stable carbon isotope composition of the calcite was not representative of the annual average, but was biased towards these conditions (Breecker et al., 2009). This indicates that mineral precipitation is an episodic event which most likely occurs when soil conditions are appropriate; i.e. when the soil is dry and the soil solution becomes saturated. Based on the well-established relationship between soil moisture and soil respiration rate, soil conditions ideal for gibbsite formation correspond with low soil respiration rates (Jia and Zhou, 2009). This is reflected in bias in the $\delta^{13}\text{C}$ value of the carbon occluded in pedogenic gibbsite toward periods of low respiration rate. Calculated soil CO_2 concentration corresponding to a respiration rate of $0.07 \text{ gC m}^{-3}\text{h}^{-1}$ is 4,400 ppm at a soil depth of 150 cm. Soil CO_2 concentrations this low are common for desert soils but temperate soils typically have soil CO_2 concentrations ranging between 10,000 and 25,000 ppm. The

concentration of CO₂ in the soil however has been shown to be related to soil moisture and soil temperature and during periods of low soil moisture or cold temperatures concentrations as low as 4000 ppm are not uncommon (Albanito et al., 2009; Ota and Yamazawa, 2010; Zhang et al., 2010). Low calculated soil CO₂ concentrations for an acceptable model solution may give some insight into the conditions that exist during gibbsite precipitation and subsequent CO₂ occlusion. Specifically, during conditions of low soil moisture content when biological activity is low; resulting in low soil CO₂ concentrations and corresponding low respiration rates.

3.6 CONCLUSIONS

The model used to predict paleo-PCO₂, based on the stable carbon isotopes in pedogenic gibbsite, incorrectly assumes the average annual soil respiration rate. A lower rate, corresponding to conditions likely for gibbsite precipitation, is more appropriate. In light of these results, it is important to consider the process by which gibbsite occludes CO₂. The location of the CO₂, incorporated into the structure or surrounded by it, will have implications for both the fractionation of carbon isotopes and the timing of the inclusion of CO₂ in the mineral. Additionally, it stands to reason that the evaporative environment that favors gibbsite precipitation may have a measurable effect of the oxygen and hydrogen stable isotopes in the gibbsite. Evaporation would serve to concentrate the heavy isotopes in the soil water. Therefore, you would predict that the $\delta^{18}\text{O}$ and δD of the gibbsite would be enriched compared to meteoric water. The seasonal variation of the $\delta^{13}\text{C}$ values of pedogenic carbonates and the model results presented in this paper indicate that the mineral precipitation process is episodic. Therefore, in order for the gibbsite paleo-PCO₂ proxy to accurately predict paleo-PCO₂, care must be taken when assigning a value for soil respiration rate.

If this method is applied to paleosol gibbsite the assumed soil respiration rate will proportionally affect the predicted PCO_2 of the atmosphere. For example, if a model assuming a soil respiration rate of $0.07 \text{ gC m}^3\text{h}^{-1}$ predicted a paleo- PCO_2 of 4000 ppm the same model assuming a respiration rate of $0.007 \text{ gC m}^3\text{h}^{-1}$ would predict a paleo- PCO_2 of 400 ppm. Therefore, it is imperative that the soil respiration rate that is assumed be correct.

3.7 ACKNOWLEDGMENTS

Thanks to Paul A. Schroeder and John F. Dowd for helpful discussions and mentoring. This manuscript was greatly improved by suggestions by Crayton Yapp and an anonymous reviewer. This work was supported by student research grants from the International Association of Mathematical Geologists, The Clay Minerals Society, the Geological Society of America, the University of Georgia Watts-Wheeler Foundation for student research, and The National Science Foundation – SGER: EAR-0501690.

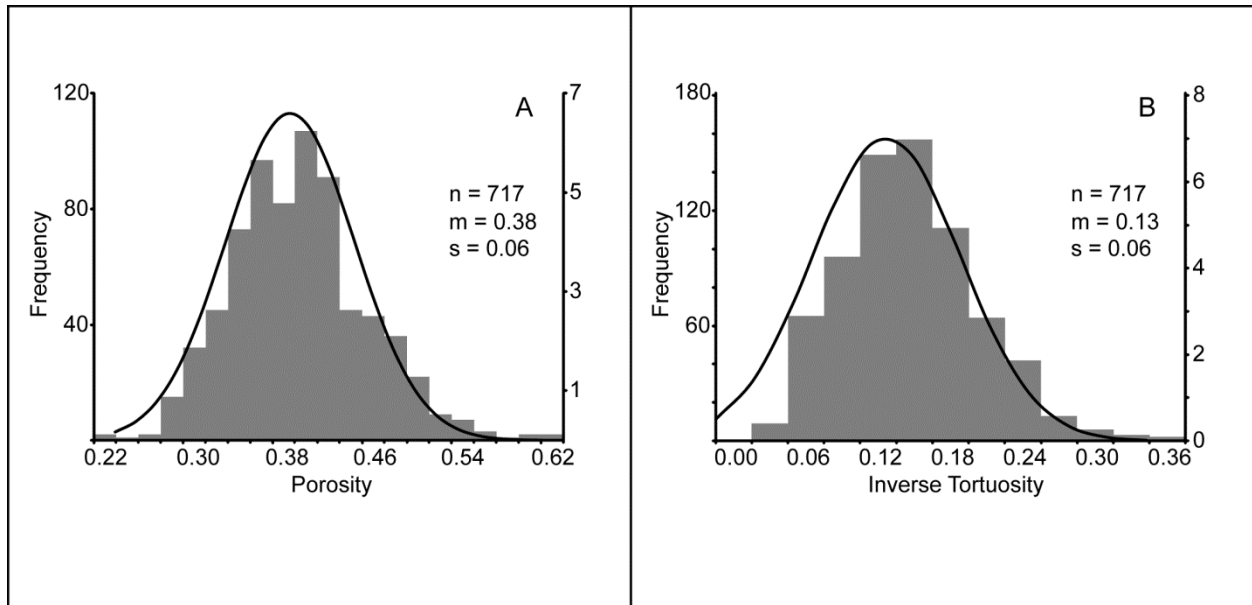


Figure 3.1: Histograms and Normal probability distribution functions for porosity (A) and inverse tortuosity (B) based on the values calculated from bulk density data (eqn 3.2 & 3.3) (Perkins, 1987).

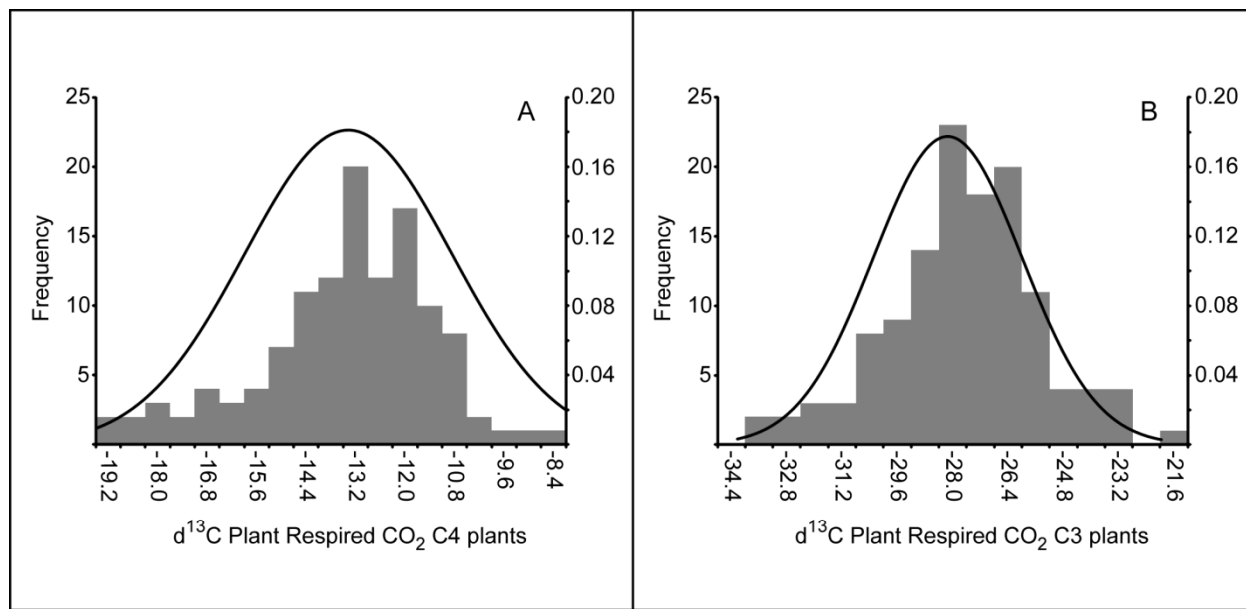


Figure 3.2: Histograms and Normal probability distribution functions for stable carbon isotope composition of CO_2 produced in soil by C_4 (A) and C_3 (B) plants (Bender, 1968, 1971; Hattersley, 1982; Smith and Epstein, 1971)

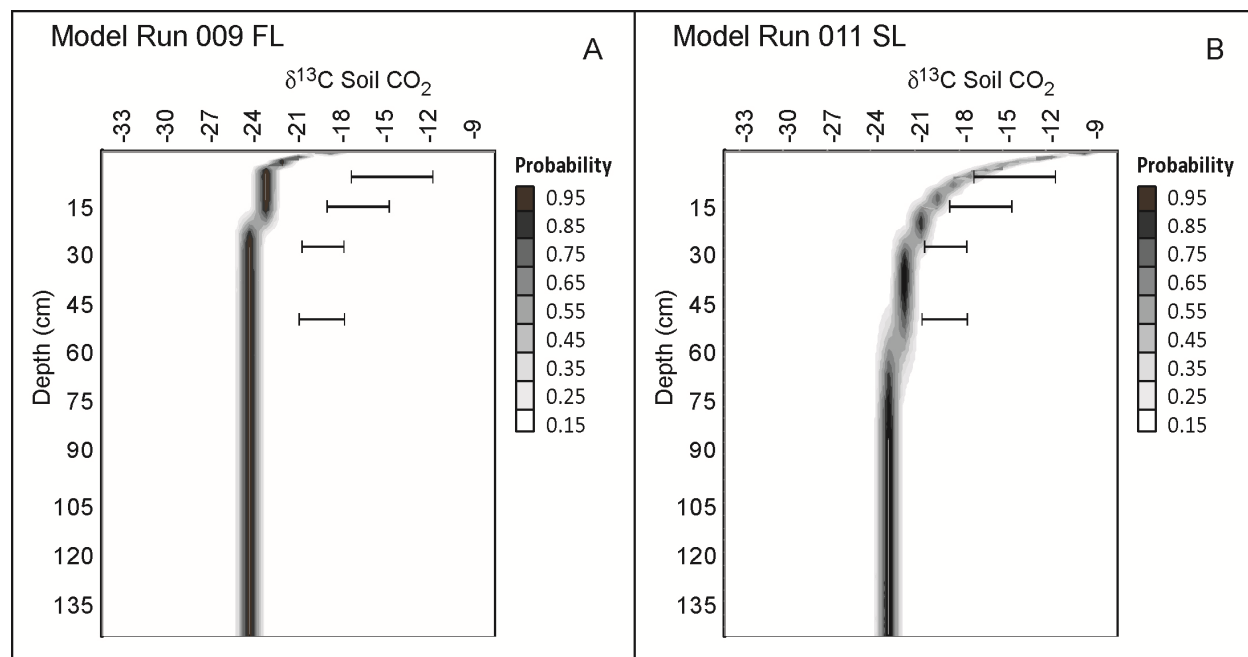


Figure 3.3 Results of FL (A) and SL (B) Monte Carlo simulations using parameters listed for model numbers 013 and 015 in table 3.1. Data points represent measured $\delta^{13}\text{C}$ measurements of the carbonate associated with pedogenic gibbsite (Schroeder et al., 2006).

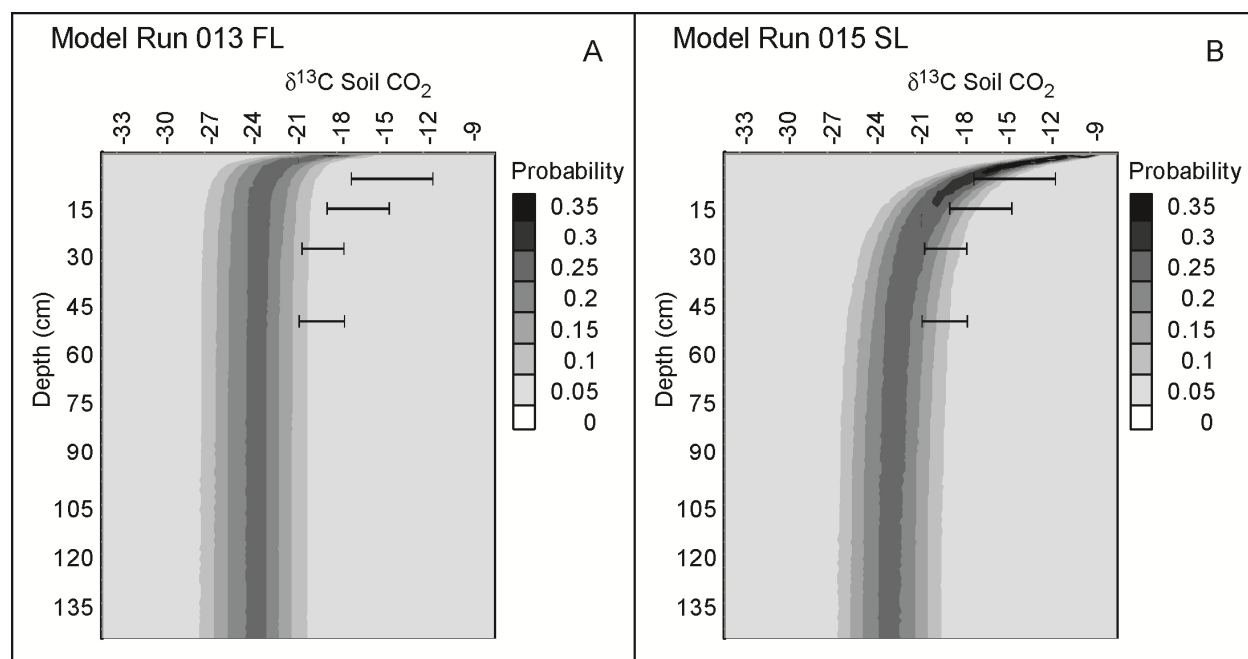


Figure 3.4. Results of FL (A) and SL (B) Monte Carlo simulations using parameters listed for run numbers 013 and 015 in table 1. Data points represent measured $\delta^{13}\text{C}$ measurements of the carbonate associated with pedogenic gibbsite (Schroeder et al., 2006).

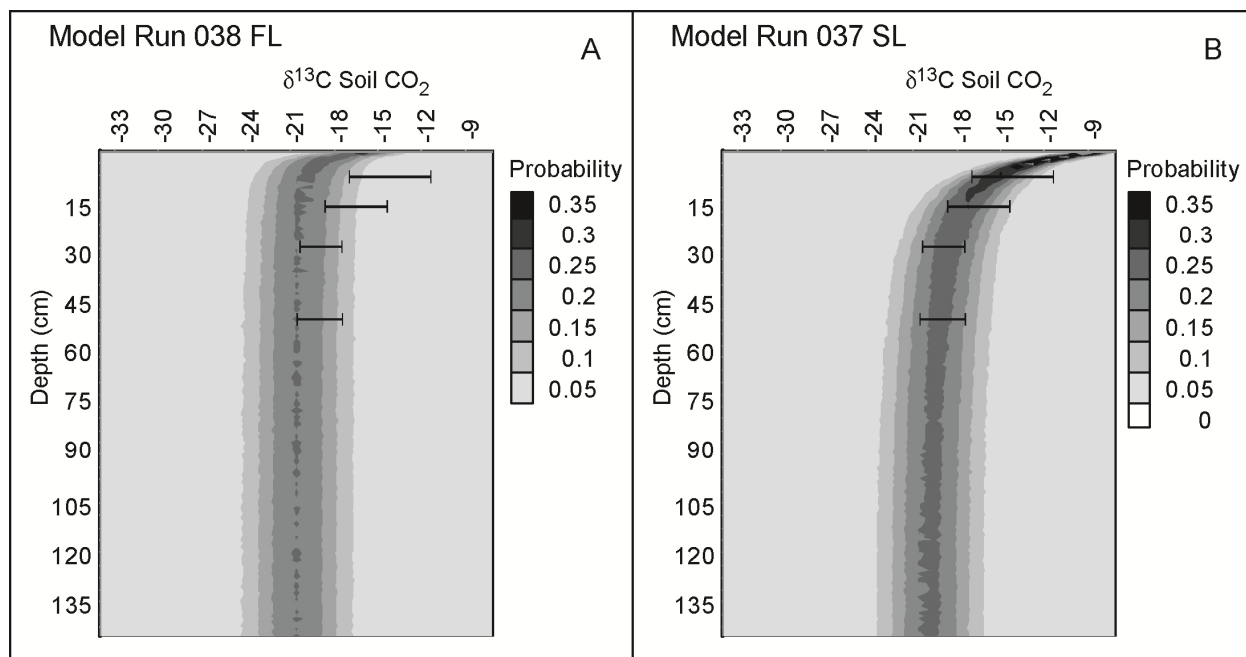


Figure 3.5: Results of FL (A) and SL (B) Monte Carlo simulations using parameters listed for model numbers 021 and 023 in table 3.1. Data points represent measured $\delta^{13}\text{C}$ measurements of the carbonate associated with pedogenic gibbsite (Schroeder et al., 2006).

Table 3.1 Model Assumptions and Coefficients

| Run Number | Soil Respiration Rate (gC m ⁻³ y ⁻¹) | ε | | τ^{-1} | | $\delta^{13}\text{C C}_3$ (‰) | | | $\delta^{13}\text{C C}_4$ (‰) | | |
|------------|--|---------------|---------------|-------------|---------------|-------------------------------|---------------|-----|-------------------------------|---------------|----|
| | | μ^{**} | σ^{**} | μ^{**} | σ^{**} | μ^{**} | σ^{**} | % | μ^{**} | σ^{**} | % |
| 009(FL)† | 647 | 0.38 | 0.06 | 0.13 | 0.06 | -28.05 | | 100 | | | 0 |
| 011(SL)† | 64.7 | 0.38 | 0.06 | 0.13 | 0.06 | -28.05 | | 100 | | | 0 |
| 013(FL)† | 647 | 0.38 | 0.06 | * | | -28.05 | 2.5 | 100 | | | |
| 015(SL)† | 64.7 | 0.38 | 0.06 | * | | -28.05 | 2.5 | 100 | | | |
| 021(FL)† | 647 | 0.38 | 0.06 | * | | -28.05 | 2.5 | 50 | -13.63 | 2.2 | 50 |
| 023(SL)† | 64.7 | 0.38 | 0.06 | * | | -28.05 | 2.5 | 50 | -13.63 | 2.2 | 50 |

* Calculated using eqn. 3.3

** Where these fields are blank, the parameter was held constant during the Monte Carlo Simulation.

Where there is an explicit value they define the mean (μ) and standard deviation (μ) of the Normal Probability Distribution used.

ε = air-filled porosity

τ^{-1} = inverse tortuosity

CHAPTER 4

FIELD-TEST OF GIBBSITE PALEO-PCO₂ PROXY

4.1 INTRODUCTION

In light of the discrepancies between the calculated $\delta^{13}\text{C}$ values of soil CO₂ and measured $\delta^{13}\text{C}$ values of CO₂ trapped in pedogenic gibbsite illustrated in chapters 2 and 3, the next logical step is to attempt to repeat the experiment in a different location to verify consistent results. Therefore, a field test was conducted to attempt to reproduce the results from the Panola Mountain site and to model the PCO₂ of the modern atmosphere.

In order to eliminate the confusion of multiple plant type inputs (i.e. C₃ vs. C₄), a field site was chosen that is believed to not have changed vegetation types over the past hundred years and shows no evidence of ever having been used for agriculture (Figure 4.2). The field site was also chosen to minimize the inputs of fluvial sediment. The benefits of conducting a field test are twofold; first, all of the parameters of the soil that are used as inputs into the model are measurable, and therefore can be more easily constrained; and second, an additional set of data will verify that the Panola Mountain data were not anomalous.

The analytical model suggested the assumption that the stable isotope composition of the pedogenic gibbsite is in equilibrium with those expected for soil CO₂ during the growing season was incorrect. Finite difference modeling of variations in the bulk density with depth proved to be an insufficient modification to the model; while Monte Carlo simulations of likely variations in bulk density also showed that this property alone could not account for the difference. Changing the distribution of soil CO₂ production with depth in the soil was able to account for the discrepancy by effectively changing the concentration of CO₂ at depth in the soil. This

method only works when the characteristic depth of soil CO₂ production is deeper in the soil than observed in nature. Because of the difference between the calculated concentration of CO₂ in the soil using this method and the analytical solution, the validity of this method is uncertain.

During the initial description of the method used to collect CO₂ from the incremental dehydration-decarbonation of goethite, Yapp and Poths (1986) described the expected response of CO₂ and H₂O collection to indicate that the collected CO₂ is in fact coming from the breakdown of the mineral structure. As indicated in chapter 1 (Figure 1.19) it is expected that the $\delta^{13}\text{C}$ values of the CO₂ will be constant over the interval where structural CO₂ is being collected, and the ratio of CO₂ to structural H₂ will be constant. Similar results are expected for gibbsite except that, because the carbonate component is not likely to be structural, the assumption that the carbonate is uniformly distributed might not be valid. The rate of mineral breakdown and the timing of the collection intervals will make it unlikely that non-uniform distribution in the gibbsite structure will be noticeable in either the gas yields or the $\delta^{13}\text{C}$ values of the CO₂. Independent soil material collection, treatment, and dehydration, allows for verification of the data collected, and perhaps a chance to look at the systematics of the CO₂ release to see if there is any more information about the process that can be discerned.

One concern that must be mentioned when discussing gibbsite as a proxy for PCO₂ is the assumption that the fractionation factor between soil CO₂ and gibbsite is about 1.000. In order to address this issue, one of the samples was treated to remove the gibbsite from one portion and the goethite from another. Because these minerals both are present in the samples, comparison of the $\delta^{13}\text{C}$ values of the CO₂ collected from the samples where one phase has been removed to the sample where both phases are present may be useful in determining how much fractionation, if any is occurring when the CO₂ is incorporated into the mineral structure.

By collecting data from a second field site for comparison to data previously collected it is hoped that the presence of CO₂ in the gibbsite structure will be confirmed, and the $\delta^{13}\text{C}$ values of the trapped CO₂ will be similar to those measured by Schroeder and Melear (1999); and will prove useful as a proxy for PCO₂ of the atmosphere using the model established in sections 2 and 3.

4.2 SITE DESCRIPTION AND METHODS

4.2.1 SITE DESCRIPTION

The sampling location is a moderately dense deciduous forest located in Watkinsville Georgia, USA on land formerly owned by the USDA (33° 51' 55"N, 83°27'23"W) (fig 4.1). This location was chosen because aerial photographs show that the forest has been in this location for at least 75 years (Figure 4.2). The parent material for the soil is Athens Gneiss and the soil is identified as CYB2 (Cecil series soil eroded, with up to two percent slope) (Soil Conservation Service, 1968).

4.2.2 SAMPLE COLLECTION

Soil material was removed from a hole that measured 1m x 1m in discrete layers based on depth (e.g. 0-5 cm, 5-10 cm, etc.). Each layer was removed using a small trowel and placed into five gallon buckets which were closed and sealed. The buckets were stored in the field and then moved into the lab for sample processing. The 0-5cm sample was top of the Oa horizon taken after removal of the recognizable leaf litter and consisted of mostly organic material and some mineral material. There was some overlap between the 5-15cm section and the 10-20cm section due to a difference in the location used to measure the depth from the top of the pit. After this point, the depth was measured from a string suspended over the center of the pit at ground level.

The pit was dug over a period of about 3 months, with any obvious loose material removed at the beginning of each day to avoid collecting material that fell into the hole after digging began.

Samples were collected from three cores extracted approximately one meter from the center of three sides of the pit for the determination of % sand, silt, and clay by weight using a settling tube and stable carbon isotope and percent carbon analysis of the bulk soil performed by the Stable Isotope & Soil Biology Laboratory at the University of Georgia.

4.2.3 SAMPLE TREATMENT

Samples were treated using the method described by Yapp and Poths (1996) and Schroeder and Melear (1999). The method is described in detail here and any changes from other procedures are noted. All treatments listed below were performed on all samples to produce about 300 to 500g of final treated samples (Figure 4.3).

The soil material that was collected in five gallon buckets was transported to the lab and disaggregated using a wooden rolling pin and passed through sieves to separate the <2 mm size fraction. The <2mm size fraction was passed through sieves using deionized (DI) water to separate the <63 μ m size fraction. Deionized water was used to prevent flocculation of the clays. The functionally defined <2 μ m size fraction (equivalent spherical diameter) was separated from the <63 μ m size fraction using Stoke's Law. The remaining <2 μ m size fraction was centrifuged again to remove any excess water and then dried in a 70°C oven.

The <2 μ m size fraction, henceforth referred to as sample material, was then treated to ensure that any source of carbon other than the trapped carbonate in the gibbsite structure was removed. The importance of this is discussed in section 1.1.8.2, but briefly, two possible sources of contamination from unwanted carbon dioxide collected during the dehydration step are labile organic carbon on the surface of the minerals and discrete carbonate phases intermixed in the

sample material. In order to eliminate these possible sources, 0.5N HCl and 30% H₂O₂ were used to treat the sample material. The 0.5N HCl was added to the sample material and stirred; it was then allowed to soak overnight. This treatment was carried out twice for each sample. There was no obvious bubbling which would indicate the presence of discrete carbonate phases of any notable amount in any sample. After the second HCl treatment, the sample material was rinsed with (DI) water and centrifuged to remove any excess water. The sample material was then treated with 30% H₂O₂ three times for periods of at least seven days. There was significant bubbling in the shallow samples (0-5, 5-15, 10-20, 20-25 cm), while the deeper samples showed moderate bubbling. Samples were analyzed with X-ray diffraction before and after these chemical treatments to verify that there was no change in mineralogy. There were no peaks for carbonate minerals in the original diffraction patterns of any sample material.

Two portions of the 25-35cm sample were separated and treated to remove either gibbsite (sample 2535Al2) or goethite (sample 2535Fe51). Goethite removal was accomplished by the HCl treatment described by Schroeder and Pruett (1996). Six grams of sample were added to 100 ml 5.8N HCl and were heated in a water bath at 65C for three hours. XRD analysis of the samples after they were filtered through #40 filter paper and rinsed with DI water showed that the goethite was removed. Gibbsite was removed by treatment with NaOH following the procedure of Singh and Gilkes (1991). Ten grams of sample 2535 were added to one liter of 5M NaOH and were boiled for 60 minutes. Water was added to the solutions during boiling to prevent them from boiling dry. After boiling, the samples were centrifuged and the supernatant was removed. The samples were rinsed two times with 0.5M HCl for 20 minutes to remove sodalite that precipitates during gibbsite removal, two times with 1N (NH₄)₂CO₃, and two times with DI water. XRD analysis of this sample after treatment indicates that the sodalite was not

removed, but it does not thermally decompose below 770C and should therefore not influence the collection of CO₂ during the dehydration of gibbsite (Figure B5) (Schipper et al., 1973).

4.2.4 DEHYDRATION/DECARBONATION PROCEDURE

The treated sample material was heated in a step-wise procedure to allow for the collection of CO₂ liberated from the mineral structure during the thermal breakdown of the gibbsite and goethite. Between 0.5 and 1.0 gram of sample was placed into a boat that was inserted into a tube. The tube was attached to the vacuum line in the University of Georgia Isotope Lab and an oven was placed over the sample to allow for heating. The extraction line was designed with two cryogenic traps so that the evolved gas could be collected from one step while the next step was in progress, allowing for continuous heating of the sample (fig 4.5). The extraction process involves two steps to ensure that there is no labile carbon on the surface of the sample after the chemical treatments, five steps to extract and collect gases evolved from the thermal breakdown of gibbsite and goethite, and one step to attempt to collect any organic material that is not removable by other treatments in the sample.

Samples were inserted into the tube and vacuum was established while the oven was heated to 115C. The sample was left in the oven under vacuum at 115C over night (at least 12 hours) to ensure that any water and CO₂ adhered to the sample surface was removed. Following this step, the sample was isolated from vacuum and 0.2 atm of pure O₂ was added to the sample tube while the sample was heated to 200C for 1 hour. After this hour, the O₂ was removed from the system and vacuum was reestablished. The temperature was raised to 235C over 15 minutes and liquid nitrogen was applied to the trap to collect the water and CO₂ that was evolved from the sample. Gas was collected at 230C for two forty-five minute intervals. Then, the temperature was raised to 240C and CO₂ was collected for forty-five minutes, one hour, and two

hours; finally, the sample was heated to 850C for thirty minutes and the gas was collected from that step (Figure 4.4).

While the sample gas was being collected in one trap, the gas from the previous trap was separated into H₂O and CO₂ and collected in break-seals for conversion to H₂ and stable isotope measurement respectively. This process was accomplished by pumping any non-condensable gases away to vacuum and thawing out the gas frozen by the liquid nitrogen trap. A mixture of crushed dry ice and ethanol was applied to freeze the water and allow the CO₂ to be collected in a cold finger using liquid nitrogen. When all of the CO₂ was transferred to the cold finger, as evidenced by measuring vacuum in the system, the cold finger was isolated from the system and the CO₂ was thawed using room temperature water. A pressure detector that was open to the cold finger and calibrated using known volumes of CO₂ was used to measure the volume of CO₂ collected in each step. This CO₂ was then transferred to the break-seal by applying liquid nitrogen and was removed from the collection line by heating the tube with a torch. The water was then thawed and re-frozen into a collection tube with shaved zinc in it to allow for conversion to H₂ gas to measure the volume of water collected. Samples starting with 253501 were collected with new, finer-grained zinc that proved to not react fully with the water so the volume of H₂ collected during these dehydrations were not able to be measured.

Collected CO₂ was analyzed by conventional dual inlet mass spectrometry on a Finnigan MAT 252 equipped with microvolume coldfinger for the stable carbon and oxygen isotope ratios. Volume of CO₂ analyzed ranged from 20 to <1 micromoles. The stable carbon isotope ratios were plotted to determine the $\delta^{13}\text{C}$ value of the plateau that indicates that the CO₂ is coming from a single source, which is believed to be the trapped CO₂ in the gibbsite structure.

4.2.5 MODELING METHODS

Soil respiration rates were modeled using the techniques discussed in sections 2.2.1 and 3.3. The constants used for model parameters are listed in tables 2.1 and 4.2. The average value of the carbon collected in the 850C step for the samples between 45 and 105 cm was used as the $\delta^{13}\text{C}$ value for the biomass. This was changed in some models because the modeled soil respiration rates were required to be higher than was physically reasonable to get the modeled soil CO_2 $\delta^{13}\text{C}$ values to match the measured values. Finite difference models using the data from the two pedons discussed in section 2.2.1 and the exponential function for soil bulk density in addition to the functions described for soil CO_2 production with depth were used to model soil respiration rate. In addition, in order to more accurately model the condition of more CO_2 being produced at 25cm depth, a gamma distribution was applied to the soil CO_2 production values with depth. Finally, in order to determine the range of conditions under which the measured $\delta^{13}\text{C}$ values were predicted by the model, Monte Carlo models were run using the distribution functions described in section 3.2.

4.3 RESULTS

4.3.1 SOIL PHYSICAL PROPERTIES

The percent clay in the soil increases from the surface to a maximum of about 60% between 40 and 60cm, and decreases to a minimum of 20% at 1m depth where it is relatively constant to 1.5m depth (Figure 4.6). The majority of the clay in the soil is kaolin and gibbsite, with minor amounts of goethite and HIV (Figure 4.7). There are two samples (0-5cm and 20-25cm) that show a mica phase that may be indicative of the lack of homogeneity of the gneissic parent material; though it should be noted that x-ray diffraction patterns of the bulk soil material do not indicate any obvious change in the mineralogical composition of the parent material

(Figure 4.8). These samples also contain more goethite than the other samples. The upper 5-10cm of the soil contains larger amounts of HIV, which is believed to be neo-formed in the shallow soil; this, along with higher organic material content may account for the increased yield of CO₂ from the samples that are shallow in the soil.

4.3.2 GIBBSITE DEHYDRATION/ DECARBONATION

In order to identify the CO₂ that is collected during the dehydration of gibbsite as representative of the trapped CO₂, the ratio, F, defined as

$$F = \frac{nCO_2}{nH_2O} \quad (4.1)$$

is plotted against X_s(CO₂) which is defined as the fraction of CO₂ that has been evolved. It is expected that when the CO₂ is being released from the mineral structure, the F value should remain constant. CO₂ collected from the shallowest sample, 0 to 5-cm, does not show a constant value of F for any part of the dehydration process (Figure 4.9). The total CO₂ yield for the 0-5cm samples, corrected for sample weight, is also least three times greater and more variable than the rest of the samples (Figure 4.10). These facts, combined with the high organic carbon content of the O horizon and the presence of large amounts of HIV indicate that the CO₂ collected from these samples is possibly from some source other than trapped CO₂.

CO₂ yields from the remainder of the samples do show constant F values (figs. 4.11, B.2 through B.4) and therefore, the CO₂ from the identified plateaus are assumed to be trapped CO₂ in the gibbsite structure. Generally, the CO₂ yield decreases from 30 μmols/gram to 4.5 μmols/gram with increasing depth in the profile. The δ¹³C values of the plateaus for each sample show a general depletion of ¹³C with depth as expected by the diffusion model with an excursion at 30cm and 40cm toward more enriched values (Figure 4.12). The depleted values

obtained at 0-5cm are suspected to be indicative of contributions from organic carbon incorporated in the HIV present in this sample.

Possible explanations for the enriched $\delta^{13}\text{C}$ value for the 35-45cm sample are analytical error or some process that has affected the stable isotope composition of the samples independent of the remaining samples. The repeatability of the three experiments conducted on the 35-45cm sample, appears to rule out the possibility of analytical error, unless the same error occurred on each of these samples (fig 4.11). There was no unusual response of the dehydration system during the collection of these samples. This leaves some process that causes this sample to have equilibrated with the soil CO_2 differently than the other portions of the depth profile. In order to attempt to determine whether the CO_2 collected from these samples is distinct from the remaining samples, the $\delta^{13}\text{C}$ values were plotted against the $\delta^{18}\text{O}$ values of these samples (Figure 4.13). The samples from the 35-45cm depth range are clearly separated from the other samples on this plot, perhaps indicating that they were formed under different conditions.

An interesting feature of the plot of $\delta^{13}\text{C}$ values vs. $\delta^{18}\text{O}$ values is the appearance of a linear trend in the data. All of the samples from the 35-45cm sample are located at the end of the line that represents enrichment in ^{13}C and ^{18}O . It is also interesting to note that a line from the stable isotope composition of the atmosphere to the organic material measured in the 850C step of the dehydration process is roughly parallel to the trend line in the trapped CO_2 data. There is no evidence of a trend in mixing from the atmosphere end member to the organic matter end member with depth, but this is not surprising because the shallow depths are clearly more influenced by organic material than the samples between 20 and 45cm (Figure 4.12).

The oxygen isotope composition of soil CO_2 is useful in determining the amount of CO_2 that is contributed to the atmosphere by soil respiration as opposed to plant leaf exchange with

the air; as such, the processes that control the oxygen isotope composition of the soil CO₂ are fairly well understood. Soil CO₂ can be said to be essentially in equilibrium with soil water, which has essentially the same isotope composition as precipitation (Amundson et al., 1998; Miller et al., 1999). In a process similar to that described for carbon, though with some small changes resulting from the greater number of mass combinations for oxygen in CO₂, the gaseous CO₂ in the soil is fractionated by the process of diffusion by 8.8 ‰; though, in some cases, the diffusion rate of CO₂ is so rapid, that the oxygen is not fully equilibrated (Stern et al., 1999). Therefore, in order to attempt to describe the process that results in the linear trend seen in figure 4.10, the starting value of -33.00 ‰ will be used as representative of average precipitation for Georgia (van der Veer et al., 2009). I propose that the CO₂ trapped in the gibbsite structure starts as soil CO₂ in the pore space and becomes dissolved in the soil water that is on the gibbsite mineral surface. Therefore to begin, the carbon isotopes in the CO₂ are in equilibrium with the organic source and enriched in ¹³C by diffusion and mixing with the atmosphere, while the oxygen isotopes are in equilibrium with the soil water. It has been reported that near the surface, the soil water is enriched in ¹⁸O relative to the rest of the soil column due to evaporation (Miller et al., 1999). This enrichment can perhaps explain the general trend in the lower half of the soil profile towards heavier values of δ¹⁸O. This carbonate ion is adsorbed to the gibbsite surface and is trapped as the gibbsite structure encloses it in an edge defect. At this point, if the oxygen in the carbonate ion is equilibrated with the oxygen isotopes in the gibbsite structure, it follows that the fractionation factor for H₂O to gibbsite of 15.69 at 15C, applies (Vitali et al., 2000). This fractionation will result in a δ¹⁸O of trapped CO₂ of ca. -17.3‰. This requires that, in order to result in the oxygen isotope ratio measured for the trapped CO₂, the fractionation due to diffusion, for the whole profile, must be at least 12‰. This is greater than the calculated

fractionation of -8.8‰, but it should be noted that the amount of water in the soil, the presence or absence of carbonic anhydrase, and the temperature of the soil all can affect the final oxygen isotope composition of the soil CO₂ (Amundson et al., 1998; Gillon and Yakir, 2012; Miller et al., 1999).

None of the processes described above are able to explain the extreme shift in oxygen isotope composition of the samples from the 35-45 cm depth range. Therefore, there is some process other than diffusion that is controlling the isotopic composition of this sample. One possible explanation for the enriched carbon and oxygen isotope compositions at this depth could be the result of C₄ plants at some period in the past at this location. The δ¹³C values would be expected to be between -19 and -8‰ (fig 3.2), and the δ¹⁸O values might be expected to be enriched if the climate was drier, allowing for C₄ plants to be expected. While this is contrary to the photographic evidence of the field site as having been covered in forest for at least 100 years (Figure 4.2), it is not likely that the gibbsite formation occurred in the past 100 years and it is possible that at some point in the past the climate was drier and C₄ plants may have dominated. However, there is evidence in the δ¹³C value of the organic carbon of the soil that indicates this was not the case.

4.3.3 MODELING RESULTS

Compared to the measured δ¹³C values of trapped CO₂ from this study to those from Panola Mountain; these are more depleted in ¹³C by ca. 4‰. This indicates that the modeled soil respiration rates will necessarily be greater than those for Panola Mountain. Initial modeling using the analytical solution of the model indicates that even using the highest soil respiration rate, 900 gC cm⁻² y⁻¹, the modeled soil CO₂ δ¹³C values are too enriched. These results are contrary to those for the Panola Mountain data discussed in chapters 2 and 3. Monte Carlo

simulations using the distribution of $\delta^{13}\text{C}$ values for C_3 vegetation from figure 3.2, and $Q = 650 \text{ gC m}^{-3} \text{ y}^{-1}$ results in a good fit for the most data points with the exception of the 15 and 30 cm samples (Figure 4.14).

Finite difference modeling using a gamma distribution for soil CO_2 production with depth centered around a characteristic depth of production of 25cm and $Q = 900 \text{ gC cm}^{-2} \text{ y}^{-1}$, results in a solution that falls between the data points but does not cross them. The variability of the data, both the $\delta^{13}\text{C}$ of the plateau values (between samples, not within samples) and the $\delta^{13}\text{C}$ values of organic matter as determined by the 850C step of the dehydration procedure will make it difficult for any single solution to match all depths. When plotted on top of the Monte Carlo simulation in M0069, this finite difference solution falls inside the highest probability area (Figure 4.14). Even if the soil respiration rate is $1500 \text{ gC m}^{-2} \text{ y}^{-1}$, the modeled $\delta^{13}\text{C}$ values of soil CO_2 are too enriched to match the data points. The $\delta^{13}\text{C}$ values of recalcitrant organic carbon measured from the 850C step of the dehydration procedure matches well with the $\delta^{13}\text{C}$ values of the bulk soil, indicating that this is a useful method of determining the $\delta^{13}\text{C}$ value of organic carbon in paleosols (Figure 4.16).

4.4 DISCUSSION

These model results are in direct opposition to the results obtained using the data from the Panola mountain field site. This disagreement raises questions about the consistency of this proxy, and whether there are local variables that are controlling the process. These discrepancies are either the result of analytical differences in the two, or some difference in the processes controlling the stable isotope composition of trapped CO_2 in gibbsite. Analytical problems can be ruled out by examining the data for inconsistent results in any of the repeated samples. Additionally, the results can be compared to the expected results, i.e. amount of CO_2 yield, and

the consistency of the yields between samples and within samples. If all analytical causes for these inconsistent results are ruled out, the implication is that there are local variables that are affecting the stable isotope composition of the CO₂ trapped in gibbsite which may invalidate the use of this proxy.

There are differences in the parent material and setting of the two sites. The parent material at Panola Mountain is homogeneous granite at a high point in the topography while the Watkinsville site has Athens gneiss for a parent material, and is a forested site that is on a very slight slope, but is near a local high in the topography ruling out fluvial inputs. The ¹⁰Be exposure age of the Panola Mountain soil profile is 10⁵ years, while the ¹⁴C model age for the soil at 250cm is 8000 years indicating that the soil is relatively young and therefore, is probably removed fairly rapidly. There is no age data for the Watkinsville site but one could imagine that its very slight slope may provide for more time for the soil to allow more generations of secondary minerals to dissolve and precipitate, thus maintaining more homogeneous δ¹³C values in trapped CO₂.

One method of assessing the validity of the analytical method is by comparing the results of this study to those of Schroeder and Melear (1999), and CO₂ collected from gibbsite in Eocene age samples by Tabor and Yapp (2005b). The δ¹³C values are plotted against the F ratio (eqn. 4.1) and they are expected to be relatively close groups (Figure 4.15). The procedure of Tabor and Yapp uses lower temperatures (190C) because the samples were broken down too rapidly at 230C. They describe the samples as losing 60% of the structural gibbsite hydrogen in the first 30 minutes. This rapid breakdown was not witnessed in any of the samples in this study. Nevertheless, it does appear that the plateau values they achieved were much more consistent

and plot in smaller groups. This seems to indicate that perhaps the dehydration process should be conducted at lower temperatures.

Figure 4.15 also indicates that the F ratio for these samples was higher than both the Schroeder and Melear (1999) and Tabor and Yapp (2005) samples. The samples of Tabor and Yapp consisted only of gibbsite, kaolinite, and boehmite, while the samples of this study and Schroeder and Melear contained gibbsite as well as goethite, both of which contribute CO₂ during dehydration at the temperatures used in these experiments. An experiment was conducted to attempt to remove the Fe or Al from two aliquots of a sample but the results were inconsistent. The 25-35cm sample was subsampled into two separate samples (2535Al2 and 2535Fe51) to remove their aluminum or iron hydroxides respectively as described in section 4.2.4. The decarbonation procedure showed that the carbon yields for the NaOH treated sample were several times greater than expected, and it is expected that the (NH₄)₂CO₃ rinse may have contaminated the sample. The average $\delta^{13}\text{C}$ value for the plateau of sample 2535Fe51 was -15.05 ‰ PDB. Comparing this to the untreated plateau value of -16.60‰ shows there is a slight enrichment in ¹³C in the CO₂ coming exclusively from the gibbsite. Therefore, it is possible that the combination of contribution of CO₂ from the goethite in the soil, and the uncertainty introduced by the rapid breakdown of the gibbsite structure at 230C resulted in the difference in the F ratio and ultimately the difference between the $\delta^{13}\text{C}$ values of trapped CO₂ in the Panola Mountain samples compared to this study.

While the F ratios of the samples in this study are not as consistent as those measured by Yapp, the results were reproduced consistently and therefore are assumed to be representative of the stable carbon and oxygen isotopes of CO₂ trapped in pedogenic gibbsite. Therefore, the difference in the results between this and previous field study should be explained with respect to

the soil forming processes in an attempt to determine where the model needs to be further refined.

Examining the trends in all data with depth, it becomes more clear that there are likely physical and chemical processes in the soil that are not well represented in the model that are controlling the variation of carbon and oxygen stable isotope compositions (fig 4.17). There are three main systems that are operating in the soil that can affect these compositions; biological systems, including the recycling of organic carbon and the initial production of CO₂ by roots; hydrologic systems, including the way water flows through the soil and how changes in texture may affect water flow and particle transport in the unsaturated zone; and isotope systematics, or the way that isotopes are fractionated in response to the conditions in the environment such as evaporation and temperature.

Based on the sharp increase in the amount of clay at the top of the B horizon (30-40cm fig 4.17a), it is likely that the change in hydraulic conductivity between the sandy loam in the A horizon to the clay loam and clay in the Bt horizon results in an increase in the water content at the top of the B horizon following precipitation events. The confluence of this change in texture with the shift in isotope compositions at this depth suggests that the process responsible for this shift is related to the change in hydrology and the implications this change has for the soil minerals and biology at this depth. This process must be able to explain the negative shift in the carbon isotope composition of the organic carbon at this depth (ca. 22.5cm), and the corresponding carbon trapped in the gibbsite structure, and a positive shift in the oxygen isotope composition.

It is generally well accepted that the soil organic matter (SOM) is enriched in ¹³C with depth in the soil, and it has been shown that this enrichment occurs through time, with ca. 3‰

enrichment over 120 days (Schweizer et al., 1999). There is some debate about the mechanism responsible for this enrichment but it is believed that the bulk of the enrichment is the result of isotopic fractionation of carbon and the mixing of soil carbon from the soil gas, which is enriched by 4.4‰ (see section 1.1.8.1) and SOM during microbial decomposition (Ehleringer et al., 2000; Nadelhoffer and Fry, 1988). The observed trend in the $\delta^{13}\text{C}$ values of the SOM match the expected trend, indicating that as the SOM is decomposed, and the %C decreases with depth in the soil, the $\delta^{13}\text{C}$ values are more enriched in ^{13}C .

There is a large shift in the $\delta^{13}\text{C}$ of the SOM collected during the 850C step of the dehydration process that occurs directly below the change in soil texture at the AB horizon. This decrease is confirmed in the treated samples. This indicates that the organic carbon that was not removed by the chemical treatments is not of the same isotopic composition as the SOM in the bulk soil. The difference between the treated value and the bulk value of about 3‰ suggests that there are temporal variations in the $\delta^{13}\text{C}$ value of SOM. The factors that determine the isotopic composition of the SOM are inputs of relatively depleted organic material into the soil and the degree of fractionation or mixing that the SOM has undergone during the decomposition process. Because the processes of mixing and fractionation proceed through time from some starting value, it stands to reason that the highly enriched organic material measured in the treated samples is the result of longer residence time in the soil or more enriched inputs. As there is no reason to believe the input value has changed, the shift appears to be the result of longer or more intense decomposition at this depth. Because this depth coincides with the change in soil texture I propose that the difference in $\delta^{13}\text{C}$ value is the result of increased decomposition either because the SOM spends a longer time at this depth due to the change in the ability of this material to

move down through the soil, or is more intensely altered due to increased soil moisture resulting from decreased hydraulic conductivity at this depth (Buchmann et al., 1997).

There is also an anomalous trend in the plateau $\delta^{13}\text{C}$ values of the trapped CO_2 . The expected trend is for mixing between the atmosphere and the soil gas CO_2 $\delta^{13}\text{C}$ values as controlled by diffusion through the soil. $\delta^{13}\text{C}$ values are more depleted at the transition from the A horizon to the B horizon, which is more representative of the SOM than the expected soil CO_2 gas. As depth increases to 40 cm, the expected enrichment of ^{13}C is evident, but at this depth it is not expected to be this enriched due solely to diffusive mixing with the atmosphere unless there are macropores at this depth that allow for very rapid diffusion directly to the surface. Macropores are not expected because this soil generally shows massive texture throughout its depth.

Another interesting point to observe is the trend of enrichment in the plateau values from 2.5 to 15cm. This is accounted for by the fact that the CO_2 collected during the dehydration process is more influenced by carbon that is associated with the HIV in the O horizon. This same trend is repeated in the interval from 22.5 to 40cm, the top of the B horizon. This suggests that if the $\delta^{13}\text{C}$ value of the trapped CO_2 is in equilibrium with the soil gas CO_2 , there is some large input of CO_2 at this depth that is in equilibrium with the SOM that is large enough to overcome the mixing of the atmosphere. Assuming that the bulk of the root mass of the trees is above the clay layer beginning at 30cm depth, and the change in hydraulic conductivity does result in accumulation of water at this depth following precipitation events, it is not unreasonable to conclude that there is more root respiration at this depth, and more microbial activity, which is supported by the more enriched SOM.

If this is correct, the shift in isotopic composition from 15 to 30 cm implies that the gibbsite at this depth is authigenic and perhaps a second or third generation. Age dating of gibbsite has shown that the top 40cm of the soil is relatively well mixed and shares a younger age than the SOM deeper in the soil (Schroeder et al., 2001). The implication is that the minerals above 40cm are continuously undergoing dissolution and precipitation while deeper in the soil the minerals are preserved. Using this model however there is no easy way to explain the enrichment of ^{13}C and ^{18}O at 40cm. It could be supposed that during dry periods, when gibbsite formation is more likely, the CO_2 production rate is at a minimum and the mixing with the atmosphere is re-established and this is when the CO_2 is trapped, but that does not explain why the data points at shallower depths do not show the expected trend with depth, increased evaporation from this layer during dry periods may explain the enriched $\delta^{18}\text{O}$ values. The simplest method of explaining the oxygen isotope trend and reconciling all the different factors affecting the carbon isotope composition is to add vertical transport of clay through the soil. The carbon and oxygen isotope compositions of the 40cm sample are most like the atmosphere (Figure 4.13); presumably, there is some fraction of the gibbsite that forms in the upper portion of the soil with the isotopic composition expected near the surface. As the gibbsite is transported through the soil, some of it is recycled and takes on the isotopic composition of the soil gas as influenced by the processes discussed above. The portion that is not recycled is concentrated in the top portion of the Bt horizon where the recycling of the gibbsite no longer occurs, allowing for the atmosphere like composition of the plateau CO_2 at this depth. If the two depths with depleted carbon isotope values and slightly depleted oxygen isotope values of trapped CO_2 are taken to be the depths in the soil where the majority of the new organic material is introduced, through the roots at 22.5cm depth and at the surface; the enrichment below these depths cannot

be explained by the enrichment of the SOM but may be indicative of transport of clay deeper in the soil. This mechanism can be tested by dating the gibbsite using ^{14}C ; there should be younger minerals at 2.5 and 22.5 cm depth and the minerals below 40cm should all belong to an older generation.

4.5 CONCLUSIONS

Modeled soil respiration rates are a good match for the stable isotope composition of the trapped CO_2 in the field study conducted here if the $\delta^{13}\text{C}$ values of the organic material is assumed to be -28‰. This is especially true in the deeper section of the soil, which from the perspective of a paleo- PCO_2 proxy is the portion of the soil that is most likely to be preserved and sampled. In fact, the soil carbonate proxy relies completely on the deep portion of the soil where the stable isotope composition is constant. These results are inconsistent with the results from previous studies of modern soils, raising doubts about the universal application of the method.

Analysis of the consistency of the CO_2 collected during the dehydration process and the stable isotope composition of the plateaus indicates that the speed of dehydration of the gibbsite may be too high at 230C. There appears to be a linear trend between the stable oxygen and carbon isotopes that may indicate that the CO_2 is in equilibrium with the gibbsite oxygen, confirming the fact that the CO_2 is associated with the gibbsite in its structure. This may be useful as an indicator that the CO_2 being analyzed is not contaminated by organic carbon, or carbon from another mineral source. The difference in the fraction factors of oxygen isotopes between H_2O and goethite (7.33‰) (Yapp, 1990), and H_2O and gibbsite (15.69‰) (Vitali et al., 2000) is also large enough that contributions from CO_2 trapped in the goethite structure, in soils where the minerals are co-existent, may be detected.

Ultimately, until the reason for the discrepancy in the two experiments conducted on gibbsite as a proxy of paleo-PCO₂ is determined, the usefulness of this proxy is in question. Analyses on the samples used in this study to determine the optimum temperature of dehydration could improve the certainty of the results. Finally, the experiments that were conducted to determine the fractionation of carbon trapped in the gibbsite structure were inconclusive due to contamination of the samples treated with NaOH with an additional source of carbon. Refinement of this method to remove contaminants will allow for the determination of fractionation and possibly help to explain if the combination of two sources of carbon, from goethite and gibbsite, are affecting the model results.

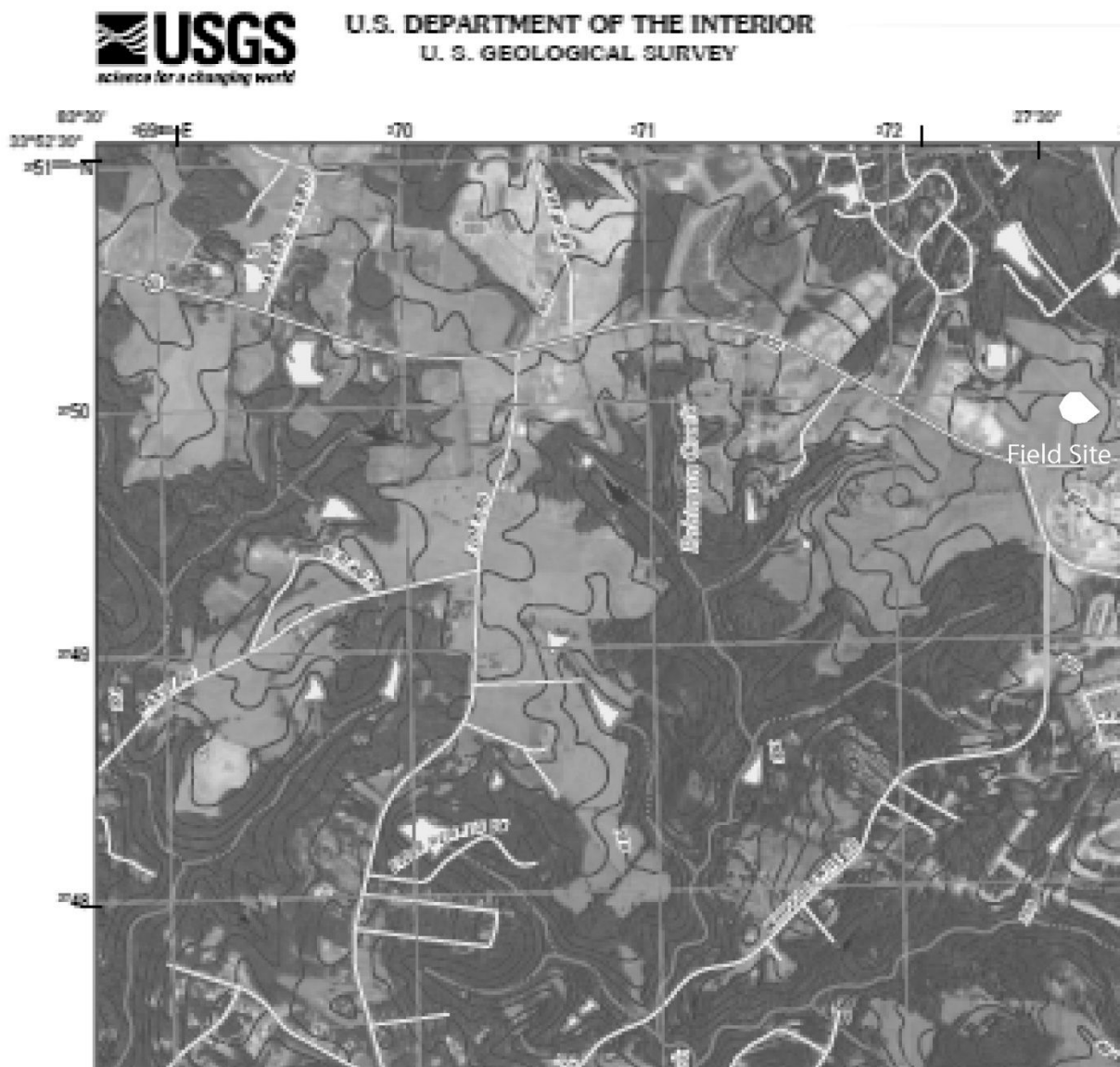


Figure 4.1. Topographic map showing location of the field site, Watkinsville Quadrangle, 7.5 minute series, 2011.

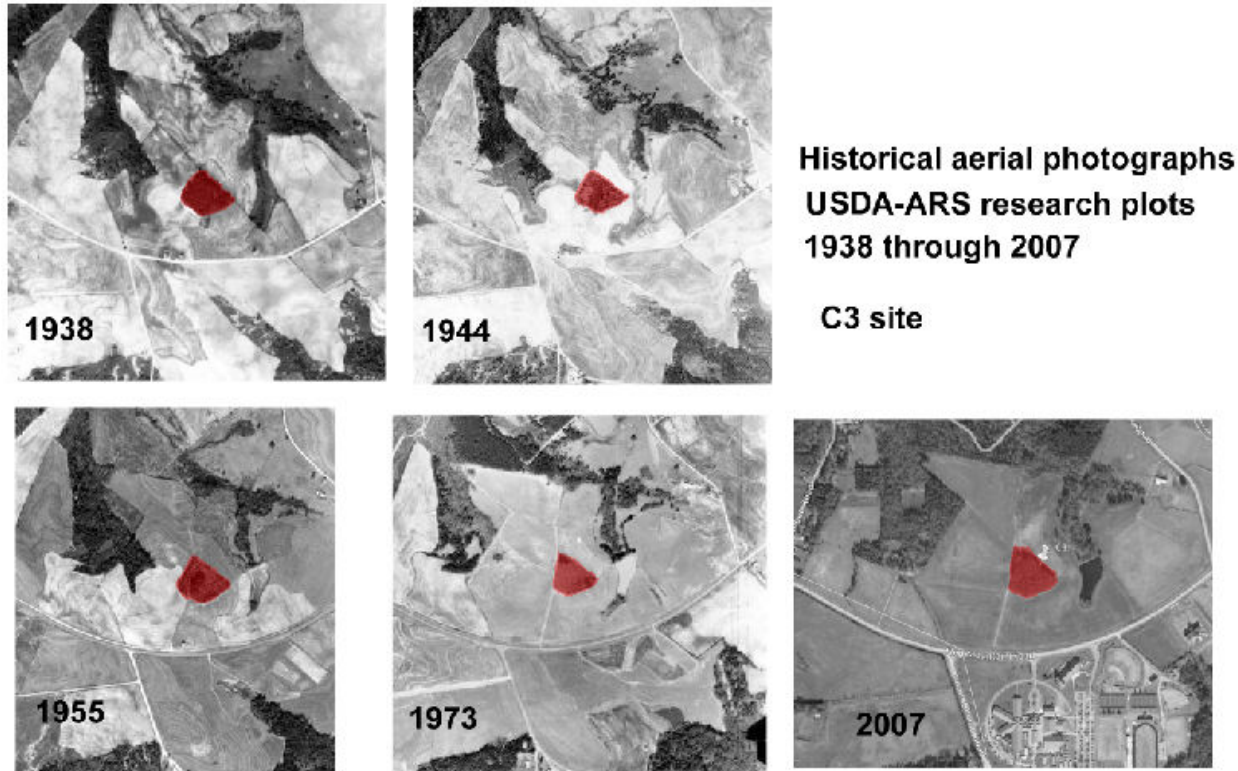


Figure 4.2. Aerial photographs of the field site from 1938 to 2007 showing the presence of wooded area through at least 75 years.

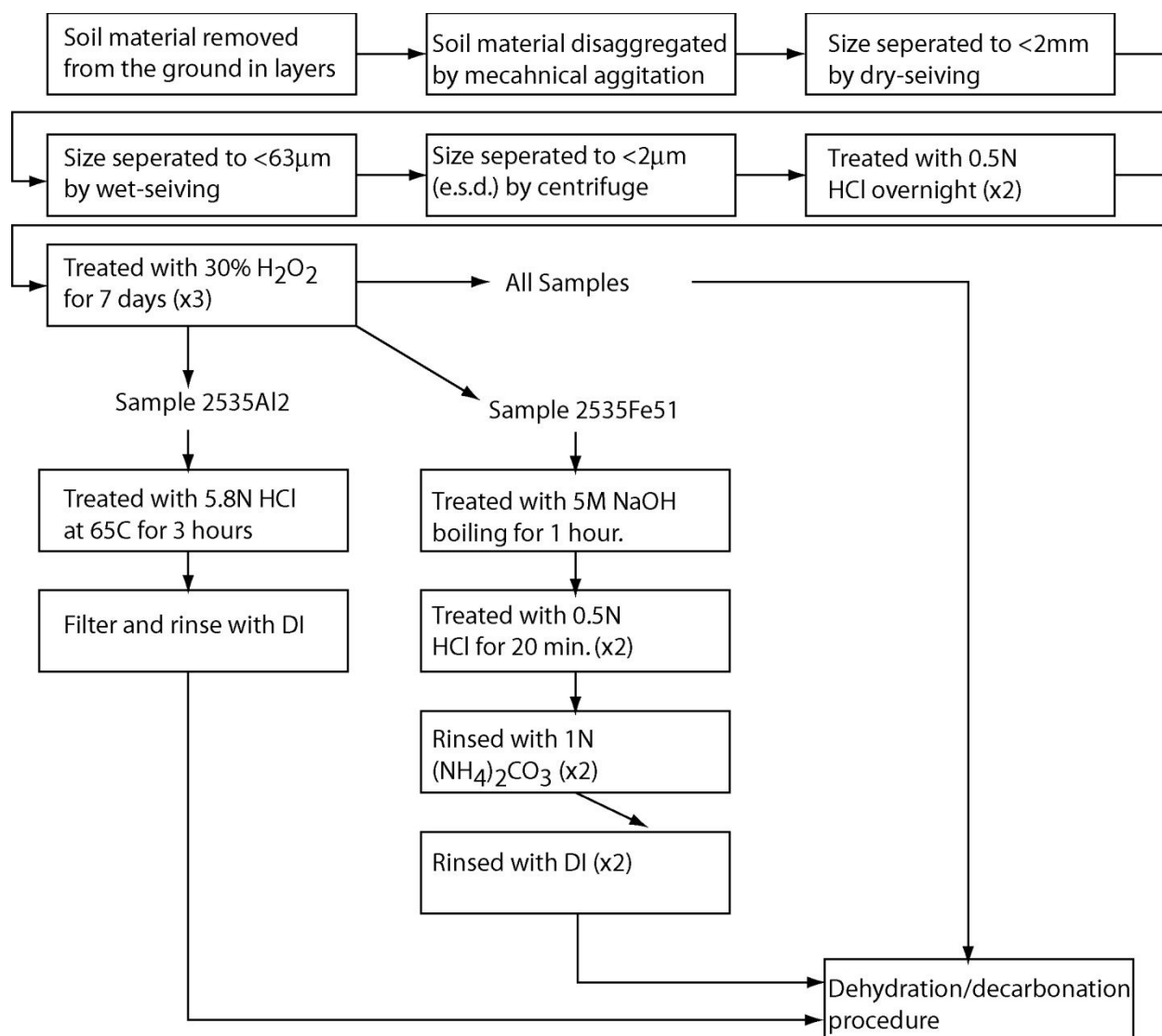


Figure 4.3 Chemical treatments used to prepare samples for carbon extraction during dehydration/decarbonation procedure.

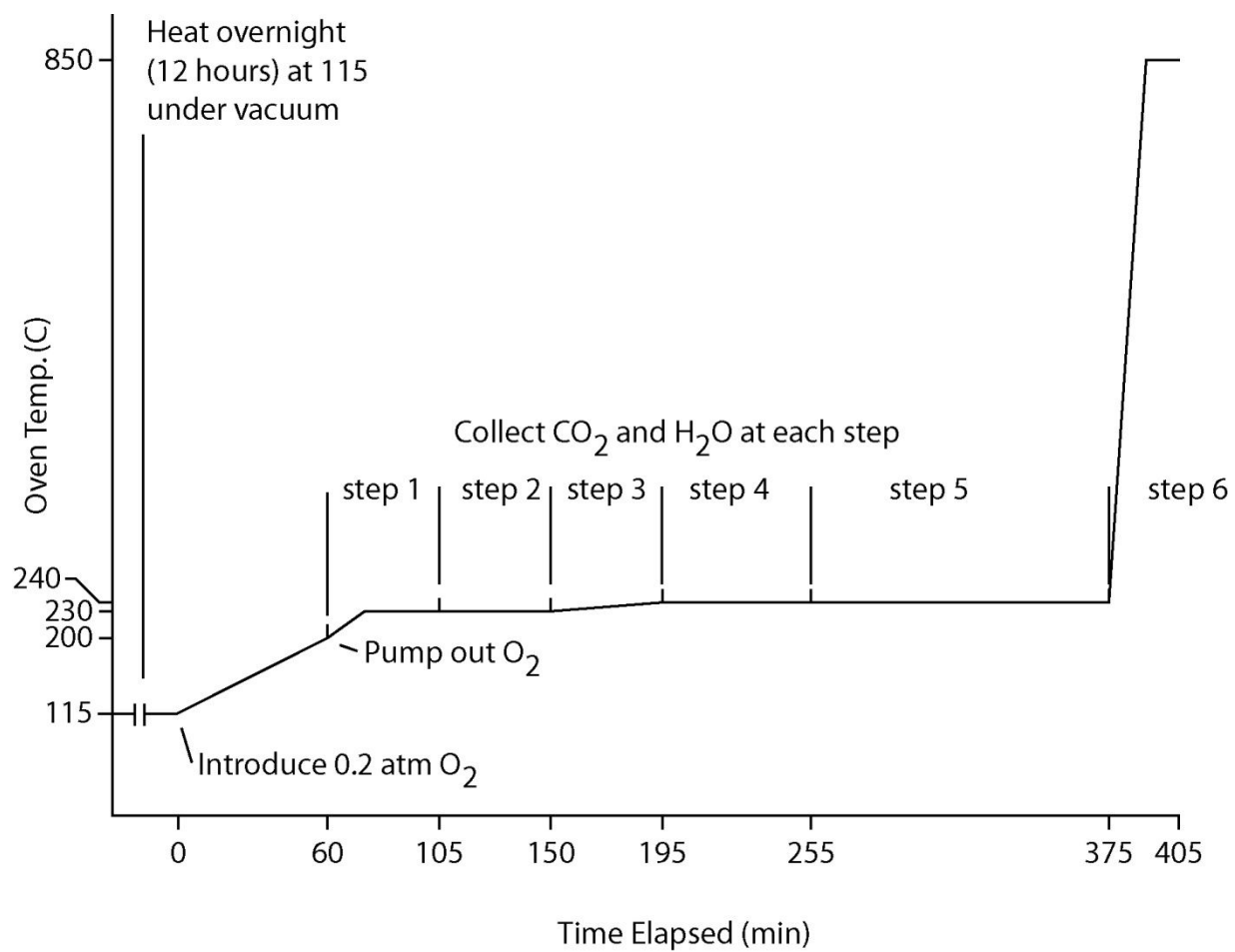


Figure 4.4 Dehydration/decarbonation heating times and sample extractions.

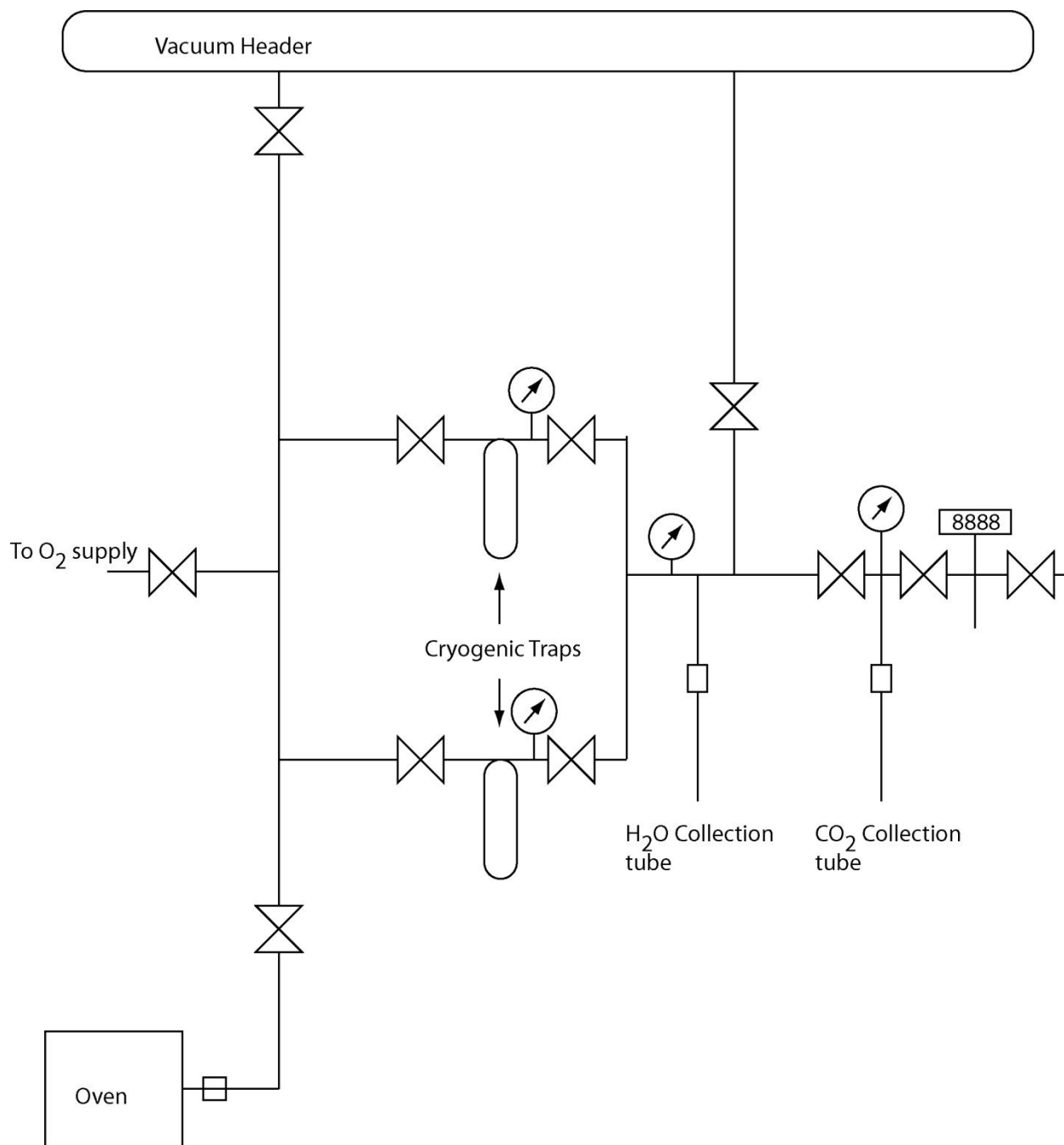


Figure 4.5 Schematic of the CO₂ extraction line. Sample is separated and collected using one cryogenic trap while the next sample is frozen in the other trap.

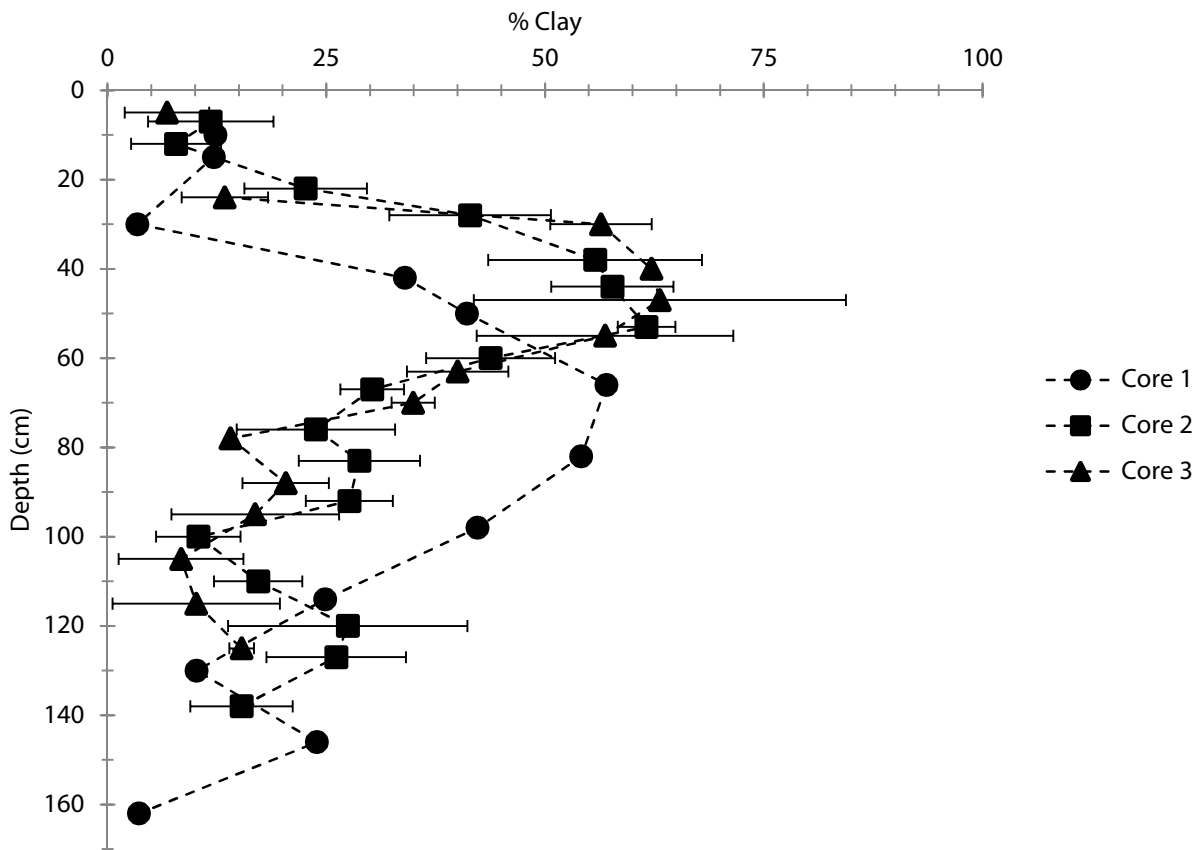


Figure 4.6 %Clay for the three cores extracted around the sides of the soil pit. Error bars represent one standard deviation of three replicate analyses.

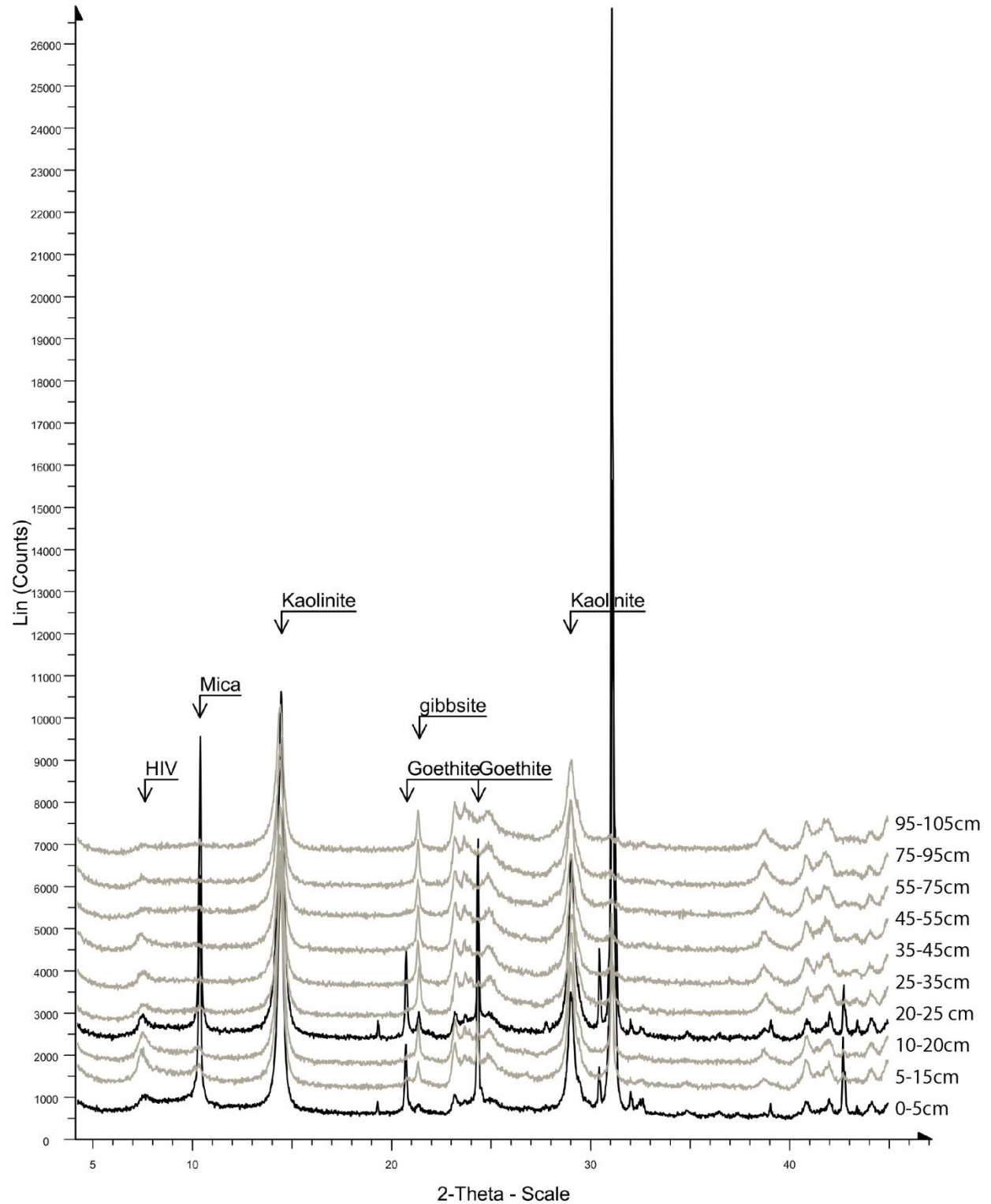


Figure 4.7. X-ray diffraction pattern of <math><2\mu\text{m}</math> size fraction of soil material (after chemical treatment).

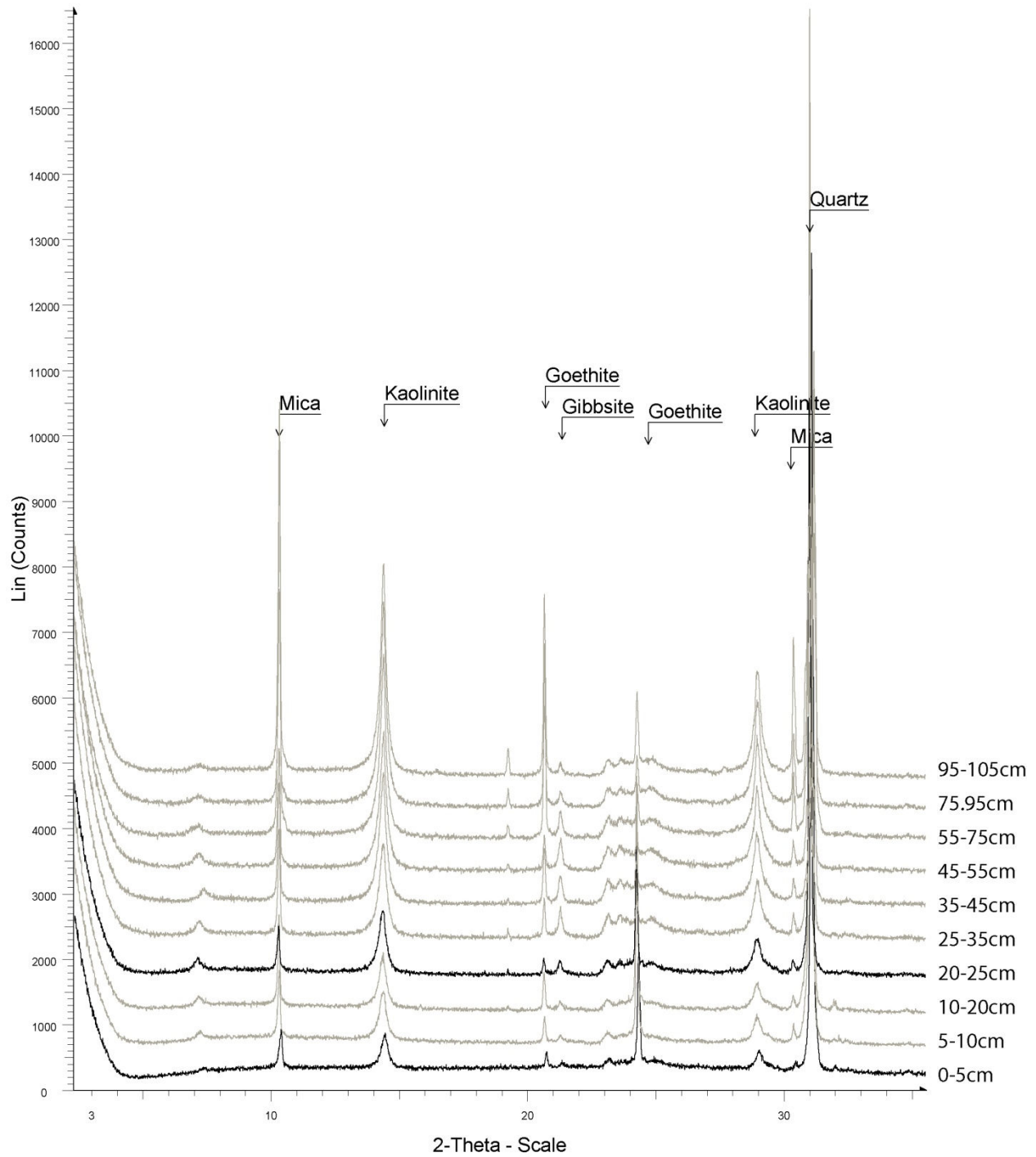


Figure 4.8. X-ray diffraction pattern of powdered bulk soil material.

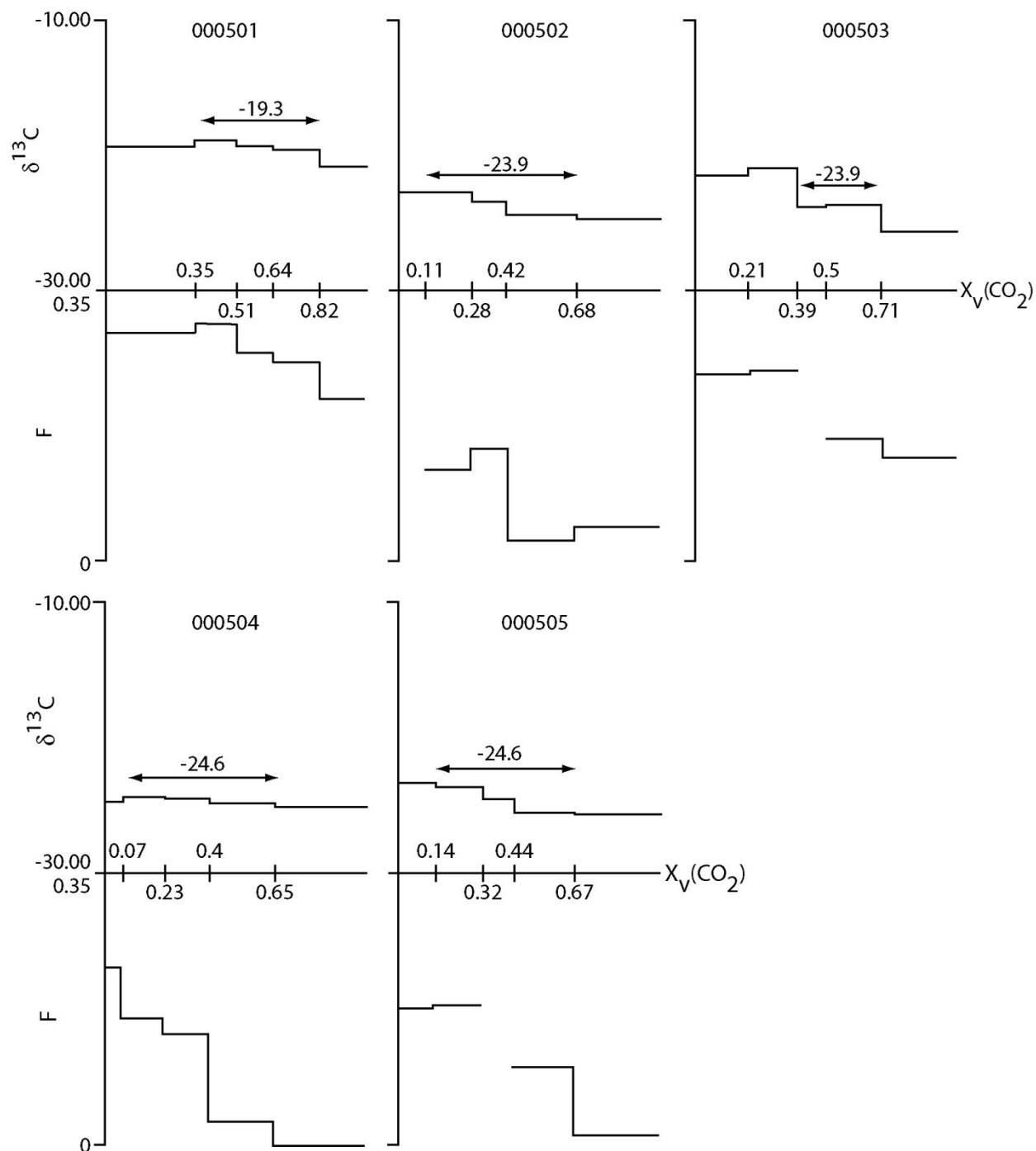


Figure 4.9. Dehydration/decarbonation steps for replicates of sample 0005. $X_v(\text{CO}_2)$ is the fraction of the total CO_2 yield in a given step. Average plateau $\delta^{13}\text{C}$ values are labeled on arrows representing the plateau region.

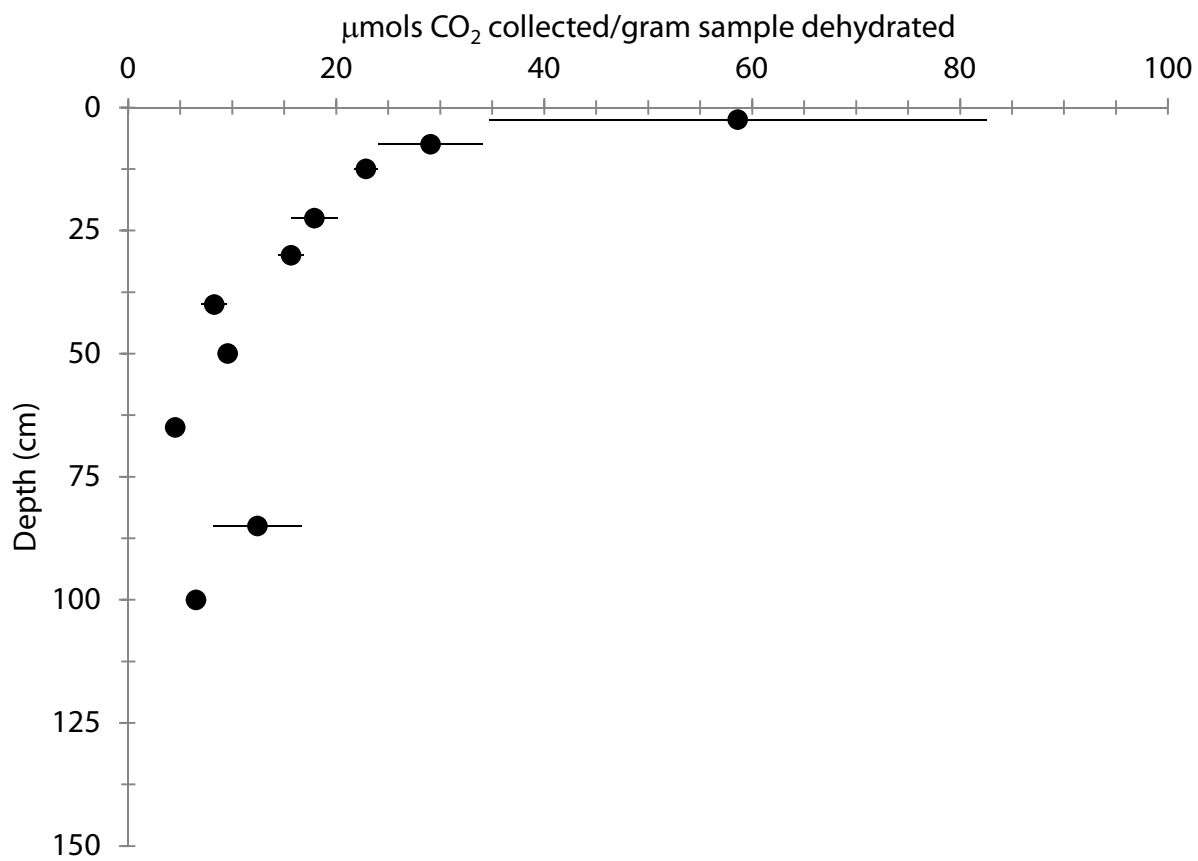


Figure 4.10. Amount of CO₂ yield (μmol/g) for each depth. Data points are the average for all replicates at each depth and error bars represent one standard deviation.

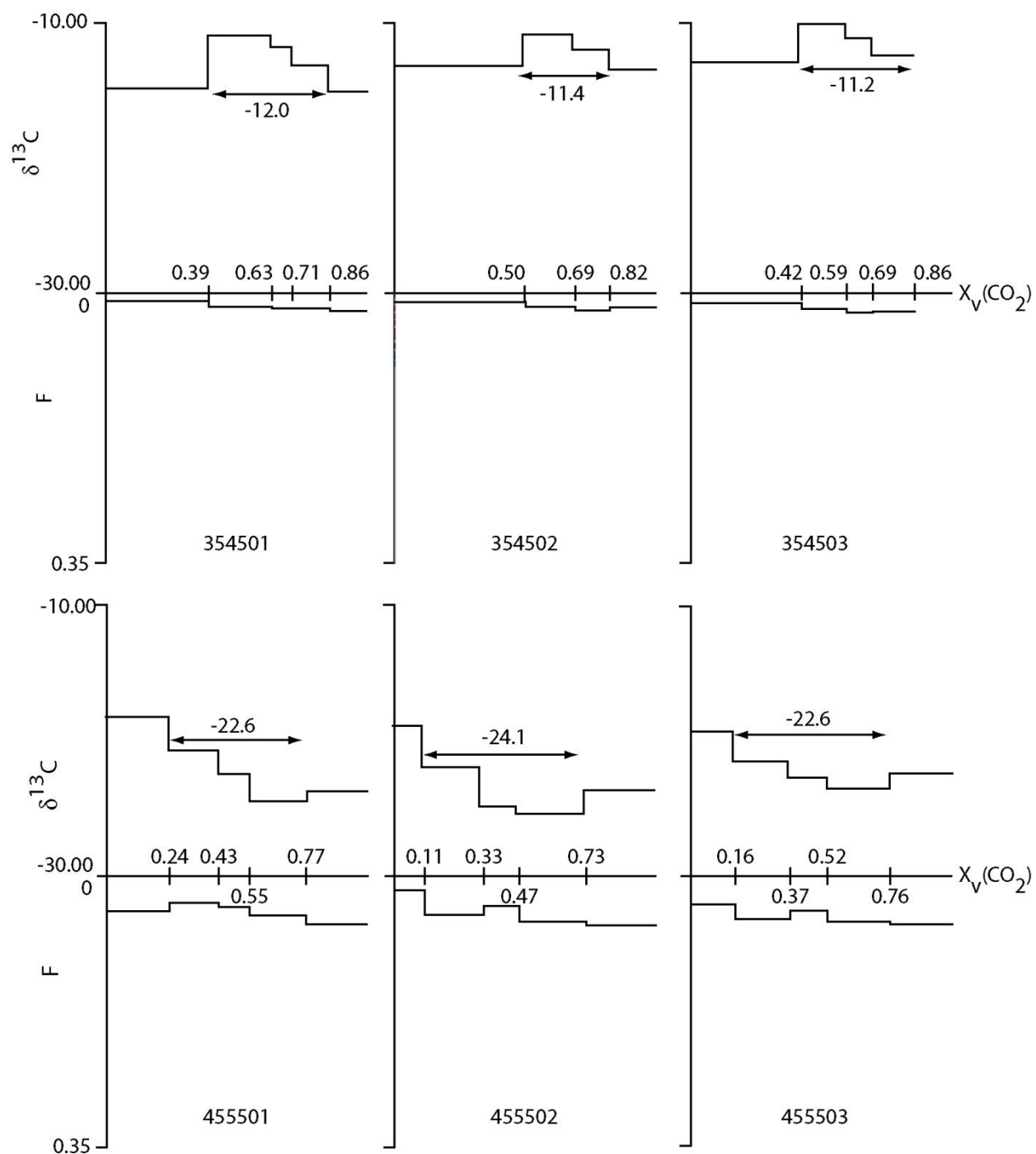


Figure 4.11. Dehydration/decarbonation steps for replicates of samples 3545 and 4555. $X_V(\text{CO}_2)$ is the fraction of the total CO_2 yield in a given step. Average plateau $\delta^{13}\text{C}$ values are labeled on arrows representing the plateau region.

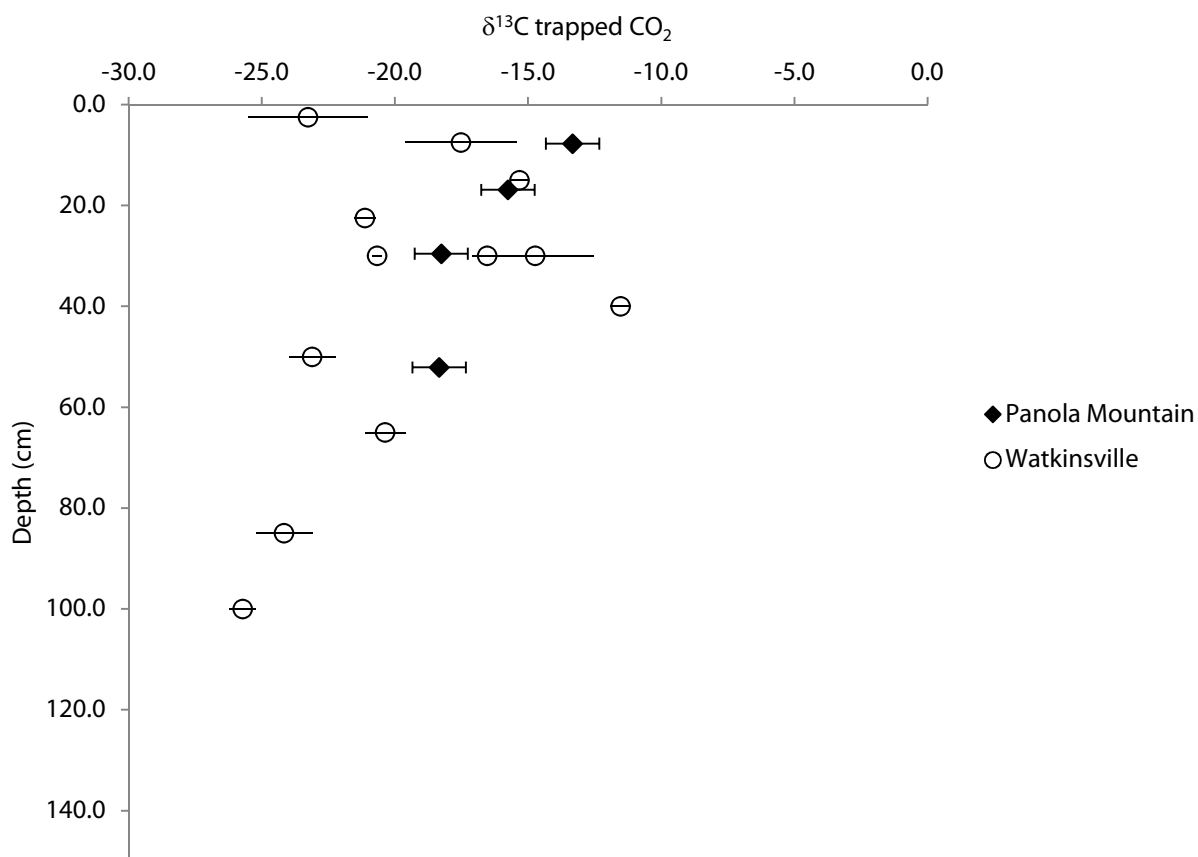


Figure 4.12. $\delta^{13}\text{C}$ values of CO_2 trapped in pedogenic gibbsite vs. depth. Data points represent the average plateau value of replicates at each depth and the error bars represent 1 standard deviation of variability between replicates.

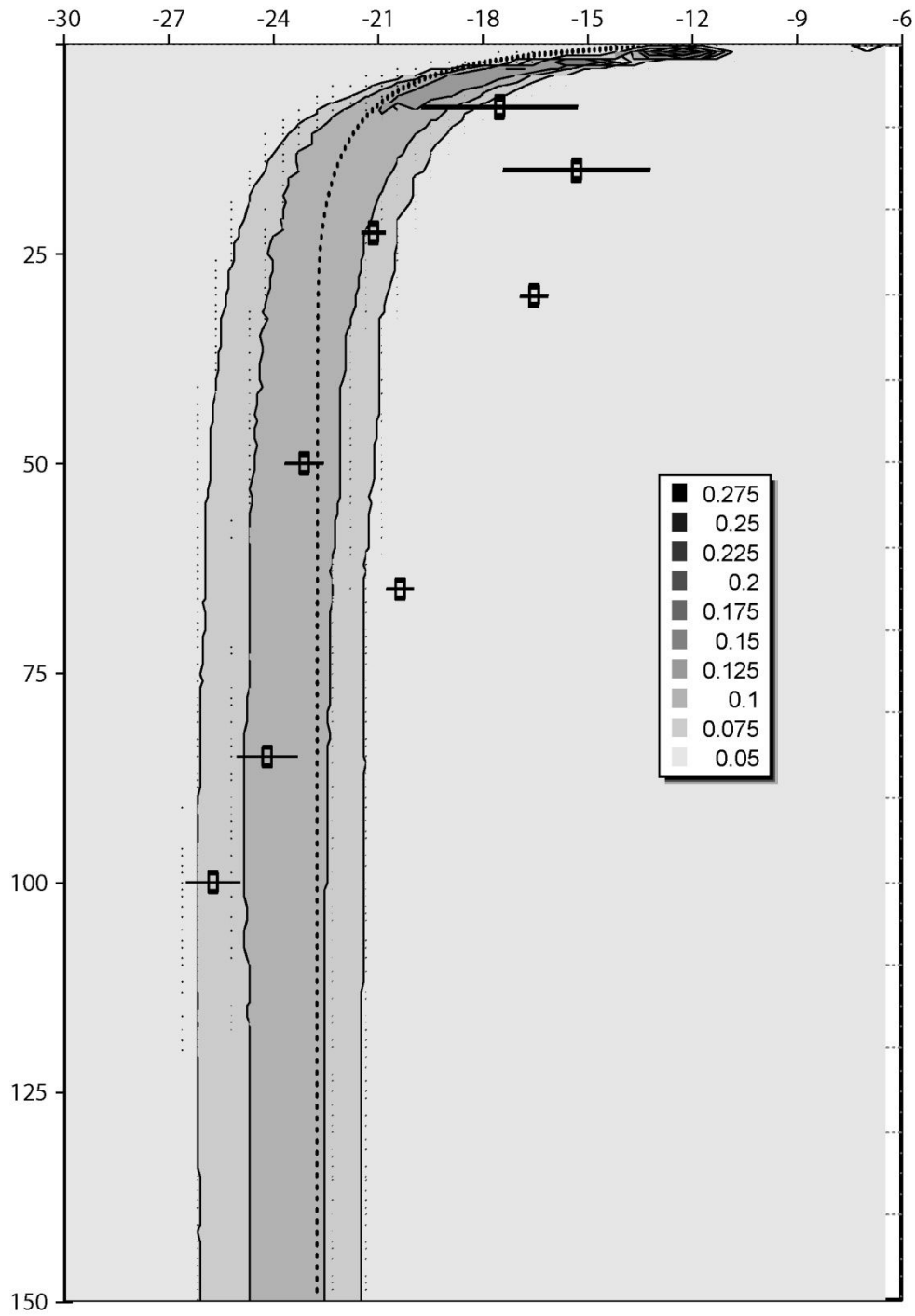


Figure 4.14. Monte Carlo simulation of soil CO₂ stable isotopic composition. Dashed line is the finite difference solution calculated using a gamma distribution for CO₂ production with depth, see table 4.2 for all parameters used.

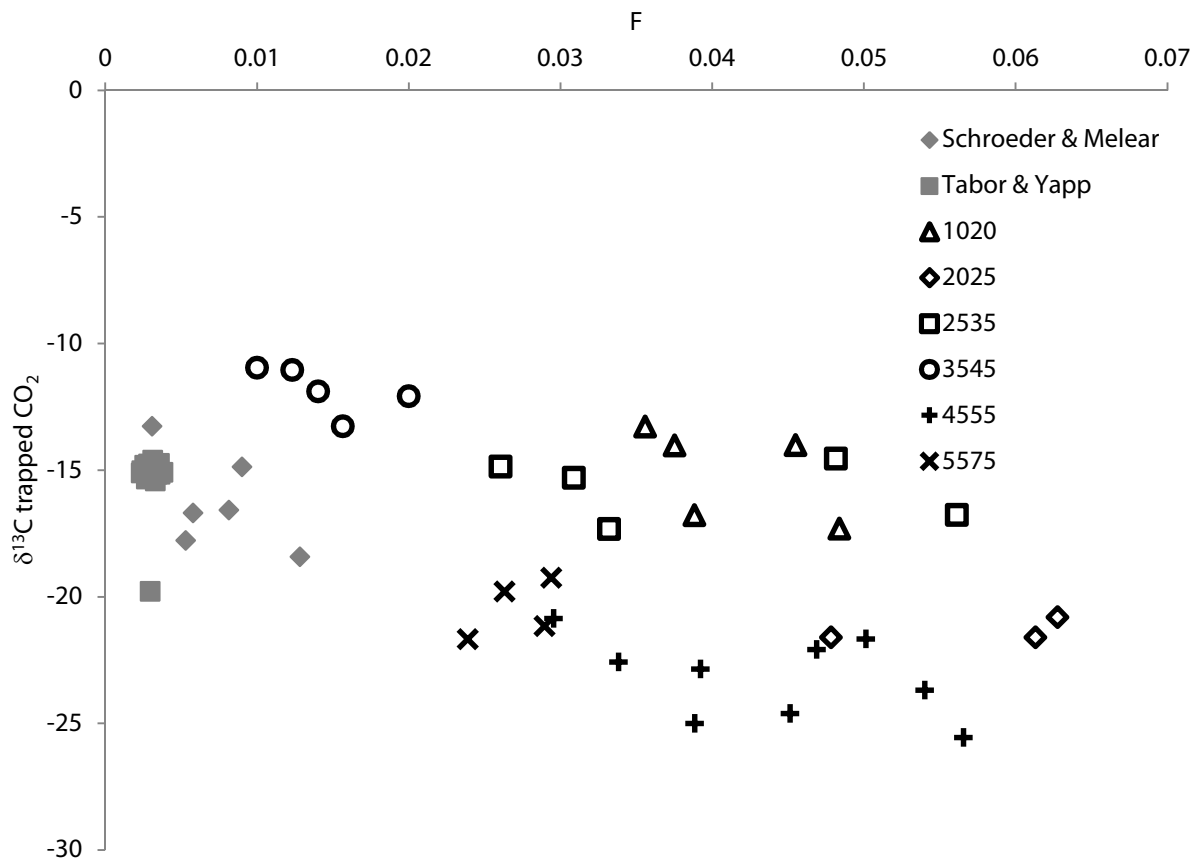


Figure 4.15. F ratio vs. $\delta^{13}\text{C}$ CO_2 trapped in pedogenic gibbsite (After Tabor & Yapp, 2005b)

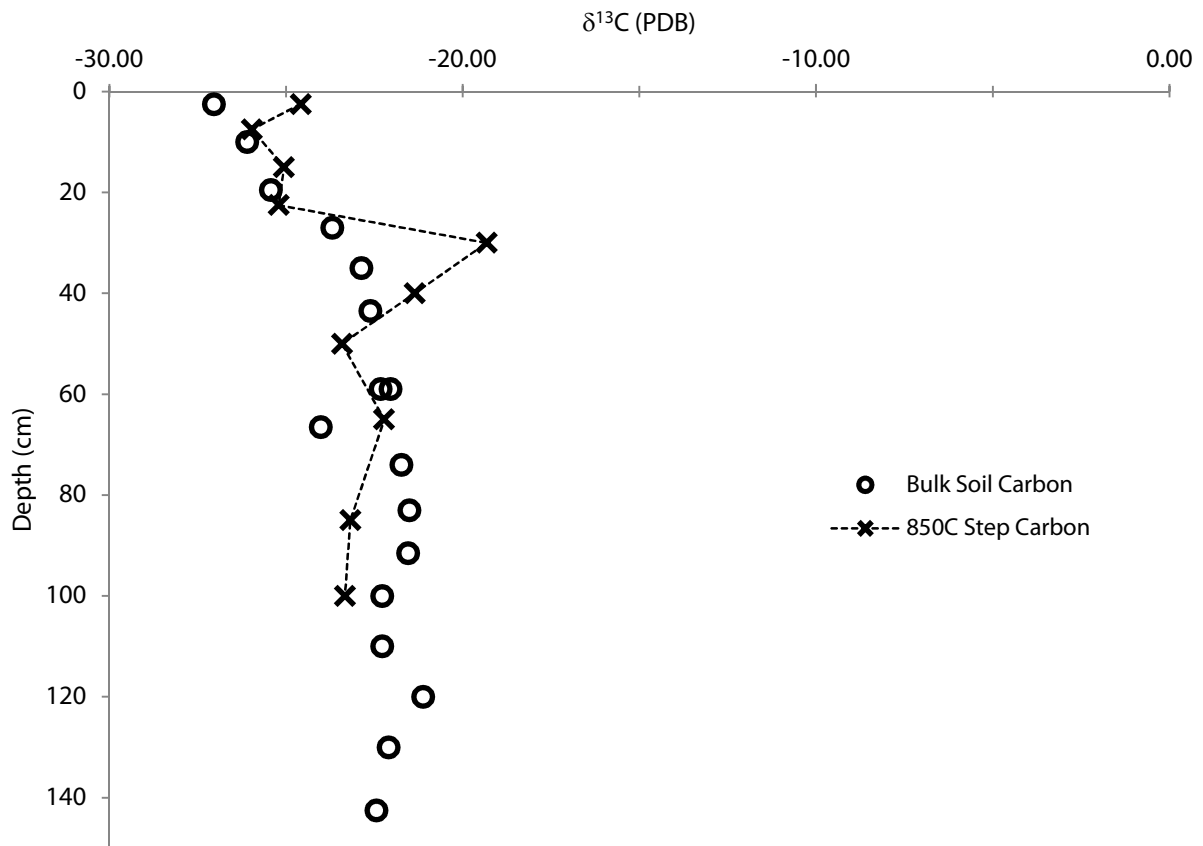


Figure 4.16. $\delta^{13}\text{C}$ values for carbon in bulk soil samples (open circles) and the 850C step of the dehydration process.

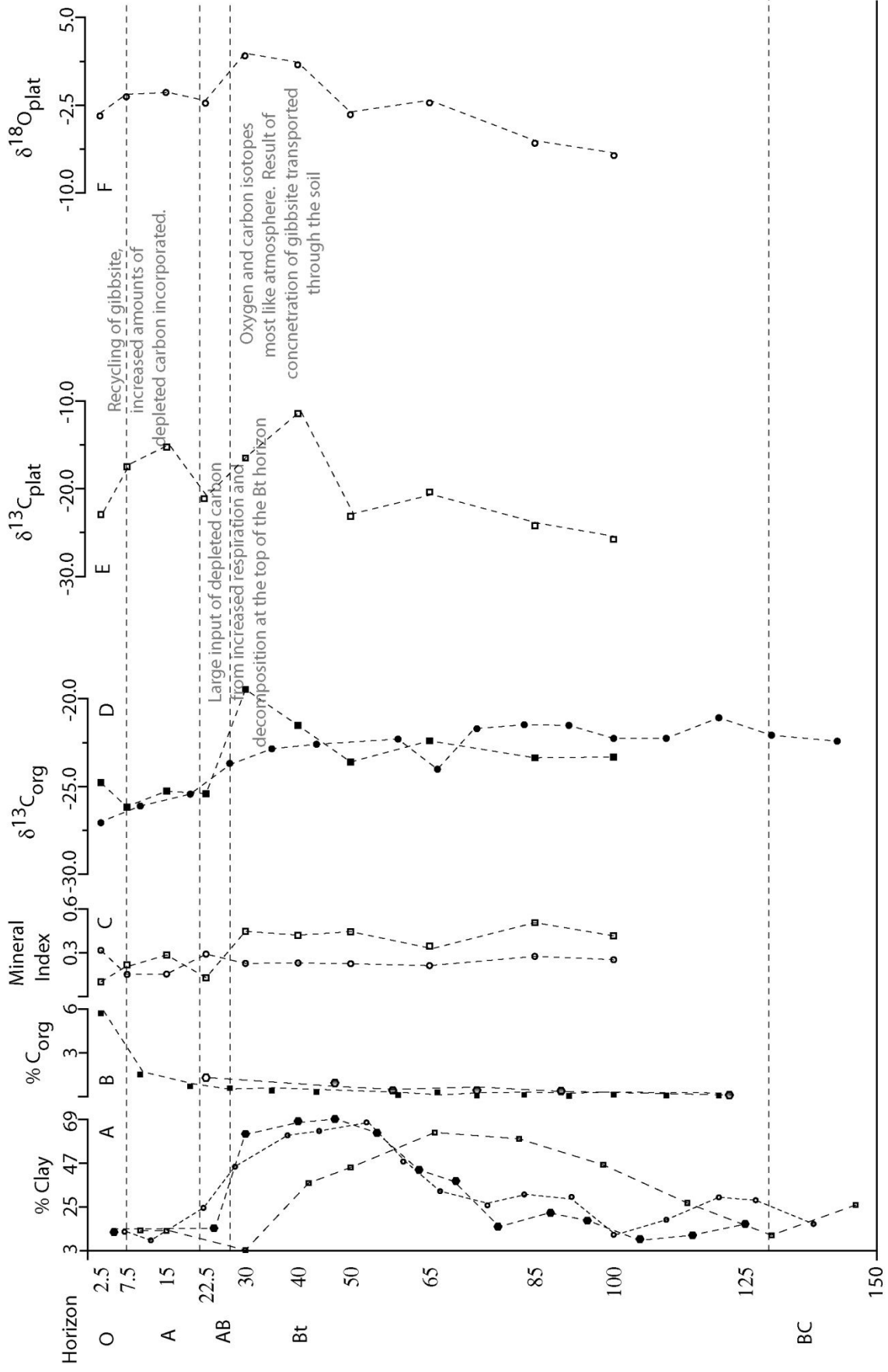


Figure 4.17 Compilation of all data collected at field site. (A) reproduction of figure 4.6, open squares – core 1, open circles – core 2, hexagons – core 3. (B) % carbon from core 3(squares) and core 1 (hexagons), (C) Mineral index defined as XRD peak height of gibbsite peak (open squares) and goethite peak (open circles) as a ratio with kaolinite peak heights. (D) $\delta^{13}\text{C}$ of organic carbon from bulk soil (circles) and 850C step of dehydration process (squares). (E) $\delta^{13}\text{C}$ of plateau values from dehydration process, (F) $\delta^{18}\text{O}$ of plateau values from dehydration.

Table 4.1 % Organic Carbon and $\delta^{13}\text{C}$ of Soil Organic Carbon

| Sample Depth (cm) | % Carbon | $\delta^{13}\text{C}$ ‰ (PDB) |
|-------------------|----------|-------------------------------|
| 0-5 | 3.62 | -27.05 |
| 5-15 | 1.53 | -26.10 |
| 15-24 | 0.71 | -25.43 |
| 24-30 | 0.17 | -23.70 |
| 30-40 | 0.43 | -22.87 |
| 40-47 | 0.32 | -21.61 |
| 47-55 | | |
| 55-63 | 0.12 | -22.05 |
| 63-70 | 0.31 | -24.02 |
| 70-78 | 0.09 | -21.74 |
| 78-88 | 0.13 | -21.51 |
| 88-95 | 0.07 | -21.55 |
| 95-105 | 0.15 | -22.28 |
| 105-115 | 0.10 | -22.28 |
| 115-125 | 0.09 | -21.12 |
| 125-135 | 0.09 | -22.10 |
| 135-150 | 0.10 | -22.44 |

Table 4.2 Model Assumptions and Coefficients

| Run Number | Soil Respiration Rate (gC m ⁻³ y ⁻¹) | ε | | τ ⁻¹ | | δ ¹³ C C ₃ (‰) | | | δ ¹³ C C ₄ (‰) | | |
|------------|--|-----------------|-----------------|-----------------|-----------------|--------------------------------------|-----------------|-----|--------------------------------------|-----------------|---|
| | | μ ^{**} | σ ^{**} | μ ^{**} | σ ^{**} | μ ^{**} | σ ^{**} | % | μ ^{**} | σ ^{**} | % |
| M0069 | 647 | 0.38 | | 0.13 | | -28.05 | 2.5 | 100 | | | 0 |

** Where these fields are blank, the parameter was held constant during the Monte Carlo Simulation.

Where there is an explicit value they define the mean (μ) and standard deviation (σ) of the Normal Probability Distribution used.

CHAPTER 5

ASSESSING THE VIABILITY OF PEDOGENIC GIBBSITE AS A PROXY FOR PALEO- PCO₂

5.1 MODEL CONSIDERATIONS

This project was inspired by the need to better understand two important points. First, is the pattern shown in the $\delta^{13}\text{C}$ values of carbon trapped in pedogenic gibbsite when plotted with depth indicative of the trapped carbon being in equilibrium with soil CO₂; and thus, a reliable proxy of PCO₂ in the same way pedogenic carbonates are? And second, why does the model require an assumed value for soil respiration rate that is at least eight to ten times less than the measured soil respiration rate? In order to address these questions, this project undertook a detailed analysis of the modeling method, including the sensitivity of the model to variations in the values of the various factors used and the mathematical construction of the model used for various processes and an independent field test to attempt to reproduce the results of an earlier study. The results of this field study did not agree with the previous study and indicate that the process may be more complicated than originally suspected rendering a simple diffusion model inadequate for the task. Nevertheless, there are some conclusions about the model that can be applied to this method when the inconsistencies are resolved and the model is modified to accommodate the complications revealed in the field data.

The first conclusion is that the results do not change significantly regardless of the function used to describe bulk density in the soil. The three methods tested were constant bulk density with depth, an exponential function and field data. In each case, the modeled soil respiration rate was not changed enough to account for the large difference between the analytical solution and the measured soil

respiration rate (Section 2.4 and 4.4). Second, if the CO₂ production in the soil is modeled as a decreasing function with depth, the characteristic depth of production had a large effect on the final solution. In unmanaged soils, most of the CO₂ is produced in the top 20cm of the soil. Assuming a production depth of 20cm resulted in modeled soil respiration rate that was higher than is reasonably expected in nature. A deeper characteristic depth resulted in reasonable modeled soil respiration rates. This condition is more reasonable to expect in natural soils, especially deeper soils. This condition may also be useful as a way to simulate the slower respiration rate of CO₂ deep in the soil that is more restricted due to smaller, less-connected pores deeper in the soil.

Ultimately, the concentration of CO₂ in the soil at depth will determine the soil respiration rate and the amount of mixing with the atmosphere; therefore, any of the methods that limit the amount of CO₂ at depth in the soil, for example assuming a shallow (20cm) soil production depth, requires a high assumed soil respiration rate in order for soil CO₂ concentration to increase. One implication of the large effect that changing the characteristic depth of production has on the modeled soil respiration rate is that understanding of the process by which CO₂ is trapped on gibbsite, i.e. what conditions are being recorded, is vitally important for the correct application of this proxy.

Monte Carlo simulations of the model, used to assess the effect of the natural variability of soil properties and the isotope composition of sources of CO₂ in the soil confirm that the natural variability of soil bulk density, as it is expressed in porosity and tortuosity do not affect the range of modeled soil respiration rates significantly. This method allows for a simple method of accounting for variations in $\delta^{13}\text{C}$ values of organic CO₂ in soil that result from the processing of organic carbon by various microbes and the fractionation of carbon isotopes associated with each step. The Monte Carlo method works well if the data have some variability, but it is not sufficient to account for large differences in the measured and modeled respiration rates. This fact seems to indicate that there is disconnect between the model assumptions and the natural process that preserves the CO₂ in the gibbsite structure.

5.2 APPLICATION TO PALEOSOLS

The inconsistent results between this and the previous (Panola Mountain) field test indicate that more information is needed before this proxy will be useful as a proxy for paleo-PCO₂. The discrepancy can indicate two possible issues with the proxy. First, the process by which carbon is associated with gibbsite and incorporated into the structure is not universal, and is dependent on local conditions to a degree that is not discernible in paleosols. If this is the case, the proxy will not likely be useful at any time because the number of variables required to accurately model PCO₂ will not be available in paleosols. There is reason to believe that this is not the case however, especially in the linear relationship between the carbon and oxygen isotopes in this field study. This indicates that there is some specific set of processes that is controlling the preservation of carbon isotopes in the gibbsite structure that is not likely to be dependent on the local environment. Also, the majority of the disagreement between the measured $\delta^{13}\text{C}$ values of the CO₂ recovered from the gibbsite and the modeled values occurs in the upper portion of the soil. There are many processes that serve to mix the soil that can add to the complexity of the real system that is not currently accounted for in the model. The second issue may be with the method by which CO₂ is collected during the dehydration of the gibbsite. It appears that slower, lower temperature dehydration results in a more consistent $\delta^{13}\text{C}$ plateau value. This can easily be tested, and if this is the case, there is a good chance that this will be a viable proxy for paleo-PCO₂.

Because the upper sections of paleosols are often either compacted or missing, the shallow samples that were used in the model testing will not be available. Therefore, only the deep samples that have the most depleted carbon isotope compositions will be preserved. The variability of the data from the samples above the Bt horizon seem to indicate that including them in the model will require adding complications to the model that are not able to be overcome when applied to paleosols for which limited information is available. Therefore, the decapitation of the upper portion of the soil may be fortuitous for the model, but it appears to conceal the true complexity of the soil formation process and the way the CO₂

is preserved in pedogenic minerals. Because the upper portion of the profile is useful to constrain the model results, PCO_2 calculated without this data will result in larger uncertainty in the result.

Therefore, it is imperative that researchers that attempt to utilize this proxy, or any proxy that assumes that the stable isotope composition of the soil CO_2 is controlled by diffusion and that is the signal that is recorded in the minerals, take into account the possibility that there are processes in the soil that move these minerals through the soil. Closer examination of Figure 4.13 shows that the samples deeper in the soil (below 55 cm), where mineral transport processes, such as water movement through the soil and bioturbation by earthworms and other burrowing animals, begin to show a trend of more depleted oxygen and carbon isotopes with depth; this trend is not present in the upper portion of the soil. In fact, for purposes of using gibbsite as a proxy for paleo- PCO_2 , the upper portion of the soil, where evidence of dense root growth and burrowing is present, should be avoided when sampling and only the lower portion of the soil profile should be considered. Figure 4.15 also seems to indicate that the deeper portion of the soil shows more consistent results with a smaller variation in the F ratio. While the F ratio variation does not decrease consistently with depth, the smallest amount of variation is in the deepest part of the soil where data is available and this is also below 55 cm (figure 5.1).

Quantifying all of the processes that can change the recorded $\delta^{13}\text{C}$ values of soil CO_2 with depth in the shallow soil will require more research and the processes that are mentioned above are at this time mostly speculative. The fact remains though that this portion of the soil does not produce consistent results in the current field study and therefore our ability to account for the various processes should be considered dubious. The conditions of this field site that differ from the Panola Mountain field site, independent of parent material, are the topography and the possibility of recent agriculture. In both cases, the Watkinsville site which is not on a ridge that is more rapidly weathered and does not show evidence of agriculture, is most likely represents an older environment where mixing is likely to be more complete. This may explain why the data from Panola Mountain is more like what is expected if the proxy data is controlled simply by diffusion.

5.3 FINAL ASSESSMENT

Once the reasons for the inconsistent results are determined, this proxy will likely be useful over the same age range as pedogenic carbonates, with a similar amount of uncertainty. Therefore, it will serve as a good method of verifying those proxy results are reasonable, and will be a valuable check for mass balance modeling. The model is simple enough when using the Monte Carlo method to apply to a paleosol where limited information is available. Testing the hypothesis that the dehydration method is the reason for the inconsistency will not require the collection and treatment of new samples, a process that takes a long time and is labor intensive, but can be completed relatively quickly using the samples that were collected during this field study. If that hypothesis is falsified, more work will be required to determine what differences in the soil formation setting, or mineralogy of the soil or parent material caused the differences in the $\delta^{13}\text{C}$ of the trapped CO_2 .

The largest barrier to the success of this proxy will be the quantification and modeling of the various processes that appear to mix the signal in the upper portion of the soil. This may be avoided by avoiding this portion of the soil and focusing on the deeper portion where many of these processes do not occur.

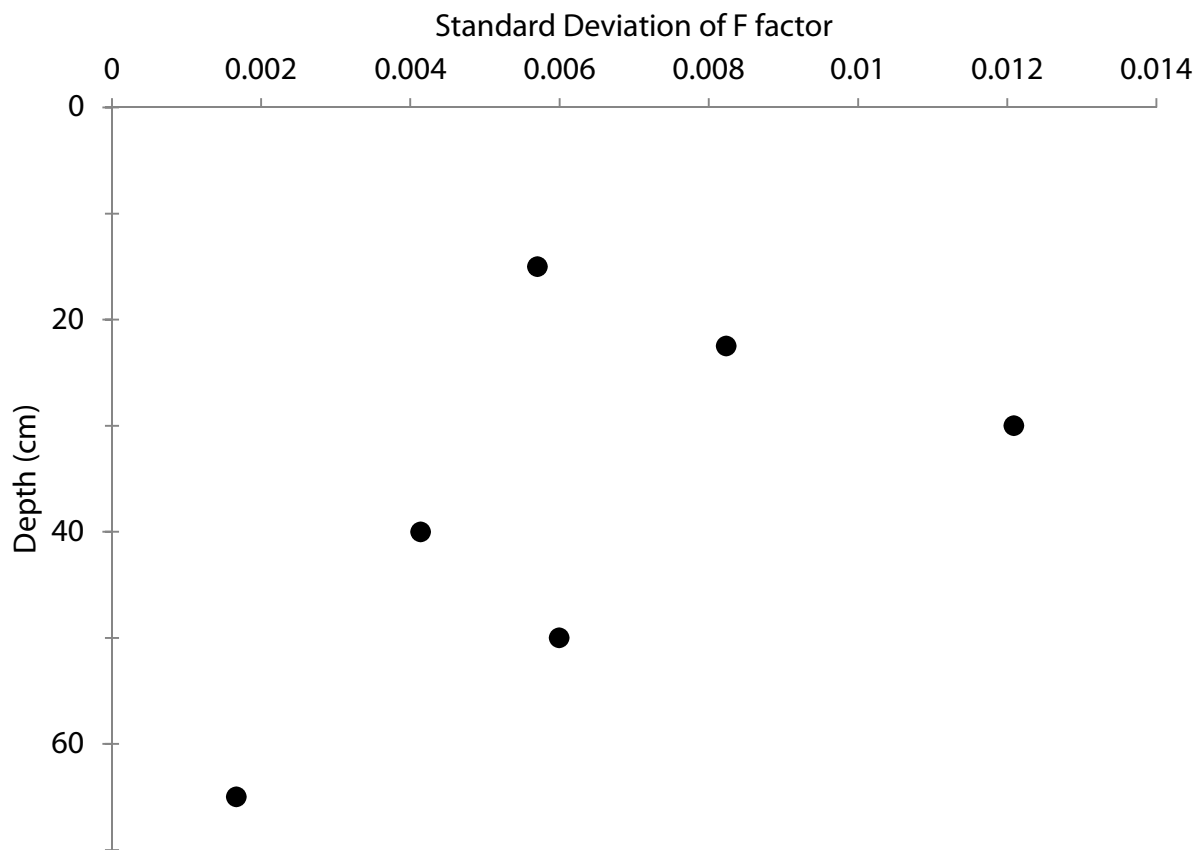


Figure 5.1 Standard deviation of F factor at each depth (see Figure 4.15 for data at each depth).

REFERENCES

- Albanito, F., Saunders, M. and Jones, M.B., 2009. Automated diffusion chambers to monitor diurnal and seasonal dynamics of the soil CO₂ concentration profile. *European Journal of Soil Science*, 60(4), 507-514.
- Amundson, R., Stern, L., Baisden, T. and Wang, Y., 1998. The isotopic composition of soil and soil-respired CO₂. *Geoderma*, 82, 83-114.
- Arthur, E., Moldrup, P., Schjonning, P. and de Jonge, L.W., 2012. Linking Particle and Pore Size Distribution Parameters to Soil Gas Transport Properties. *Soil Science Society of America Journal*, 76(1), 18-27.
- Augustin, L. et al., 2004. Eight glacial cycles from an Antarctic ice core. *Nature*, 429(6992), 623-628.
- Barnett, T.P., Pierce, D.W. and Schunur, R., 2001. Detection of anthropogenic climate change in the world's oceans. *Science*, 292, 270-274.
- Bazzaz, F.A. and Williams, W.E., 1991. Atmospheric CO₂ concentrations within a mixed forest: implications for seedling growth. *Ecology*, 72, 12-16.
- Berling, D.J., 1999. Stomatal density and index: theory and application. In: T.P. Jones and N.P. Rowe (Editors), *Fossil Plants and Spores: Modern Techniques*. Geological Society, London, pp. 251-256.
- Berling, D.J. and Chaloner, W.G., 1992. Stomatal density as an indicator of atmospheric CO₂ concentration. *Holocene*, 2, 71-78.
- Berling, D.J. and Royer, D.L., 2002. Fossil plants as indicators of the Phanerozoic Carbon Cycle. *Annual Review of Earth and Planetary Sciences*, 30, 527-556.
- Bender, M.M., 1968. Mass spectrometric studies of carbon 13 variations in corn and other grasses. *Radiocarbon*, 10(2), 468-472.
- Bender, M.M., 1971. Variations in C-13/C-12 ratios of plants in relation to pathway of photosynthetic carbon dioxide fixation. *Phytochemistry*, 10(6), 1239-&.
- Berner, R.A., 2004. *The Phanerozoic Carbon Cycle: CO₂ and O₂*. Oxford University Press, New York, New York, 150 pp.
- Berner, R.A. and Ji-Long, R., 1997. Alkialinity buildup during silicate weathering under a snow cover. *Aquatic Geochemistry*, 2, 301-312.
- Bidigare, R.R. et al., 1999. Consistent fractionation of C-13 in nature and in the laboratory: Growth-rate effects in some haptophyte algae (vol 11, pg 279, 1997). *Global Biogeochemical Cycles*, 13(1), 251-252.

- Bowen, G.J. and Beerling, D.J., 2004. An integrated model for soil organic carbon and CO₂: Implications for paleosol carbonate pCO₂ paleobarometry. *Global Biogeochemical Cycles*, 18, GB1026 1-12.
- Breecker, D.O., Sharp, Z.D. and McFadden, L.D., 2009. Seasonal bias in the formation and stable isotopic composition of pedogenic carbonate in modern soils from central New Mexico, USA. *GSA Bulletin*, 121(3/4), 630-640.
- Brooks, A. and Farquhar, G.D., 1985. Effect of temperature on the CO₂/O₂ specificity of ribulose-1,5-biphosphate carboxylase oxygenase and the rate of respiration in the light - estimates from gas-exchange measurements on spinach. *Planta*, 165(3), 397-406.
- Bruce, R.R., CDane, J.H., Quisenberry, V.L., Powell, N.L. and Thomas, A.W., 1983. Physical Characteristics of soil in the southern region: Cecil. *Southern Cooperative Series Bulletin*, 267, 185.
- Buchmann, N., Kao, W.-Y. and Ehleringer, J., 1997. Influence of stand structure on carbon-13 of vegetation, soils, and canopy air within deciduous and evergreen forests in Utah, United States. *Oecologia*, 110, 109-119.
- Buyanovsky, G.A. and Wagner, G.H., 1983. Annual cycles of carbon-dioxide level in soil air. *Soil Science Society of America Journal*, 47(6), 1139-1145.
- Came, R.E. et al., 2007. Coupling of surface temperature and CO₂ concentrations during the Paleozoic era. *Nature*, 449(7159), 198-203.
- Camporese, M., Putti, M., Salandin, P. and Teatini, P., 2008. Spatial variability of CO₂ efflux in a drained cropped peatland south of Venice, Italy. *Journal of Geophysical Research-Biogeosciences*, 113(G4), 12.
- Cerling, T.E., 1984. The stable isotopic composition of modern soil carbonate and its relationship to climate. *Earth and Planetary Science Letters*, 71, 229-240.
- Cerling, T.E., 1991. Carbon dioxide in the atmosphere: evidence from Cenozoic and Mesozoic Paleosols. *American Journal of Science*, 291, 377-400.
- Cerling, T.E., 1999. Stable carbon isotopes in paleosol carbonates. In: M. Thiry and Simon-Coinçon (Editors), *Palaeoweathering, Palaeosurfaces and Related Continental Deposits*. Special Publications of the International Association of Sedimentologists. Blackwell Science Ltd, Oxford, pp. 406.
- Cerling, T.E., Quade, J. and Bowman, J.R., 1989. Carbon isotopes in soils and palaeosols as ecology and palaeoecology indicators *Nature*, 341(14), 138-139.
- Crowley, T.J., 2000. Causes of climate change over the past 1000 years. *Science*, 289, 270-274.
- Davidson, E., A., Verchot, L.V., Henrique, C.J., Ackerman, I.L. and Carvalho, J.E.M., 2000. Effects of soil water content on soil respiration in forests and cattle pastures of eastern Amazonia. *Biogeochemistry*, 48, 53-69.
- Dorner, J., Sandoval, P. and Dec, D., 2010. The role of soil structure on the pore functionality of an ultisol. *Journal of Soil Science and Plant Nutrition*, 10(4), 495-508.

- Dorr, H. and Munnich, O., 1980. Carbon-14 and Carbon -13 in soil CO₂. *Radiocarbon*, 22(3), 909-918.
- Dvorak, V., Feitknecht, W. and Georges, P., 1969. Basic iron(III) carbonates 1. Basic amorphous iron(III) carbonate. *Helvetica Chimica Acta*, 52(2), 501-515.
- Ehleringer, J.R., Buchmann, N. and Flanagan, L.B., 2000. Carbon isotope ratios in belowground carbon cycle processes. *Ecological Applications*, 10(2), 412-422.
- Ekart, D.D., Cerling, T., Montanez, I. and Tabor, N.J., 1999. A 400 Million year carbon isotope record of pedogenic carbonate: Implications for paleoatmospheric carbon dioxide. *American Journal of Science*, 299, 805-827.
- Epstein, S., Buchsbaum, R., Lowenstam, H.A. and Urey, H.C., 1951. Carbonate-water isotopic temperature scale. *Geological Society of America Bulletin*, 62, 417-426.
- Farquhar, G.D., Ehleringer, J.R. and Hubick, K.T., 1989. Carbon isotope discrimination and photosynthesis. *Annual Review of Plant Physiology and Plant Molecular Biology*, 40, 503-537.
- Farquhar, G.D. and Richards, P.A., 1984. Isotopic composition of plant carbon correlates with water use efficiency of wheat genotypes. *Australian Journal of Earth Sciences*, 11, 539-552.
- Fletcher, B.J., Beerling, D.J., Brentnall, S.J. and Royer, D.L., 2005. Fossil bryophytes as recorders of ancient CO₂ levels: Experimental evidence and a Cretaceous case study. *Global Biogeochemical Cycles*, 19(3).
- Fletcher, B.J., Brentnall, S.J., Anderson, C.W., Berner, R.A. and Beerling, D.J., 2008. Atmospheric carbon dioxide linked with Mesozoic and early Cretaceous climate changes. *Nature Geoscience*, 1(1), 43-48.
- Fletcher, B.J., Brentnall, S.J., Quick, W.P. and Beerling, D.J., 2006. BRYOCARB: A process-based model of thallose liverwort carbon isotope fractionation in response to CO₂, O₂, light and temperature. *Geochimica Et Cosmochimica Acta*, 70(23), 5676-5691.
- Fox, D., L. and Koch, P., L., 2004. Carbon and oxygen isotopic variability in Neogene palaeosol carbonates: constraints on the evolution of the Great Plains, USA. *Palaeogeography, Palaeoclimatology, Palaeoecology*, 207, 305-329.
- Frakes, L.A., Francis, J.E. and Syktus, J.I., 1992. *Climate Modes of the Phanerozoic*. Cambridge University Press, Cambridge, 274 pp.
- Gillon, J. and Yakir, D., 2012. Influence of carbonic anhydrase activity in terrestrial vegetation on the ¹⁸O content of atmospheric CO₂. *Science*, 291, 2584-2587.
- Guyodo, Y., Mostrom, A., Penn, R.L. and Banerjee, S.K., 2003. From nanodots to nanorods: Oriented aggregation and magnetic evolution of nanocrystalline goethite. *Geophysical Research Letters*, 30(10), 19-1 - 19-4.
- Hattersley, P.W., 1982. Delta-13-C values of C-4 types in grasses. *Australian Journal of Plant Physiology*, 9(2), 139-154.

- Hinga, K.R., Arthur, M.A., Pilson, M.E.Q. and Whitaker, D., 1994. Carbon Isotope fractionation by marine phytoplankton in culture: The effects of CO₂ concentration, pH, temperature and species. *Global Biogeochemical Cycles*, 8, 91-102.
- Huntington, T.G., 1995. Carbon sequestration in an aggrading forest ecosystem in the southeastern USA. *Soil Science Society of America Journal*, 59(5), 1459-1467.
- Irvine, J., Law, B.E., Martin, J.G. and Vickers, D., 2008. Interannual variation in soil CO₂ efflux and the response of root respiration to climate and canopy gas exchange in mature ponderosa pine. *Global Change Biology*, 14(12), 2848-2859.
- Jassal, R. et al., 2005. Relationship between soil CO₂ concentrations and forest-floor CO₂ effluxes. *Agricultural and Forest Meteorology*, 130(3-4), 176-192.
- Jia, B. and Zhou, G., 2009. Integrated diurnal soil respiration model during growing season of a typical temperate steppe: Effects of temperature, soil water content and biomass production. *Soil Biology and Biochemistry*, 41, 681-686.
- Karhu, J. and Epstein, S., 1986. The implication of the oxygen isotope records in coexisting cherts and phosphates. *Geochimica Et Cosmochimica Acta*, 50(8), 1745-1756.
- Karoly, D.J. et al., 2003. Detection of a Human Influence on North America. *Science*, 302, 1200-1203.
- Krull, E.S. and Skjemstad, J.O., 2003. delta C-13 and delta N-15 profiles in C-14-dated Oxisol and Vertisols as a function of soil chemistry and mineralogy. *Geoderma*, 112(1-2), 1-29.
- Kump, L.R. and Arthur, M.A., 1999. Interpreting carbon-isotope excursions: carbonates and organic matter. *Chemical Geology*, 161(1-3), 181-198.
- Lemarchand, D., Gaillardet, J., Lewin, E. and Allegre, C.J., 2000. The influence of rivers on marine boron isotopes and implications for reconstructing past ocean pH. *Nature*, 408(6815), 951-954.
- McElwain, J.C. and Chaloner, W., G., 1995. Stomatal density and index fossil plants track atmospheric carbon dioxide in the Palaeozoic. *Annals of Botany*, 76, 389-395.
- Miller, J., B., Yakir, D., White, J.W.C. and Tans, P.P., 1999. Measurement of ¹⁸O/¹⁶O in the soil-atmosphere CO₂ flux. *Global Biogeochemical Cycles*, 13(3), 761-774.
- Millington, R.J. and Quirk, J.M., 1961. Permeability of porous solids. *Transactions of the Faraday Society*, 57, 1200-1207.
- Nadelhoffer, K.J. and Fry, B., 1988. Controls on natural Nitrogen-15 and Carbon-13 abundances in forest soil organic matter. *Soil Science Society of America Journal*, 52, 1633-1640.
- Norton, S.A., Cosby, B.J., Fernandez, I.J., Kahl, J.S. and Church, M.R., 2001. Long-term and seasonal variations in CO₂: linkages to catchment alkalinity generation. *Hydrology and Earth System Sciences*, 5(1), 83-91.
- O'Leary, M.H., 1988. Carbon Isotopes in photosynthesis. *BioScience*, 38(5), 328-336.
- Ota, M. and Yamazawa, H., 2010. Forest floor CO₂ flux estimated from soil CO₂ and radon concentrations. *Atmospheric Environment*, 44(36), 4529-4535.

- Pagani, M., Arthur, M.A. and Freeman, K.H., 1999. Miocene evolution of atmospheric carbon dioxide. *Paleoceanography*, 14(3), 273-292.
- Pagani, M., Freeman, K.H., Ohkouchi, N. and Caldeira, K., 2002. Comparison of water column [CO₂] with sedimentary alkenone-based estimates: a test of the alkenone-CO₂ proxy. *Paleoceanography*, 17(4), 21-1, 21-12.
- Parker, D.E., Jones, P.D., Folland, C.K. and Bevan, A., 1994. Interdecadal changes of surface-temperature since the late-19th-century. *Journal of Geophysical Research-Atmospheres*, 99(D7), 14373-14399.
- Pearson, P.N. and Palmer, M.R., 1999. Middle Eocene seawater pH and atmospheric carbon dioxide concentrations. *Science*, 284, 1824-1826.
- Pearson, P.N. and Palmer, M.R., 2000. Atmospheric carbon dioxide concentrations over the past 60 million years. *Nature*, 406, 695-699.
- Perkins, H.F., 1987. Characterization Data for Selected Georgia Soils. Special Publications 43. The Georgia Agricultural Experiment Station, College of Agriculture, The University of Georgia, Athens, 545 pp.
- Perry, E.C. and Tan, F.C., 1972. Significance of oxygen and carbon isotope variations in Early Precambrian cherts and carbonate rocks of Southern Africa. *Geological Society of America Bulletin*, 83(3), 647-664.
- Raich, J.W. and Schlesinger, W.H., 1992. The global carbon-dioxide flux in soil respiration and its relationship to the vegetation and climate. *Tellus Series B-Chemical and Physical Meteorology*, 44(2), 81-99.
- Railsback, L.B., 1990. Influence of changing deep ocean circulation on the Phanerozoic oxygen isotopic record. *Geochimica Et Cosmochimica Acta*, 54(5), 1501-1509.
- Reardon, E.J., Allison, G.B. and Fritz, P., 1979. Seasonal chemical and isotopic variations of soil CO₂ at Trout Creek, Ontario. *Journal of Hydrology*, 43(1-4), 355-371.
- Retallack, G.J., 2002. Carbon dioxide and climate over the past 300 Myr. *Philosophical Transactions: Mathematical, Physical and Engineering Sciences*, 360(1793), 659-673.
- Richter, D.D. and Markewitz, D., 1995. How deep is soil? . *Bioscience*, 45(9), 600-609.
- Rosso, K.M. and Rustad, J.R., 2001. Structures and energies of AlOOH and FeOOH polymorphs from plane wave pseudopotential calculations. *American Mineralogist*, 86(3), 312-317.
- Royer, D.L., 2006. CO₂-forced climate thresholds during the Phanerozoic. *Geochimica et Cosmochimica Acta*, 70(2006), 5665-5675.
- Royer, D.L., Berner, R.A. and Beerling, D.J., 2001. Phanerozoic atmospheric CO₂ change: evaluating geochemical and paleobiological approaches. *Earth Science Reviews*, 54(2001), 349-392.
- Royer, D.L., Berner, R.A. and Park, J., 2007. Climate sensitivity constrained by CO₂ concentrations over the past 420 million years. *Nature*, 446(7135), 530-532.

- Russell, J.D., Paterson, E., Fraser, A.R. and Farmer, V.C., 1975. Adsorption of carbon dioxide on goethite (α -FeOOH) surfaces, and its implications for anion adsorption. *J. Chem. Soc. Faraday Trans.*, 71, 1623-1630.
- Sanyal, A. et al., 1996. Oceanic pH control on the boron isotopic composition of foraminifera: Evidence from culture experiments. *Paleoceanography*, 11(5), 513-517.
- Savin, S.M., 1977. The history of the earth's surface temperature during the past 100 million years. *Annual Review of Earth and Planetary Sciences*, 1977(5), 319-355.
- Schipper, D.J., Lathouwe, Tw and Vandoorn, C.Z., 1973. Thermal-decomposition of sodalites. *Journal of the American Ceramic Society*, 56(10), 523-525.
- Schlesinger, W.H., 1977. Carbon balance in terrestrial detritus. *Annual Review of Ecology and Systematics*, 8, 51-81.
- Schroeder, P.A., Austin, J.C. and Dowd, J.F., 2006. Estimating long-term soil respiration rates from carbon isotopes occluded in gibbsite. *Geochimica et Cosmochimica Acta*, 70, 5692-5697.
- Schroeder, P.A. and Melear, N.D., 1999. Stable carbon isotope signatures preserved in authigenic gibbsite from a forested granitic-regolith: Panola Mountain, Georgia, USA. *Geoderma*, 91, 261-279.
- Schroeder, P.A., Melear, N.D., Bierman, P., Kashgarian, M. and Caffee, M.W., 2001. Apparent gibbsite growth ages for regolith in the Georgia Piedmont. *Geochimica et Cosmochimica Acta*, 65(3), 381-386.
- Schroeder, P.A. and Pruett, R.J., 1996. Fe ordering in kaolinite: Insights from Si-29 and Al-27 MAS NMR spectroscopy. *American Mineralogist*, 81(1-2), 26-38.
- Schweizer, M., Fear, J. and Cadisch, G., 1999. Isotopic (^{13}C) fractionation during plant residue decomposition and its implications for soil organic matter studies. *Rapid Communications in Mass Spectrometry*, 13, 1284-1290.
- Service, U.S.C., 1968. Soil Survey Clarke and Oconee Counties, Georgia. In: D.o. Agriculture (Editor). United States Department of Agriculture.
- Singh, B. and Gilkes, R.J., 1991. Concentration of iron oxides from soil clays by 5M NaOH treatment: the complete removal of sodalite and kaolin. *Clay Minerals*, 26, 463-472.
- Singh, J.S. and Gupta, S.R., 1977. Plant decomposition and soil respiration in terrestrial ecosystems. *The Botanical Review*, 43(4), 449-528.
- Smith, B.N. and Epstein, S., 1971. 2 categories of C-13/C-12 ratios for higher plants. *Plant Physiology*, 47(3), 380-384.
- Spivack, A.J., You, C.F. and Smith, H.J., 1993. Foraminiferal boron isotope ratios as a proxy for surface ocean pH over the past 21 Myr. *Nature*, 363, 149-151.
- Stanhill, G., 1986. Water-use efficiency. *Advances in Agronomy*, 39, 53-85.
- Stern, L., Baisden, W.T. and Amundson, R., 1999. Processes controlling the oxygen isotope ratio of soil CO₂: Analytic and numerical modeling. *Geochimica Et Cosmochimica Acta*, 63(6), 799-814.

- Tabor, N.J., Montanez, I.P., Zierenberg, R.P. and Currie, B.S., 2004. Mineralogical and geochemical evolution of a basaltic-hosted fossil soil (Late Triassic, Ischigualasto Formation, northwest Argentina): Potential for paleoenvironmental reconstruction. *GSA Bulletin*, 116(9/10), 1280-1293.
- Tabor, N.J. and Yapp, C.J., 2005a. Coexisting goethite and gibbsite from a high-paleolatitude (55°N) Late paleocene laterite: Concentration and $^{13}\text{C}/^{12}\text{C}$ ratios of occluded CO_2 and associated organic matter. *Geochimica et Cosmochimica Acta*, 69(23), 5495-5510.
- Tabor, N.J. and Yapp, C.J., 2005b. Incremental vacuum dehydration-decarbonation experiments on a natural gibbsite ($\alpha\text{-Al}(\text{OH})_3$): CO_2 abundance and $\delta^{13}\text{C}$ values. *Geochimica et Cosmochimica Acta*, 69(3), 519-527.
- Tajika, E., 1998. Climate change during the last 150 million years: reconstruction from carbon cycle model. *Earth and Planetary Science Letters*, 160, 695-77.
- Tett, S.F.B., Stott, P.A., Allen, M.R., Ingram, W.J. and Mitchell, J.F.B., 2001. Causes of twentieth-century temperature change near the Earth's surface. *Nature*, 399, 569-571.
- Urey, H.C., 1952. *The planets: their origin and development*. Yale University Press, New Haven, Connecticut.
- Urey, H.C., Lowenstam, H.A. and Epstein, S., 1951. Measurement of paleotemperatures and temperatures of the upper Cretaceous of England, Denmark, and the southeastern United States. *Geological Society of America Bulletin*, 62, 399-416.
- van der Veer, G., Voerkelius, S., Lorentz, G., Heiss, G. and Hoogewerff, J.A., 2009. Spatial interpolation of the deuterium and oxygen-18 composition of global precipitation using temperature as ancillary variable. *Journal of Geochemical Exploration*, 101(2), 175-184.
- Veizer, J., 1999. $^{87}\text{Sr}/^{86}\text{Sr}$, $\delta^{13}\text{C}$ and $\delta^{18}\text{O}$ evolution of Phanerozoic seawater. *Chemical Geology*, 161(1999), 59-88.
- Veizer, J., Godderis, Y. and Francois, L.M., 2000. Evidence for decoupling of atmospheric CO_2 and global climate change during the Phanerozoic eon. *Nature*, 408, 698-701.
- Vitali, F., Longstaffe, F.J., Bird, M.I. and Caldwell, W.G.E., 2000. Oxygen-isotope fractionation between aluminum-hydroxide phases and water at $<60\text{C}$: Results of decade-long synthesis experiments. *Clays and Clay Minerals*, 48, 230-237.
- Wallmann, K., 2001. Controls on the Cretaceous and Cenozoic evolution of seawater composition, atmospheric CO_2 and climate. *Geochimica et Cosmochimica Acta*, 65(18), 3005-3025.
- Wilkinson, M.T., Richards, P.J. and Humphreys, G.S., 2009. Breaking ground: Pedological, geological, and economical implications of soil bioturbation. *Earth-Science Reviews*, 97(2009), 254-269.
- Wilson, B.R., Koen, T.B., Barnes, P., Ghosh, S. and King, D., 2011. Soil carbon and related soil properties along a soil type and land-use intensity gradient, New South Wales, Australia. *Soil Use and Management*, 27(4), 437-447.

- Woodward, F.I., 1987. Stomatal numbers are sensitive to increases in CO₂ from pre-industrial levels. *Nature*, 327, 617-618.
- Woodward, F.I. and Bazzaz, F.A., 1988. The responses of stomatal density to CO₂ partial pressure. *Journal of Experimental Botany*, 39, 1771-1781.
- Yapp, C.J., 1983. Stable hydrogen isotopes in iron-oxides: Isotope effects associated with dehydration of a natural goethite. *Geochimica Et Cosmochimica Acta*, 47(7), 1277-1287.
- Yapp, C.J., 1987. A possible goethite-iron(III) carbonate solid solution and the determination of CO₂ partial pressures in low-temperature geologic systems. *Chemical Geology*, 64, 259-268.
- Yapp, C.J., 1990. Oxygen isotopes in iron (III) oxides. 1. Mineral -water fractionation factors. *Chemical Geology*, 85, 329-335.
- Yapp, C.J., 1993. Paleoenvironment and the oxygen isotope geochemistry of ironstone of the Upper Ordovician Neda Formation, Wisconsin, USA. *Geochimica et Cosmochimica Acta*, 57, 2319-2327.
- Yapp, C.J., 2001. Rusty Relics of Earth History: Iron(III) Oxides, Isotopes, and Surficial Environments. *Annual Review of Earth and Planetary Sciences*, 29, 165-199.
- Yapp, C.J. and Poths, H., 1986. Carbon in natural goethites. *Geochimica et Cosmochimica Acta*, 50, 1213-1220.
- Yapp, C.J. and Poths, H., 1990. Infrared spectral evidence for a minor Fe(III) carbonate bearing component in natural goethite. *Clays and Clay Minerals*, 38(4), 442-444.
- Yapp, C.J. and Poths, H., 1991. ¹³C/¹²C ratios of the Fe(III) carbonate component in natural goethites. In: H.P. Taylor, J.R. O'Neil and I.R. Kaplan (Editors), *Stable Isotope Geochemistry: A Tribute to Samuel Epstein*. The Geochemical Society pp. 257-270.
- Yapp, C.J. and Poths, H., 1992. Ancient atmospheric CO₂ pressures inferred from natural goethites. *Nature*, 355, 342-344.
- Yapp, C.J. and Poths, H., 1993. The carbon isotope geochemistry of goethite (α-FeOOH) in ironstone of the Upper Ordovician Neda Formation, Wisconsin, USA: Implications for early Paleozoic continental environments. *Geochimica et Cosmochimica Acta*, 57, 2599-2611.
- Yapp, C.J. and Poths, H., 1996. Carbon isotopes in continental weathering environments and variations in ancient atmospheric CO₂ pressure. *Earth and Planetary Science Letters*, 137, 71-82.
- Zhang, J.Y., Lin, Z.B., Zhang, R.D. and Shen, J., 2010. Effects of simulated rainfall events on soil carbon transformation. *Australian Journal of Soil Research*, 48(5), 404-412.

APPENDIX A

C++ CODE FOR SOLVING MODEL

A1 RUNNING MODEL

The code for all functions called in this function is also listed. Functions that are called multiple times will be listed the first time and referred to each subsequent time. This section will list the code that is called when the model is run, it makes decisions about what parts to run based on the settings input by the user. Each section of code will have two subsections; section 1 will be the relevant information from the header file for the class the function is in and the second section will be the code that the function uses. Comments will be preceded by *//* and will be in italics.

A1.1 MAIN HEADER FILE (RELEVANT TO THE FUNCTION `BTNRUNCLICK`)

```
#include <MtxVecCpp.h>
#include "MtxBaseComp.hpp"
#include "MtxVecEdit.hpp"
#include <MtxVec.hpp>
#include "LMDBaseControl.hpp"
#include "LMDBaseGraphicControl.hpp"
#include "LMDBaseImage.hpp"
#include "LMDCustomImageList.hpp"
#include "LMDCustomLImage.hpp"
#include "LMDGraphicControl.hpp"
#include "LMDImageList.hpp"
#include "LMDLImage.hpp"
#include "Cipher.h"
#include "Units.h"
#include <Chart.hpp>
#include <TeEngine.hpp>
#include <TeeProcs.hpp>
#include "MtxGrid.hpp"
#include <Grids.hpp>
#include <Series.hpp>
#include <XLSReadWriteII2.hpp>
#include <Dialogs.hpp>
#include "Bowen.h"
```

```

#include "LMDCustomComponent.hpp"
#include "LMDStopWatch.hpp"
#include <StatTimeSerAnalysis.hpp>
#include <Regress.hpp>
#include "StatRandom.hpp"
#include "Math387.hpp"
#include "StatProbPlots.hpp"
#include "StatSeries.hpp"
#include "TeeSurfa.hpp"
#include "LMDButton.hpp"
#include "LMDCustomButton.hpp"
#include "LMDBaseMeter.hpp"
#include "LMDCustomProgress.hpp"
#include "LMDProgress.hpp"

using namespace std;

class TfrmMain : public TForm
{
    __published: // IDE-managed Components, not listed
private: // User declarations
    Vector v_Parameters, v_depthProfile; //Vectors are created and used by the MtxVec library
    included in lines 1-4.
    Vector v_BDProfile, v_DCProfile;
    Vector v_DataDepths, v_DataBulkDensities;
    Vector v_PhiProfile, v_d13CPhiProfile;
    Vector v_C12, v_C13, v_Solution;
    Vector v_Prev12, v_Prev13, v_difference;
    Vector v_MCPorosity, v_MCTortuosity, v_MCC3, v_MCC4, v_MCWater;
    Matrix m_Parameters, m_Solutions, m_Histogram;
    Cipher Calculate; // This class includes all calculations, the header is listed in section A1.2.1
    Units Convert; //This class is used for all unit conversions, the header is listed in section A1.3.1
    void TfrmMain::RecordParameters();//See section A1.1.3 for implementation.
    void TfrmMain::SaveResults(Vector parameters);
    Vector TfrmMain::FillDist(int iter, double m, double s); //See section A1.1.4 for implementation.
    Vector TfrmMain::SortVector(Vector Input); //See section A1.1.5 for implementation.
    void TfrmMain::SetUpMCVectors();//See section A1.1.6 for implementation.
    void TfrmMain::SetUpParameters(int rows, int cols); //See section A1.1.7 for implementation.
    void TfrmMain::PlotMCSolution(int step); //See section A1.1.8 for implementation.
    void __fastcall btnRunClick(TObject *Sender); //See section A1.1.2 for implementation.
    void __fastcall btnMCRunClick(TObject *Sender); //See section A1.1.9 for implementation.
    void __fastcall chkMCporosityClick(TObject *Sender); //See section A1.1.10 for implementation.
    void __fastcall ckhMCTortuosityClick(TObject *Sender); //See section A1.1.11 for
        implementation.
    void __fastcall chkMCPhiClick(TObject *Sender); //See section A1.1.12 for implementation.
public: // User declarations
    __fastcall TfrmMain(TComponent* Owner);
};

```

A1.2 BTNRUNCLICK FUNCTION

```

void __fastcall TfrmMain::btnRunClick(TObject *Sender)
{
    cbxPlot->ItemIndex = 2;
    v_Parameters->Clear();
    RecordParameters(); //See section A1.1.3 for implementation.
    Vector v_steps, v_sos;
    int steps = 0;
    double sumofsquares = 50000;
    int sol = v_Parameters->Values[0];
    int bound = v_Parameters->Values[1];
    switch (sol) {
        case 0: //Analytical Solution
            switch (bound) {
                case 0: //Neuman Boundary
                    v_C13 = Calculate.AnalNeuman(v_Parameters, 13); //See section
                        A1.2.36 for implementation.
                    v_C12 = Calculate.AnalNeuman(v_Parameters, 12);
                    v_Solution->Resize(v_C12->Length);
                    for (int i = 0; i < v_C12->Length; i++) {
                        v_Solution->Values[i] = Calculate.Solved13C(v_C12-
                            >Values[i], v_C13->Values[i]); //See section
                            A1.2.20 for implementation.
                    }
                    break;
                case 1: //Dirichlet Boundary
                    v_C13 = Calculate.AnalDirichlet(v_Parameters, 13); //See section
                        A1.2.37 for implementation.
                    v_C12 = Calculate.AnalDirichlet(v_Parameters, 12);
                    v_Solution->Resize(v_C12->Length);
                    for (int i = 0; i < v_C12->Length; i++) {
                        v_Solution->Values[i] = Calculate.Solved13C(v_C12-
                            >Values[i], v_C13->Values[i]);
                    }
                    break;
                default:
                    ;
            }
            break;
        case 1: //Finite Difference Solution
            Stopwatch->Start();
            Calculate.SetupPreviousSol(v_Parameters); //See section A1.2.30 for implementation.
            chtMain->Axes->Top->Minimum = -30;
            chtMain->Axes->Top->Maximum = 0;
            while (sumofsquares > 1E-24){
                steps++;
                v_Prev12 = Calculate.GetPrevSol(12);
                if (steps == 1) {
                    Calculate.FiniteDifferencePrep(v_Parameters, v_Parameters->Values[2],
                        v_Parameters->Values[3]); //See section
                        A1.2.38 for implementation.
                }
            }
    }
}

```

```

v_C13 = Calculate.FiniteDiff(v_Parameters, 13); //See section A1.2.39 for
implementation.
v_C12 = Calculate.FiniteDiff(v_Parameters, 12);
v_difference = v_Prev12-v_C12;
sumofsquares = v_difference->SumOfSquares(); //included in the MtxVec
library.

lblSOS->Caption = "SOS: " + FormatFloat("#.##E+0",sumofsquares);
lblSOS->Repaint();
v_Solution->Resize(v_C12->Length-1);
for (int i = 0; i < v_C12->Length-1; i++) {
    v_Solution->Values[i] = Calculate.Solved13C(v_C12->Values[i],
        v_C13->Values[i]);
}
Series5->Clear();
Series5->XValues->Order = loNone;
for (int i = 0; i < v_Solution->Length; i++) {
    Series5->AddXY(v_Solution->Values[i], v_depthProfile->Values[i], "",
        clRed);
}
chtMain->Repaint();
if (steps%5000 == 0) {
    v_steps->Resize(steps/5000);
    v_sos->Resize(steps/5000);
    v_steps->Values[steps/5000-1] = steps;
    v_sos->Values[steps/5000-1] = sumofsquares;
    Series7->XValues->Order = loNone;
    for (int i = 0; i < steps/5000; i++) {
        Series7->AddXY(v_sos->Values[i], v_steps->Values[i], "",
            clRed);
    }
    Chart1->Repaint();
}
};
v_Solution->Resize(v_C12->Length-1);
for (int i = 0; i < v_C12->Length-1; i++) {
    v_Solution->Values[i] = Calculate.Solved13C(v_C12->Values[i],
        v_C13->Values[i]);
}
StopWatch->Stop();
lblTime->Caption = StopWatch->TimeString;
lblElapsedTime->Caption = steps;
break;
default:
    ;
}

cbxPlotChange(btnRun);
    SaveResults(v_Parameters);
}

```

A1.3 RECORDPARAMETERS()

```

void TfrmMain::RecordParameters()
{
    //This will record the values of all of the model parameters.
    int temp = v_Parameters->Length;
    if (temp != 43) {
        v_Parameters->Clear();
        v_Parameters->Resize(43);
    }
    //Begin to record the parameters
    v_Parameters->Values[0] = cbxSolutionType->ItemIndex;
    v_Parameters->Values[1] = cbxBoundType->ItemIndex;
    v_Parameters->Values[2] = cbxSoilProp->ItemIndex;
    v_Parameters->Values[3] = cbxCO2Prop->ItemIndex;
    v_Parameters->Values[4] = chkMonteCarlo->Checked;
    v_Parameters->Values[5] = Convert.RespirationRate(StrToFloat(edQ->Text),cbxQUnits->ItemIndex);
    v_Parameters->Values[6] = Convert.Depth(StrToFloat(edL->Text),cbxLUnits->ItemIndex);
    v_Parameters->Values[7] = Convert.Concentration(StrToFloat(edCatm->Text),cbxCatmUnits->ItemIndex);
    v_Parameters->Values[8] = Convert.Concentration(StrToFloat(edCl->Text),cbxCiUnits->ItemIndex);
    v_Parameters->Values[9] = Convert.Depth(StrToFloat(edDz->Text),cbxDzUnits->ItemIndex);
    v_Parameters->Values[10] = StrToFloat(edD13Catm->Text);
    v_Parameters->Values[11] = StrToFloat(edD13CC3->Text);
    v_Parameters->Values[12] = StrToFloat(edD13CC4->Text);
    v_Parameters->Values[13] = tbrC3C4->Position;
    v_Parameters->Values[14] = 9999;
    v_Parameters->Values[15] = Convert.Time(StrToFloat(edDtime->Text),cbxDtimeUnits->ItemIndex);
    v_Parameters->Values[16] = Convert.Diffusion(StrToFloat(edDair->Text),cbxDairUnits->ItemIndex);
    v_Parameters->Values[17] = StrToFloat(edPorosity->Text);
    v_Parameters->Values[18] = StrToFloat(edTortuosity->Text);
    v_Parameters->Values[19] = chkTortuosity->Checked;
    v_Parameters->Values[20] = cbxTortCalc->ItemIndex;
    v_Parameters->Values[21] = StrToFloat(edWaterContent->Text);
    v_Parameters->Values[22] = StrToFloat(edA->Text);
    v_Parameters->Values[23] = StrToFloat(edB->Text);
    v_Parameters->Values[24] = StrToFloat(edC->Text);
    v_Parameters->Values[25] = StrToFloat(edD->Text);
    v_Parameters->Values[26] = StrToFloat(edE->Text);
    v_Parameters->Values[27] = Convert.Depth(StrToFloat(edZ->Text),cbxZ->ItemIndex);
    v_Parameters->Values[28] = StrToFloat(edAdvection0->Text);
    v_Parameters->Values[29] = StrToFloat(edDadt->Text);
    v_Parameters->Values[30] = StrToFloat(edFractionation->Text);
    v_Parameters->Values[31] = StrToFloat(edFastLitIn->Text);
    v_Parameters->Values[32] = StrToFloat(edSlowLitIn->Text);
    v_Parameters->Values[33] = StrToFloat(edFastRootProd->Text);
    v_Parameters->Values[34] = StrToFloat(edSlowRootProd->Text);
    v_Parameters->Values[35] = StrToFloat(edFastk->Text);
    v_Parameters->Values[36] = StrToFloat(edSlowk->Text);
}

```

```

v_Parameters->Values[37] = StrToFloat(edStablek->Text);
v_Parameters->Values[38] = StrToFloat(edFaste->Text);
v_Parameters->Values[39] = StrToFloat(edSlowe->Text);
v_Parameters->Values[40] = StrToFloat(edStablee->Text);
v_Parameters->Values[41] = StrToFloat(edFastt->Text);
v_Parameters->Values[42] = StrToFloat(edSlowt->Text);
//After this I will set up the vectors for the solutions.
v_depthProfile = Calculate.SetDepthProfile(v_Parameters->Values[6], v_Parameters-
    >Values[9]); //See section A1.2.2 for implementation.
}

```

A1.4 FILLDIST(INT ITER, DOUBLE M, DOUBLE S)

```

Vector TfrmMain::FillDist(int iter, double m, double s)
{
    //Used to fill the Vectors that will hold the random distributions that are used for the Monte Carlo
    simulations (Called by btnMCRunClick, see A1.1.9).
    double mean, sd;
    Vector temp;
    temp->Resize(iter);
    mean = m;
    sd = s;
    RandomNormal(mean, sd, temp);
    return temp;
}

```

A1.5 SORTVECTOR(VECTOR INPUT)

```

Vector TfrmMain::SortVector(Vector input)
{
    //Sorts vector in ascending value for use by the Histogram function included in the MtxVec
    library.
    Vector temp;
    temp = input;
    temp->SortAscend();
    return temp;
}

```

A1.6 SETUPMCVECTORS()

```

void TfrmMain::SetUpMCVectors()
{
    //Sets up the vectors needed to complete the Monte Carlo Simulations; this function simply sizes
    the vectors and fills them with a constant value.
    int reps = StrToInt(edMCReps->Text);
    if (v_MCPorosity->Length==0) {
        v_MCPorosity->Resize(reps);
        for (int i = 0; i < reps; i++) {
            v_MCPorosity->Values[i] = v_Parameters->Values[17];
        }
    }
}

```

```

if (v_MCTortuosity->Length==0) {
    v_MCTortuosity->Resize(reps);
    for (int i = 0; i < reps; i++) {
        v_MCTortuosity->Values[i] = v_Parameters->Values[18];
    }
}
if (v_MCC3->Length==0) {
    v_MCC3->Resize(reps);
    for (int i = 0; i < reps; i++) {
        v_MCC3->Values[i] = v_Parameters->Values[11];
    }
}
if (v_MCC4->Length==0) {
    v_MCC4->Resize(reps);
    for (int i = 0; i < reps; i++) {
        v_MCC4->Values[i] = v_Parameters->Values[12];
    }
}
}
}

```

A1.7 SETUPPARAMETERS(INT ROWS, INT COLS)

```

void TfrmMain::SetUpParameters(int rows, int cols)
{
    //This function sets up a matrix of all parameters, and changes the value of the porosity,
    tortuosity, or  $\delta^{13}C$  value of the biomass according to the distributions that are established by
    chkMCPorosityClick (A1.1.10), chkMCTortuosityClick (A1.1.11), and chkMCPhiClick (A1.1.12).
    m_Parameters->Resize(rows, cols);
    for (int i = 0; i < rows; i++) {
        for (int j = 0; j < cols; j++) {
            m_Parameters->Values[i][j] = v_Parameters->Values[i];
        }
    }
    SetUpMCVectors();
    m_Parameters->SetRow(v_MCC3,11);
    m_Parameters->SetRow(v_MCC4,12);
    m_Parameters->SetRow(v_MCPorosity,17);
    m_Parameters->SetRow(v_MCTortuosity,18);
}

```

A1.8 PLOTMCSOL (INT STEP)

```

void TfrmMain::PlotMCSolution(int step){
    //This plots a histogram of the solutions at each depth for the Monte Carlo simulation.
    double bins = 50;
    double bottom, top, inc;
    Vector v_bins, hist, temp;
    Matrix m_ConvHist;
    m_Histogram->Resize(m_Solutions->Rows,bins);
    m_ConvHist->Resize(m_Solutions->Rows,bins);
    v_bins->Resize(bins);
    temp->Resize(StrToInt(edMCReps->Text));
    bottom = -30;
}

```

```

top = -6;
inc = (top-bottom)/bins;
v_bins->Values[0] = bottom;
for (int i = 1; i < bins; i++) {
    v_bins->Values[i] = v_bins->Values[i-1]+inc;
}
for (int i = 0; i < m_Solutions->Rows; i++) {
    temp->GetRow(m_Solutions,i);
    Histogram(temp,v_bins,hist); //Function included in MtxVec Library
    m_Histogram->SetRow(hist,i);
}
for (int i = 0; i < m_Histogram->Rows; i++) {
    for (int j = 0; j < m_Histogram->Cols; j++) {
        m_Histogram->Values[i][j] = m_Histogram->Values[i][j]/step; //convert to
        probabilites
    }
}
Series9->IrregularGrid = true;
Series9->Clear();
chtMC->LeftAxis->SetMinMax(m_Histogram->Min(),m_Histogram->Max());
chtMC->BottomAxis->SetMinMax(v_depthProfile->Min(), v_depthProfile->Max());
chtMC->DepthAxis->SetMinMax(v_bins->Min(),v_bins->Max());
if (chkMCPhi->Checked) {
    Series9->PaletteMin = 0.05;
    Series9->PaletteStep = 0.025;
}
else {
    Series9->PaletteMin = 0.50;
    Series9->PaletteStep = 0.05;
}
for (int z = 0; z < v_depthProfile->Length; z++) {
    for (int x = 0; x < bins; x++) {
        Series9->AddXYZ(v_depthProfile->Values[z],m_Histogram-
        >Values[z][x],v_bins->Values[x]);
    }
}
chtMC->Repaint();
}

```

A1.9 BTNMCRUNCLICK

```
void __fastcall TfrmMain::btnMCRunClick(TObject *Sender)
```

```
{
```

```
//For solving the Monte Carlo Simulation
```

```
/*Steps for solution:
```

1. Get the parameters in a list.
2. run the model as before, saving the solution each time.
3. replace the factors that need to be changed with new values.
4. group the solutions into a historgam and plot it.
5. Before all of this, I need to set up a matrix of parameters that will be modified based on the variables that are varying. I will do this by setting up three vectors, regardless of what is varying and plug them into the matrix while adding the

```

    other parameters in wholesale. (Section A1.1.6)*/
v_Parameters->Clear();
RecordParameters(); //See section A1.1.3 for implementation.

int rows, columns; //rows is the number of depth steps, columns is the number of iters.
                    //The solutions will be stored in columns.
columns = StrToInt(edMCReps->Text);
SetUpParameters(43, columns); //See section A1.1.7 for implementation.
if (v_depthProfile->Length < 1) {
    v_depthProfile = Calculate.SetDepthProfile(v_Parameters->Values[6], v_Parameters-
        >Values[9]); //See section A1.2.2 for implementation.
}
rows = v_depthProfile->Length;
m_Solutions->Resize(rows,columns);
Vector tempParameters;
tempParameters->Resize(43);
double sumofsquares = 500000;
int step = 0;
int steps = 0;
int pbarstep = columns/100;
int sol = v_Parameters->Values[0];
int bound = v_Parameters->Values[1];
switch (sol) {
    case 0: //Analytical Solution
        switch (bound) {
            case 0://Neuman Boundary
                for (int j = 0; j < columns; j++) {
                    //this is the main loop for the mulitple runs of the model.
                    step++;
                    tempParameters->GetCol(m_Parameters,j);
                    v_C13->Clear();
                    v_C12->Clear();
                    v_Solution->Clear();
                    v_C13 = Calculate.AnalNeuman(tempParameters,13);
                    //See section A1.2.36 for implementation.

                    v_C12 = Calculate.AnalNeuman(tempParameters,12);
                    v_Solution->Resize(v_C12->Length);
                    for (int i = 0; i < v_C12->Length; i++) {
                        v_Solution->Values[i] =
Calculate.Solved13C(v_C12->Values[i], v_C13->Values[i]); //See section
                    A1.2.20 for implementation.
                    }
                    m_Solutions->SetCol(v_Solution,j);
                    if (step%pbarstep==0) {
                        PlotMCSolution(step); //See section A1.1.8 for
                        implementation.
                        pgbMCTotal->StepAdd();
                    }
                }
            }
        }
}

```

```

    }
    break;
    case 1://Dirichlet Boundary
        for (int j = 0; j < columns; j++) {
            step++;
            tempParameters->GetCol(m_Parameters,j);
            v_C13->Clear();
            v_C12->Clear();
            v_Solution->Clear();
            v_C13 = Calculate.AnalDirichlet(tempParameters,13);
                //See section A1.2.37 for implementation.

            v_C12 = Calculate.AnalDirichlet(tempParameters,12);
            v_Solution->Resize(v_C12->Length);
            for (int i = 0; i < v_C12->Length; i++) {
                v_Solution->Values[i] =
                Calculate.Solved13C(v_C12->Values[i], v_C13->Values[i]);
            }
            m_Solutions->SetCol(v_Solution,j);
            if (step%pbarstep==0) {
                PlotMCSolution(step);
                pgbMCTotal->StepAdd();
            }
        }
        break;
    default:
        ;
    }
    break;
    default:
        ;
}
//Plot The Solution
PlotMCSolution(step);
}

```

A1.10 CHKMCPOROSITYCLICK

```

void __fastcall TfrmMain::chkMCporosityClick(TObject *Sender)
{

```

*/*Need to assess what the conditions are. Possibilities are:*

1. Porosity is varying

a. Tortuosity is a function of porosity

i. if yes,

z. (x)Do what it did before

a. (x)Show the Water Content panel

b. (x)Show and Disable the Tortuosity Panel

c. (x)disable the MC Tort checkbox and uncheck it.

d. (x)Set up porosity and w.c. random variables

1. ()Add w.c. Vector to the various setup spots for the solution.

2. ()or decide to just use the calculated tortuosity.

e. ()use them to solve for tortuosity at each step

f. ()calculate the mean and s.d. of tortuosity and plot function

b. Tortuosity is not a function of porosity

- 1. (x)Do what it did before.*
- 2. (x)Make the tortuosity panel go away*
- 3. (x)enable the tortuosity panel*

2. porosity is not varying

a. (x)Do What it Did before

```

*/
Vector v_MCPorositySorted, v_MCPorosityPDF;
Vector v_MCWaterSorted, v_MCWaterPDF;
Vector v_MCTortSorted, v_MCTortPDF;
int iter = 0;
double mean = 0;
double watermean = 0;
double tortmean = 0;
double sd = 0;
double watersd = 0;
double tortsd = 0;
int size = 0;
if (chkMCporosity->Checked) { //if the porosity will vary in the Monte Carlo Simulation
    pnlMCPorosity->Visible = true;
    iter = StrToInt(edMCReps->Text);
    v_MCPorosity->Resize(iter);
    mean = StrToFloat(edMCPorMean->Text);
    sd = StrToFloat(edMCPorsd->Text);
    v_MCPorosity = FillDist(iter, mean, sd); //See section A1.1.4 for implementation.
    size = v_MCPorosity->Length;
    v_MCPorositySorted = SortVector(v_MCPorosity); //See section A1.1.5 for
implementation.
    v_MCPorosityPDF->Resize(size);
    //calculate the Normal PDF based on the random variables.
    for (int i = 0; i < size; i++) {
        v_MCPorosityPDF->Values[i] = (1/sqrt(2*PI*pow(sd,2)))*exp(-
            (pow(v_MCPorositySorted->Values[i]-mean,2))/(2*pow(sd,2)));
    }
    Series8->Clear();
    for (int i = 0; i < size; i++) {
        Series8->AddXY(v_MCPorositySorted->Values[i], v_MCPorosityPDF-
>Values[i], "", clRed);
    }
}
if (chkTortuosity->Checked) { //if the tortuosity is a function of porosity
    pnlMCWater->Visible = true;
    pnlMCTortuosity->Visible = true;
    pnlMCTortuosity->Enabled = false;
    //Water Content Vector Handling – the water content is allowed to vary normally
    if the tortuosity is a function of porosity.
    v_MCWater->Resize(iter);
    watermean = StrToFloat(edMCWaterMean->Text);
    watersd = StrToFloat(edMCWatersd->Text);
    v_MCWater = FillDist(iter, watermean, watersd);
}

```

```

size = v_MCWater->Length;
for (int i = 0; i < size; i++) {
    if (v_MCWater->Values[i] < 0) {
        v_MCWater->Values[i] = 0;
    }
}
v_MCWaterSorted = SortVector(v_MCWater);
v_MCWaterPDF->Resize(size);
//Calculate the Normal PDF based on the random variables
for (int i = 0; i < size; i++) {
    v_MCWaterPDF->Values[i] = (1/sqrt(2*PI*pow(watersd,2)))*exp(-
(pow(v_MCWaterSorted->Values[i]-watermean,2))/(2*pow(watersd,2)));
}
Series11->Clear();
for (int i = 0; i < size; i++) {
    Series11->AddXY(v_MCWaterSorted->Values[i], v_MCWaterPDF-
>Values[i], "", clRed);
}
//This is where tortuosity is finally calculated;
v_MCTortuosity->Resize(size);
for (int i = 0; i < size; i++) {
    v_MCTortuosity->Values[i] = Calculate.Tortuosity(cbxTortCalc-
>ItemIndex,v_MCPorosity->Values[i], v_MCWater->Values[i]);
}
//See section A1.2.4 for implementation.
}
//Calculate the mean and s.d., plot the PDF.
tortmean = v_MCTortuosity->Mean();
tortsd = v_MCTortuosity->StdDev();
edMCTortMean->Text = FormatFloat("0.##",tortmean);
edMCTortsd->Text = FormatFloat("0.##", tortsd);
v_MCTortSorted = SortVector(v_MCTortuosity);
v_MCTortPDF->Resize(size);
for (int i = 0; i < size; i++) {
    v_MCTortPDF->Values[i] = (1/sqrt(2*PI*pow(tortsd,2)))*exp(-
(pow(v_MCTortSorted->Values[i]-tortmean,2))/(2*pow(tortsd,2)));
}
//plot the values.
Series10->Clear();
for (int i = 0; i < size; i++) {
    Series10->AddXY(v_MCTortSorted->Values[i], v_MCTortPDF-
>Values[i], "", clRed);
}
}
else { //if tortuosity is not a function of porosity
    pnlMCWater->Visible = false;
    pnlMCTortuosity->Visible = false;
    pnlMCTortuosity->Enabled = true;
}
}
}

```

```

else { //if porosity is not varying in the Monte Carlo Simulation
    v_MCPorositySorted->Clear();
    v_MCPorosityPDF->Clear();
    Series8->Clear();
    pnlMCPorosity->Visible = false;
    pnlMCWater->Visible = false;
    pnlMCTortuosity->Visible = false;
    if (ckhMCTortuosity->Checked) {
        pnlMCTortuosity->Visible = true;
    }
}
}
}

```

A1.11 CHKMCTORTUOSITYCLICK

```

void __fastcall TfrmMain::ckhMCTortuosityClick(TObject *Sender)
{
    //Does the same thing as chkMCPorosity (A1.1.10) but applies to the tortuosity. This is not
    //available if the tortuosity is a function of porosity.
    Vector v_MCTortSorted, v_MCTortPDF;
    int calctort = chkTortuosity->Checked;
    double mean,sd;
    int size = 0;
    if (ckhMCTortuosity->Checked) { //tortuosity IS varying
        pnlMCTortuosity->Visible = true;
        int iter = StrToInt(edMCReps->Text);
        v_MCTortuosity->Resize(iter);
        mean = StrToFloat(edMCTortMean->Text);
        sd = StrToFloat(edMCTortsd->Text);
        v_MCTortuosity = FillDist(iter, mean, sd); //See section A1.1.4 for implementation.
        size = v_MCTortuosity->Length;
        v_MCTortSorted = SortVector(v_MCTortuosity); //See section A1.1.5 for
            //implementation.
        v_MCTortPDF->Resize(size);
        //calculate the Normal PDF for the random variables
        for (int i = 0; i < size; i++) {
            v_MCTortPDF->Values[i]=(1/sqrt(2*PI*pow(sd,2)))
                *exp((pow(v_MCTortSorted->Values[i]-mean,2))/(2*pow(sd,2)));
        }
        Series10->Clear();
        for (int i = 0; i < size; i++) {
            Series10->AddXY(v_MCTortSorted->Values[i], v_MCTortPDF->Values[i], "",
                clRed);
        }
    }
    else { //Tortuosity is NOT varying
        pnlMCTortuosity->Visible = false;
        Series10->Clear();
        v_MCTortSorted->Clear();
        v_MCTortPDF->Clear();
    }
    chtMCTort->Repaint();
}
}

```

A1.12 CHKMCPHICLICK

```

void __fastcall TfrmMain::chkMCPHiClick(TObject *Sender)
{
    //Serves the same purpose as chkMCPorosityClick (A1.1.10) except for the  $\delta^{13}C$  value of C3 and
    C4 biomass
    Vector v_MCC3Sorted, v_MCC4Sorted, v_MCC3PDF, v_MCC4PDF;
    int iter = 0;
    double c3mean = 0;
    double c4mean = 0;
    double c3sd = 0;
    double c4sd = 0;
    int size = 0;
    if (chkMCPHi->Checked) { //C3 and/or C4 biomass  $\delta^{13}C$  values will vary in Monte Carlo
        simulation
        pnlMCC3->Visible = true;
        lblMCC3->Caption = "D13C Plants";
        iter = StrToInt(edMCReps->Text);
        v_MCC3->Resize(iter);
        c3mean = StrToFloat(edMCC3Mean->Text);
        c3sd = StrToFloat(edMCC3sd->Text);
        size = v_MCC3->Length;
        v_MCC3 = FillDist(iter, c3mean, c3sd); //See section A1.1.4 for implementation.
        v_MCC3Sorted = SortVector(v_MCC3); //See section A1.1.5 for implementation.
        v_MCC3PDF->Resize(size);
        //Calculate the Normal PDF for the random variables
        for (int i = 0; i < size; i++) {
            v_MCC3PDF->Values[i] = (1/sqrt(2*PI*pow(c3sd,2)))*exp(-
                (pow(v_MCC3Sorted->Values[i]-c3mean,2))/(2*pow(c3sd,2)));
        }
        Series12->Clear();
        for (int i = 0; i < size; i++) {
            Series12->AddXY(v_MCC3Sorted->Values[i], v_MCC3PDF->Values[i], "",
                clRed);
        }
        if (cbxC3C4->Checked) { //There is a mix of C3 and C4 biomass
            Vector v_PhiCombo, v_PhiComboSorted, v_PhiComboPDF;
            chtMCC3->Left = 458;
            lblMCC3->Caption = "D13C C3 Plants";
            v_MCC4->Resize(iter);
            c4mean = StrToFloat(edMCC4Mean->Text);
            c4sd = StrToFloat(edMCC4sd->Text);
            v_MCC4 = FillDist(iter, c4mean, c4sd); //See section A1.1.4 for implementation.
            size = v_MCC4->Length;
            v_MCC4Sorted = SortVector(v_MCC4); //See section A1.1.5 for implementation.
            v_MCC4PDF->Resize(size);
            //calculate Normal PDF for random variables
            for (int i = 0; i < size; i++) {
                v_MCC4PDF->Values[i] = (1/sqrt(2*PI*pow(c4sd,2)))*exp(-
                    (pow(v_MCC4Sorted->Values[i]-c4mean,2))/(2*pow(c4sd,2)));
            }
        }
    }
}

```

```

Series13->Clear();
for (int i = 0; i < size; i++) {
    Series13->AddXY(v_MCC4Sorted->Values[i], v_MCC4PDF-
        >Values[i], "", clRed);
}
v_PhiCombo->Resize(size);
for (int i = 0; i < size; i++) {
    v_PhiCombo->Values[i] = Calculate.D13CMixer(v_MCC3->Values[i],
        v_MCC4->Values[i], tbrC3C4->Position); //See section A1.2.19 for
        implementation.
}
double combomean = v_PhiCombo->Mean();
double combosd = v_PhiCombo->StdDev();
lblMCPhiMeancal->Caption = FormatFloat("0.00", combomean);
lblMCPhisdcal->Caption = FormatFloat("0.00", combosd);
v_PhiComboSorted = SortVector(v_PhiCombo);
v_PhiComboPDF->Resize(size);
//calculate Normal PDF for random variables
for (int i = 0; i < size; i++) {
    v_PhiComboPDF->Values[i] = (1/sqrt(2*PI*pow(combosd,2)))*exp(-
        (pow(v_PhiComboSorted->Values[i]-
            combomean,2))/(2*pow(combosd,2)));
}
Series15->Clear();
for (int i = 0; i < size; i++) {
    Series15->AddXY(v_PhiComboSorted->Values[i], v_PhiComboPDF-
        >Values[i], "", clRed);
}
}
else {
    v_MCC4PDF->Clear();
    v_MCC4Sorted->Clear();
    Series13->Clear();
    chtMCC3->Left = 170;
}
}
else {
    pnlMCC3->Visible = false;
    v_MCC3PDF->Clear();
    v_MCC4PDF->Clear();
    v_MCC3Sorted->Clear();
    v_MCC4Sorted->Clear();
    Series12->Clear();
    Series13->Clear();
    Series15->Clear();
}
}
}

```

A2 CLASS CIPHER

A2.1 HEADER

```

#ifndef CipherH
#define CipherH
//-----
#include "Bowen.h" //See section A1.4.1 for implementation.
#include <math.h>
#include <MtxVecCpp.h>
#include "MtxBaseComp.hpp"
#include "MtxVecEdit.hpp"
#include <MtxVec.hpp>
//-----
class Cipher
{
public:
    Cipher();
    ~Cipher();
    double Cipher::Tortuosity(int equation, double porosity, double watercontent);
    double Cipher::BulkDensity(double porosity);
    double Cipher::BulkDensity(double tortuosity, double diffcoef);
    double Cipher::DiffCoef(double dair, double porosity, double tortuosity);
    double Cipher::DiffCoef(double depth);
    double Cipher::Porosity(double bulkdensity);
    double Cipher::Solved13C(double c12, double c13);
    Vector Cipher::SetDepthProfile(double maxDepth, double dz);
    Vector Cipher::SetDepthProfile(double maxDepth, double dz, Vector data);
    Vector Cipher::SetBulkDensityProfile(double porosity, int size);
    Vector Cipher::SetBulkDensityProfile(double tortuosity, Vector diffcoef);
    Vector Cipher::SetBulkDensityProfile(Vector depths, Vector bulkdensities, Vector
        depthprofile);
    Vector Cipher::SetDiffCoefProfile(double dair, double porosity, double tortuosity, int
        equation, int size);
    Vector Cipher::SetDiffCoefProfile(Vector depths);
    Vector Cipher::SetDiffCoefProfile(Vector depths, Vector bulkdensities, double dair,
        double tortuosity);
    void Cipher::SetExpParams(double ina, double inb, double inc, double ind, double ine,
        double indair);
    double Cipher::Phi(double q, double l);
    double Cipher::Phi(double zmax, double depth, double phi);
    double Cipher::D13CMixer(double c3, double c4, double mix);
    Vector Cipher::SetPhiProfile(int size, double q, double l);
    Vector Cipher::SetPhiProfile(Vector phis, double zmax, Vector depths);
    Vector Cipher::SetD13CPhiProfile(int size, double c3, double c4, double mix);
    Vector Cipher::SetD13CPhiProfile(Vector c12, Vector c13);
    Vector Cipher::AnalNeuman(Vector parameters, int pool);
    Vector Cipher::AnalDirichlet(Vector parameters, int pool);
    Vector Cipher::FiniteDiff(Vector parameters, int pool);
    void Cipher::SetupPreviousSol(Vector parameters);
    Vector Cipher::GetPrevSol(int pool);
    void Cipher::FiniteDifferencePrep(Vector parameters, int diff, int phi);

```

```

        void Cipher::SetData(Vector depths, Vector bds);
        Vector Cipher::Phi13Profiler(Vector phi, Vector d13cphi);
private:
    Vector v_depthProfile, v_porosityProfile;
    double a,b,c,d,e,dair;
    double Cipher::C13Solver(double phi, double d13cphi);
    Vector Cipher::C13Profiler(int size, double catm, double d13catm);
    Vector Cipher::C12Profiler(Vector C13, double catm);
    Vector Cipher::D13Profiler(Vector D12);
    Vector Cipher::Phi13Profiler(Vector phi, double d13cphi);
    Vector Cipher::Phi12Profiler(Vector phi13, Vector phi);
    Vector v_PreviousFDSol12, v_PreviousFDSol13;
    Vector FDCatm12, FDCatm13, FDPPhi12, FDPPhi13, FDD12, FDD13, FDCI12, FDCI13,
        FDDepths;
    Vector FDDDataDepths, FDDDataBD, FDPPhi, BBd13cPhi;
};
#endif

```

A2.2 SETDEPTHPROFILE(DOUBLE , DOUBLE)

```

Vector Cipher::SetDepthProfile(double maxDepth, double dz)
{
    //Sets up the vector v_depth in Main to use for solving model and plotting solutions
    int temp = maxDepth/dz+1;
    v_depthProfile->Resize(temp);
    v_depthProfile->Values[0] = 0;
    for (int i = 1; i < temp; i++) {
        v_depthProfile->Values[i] = v_depthProfile->Values[i-1]+dz;
    }
    return v_depthProfile;
}

```

A2.3 SETDEPTHPROFILE (DOUBLE , DOUBLE, VECTOR)

```

Vector Cipher::SetDepthProfile(double maxDepth, double dz, Vector data)
{
    //Sets up the depth profile used for solving model and plotting solutions for models that use data entered for bulk density.
    if (data->Max() > maxDepth) maxDepth = data->Max();
    int temp = maxDepth/dz+1;
    v_depthProfile->Resize(temp);
    v_depthProfile->Values[0] = 0;
    for (int i = 1; i < temp; i++) {
        v_depthProfile->Values[i] = v_depthProfile->Values[i-1]+dz;
    }
    return v_depthProfile;
}

```

A2.4 TORTUOSITY(INT, DOUBLE, DOUBLE)

```

double Cipher::Tortuosity(int equation, double porosity, double watercontent)
{
    //calculates the tortuosity as a function of porosity depending on the function that is chosen by the user.
    double temp = 999;

```

```

double airfilledporosity = porosity-watercontent;
switch (equation) {
    case 0: //WLR Marshall
        temp = pow(airfilledporosity,(3/2))/porosity;
    break;
    case 1: //WLR Millington
        temp = pow(airfilledporosity,(4/3))/porosity;
    break;
    case 2: //Millington, 1959
        temp = pow(airfilledporosity,0.333)*pow((airfilledporosity/porosity),2);
    break;
    case 3: //Millington & Quirk, 1960
        temp = airfilledporosity/pow(porosity,(2/3));
    break;
    case 4: //Millington & Quirk, 1961
        temp = pow(airfilledporosity,(7/3))/pow(porosity,2);
    break;
    case 5: //Wessling, 1962
        temp = 0.9*airfilledporosity - 0.1;
    break;
    case 6: //Grabble & Siever, 1968
        temp = 5.25*pow(airfilledporosity,2.36);
    break;
    case 7: //Currie, 1970
        temp = pow(porosity,0.5)*pow((airfilledporosity/porosity),4);
    break;
    case 8: //deJung & Schappert, 1972
        temp = 0.31-0.59*(porosity-airfilledporosity);
    break;
    case 9: //Lai et al., 1976
        temp = pow(airfilledporosity,(4/3));
    break;
    case 10: //Albertson, 1979
        temp = 0.777*(airfilledporosity/porosity)-0.274;
    break;
    case 11: //General PMQ
        temp = 0.66*pow((airfilledporosity/porosity),3);
    break;
    case 12: //PMQ
        temp = 0.66*(porosity/airfilledporosity)*pow((airfilledporosity/porosity),3);
    break;
    case 13: //Modified PMQ
        temp = 0.66*porosity*pow((airfilledporosity/porosity),2);
    break;
default:
    ;
}
return temp;
}

```

A2.5 POROSITY(DOUBLE)

```
double CIPHER::Porosity(double bulkdensity)
{
    //calculates the porosity using equation 16
    double temp;
    temp = 1-(bulkdensity/2.65);
    return temp;
}
```

A2.6 DIFFCOEF(DOUBLE, DOUBLE, DOUBLE)

```
double CIPHER::DiffCoef(double dair, double porosity, double tortuosity)
{
    //calculates the diffusion coefficient of bulk CO2 through soil
    double temp = dair*porosity*tortuosity;
    return temp;
}
```

A2.7 DIFFCOEF(DOUBLE)

```
double CIPHER::DiffCoef(double depth)
{
    //calculates the diffusion coefficient of CO2 through soil for bulk density as a function of depth.
    double temp = dair*(a+(b*pow(depth,c)))*(e/d);
    return temp;
}
```

A2.8 SETDIFFCOEFPROFILE(DOUBLE, DOUBLE, DOUBLE, INT, INT)

```
Vector CIPHER::SetDiffCoefProfile(double dair, double porosity, double tortuosity, int equation, int size)
{
    //Sets up the Vector that has the diffusion coefficients of CO2 in soil for each depth
    Vector temp;
    temp->Resize(size);
    if (equation != 99) {
        tortuosity = Tortuosity(equation, porosity, tortuosity);
    }
    for (int i = 0; i < size; i++) {
        temp->Values[i] = DiffCoef(dair, porosity, tortuosity); //See section A1.2.6 for
implementation.
    }
    return temp;
}
```

A2.9 SETDIFFCOEFPROFILE(VECTOR)

```
Vector CIPHER::SetDiffCoefProfile(Vector depths)
{
    //Sets up the Vector that has the diffusion coefficients calculated as a function of depth.
    int size = depths->Length;
    Vector temp;
    temp->Resize(size);
    if (a==1) {
        ShowMessage("diffusion coefficient values not set");
    }
}
```

```

    }
    for (int i = 0; i < size; i++) {
        temp->Values[i] = DiffCoef(depths->Values[i]); //See section A1.2.7 for implementation.
    }
    return temp;
}

```

A2.10 SETDIFFCOEFPROFILE(VECTOR, VECTOR, DOUBLE, DOUBLE)

```

Vector Cipher::SetDiffCoefProfile(Vector depths, Vector bulkdensities, double dair, double tortuosity)
{
    //calculates the diffusion coefficients using the values for bulk density at each depth based on
    entered data.
    int size = depths->Length;
    Vector temp;
    temp->Resize(size);
    double tempor;
    for (int i = 0; i < size; i++) {
        tempor = Porosity(bulkdensities->Values[i]);
        temp->Values[i] = DiffCoef(dair, tempor, tortuosity); //See section A1.2.6 for
        implementation.
    }
    return temp;
}

```

A2.11 BULKDENSITY(DOUBLE)

```

double Cipher::BulkDensity(double porosity)
{
    //Calculates the bulk density from porosity using equation 16 and assuming 2.65g/cm3 for parent
    material density used for plots.
    double temp;
    temp = 2.65*(1-porosity);
    return temp;
}

```

A2.12 BULKDENSITY(DOUBLE, DOUBLE)

```

double Cipher::BulkDensity(double tortuosity, double diffcoef)
{
    //Calculates the bulk density for plots.
    double temp;
    double portemp;
    portemp = diffcoef/(tortuosity*dair);
    temp = BulkDensity(portemp); //See section A1.2.11 for implementation.
    return temp;
}

```

A2.13 SETBULKDENSITYPROFILE(DOUBLE, INT)

```

Vector Cipher::SetBulkDensityProfile(double porosity, int size)
{
    //fills the vector that has bulk density value for each depth
    Vector temp;
    temp->Resize(size);
}

```

```

    for (int i = 0; i < size; i++) {
        temp->Values[i] = BulkDensity(porosity); //See section A1.2.11 for implementation.
    }
    return temp;
}

```

A2.14 SETBULKDENSITYPROFILE(DOUBLE, VECTOR)

Vector Cipher::SetBulkDensityProfile(double tortuosity, Vector diffcoef)

```

{
    //fills the vector that has bulk density value for each depth
    Vector temp;
    int size = diffcoef->Length;
    temp->Resize(size);
    for (int i = 0; i < size; i++) {
        temp->Values[i] = BulkDensity(tortuosity, diffcoef->Values[i]); //See section A1.2.12 for
implementation.
    }
    return temp;
}

```

A2.15 SETBULKDENSITYPROFILE(VECTOR, VECTOR, VECTOR)

Vector Cipher::SetBulkDensityProfile(Vector depths, Vector bulkdensities, Vector depthprofile)

```

{
    //fills the vector that has bulk density value for each depth (used when the bulk density with depth
data is entered
    Vector temp;
    int breaks = depths->Length;
    int size = depthprofile->Length;
    temp->Resize(size);
    int midpoint = (depths->Values[1] - depths->Values[0])/2 + depths->Values[0];
    int lastmidpoint = 0;
    for (int i = 0; i < midpoint; i++) {
        temp->Values[i] = bulkdensities->Values[0];
    }
    lastmidpoint = midpoint;
    for (int i = 2; i < breaks; i++) {
        midpoint = (depths->Values[i] - depths->Values[i-1])/2 + depths->Values[i-1];
        for (int j = lastmidpoint; j < midpoint; j++) {
            temp->Values[j] = bulkdensities->Values[i-1];
        }
        lastmidpoint = midpoint;
    }
    int bottom = depthprofile->Max();
    for (int i = lastmidpoint; i < bottom; i++) {
        temp->Values[i] = bulkdensities->Values[breaks-1];
    }
    temp->Values[size-1] = bulkdensities->Values[breaks-1];
    return temp;
}

```

```

A2.16 SETEXPPARAMS(DOUBLE, DOUBLE, DOUBLE, DOUBLE, DOUBLE, DOUBLE)
void CIPHER::SetExpParams(double ina, double inb, double inc, double ind, double ine, double indair)
{
//Sets up the coefficients for calculating bulk density as a function of depth.
    a = ina;
    b = inb;
    c = inc;
    d = ind;
    e = ine;
    dair = indair;
}

```

```

A2.17 PHI(DOUBLE, DOUBLE)
double CIPHER::Phi(double q, double l)
{
//Calculates  $\phi$  using equation 17
    double temp;
    temp = q/l; //equation 17
    return temp;
}

```

```

A2.18 PHI(DOUBLE, DOUBLE, DOUBLE)
double CIPHER::Phi(double zmax, double depth, double phi)
{
//Calculates phi as a function of depth using equation 19.
    double temp;
    temp = phi*exp(-(depth/zmax));
    return temp;
}

```

```

A2.19 D13CMIXER(DOUBLE, DOUBLE, DOUBLE)
double CIPHER::D13CMixer(double c3, double c4, double mix)
{
//calculates the  $\delta^{13}C$  of biomass if there is a mixture of  $C_3$  and  $C_4$ 
    double temp;
    double c3mix = mix/100;
    double c4mix = (100-mix)/100;
    temp = (c3*c3mix)+(c4*c4mix);
    return temp;
}

```

```

A2.20 SOLVED13C(DOUBLE, DOUBLE)
double CIPHER::Solved13C(double c12, double c13)
{
//calculates the  $\delta^{13}C$ , given  $^{13}C$  and  $^{12}C$ 
    double temp;
    double rpdb = 0.0112372;
    double r = c13/c12;
    temp = ((r/rpdb)-1)*1000;
    return temp;
}

```

}

A2.21 SETPHIPROFILE(INT, DOUBLE, DOUBLE)

Vector Cipher::SetPhiProfile(int size, double q, double l)

```
{
    //Sets up the vector that holds phi values with depth, used when phi is constant with depth.
    Vector temp;
    temp->Resize(size);
    for (int i = 0; i < size; i++) {
        temp->Values[i] = Phi(q,l); //See section A1.2.17 for implementation
    }
    return temp;
}
```

A2.22 SETPHIPROFILE(VECTOR, DOUBLE, VECTOR)

Vector Cipher::SetPhiProfile(Vector phis, double zmax, Vector depths)

```
{
    //Prepares the Vector that holds phi values with depth, used for exponential function of phi with
    //depth
    Vector temp;
    int size;
    size = depths->Length;
    temp->Resize(size);
    for (int i = 0; i < size; i++) {
        temp->Values[i] = Phi(zmax, depths->Values[i], phis->Values[i]); //See section A1.2.18
        //for implementation.
    }
    return temp;
}
```

A2.23 SETD13CPHIPROFILE(INT, DOUBLE, DOUBLE, DOUBLE)

Vector Cipher::SetD13CPhiProfile(int size, double c3, double c4, double mix)

```
{
    //sets up the vector that holds the  $\delta^{13}C$  value of phi for each depth, used when there are mixed  $C_3$ 
    //and  $C_4$  sources
    Vector temp;
    temp->Resize(size);
    for (int i = 0; i < size; i++) {
        temp->Values[i] = D13CMixer(c3, c4, mix); //See section A1.2.19 for implementation.
    }
    return temp;
}
```

A2.24 SETD13CPHIPROFILE(VECTOR, VECTOR)

Vector Cipher::SetD13CPhiProfile(Vector c12, Vector c13)

```
{
    //sets up the vector that holds the  $\delta^{13}C$  value of phi for each depth, used for one source
    Vector temp;
    temp->Resize(c12->Length);
    for (int i = 0; i < c12->Length; i++) {
```

```

        temp->Values[i] = Solved13C(c12->Values[i], c13->Values[i]);
    }
    return temp;
}

```

A2.25 C13PROFILER(INT, DOUBLE, DOUBLE)

```

Vector Cipher::C13Profiler(int size, double catm, double d13catm)
{
    //used to calculate the concentration of 13C in the atmosphere or the soil CO2
    Vector temp;
    double rpdb = 0.0112372;
    double r;
    r = ((d13catm/1000)+1)*rpdb;
    temp->Resize(size);
    for (int i = 0; i < size; i++) {
        temp->Values[i] = catm*(r/(1+r));
    }
    return temp;
}

```

A2.26 C13SOLVER(DOUBLE, DOUBLE)

```

double Cipher::C13Solver(double phi, double d13cphi)
{
    //used to calculate the concentration of 13C produced by plants.
    double temp;
    double rpdb = 0.0112372;
    double r = ((d13cphi/1000)+1)*rpdb;
    temp = phi*(r/(1+r));
    return temp;
}

```

A2.27 C12PROFILER(VECTOR, DOUBLE)

```

Vector Cipher::C12Profiler(Vector C13, double catm)
{
    //used to calculate the concentration of 12C.
    Vector temp;
    temp->Resize(C13->Length);
    for (int i = 0; i < C13->Length; i++) {
        temp->Values[i] = catm - C13->Values[i];
    }
    return temp;
}

```

A2.28 D13PROFILER(VECTOR)

```

Vector Cipher::D13Profiler(Vector D12)
{
    //Used to calculate the diffusion coefficient of 13C through soil
    Vector temp;
    temp->Resize(D12->Length);
    for (int i = 0; i < D12->Length; i++) {
        temp->Values[i] = D12->Values[i]/1.0044434;
    }
}

```

```

    }
    return temp;
}

```

A2.29 PHI13PROFILER(VECTOR, DOUBLE)

Vector Cipher::Phi13Profiler(Vector phi, double d13cphi)

```

{
    //used to set up the vector that holds the values of phi for 13C for solving the model
    Vector temp;
    temp->Resize(phi->Length);
    double dphi;
    int max = phi->Length;
    for (int i = 0; i < max; i++) {
        dphi = phi->Values[i];
        temp->Values[i] = C13Solver(dphi, d13cphi);
    }
    return temp;
}

```

A2.30 PHI13PROFILER(VECTOR, VECTOR)

Vector Cipher::Phi13Profiler(Vector phi, Vector d13cphi)

```

{
    //used to set up the vector that holds the values of phi for 13C for solving the model
    Vector temp;
    temp->Resize(phi->Length);
    double dphi;
    int max = phi->Length;
    for (int i = 0; i < max; i++) {
        dphi = phi->Values[i];
        temp->Values[i] = C13Solver(dphi, d13cphi->Values[i]);
    }
    return temp;
}

```

A2.31 PHI12PROFILER(VECTOR, VECTOR)

Vector Cipher::Phi12Profiler(Vector phi13, Vector phi)

```

{
    //Sets up the vector with values of phi for 12C for each depth
    Vector temp;
    temp->Resize(phi->Length);
    for (int i = 0; i < phi->Length; i++) {
        temp->Values[i] = phi->Values[i]-phi13->Values[i];
    }
    return temp;
}

```

A2.32 SETUPPREVIOUSOL(VECTOR)

void Cipher::SetupPreviousSol(Vector parameters)

```

{

```

```

//Sets up the vectors needed for the finite difference solution
Vector depths;
depths = SetDepthProfile(parameters->Values[6], parameters->Values[9]);
int profilesize = depths->Length;
int solutionsize = profilesize+1;
int bound = parameters->Values[1];
double catm13 = C13Solver(parameters->Values[7], parameters->Values[10]);
double catm12 = parameters->Values[7]-catm13;
double cl12, cl13;
v_PreviousFDSol12->Resize(solutionsize);
v_PreviousFDSol13->Resize(solutionsize);
for (int i = 0; i <= solutionsize; i++) {
    v_PreviousFDSol12 = catm12;
    v_PreviousFDSol13 = catm13;
}
}

```

A2.33 GETPREVSOL(INT)

```

Vector Cipher::GetPrevSol(int pool){
    //retrieves the vector that contain the previous solutions for the finite difference model.
    Vector temp;
    if (pool == 12) {
        temp = v_PreviousFDSol12;
    }
    else temp = v_PreviousFDSol13;
    return temp;
}

```

A2.34 SETDATA(VECTOR, VECTOR)

```

void Cipher::SetData(Vector depths, Vector bds)
{
    //Sets up the vectors that will be used for bulk density data for the finite difference solution
    FDDataDepths = depths;
    FDDataBD = bds;
}

```

A2.35 ANALNEUMAN(VECTOR, INT)

```

Vector Cipher::AnalNeuman(Vector parameters, int pool)
{
    //Solves the Analytical solution using Neuman boundary conditions. Solves individually for 12C
    and 13C and then calculates the  $\delta^{13}C$ .
    Vector depths, catm12, catm13, d12, d13, phi12, phi13;
    int size;
    depths = SetDepthProfile(parameters->Values[6], parameters->Values[9]); //See section A1.2.2
    //for implementation.
    size = depths->Length;
    catm13 = C13Profiler(size, parameters->Values[7], parameters->Values[10]); //See section
    //A1.2.25 for implementation.
    catm12 = C12Profiler(catm13, parameters->Values[7]); //See section A1.2.27 for implementation.
    if (parameters->Values[19]) {

```

```

        d12 = SetDiffCoefProfile(parameters->Values[16], parameters->Values[17], parameters-
        >Values[21], parameters->Values[20], size); //See section A1.2.8 for implementation.
    }
    else d12 = SetDiffCoefProfile(parameters->Values[16], parameters->Values[17], parameters-
        >Values[18], 99, size); //See section A1.2.8 for implementation
    d13 = D13Profiler(d12); //See section A1.2.28 for implementation
    phi13 = SetPhiProfile(size, parameters->Values[5], parameters->Values[6]); //See section A1.2.21
        for implementation
    phi13 = Phi13Profiler(phi13, D13CMixer(parameters->Values[11], parameters->Values[12],
        parameters->Values[13])); //See section A1.2.29 & A1.2.19 for implementation
    phi12 = Phi12Profiler(phi13, SetPhiProfile(size, parameters->Values[5], parameters-
        >Values[6])); //See section A1.2.31 for implementation
    Vector temp;
    temp->Resize(size);
    switch (pool) {
        case 12:
            for (int i = 0; i < size; i++) {
                temp->Values[i] = (phi12->Values[i]/d12->Values[i])*(parameters-
                >Values[6]*depths->Values[i]-(pow(depths->Values[i],2)/2))+catm12->Values[i];
            }
            break;
        case 13:
            for (int i = 0; i < size; i++) {
                temp->Values[i] = (phi13->Values[i]/d13->Values[i])*(parameters-
                >Values[6]*depths->Values[i]-(pow(depths->Values[i],2)/2))+catm13->Values[i];
            }
            break;
        default:
            ;
    }
    return temp;
}

```

A2.37 ANALDIRICHLET(VECTOR, INT)

Vector Cipher::AnalDirichlet(Vector parameters, int pool)

```

{
    //Solves the Analytical solution for Dirichlet boundary conditions. Solves for 13C and 12C then
calculates the δ13C.
    Vector depths, catm12, catm13, d12, d13, phi12, phi13, cl12, cl13;
    depths = SetDepthProfile(parameters->Values[6], parameters->Values[9]); //See section A1.2.2
        for implementation
    int size = depths->Length;
    double d13cl = D13CMixer(parameters->Values[11], parameters->Values[12], parameters-
        >Values[13]); //See section A1.2.19 for implementation
    catm13 = C13Profiler(size, parameters->Values[7], parameters->Values[10]);
    catm12 = C12Profiler(catm13, parameters->Values[7]);
    cl13 = C13Profiler(size, parameters->Values[8], d13cl);
    cl12 = C12Profiler(cl13, parameters->Values[8]);
    if (parameters->Values[19]) {
        d12 = SetDiffCoefProfile(parameters->Values[16], parameters->Values[17], parameters-
        >Values[21], parameters->Values[20], size); //See section A1.2.8 for implementation
    }
}

```

```

}
else d12 = SetDiffCoefProfile(parameters->Values[16], parameters->Values[17], parameters-
    >Values[18], 99, size); //See section A1.2.8 for implementation
d13 = D13Profiler(d12); //See section A1.2.28 for implementation
phi13 = SetPhiProfile(size, parameters->Values[5], parameters->Values[6]); //See section A1.2.21
    for implementation
phi13 = Phi13Profiler(phi13, D13CMixer(parameters->Values[11], parameters->Values[12],
    parameters->Values[13])); // See section A1.2.29 & A1.2.19 for implementation
phi12 = Phi12Profiler(phi13, SetPhiProfile(size, parameters->Values[5], parameters-
    >Values[6])); //See section A1.2.31 for implementation
Vector temp;
temp->Resize(size);
switch (pool) {
    case 12:
        for (int i = 0; i < size; i++) {
            //temp->Values[i] = ((phi12->Values[i]/d12->Values[i])*(pow(depths-
            >Values[i],2)/2))+((cl12->Values[i]-catm12->Values[i]+((phi12->Values[i]/d12-
            >Values[i])/(pow(parameters->Values[6],2)*2))/parameters->Values[6]))*depths-
            >Values[i]+catm12->Values[i];
            temp->Values[i] = (phi12->Values[i]/d12->Values[i])*((parameters-
            >Values[6]*depths->Values[i]-pow(depths->Values[i],2)/2)+((cl12->Values[i]-catm12-
            >Values[i])/parameters->Values[6])*depths->Values[i]+catm12->Values[i];
        }
        break;
    case 13:
        for (int i = 0; i < size; i++) {
            //temp->Values[i] = ((phi13->Values[i]/d13->Values[i])*(pow(depths-
            >Values[i],2)/2))+((cl13->Values[i]-catm13->Values[i]+((phi13->Values[i]/d13-
            >Values[i])/(pow(parameters->Values[6],2)*2))/parameters->Values[6]))*depths-
            >Values[i]+catm13->Values[i];
            temp->Values[i] = (phi13->Values[i]/d13->Values[i])*((parameters-
            >Values[6]*depths->Values[i]-pow(depths->Values[i],2)/2)+((cl13->Values[i]-catm13-
            >Values[i])/parameters->Values[6])*depths->Values[i]+catm13->Values[i];
        }
        break;
    default:
        ;
}
return temp;

```

A2.38 FINITEDIFFERENCEPREP(VECTOR, INT, INT)

```
void Cipher::FiniteDifferencePrep(Vector parameters, int diff, int phi)
```

```

{
    //Used to set up all of the vectors that will be used for the finite difference solution
    FDDepths = SetDepthProfile(parameters->Values[6], parameters->Values[9]); //See section
        A1.2.2 for implementation.
    int size = FDDepths->Length+1;
    FDCatm13 = C13Profiler(size, parameters->Values[7], parameters->Values[10]); //See section
        A1.2.25 for implementation.
    FDCatm12 = C12Profiler(FDCatm13, parameters->Values[7]); //See section
        A1.2.27 for implementation.

```

```

Bowen Beerling(parameters); //See section A1.4 for implementation.
switch (phi) {
  case 0:
    FDPHi13 = SetPhiProfile(size-1, parameters->Values[5], parameters-
      >Values[6]); //See section A1.2.21 for implementation.

    FDPHi13 = Phi13Profiler(FDPhi13, D13CMixer(parameters->Values[11],
      parameters->Values[12], parameters->Values[13])); //See section
      A1.2.29 & A1.2.19 for implementation.
    FDPHi12 = Phi12Profiler(FDPhi13, SetPhiProfile(size-1, parameters->Values[5],
      parameters->Values[6])); //See section A1.2.31 for implementation.
    break;
  case 1:
    FDPHi = SetPhiProfile(size-1, parameters->Values[5], parameters->Values[6]);
      //See section A1.2.21 for implementation.
    FDPHi = SetPhiProfile(FDPhi, parameters->Values[27], FDDepths); //Apply the
      exp function to the total phi value. //See section A1.2.22 for implementation.
    FDPHi13 = Phi13Profiler(FDPhi, D13CMixer(parameters->Values[11],
      parameters->Values[12], parameters->Values[13])); //See section
      A1.2.29 & A1.2.19 for implementation.
    FDPHi12 = Phi12Profiler(FDPhi13, FDPHi); //See section A1.2.31 for
      implementation
    break;
  case 2:
    FDPHi13 = SetPhiProfile(size, parameters->Values[5], parameters->Values[6]);
      //See section A1.2.21 for implementation
    Beerling.AdvectionConstant(); //See section A1.4.4 for implementation
    Beerling.RootProduction(); //See section A1.4.5 for implementation
    Beerling.RootCarbon(); //See section A1.4.7 for implementation
    Beerling.CO2Production(); //See section A1.4.8 for implementation
    FDPHi12 = Beerling.GetPhi12(); //See section A1.4.9 for implementation
    FDPHi13 = Beerling.GetPhi13(); //See section A1.4.10 for implementation
    break;
default:
  ;
}
switch (diff) {
  case 0:
    if (parameters->Values[19]) {
      FDD12 = SetDiffCoefProfile(parameters->Values[16], parameters->Values[17],
        parameters->Values[21], parameters->Values[20], size); //See section A1.2.8 for
        implementation
    }
    else FDD12 = SetDiffCoefProfile(parameters->Values[16], parameters->Values[17], parameters-
      >Values[18], 99, size); //See section A1.2.8 for implementation
    FDD13 = D13Profiler(FDD12); //See section A1.2.28 for implementation
    break;
  case 1:
    SetExpParams(parameters->Values[22], parameters->Values[23], parameters-
      >Values[24], parameters->Values[25], parameters->Values[26], parameters-
      >Values[16]); //See section A1.2.16 for implementation

```

```

FDD12 = SetDiffCoefProfile(FDDepths); //See section A1.2.8 for implementation
FDD13 = D13Profiler(FDD12); //See section A1.2.28 for implementation
break;
case 2:
FDDepths = SetDepthProfile(parameters->Values[6], parameters->Values[9],
FDDDataDepths); //See section A1.2.2 for implementation
FDD12 = SetBulkDensityProfile(FDDDataDepths, FDDDataBD, FDDepths); //See section
A1.2.15 for implementation
FDD12 = SetDiffCoefProfile(FDDepths, FDD12, parameters->Values[16], parameters-
>Values[18]); //See section A1.2.10 for implementation
FDD13 = D13Profiler(FDD12); //See section A1.2.28 for implementation
break;
default:
;
}
}

```

A2.39 FINITEDIFF(VECTOR, INT)

Vector Cipher::FiniteDiff(Vector parameters, int pool)

```

{
//Solves the finite difference solution. Solves the 13C and 12C separately, then calculates  $\delta^{13}C$ .
int size = FDDepths->Length+1;
Vector temp;
temp->Resize(size);
double dt = 15;
switch (pool) {
case 12:
temp->Values[0] = FDCatm12->Values[0];
for (int i = 1; i < size-1; i++) {
temp->Values[i] = dt*(FDD12->Values[i]*((v_PreviousFDSol12-
>Values[i+1])-(2*v_PreviousFDSol12->Values[i])+v_PreviousFDSol12-
>Values[i-1])/pow(parameters->Values[9],2))+FDPHi12-
>Values[i]+v_PreviousFDSol12->Values[i];
}
if (parameters->Values[1] == 0) temp->Values[size-1] = temp->Values[size-2];
v_PreviousFDSol12 = temp;
break;
case 13:
temp->Values[0] = FDCatm13->Values[0];
for (int i = 1; i < size-1; i++) {
temp->Values[i] = dt*(FDD13->Values[i]*((v_PreviousFDSol13-
>Values[i+1])-(2*v_PreviousFDSol13->Values[i])+v_PreviousFDSol13-
>Values[i-1])/pow(parameters->Values[9],2))+FDPHi13-
>Values[i]+v_PreviousFDSol13->Values[i];
}
if (parameters->Values[1] == 0) temp->Values[size-1] = temp->Values[size-2];
v_PreviousFDSol13 = temp;
break;
default:
;
}
}

```

```

    return temp;
}

```

A3 UNITS CLASS

A3.1 UNITS HEADER FILE

```

#ifndef UnitsH
#define UnitsH
//-----
#include <math.h>
#include <MtxVecCpp.h>
#include "MtxBaseComp.hpp"
#include "MtxVecEdit.hpp"
#include <MtxVec.hpp>
//-----
class Units
{
public:
    Units::Units();
    Units::~Units();
    double Units::RespirationRate(double value, int unit); //See section A1.3.2 for
implementation.
    double Units::Depth(double value, int unit); //See section A1.3.3 for implementation.
    double Units::Concentration(double value, int unit); //See section A1.3.4 for
implementation.
    double Units::Time(double value, int unit); //See section A1.3.5 for implementation.
    double Units::Diffusion(double value, int unit); //See section A1.3.6 for implementation.
private:
};

```

A3.2 RESPIRATIONRATE(DOUBLE, INT)

```

double Units::RespirationRate(double value, int unit)
{
    double temp;
    switch (unit) {
        case 0:  //(gC m-2 y-1)
            temp = (value)/(3600*24*365.25*10000);
            break;
        case 1:  //(gC cm-2 y-1)
            temp = value/(3600*24*365.25);
            break;
        case 2:  //kgC/cm2 s
            temp = value*1000;
            break;
        case 3:  //This is the unit we are converting to (gC cm-2 s-1)
            temp = value;
            break;
    default:
        ;
}

```

```

    }
    return temp;
}

```

A3.3 DEPTH(DOUBLE, INT)

```
double Units::Depth(double value, int unit)
```

```

{
    double temp;
    switch (unit) {
        case 0: //meters
            temp = value*100;
            break;
        case 1: //cm - convert to this
            temp = value;
            break;
        case 2: //mm
            temp = value/10;
            break;
    default:
        ;
    }
    return temp;
}

```

A3.3 CONCENTRATION(DOUBLE, INT)

```
double Units::Concentration(double value, int unit)
```

```

{
    double temp;
    switch (unit) {
        case 0://ppm
            temp = (value*12)/(1000000*22.4*1000);
            break;
        case 1://gC cm-3 convert to this.
            temp = value;
            break;
        case 2://gC m-3
            temp = value*1000000000;
            break;
        case 3://kgC m-3
            temp = (value*1000000000)/1000;
            break;
    default:
        ;
    }
    return temp;
}

```

A3.4 TIME(DOUBLE, INT)

```
double Units::Time(double value, int unit)
```

```

{
    double temp;

```

```

    switch (unit) {
        case 0: //hours
            temp = value*3600;
            break;
        case 1: //min
            temp = value*60;
            break;
        case 2: //sec - convert to this
            temp = value;
            break;
    default:
        ;
    }
    return temp;
}

```

A3.5 DIFFUSION(DOUBLE, INT)

```

double Units::Diffusion(double value, int unit)
{
    double temp;
    switch (unit) {
        case 0: //cm2 h-1
            temp = value/3600;
            break;
        case 1: //cm2 sec-1 - convert to this
            temp = value;
            break;
    default:
        ;
    }
    return temp;
}

```

A4 BOWEN CLASS

A4.1 HEADER FILE

```

#ifndef BowenH
#define BowenH
//-----
#include "Cipher.h"
#include <math.h>
#include <MtxVecCpp.h>
#include "MtxBaseComp.hpp"
#include "MtxVecEdit.hpp"
#include <MtxVec.hpp>
//-----
using namespace std;
class Bowen
{
    public:

```

```

Bowen();
Bowen(Vector InputParameters); //See section A1.4.1 for implementation.
~Bowen();
void Bowen::AdvectionConstant(); //See section A1.4.2 for implementation.
void Bowen::RootProduction(); //See section A1.4.3 for implementation.
double Bowen::FixedPointSolver(int j, int speed, int pool); //See section A1.4.4 for
implementation.
void Bowen::RootCarbon(); //See section A1.4.5 for implementation.
void Bowen::CO2Production(); //See section A1.4.6 for implementation.
Vector Bowen::GetPhi12();
Vector Bowen::GetPhi13();
private:
//Cipher Calculate;
Vector v_Parameters, v_depths;
Vector v_AdvectionConstant;
Vector v_FastRootProd, v_SlowRootProd, v_FastRoot13Prod, v_SlowRoot13Prod;
Vector v_guess, v_residuals;
Vector v_FastRootCarbon, v_FastRootCarbon13, v_SlowRootCarbon,
v_SlowRootCarbon13;
Vector v_StableRootCarbon, v_StableRootCarbon13, v_TotalSOM, v_TotalSOM13;
Vector v_wRoots, v_wRoots13, v_12CO2Production, v_13CO2Production;
int size;
double rVeg, d13CVeg;
double fastCveg, slowCveg, fastRoot, slowRoot;
double kst, ksl, kf;
double est, esl, ef;
double tsl, tf;
double aZeroDepth, aScaler, alpha, zScaler;
};
//-----
#endif

```

A4.2 BOWEN(VECTOR)

```

Bowen::Bowen(Vector InputParameters)
{

```

```

//Sets up all of the vectors needed to run the Bowen-Beerling Model described in Section
2.2
Cipher Calculate;
v_Parameters->Clear();
v_Parameters->Resize(InputParameters->Length);
v_Parameters = InputParameters;
v_depths = Calculate.SetDepthProfile(v_Parameters->Values[6], v_Parameters-
>Values[9]); //See section A1.2.2 for implementation.
size = v_depths->Length;
d13CVeg = Calculate.D13CMixer(v_Parameters->Values[11], v_Parameters-
>Values[12], v_Parameters->Values[13]); //See section A1.2.19 for implementation.
fastCveg = v_Parameters->Values[31];
slowCveg = v_Parameters->Values[32];
fastRoot = v_Parameters->Values[33];

```

```

slowRoot = v_Parameters->Values[34];
kf = v_Parameters->Values[35];
ksl = v_Parameters->Values[36];
kst = v_Parameters->Values[37];
ef = v_Parameters->Values[38];
esl = v_Parameters->Values[39];
est = v_Parameters->Values[40];
tf = v_Parameters->Values[41];
tsl = v_Parameters->Values[42];
aZeroDepth = v_Parameters->Values[28];
aScaler = v_Parameters->Values[29];
alpha = v_Parameters->Values[30];
zScaler = v_Parameters->Values[27]/100;
Vector v_BowenParameters;
v_BowenParameters->Resize(17);
v_BowenParameters->Values[0] = d13CVeg;
v_BowenParameters->Values[1] = fastCVeg;
v_BowenParameters->Values[16] = slowCVeg;
v_BowenParameters->Values[2] = fastRoot;
v_BowenParameters->Values[3] = slowRoot;
v_BowenParameters->Values[4] = kf;
v_BowenParameters->Values[5] = ksl;
v_BowenParameters->Values[6] = kst;
v_BowenParameters->Values[7] = ef;
v_BowenParameters->Values[8] = esl;
v_BowenParameters->Values[9] = est;
v_BowenParameters->Values[10] = tf;
v_BowenParameters->Values[11] = tsl;
v_BowenParameters->Values[12] = aZeroDepth;
v_BowenParameters->Values[13] = aScaler;
v_BowenParameters->Values[14] = alpha;
v_BowenParameters->Values[15] = zScaler;
}

A4.3 ADVECTIONCONSTANT()
void Bowen::AdvectionConstant()
{
    //used to calculate the advection coefficient at each depth.
    v_AdvectionConstant->Clear();
    v_AdvectionConstant->Resize(size);
    for (int i = 0; i < size; i++) {
        v_AdvectionConstant->Values[i] = aZeroDepth*(v_depths->Values[i]*aScaler);
    }
}

A4.4 ROOTPRODUCTION()
void Bowen::RootProduction()

```

```

{
    //calculates the Root Production for each depth in the Bowen & Beerling model.
    rVeg = 0.0112372*((d13CVeg/1000)+1);
    v_FastRootProd->Resize(size);
    v_FastRoot13Prod->Resize(size);
    v_SlowRootProd->Resize(size);
    v_SlowRoot13Prod->Resize(size);
    for (int i = 0; i < size; i++) {
        v_FastRootProd->Values[i] = (fastRoot/zScaler)*exp(-(v_depths-
        >Values[i]/zScaler));
        v_SlowRootProd->Values[i] = (slowRoot/zScaler)*exp(-(v_depths-
        >Values[i]/zScaler));
        v_FastRoot13Prod->Values[i] = v_FastRootProd->Values[i]*rVeg;
        v_SlowRoot13Prod->Values[i] = v_SlowRootProd->Values[i]*rVeg;
        v_SlowRoot13Prod->Values[i];
    }
}

```

A4.5 FIXEDPOINTSOLVER(INT, INT, INT)

```
double Bowen::FixedPointSolver(int j, int speed, int pool)
```

```

{
    //This function solves the model using a fixed point method. The value of the variable
    //being solved for is guessed at until the equation is equal to 0.
    double min = 0;
    double max = 6000;
    double guess = (min+max)/2;
    double temp;
    v_guess->Resize(size);
    v_residuals->Resize(size);
    switch (pool) {
        case 1: //Carbon 12
            switch (speed) {
                case 1: //fast
                    for (int i = 0; i < 1000; i++) {
                        v_guess->Values[i] = guess;
                        temp = (-v_AdvectionConstant->Values[j]*((guess-
                        v_FastRootCarbon->Values[j-1])/(v_depths->Values[j]-v_depths->Values[j-1]
                        )))+(v_FastRootProd[j])-(kf*guess*(1-ef*(1-tf)));

                        v_residuals->Values[i] = temp;
                        if (temp > 0) {
                            min = guess;
                            max = max;
                            guess = (min+max)/2;
                        }
                        else if (temp < 0) {
                            min = min;

```



```

        break;
    default:
        ;
    }
break;
case 2: //Carbon 13
    switch (speed) {
        case 1: //fast
            for (int i = 0; i < 1000; i++) {
                v_guess->Values[i] = guess;
                temp = (-v_AdvectionConstant->Values[j]*((guess-
v_FastRootCarbon13->Values[j-1])/(v_depths->Values[j]-v_depths->Values[j-
1])))+(v_FastRoot13Prod->Values[j])-(kf*guess*(1-(1-(1-ef)*alpha)*(1-tf)));
                v_residuals->Values[i] = temp;
                if (temp > 0) {
                    min = guess;
                    max = max;
                    guess = (min+max)/2;
                }
                else if (temp < 0) {
                    min = min;
                    max = guess;
                    guess = (min+max)/2;
                }
                else guess = guess;
            }
        break;
        case 2: //slow
            for (int i = 0; i < 1000; i++) {
                v_guess->Values[i] = guess;
                temp = (-v_AdvectionConstant->Values[j]*((guess-
v_SlowRootCarbon13->Values[j-1])/(v_depths->Values[j]-v_depths->Values[j-
1])))+(v_SlowRoot13Prod->Values[j])-(ksl*guess*(1-(1-(1-esl)*alpha)*(1-
tsl)))+(kf*v_FastRootCarbon13->Values[j]*(1-(1-ef)*alpha)*tf);
                v_residuals->Values[i] = temp;
                if (temp > 0) {
                    min = guess;
                    max = max;
                    guess = (min+max)/2;
                }
                else if (temp < 0) {
                    min = min;
                    max = guess;
                    guess = (min+max)/2;
                }
                else guess = guess;
            }
    }
}

```

```

    }
    break;
    case 3: //stable
        for (int i = 0; i < 1000; i++) {
            v_guess->Values[i] = guess;
            temp = (-v_AdvectionConstant->Values[j]*((guess-
v_StableRootCarbon13->Values[j-1])/(v_depths->Values[j]-v_depths->Values[j-1])))-
(kst*guess*(1-est)*alpha)+(ksl*v_SlowRootCarbon13->Values[j]*(1-(1-esl)*alpha)*tsl);
            v_residuals->Values[i] = temp;
            if (temp > 0) {
                min = guess;
                max = max;
                guess = (min+max)/2;
            }
            else if (temp < 0) {
                min = min;
                max = guess;
                guess = (min+max)/2;
            }
            else guess = guess;
        }
    break;
    default:
        ;
}
break;
default:
;
}
return guess;
}

```

A4.6 ROOTCARBON()

```
void Bowen::RootCarbon()
```

```

{
    v_FastRootCarbon->Resize(size);
    v_FastRootCarbon13->Resize(size);
    v_SlowRootCarbon->Resize(size);
    v_SlowRootCarbon13->Resize(size);
    v_StableRootCarbon->Resize(size);
    v_StableRootCarbon13->Resize(size);
    v_TotalSOM->Resize(size);
    v_TotalSOM13->Resize(size);
    v_StableRootCarbon->Values[0] = 0;
    v_SlowRootCarbon->Values[0] = (slowCveg/aZeroDepth);
    v_FastRootCarbon->Values[0] = (fastCveg/aZeroDepth);
    v_StableRootCarbon13->Values[0] = 0;
}

```

```

v_SlowRootCarbon13->Values[0] = ((slowCveg*rVeg)/aZeroDepth);
v_FastRootCarbon13->Values[0] = ((fastCveg*rVeg)/aZeroDepth);
v_TotalSOM->Values[0] = v_FastRootCarbon->Values[0]+v_SlowRootCarbon-
>Values[0]+v_StableRootCarbon->Values[0];
v_TotalSOM13->Values[0] = v_FastRootCarbon13->Values[0]+v_SlowRootCarbon13-
>Values[0]+v_StableRootCarbon13->Values[0];
for (int i = 1; i < size; i++) {
    v_FastRootCarbon->Values[i] = FixedPointSolver(i,1,1);
    v_SlowRootCarbon->Values[i] = FixedPointSolver(i,2,1);
    v_StableRootCarbon->Values[i] = FixedPointSolver(i,3,1);
    v_FastRootCarbon13->Values[i] = FixedPointSolver(i,1,2);
    v_SlowRootCarbon13->Values[i] = FixedPointSolver(i,2,2);
    v_StableRootCarbon13->Values[i] = FixedPointSolver(i,3,2);
    v_TotalSOM->Values[i] = v_FastRootCarbon->Values[i]+v_SlowRootCarbon-
>Values[i]+v_StableRootCarbon->Values[i];
    v_TotalSOM13->Values[i] = v_FastRootCarbon13-
>Values[i]+v_SlowRootCarbon13->Values[i]+v_StableRootCarbon13->Values[i];
}
}

```

A4.7 CO2PRODUCTION()

```
void Bowen::CO2Production()
```

```

{
    v_wRoots->Resize(size);
    v_wRoots13->Resize(size);
    for (int i = 0; i < size; i++) {
        v_wRoots->Values[i] = (v_FastRootProd->Values[i]+v_SlowRootProd-
>Values[i]);
        v_wRoots13->Values[i] = (v_FastRoot13Prod->Values[i]+v_SlowRoot13Prod-
>Values[i]);
    }
    double temp, temq, temr;
    v_12CO2Production->Resize(size);
    for (int i = 0; i < size; i++) {
        temp = (kf*v_FastRootCarbon->Values[i]*(1-ef))+(ksl*v_SlowRootCarbon-
>Values[i]*(1-esl))+(kst*v_StableRootCarbon->Values[i]*(1-est))+(v_wRoots-
>Values[i]);
        temq = (temp*12)/(100*100*365.25*24);
        temr = temq/v_depths->Values[size-1];
        v_12CO2Production->Values[i] = temr;
    }
    v_13CO2Production->Resize(size);
    for (int i = 0; i < size; i++) {
        temp = (kf*v_FastRootCarbon13->Values[i]*(1-
ef)*alpha)+(ksl*v_SlowRootCarbon13->Values[i]*(1-
esl)*alpha)+(kst*v_StableRootCarbon13->Values[i]*(1-est)*alpha)+(v_wRoots13-
>Values[i]);
    }
}

```

```
temq = (temp*12)/(100*100*365.25*24);  
temr = temq/v_depths->Values[size-1];  
v_13CO2Production->Values[i] = temr;
```

```
}
```

APPENDIX B

SUPPLEMENTAL DATA AND FIGURES FOR FIELD TEST

Table B1. Gibbsite Dehydration CO₂ and H₂O Yields

| Sample ID | Sample Wt. (g) | Weight Lost (g) | Step | CO ₂ Yield (μmols) | H ₂ O Yield (μmols) | δ ¹³ C | δ ¹³ C σ | δ ¹⁸ O | δ ¹⁸ O σ |
|-----------|----------------|-----------------|------|-------------------------------|--------------------------------|-------------------|---------------------|-------------------|---------------------|
| 000501 | 0.554 | 0.051 | 1 | 4.9 | 85.8 | -19.4 | 0.024 | -2.3 | 0.036 |
| | | | 2 | 2.3 | 49.1 | -19.9 | 0.004 | -3.3 | 0.077 |
| | | | 3 | 2 | 23.6 | -19.4 | 0.061 | -3.6 | 0.042 |
| | | | 4 | 2.5 | 26.9 | -19.6 | 0.024 | -2.7 | 0.055 |
| | | | 5 | 2.6 | 18.6 | -20.9 | 0.027 | -3.8 | 0.039 |
| | | | 6 | 11.5 | 717.1 | | | | |
| 000502 | 0.731 | 0.069 | 1 | 4.75 | | -23.1 | 0.045 | -4.6 | 0.046 |
| | | | 2 | 8.03 | 34.6 | -23.0 | 0.029 | -2.3 | 0.078 |
| | | | 3 | 6.1 | 29.2 | -23.8 | 0.035 | -2.1 | 0.035 |
| | | | 4 | 11.9 | 26.8 | -24.7 | 0.021 | -1.8 | 0.02 |
| | | | 5 | 14.4 | 46.3 | -25.0 | 0.074 | -2.1 | 0.078 |
| | | | 6 | 30.1 | 81 | -24.7 | 0.035 | -4.6 | 0.03 |
| 000503 | 0.62 | 0.058 | 1 | 6.1 | 56.7 | -21.6 | 0.024 | 0.10 | 0.06 |
| | | | 2 | 5.5 | 51.5 | -21.1 | 0.039 | -0.12 | 0.033 |
| | | | 3 | 3.2 | | -23.9 | 0.025 | -1.3 | 0.069 |
| | | | 4 | 6.5 | 33.1 | -23.8 | 0.027 | -1.4 | 0.049 |
| | | | 5 | 8.4 | 38.8 | -25.8 | 0.055 | -1.7 | 0.061 |
| | | | 6 | 31 | 285.81 | -21.4 | 0.084 | -4.7 | 0.088 |
| 000504 | 0.508 | 0.05 | 1 | 3 | 24.4 | -24.8 | 0.048 | -6.1 | 0.058 |
| | | | 2 | 7.5 | 39.5 | -24.5 | 0.019 | -5.3 | 0.023 |
| | | | 3 | 8 | 36.9 | -24.6 | 0.016 | -5.6 | 0.033 |
| | | | 4 | 11.4 | 35 | -24.9 | 0.029 | -7.1 | 0.044 |
| | | | 5 | 16 | 44.8 | -25.2 | 0.015 | -7.8 | 0.028 |
| | | | 6 | 14 | 51.3 | -26.2 | 0.022 | -9.9 | 0.028 |
| 000505 | 0.697 | 0.064 | 1 | 6.3 | 36.5 | | | | |
| | | | 2 | 8.6 | 49.8 | -23.7 | 0.032 | -3.6 | 0.027 |
| | | | 3 | 5.7 | | -24.6 | 0.028 | -3.4 | 0.055 |
| | | | 4 | 10.9 | 43.7 | -25.6 | 0.044 | -4.2 | 0.045 |
| | | | 5 | 15.4 | 44.7 | -25.7 | 0.055 | -3.3 | 0.031 |
| | | | 6 | 20.7 | 62.1 | -26.1 | 0.024 | -5.5 | 0.049 |
| 051501 | 0.573 | 0.081 | 1 | 2.3 | 42.5 | -14.3 | 0.023 | -3.4 | 0.03 |
| | | | 2 | 3 | 55.3 | -15.3 | 0.015 | -2.6 | 0.066 |
| | | | 3 | 2.2 | 33.1 | -15.0 | 0.083 | -1.8 | 0.199 |
| | | | 4 | 3.1 | | -21.1 | 0.03 | -2.7 | 0.077 |
| | | | 5 | 6.3 | 78.4 | -22.7 | 0.027 | -0.3 | 0.062 |
| | | | 6 | 6.7 | 98.3 | -26.1 | 0.036 | -9.7 | 0.04 |
| 051502 | 0.541 | 0.076 | 1 | 1.8 | | -15.6 | 0.014 | -2.6 | 0.042 |
| | | | 2 | 2.8 | 36.3 | -18.0 | 0.025 | -1.0 | 0.024 |
| | | | 3 | 2.4 | 27.1 | -20.2 | 0.041 | -0.2 | 0.108 |
| | | | 4 | 2.9 | 37.8 | -22.7 | 0.01 | -2.7 | 0.046 |
| | | | 5 | 8.5 | | | | | |
| | | | 6 | | | | | | |

Table B1. Gibbsite Dehydration CO₂ and H₂O Yields

| Sample ID | Sample Wt. (g) | Weight Lost (g) | Step | CO ₂ Yield (μmols) | H ₂ O Yield (μmols) | δ ¹³ C | δ ¹³ C σ | δ ¹⁸ O | δ ¹⁸ O σ |
|-----------|----------------|-----------------|------|-------------------------------|--------------------------------|-------------------|---------------------|-------------------|---------------------|
| 051503 | 0.668 | 0.096 | 1 | 4.3 | 255.9 | -13.9 | 0.018 | -1.1 | 0.036 |
| | | | 2 | 3.7 | 103.9 | -15.1 | 0.027 | -0.7 | 0.115 |
| | | | 3 | 1.9 | 40.6 | -18.3 | 0.013 | -1.0 | 0.026 |
| | | | 4 | 2.7 | 54 | -21.6 | 0.027 | -2.6 | 0.049 |
| | | | 5 | 3.3 | 122.6 | -23.8 | 0.016 | -2.5 | 0.051 |
| | | | 6 | 10.8 | 64.7 | -25.8 | 0.024 | -5.2 | 0.048 |
| 102001 | 0.607 | | 1 | 2.8 | | -12.1 | 0.018 | -1.2 | 0.029 |
| | | | 2 | 3.2 | 75.5 | -11.9 | 0.02 | -0.5 | 0.027 |
| | | | 3 | 1.9 | 41 | -13.9 | 0.02 | -0.2 | 0.026 |
| | | | 4 | 2.5 | 51.2 | -17.2 | 0.043 | -2.0 | 0.107 |
| | | | 5 | 2.8 | 48.8 | | | | |
| | | | 6 | 4.4 | 48.4 | -23.3 | 0.014 | -7.6 | 0.025 |
| 102002 | 0.919 | 0.136 | 1 | 5.7 | 201.1 | | | | |
| | | | 2 | 6.2 | 188.9 | -11.5 | 0.016 | -1.6 | 0.049 |
| | | | 3 | 2.7 | 75.2 | -13.2 | 0.051 | 0.3 | 0.126 |
| | | | 4 | 3.3 | 83.9 | -16.7 | 0.025 | -1.4 | 0.051 |
| | | | 5 | 3.6 | 71.5 | | | | |
| | | | 6 | | 63.2 | -26.9 | 0.032 | -13.7 | 0.117 |
| 102003 | 0.662 | 0.098 | 1 | 2.4 | 102 | -13.4 | 0.03 | -3.0 | 0.057 |
| | | | 2 | 4.1 | 46.8 | -12.6 | 0.019 | -2.1 | 0.05 |
| | | | 3 | 3.1 | 82 | -13.9 | 0.018 | -1.2 | 0.021 |
| | | | 4 | 2.8 | | -17.0 | 0.033 | -2.9 | 0.032 |
| | | | 5 | 3.3 | 75.3 | -18.7 | 0.033 | -1.2 | 0.094 |
| | | | 6 | | | | | | |
| 202501 | 0.825 | 0.094 | 1 | 2.1 | 106.1 | -14.9 | 0.021 | -2.0 | 0.069 |
| | | | 2 | 3.1 | 75.1 | -16.4 | 0.007 | -1.7 | 0.029 |
| | | | 3 | 2.1 | 41 | -21.2 | 0.039 | -2.8 | 0.057 |
| | | | 4 | 3.1 | | -20.7 | 0.011 | -2.6 | 0.035 |
| | | | 5 | 3.5 | 51 | -21.8 | 0.031 | -2.5 | 0.044 |
| | | | 6 | 7.6 | 62.3 | -25.0 | 0.031 | -7.0 | 0.046 |
| 202502 | 0.578 | 0.067 | 1 | 4.5 | 229.1 | -14.0 | 0.045 | 0.6 | 0.125 |
| | | | 2 | 2.9 | 65.7 | -18.3 | 0.031 | -1.5 | 0.026 |
| | | | 3 | 1.8 | 39.2 | | | | |
| | | | 4 | 3.6 | 56.9 | -20.7 | 0.018 | -2.6 | 0.035 |
| | | | 5 | 3.5 | 42.9 | -20.1 | 0.017 | -3.1 | 0.022 |
| | | | 6 | 7.5 | | -25.5 | 0.055 | -5.8 | 0.068 |
| 202503 | 0.579 | 0.067 | 1 | 1.5 | 54.9 | -15.9 | 0.011 | -1.9 | 0.027 |
| | | | 2 | 2.9 | 48.3 | -17.1 | 0.024 | 0.8 | 0.035 |
| | | | 3 | 1.8 | 30.3 | -19.1 | 0.016 | -0.1 | 0.088 |
| | | | 4 | 2.5 | 40.8 | -21.5 | 0.019 | -2.5 | 0.03 |
| | | | 5 | 3.2 | 66.2 | -21.5 | 0.016 | -1.4 | 0.048 |
| | | | 6 | | | | | | |

Table B1. Gibbsite Dehydration CO₂ and H₂O Yields

| Sample ID | Sample Wt. (g) | Weight Lost (g) | Step | CO ₂ Yield (μmols) | H ₂ O Yield (μmols) | δ ¹³ C | δ ¹³ C σ | δ ¹⁸ O | δ ¹⁸ O σ |
|-----------|----------------|-----------------|------|-------------------------------|--------------------------------|-------------------|---------------------|-------------------|---------------------|
| 253501 | 0.639 | 0.149 | 1 | 2.6 | 336.2 | -16.2 | 0.027 | 0.5 | 0.071 |
| | | | 2 | 3.2 | 298.6 | -12.0 | 0.026 | 1.3 | 0.039 |
| | | | 3 | 0.7 | 27 | -14.8 | 0.018 | 0.9 | 0.013 |
| | | | 4 | 1.5 | 44.3 | -17.2 | 0.017 | -0.8 | 0.066 |
| | | | 5 | 2.1 | 39.7 | | | | |
| | | | 6 | 2.8 | 35 | -19.6 | 0.014 | -4.7 | 0.068 |
| 253502 | 0.742 | 0.115 | 1 | 2.5 | 229 | -11.0 | 0.027 | 4.7 | .043 |
| | | | 2 | 2.3 | 98.9 | -11.9 | 0.036 | 0.9 | 0.118 |
| | | | 3 | 1.4 | 44.5 | -15.2 | 0.02 | 0.9 | 0.087 |
| | | | 4 | 2.1 | | -17.9 | 0.052 | 2.0 | 0.102 |
| | | | 5 | 2.4 | | -18.2 | 0.034 | -0.6 | 0.038 |
| | | | 6 | 6.1 | 57 | -19.8 | 0.017 | -3.2 | 0.058 |
| 253503 | 0.909 | 0.141 | 1 | 2.2 | | -13.1 | 0.044 | 2.4 | 0.094 |
| | | | 2 | 3.5 | 72.2 | -14.4 | 0.043 | 4.2 | 0.087 |
| | | | 3 | 2.5 | 43.6 | -16.7 | 0.025 | 4.8 | 0.047 |
| | | | 4 | 3.3 | 58 | -18.5 | 0.031 | 2.3 | 0.042 |
| | | | 5 | 4 | 57.2 | | | | |
| | | | 6 | 4.4 | 54.2 | -18.5 | 0.04 | -3.0 | 0.061 |
| 354501 | 0.715 | 0.115 | 1 | 2.6 | 516 | -14.9 | 0.02 | 1.9 | 0.08 |
| | | | 2 | 1.7 | 134.2 | -10.9 | 0.004 | 1.7 | 0.018 |
| | | | 3 | 0.6 | 38.2 | -17.6 | 0.016 | -1.2 | 0.03 |
| | | | 4 | 1 | 63.6 | -13.2 | 0.03 | 2.8 | 0.043 |
| | | | 5 | 1 | 51.5 | -15.1 | 0.049 | 2.4 | 0.127 |
| | | | 6 | 8.2 | 112.1 | -21.5 | 0.03 | -7.4 | 0.051 |
| 354502 | 0.911 | 0.326 | 1 | 3.1 | 569.1 | -13.2 | .023 | -0.7 | 0.022 |
| | | | 2 | 1.2 | 101.8 | -10.9 | 0.088 | -0.8 | 0.243 |
| | | | 3 | 0.8 | 51.2 | -12.0 | 0.026 | 0.7 | 0.042 |
| | | | 4 | 1.1 | 82 | -13.5 | 0.033 | -3.1 | 0.048 |
| | | | 5 | | | | | | |
| | | | 6 | 25.1 | | -21.5 | 0.023 | -7.5 | 0.065 |
| 455501 | 0.833 | | 1 | 2 | 49.5 | -18.2 | 0.005 | -2.0 | 0.049 |
| | | | 2 | 1.6 | 53 | -20.8 | 0.009 | -3.1 | 0.023 |
| | | | 3 | 1 | 29.1 | -22.5 | 0.015 | -1.6 | 0.029 |
| | | | 4 | 1.8 | 40.1 | -24.5 | 0.024 | -4.0 | 0.071 |
| | | | 5 | 1.9 | 32.9 | -23.8 | 0.01 | -2.3 | 0.022 |
| | | | 6 | | | | | | |
| 455502 | 0.983 | 0.148 | 1 | 1 | 60.8 | | | | |
| | | | 2 | 2.1 | 44 | -22.0 | 0.027 | -3.1 | 0.016 |
| | | | 3 | 1.2 | 31.9 | -24.9 | 0.033 | -3.5 | 0.076 |
| | | | 4 | 2.3 | 41.1 | -25.5 | 0.006 | -4.4 | 0.053 |
| | | | 5 | 2.4 | 39.6 | -23.7 | 0.011 | -4.4 | 0.017 |
| | | | 6 | 14.5 | 24.5 | | | | |

Table B1. Gibbsite Dehydration CO₂ and H₂O Yields

| Sample ID | Sample Wt. (g) | Weight Lost (g) | Step | CO ₂ Yield (μmols) | H ₂ O Yield (μmols) | δ ¹³ C | δ ¹³ C σ | δ ¹⁸ O | δ ¹⁸ O σ | |
|-----------|----------------|-----------------|------|-------------------------------|--------------------------------|-------------------|---------------------|-------------------|---------------------|--|
| 455503 | 1.038 | 0.16 | 1 | 1.6 | 52 | -19.3 | 0.021 | -2.7 | 0.011 | |
| | | | 2 | 2.1 | 42.6 | -21.6 | 0.022 | -3.5 | 0.013 | |
| | | | 3 | 1.4 | 36.5 | -22.7 | 0.021 | -2.4 | 0.032 | |
| | | | 4 | 2.4 | 45.2 | -23.6 | 0.024 | -4.0 | 0.062 | |
| | | | 5 | 2.4 | 42.3 | -22.4 | 0.027 | -3.2 | 0.045 | |
| | | | 6 | 7.7 | 38 | -23.4 | 0.057 | -8.3 | 0.062 | |
| 557501 | 0.935 | 0.128 | 1 | 0.7 | 39.5 | -19.0 | 0.011 | -2.9 | 0.024 | |
| | | | 2 | 0.8 | 25.4 | -20.9 | 0.037 | -2.5 | 0.015 | |
| | | | 3 | 0.8 | 34.3 | -21.6 | 0.022 | -1.4 | 0.019 | |
| | | | 4 | | | | | | | |
| | | | 5 | 1.3 | 28.7 | -21.2 | 0.04 | -2.4 | 0.126 | |
| | | | 6 | 2 | 19.7 | -22.5 | 0.013 | -9.0 | 0.025 | |
| 557502 | 1.033 | 0.147 | 1 | 0.8 | 45.9 | -18.1 | 0.029 | -2.6 | 0.091 | |
| | | | 2 | 1.2 | 39.7 | -19.1 | 0.04 | -2.6 | 0.059 | |
| | | | 3 | 0.9 | 32.7 | -19.8 | 0.021 | -1.6 | 0.066 | |
| | | | 4 | 1.1 | 37.8 | -21.1 | 0.025 | -3.2 | 0.132 | |
| | | | 5 | 1.3 | 34.6 | -20.4 | 0.002 | -2.4 | 0.031 | |
| | | | 6 | 1.6 | 24.5 | -21.9 | 0.036 | -7.5 | 0.108 | |
| 557503 | 0.94 | 0.12 | 1 | | | | | | | |
| | | | 2 | 0.3 | | -19.7 | 0.009 | -3.4 | 0.029 | |
| | | | 3 | 0.4 | | -20.0 | 0.05 | 6.5 | 0.129 | |
| | | | 4 | 0.2 | | -22.6 | 0.023 | -4.3 | 0.014 | |
| | | | 5 | 0.2 | | -21.5 | 0.038 | -3.0 | 0.083 | |
| | | | 6 | 0.2 | | | | | | |
| 759501 | 1.005 | 0.111 | 1 | 2.4 | | -19.7 | 0.016 | -2.1 | 0.037 | |
| | | | 2 | 2.8 | | -21.3 | 0.017 | -1.9 | 0.061 | |
| | | | 3 | 0.4 | | -24.1 | 0.067 | -2.9 | 0.17 | |
| | | | 4 | 2.2 | | -24.5 | 0.022 | -4.0 | 0.04 | |
| | | | 5 | 3.6 | | -21.8 | 0.059 | -3.8 | 0.195 | |
| | | | 6 | 6.4 | | -22.4 | 0.043 | -6.5 | 0.026 | |
| 759502 | 0.916 | 0.145 | 1 | 3.8 | | -21.5 | 0.012 | -4.1 | 0.026 | |
| | | | 2 | 1.5 | | -25.5 | 0.023 | -8.6 | 0.023 | |
| | | | 3 | 0.4 | | -25.5 | 0.045 | -10.3 | 0.046 | |
| | | | 4 | 1.1 | | -24.5 | 0.036 | -13.1 | 0.122 | |
| | | | 5 | 1.2 | | -23.3 | 0.037 | -13.6 | 0.06 | |
| | | | 6 | 28 | | | | | | |
| 759503 | 0.976 | 0.156 | 1 | 3.7 | | -21.9 | 0.011 | -1.4 | 0.027 | |
| | | | 2 | 1.9 | | -30.3 | 0.055 | -9.4 | 0.139 | |
| | | | 3 | 1.4 | | -23.8 | 0.006 | -3.5 | 0.028 | |
| | | | 4 | 0.6 | | -22.3 | 0.032 | -5.1 | 0.086 | |
| | | | 5 | 9.2 | | -19.1 | 0.043 | -0.1 | 0.069 | |
| | | | 6 | 28 | | -22.9 | 0.029 | -11.0 | 0.051 | |

Table B1. Gibbsite Dehydration CO₂ and H₂O Yields

| Sample ID | Sample Wt. (g) | Weight Lost (g) | Step | CO ₂ Yield (μmols) | H ₂ O Yield (μmols) | δ ¹³ C | δ ¹³ C σ | δ ¹⁸ O | δ ¹⁸ O σ | |
|------------|----------------|-----------------|------|-------------------------------|--------------------------------|-------------------|---------------------|-------------------|---------------------|--|
| 9510501 | 0.977 | 0.142 | 1 | 2.8 | | -19.7 | 0.017 | -4.8 | 0.041 | |
| | | | 2 | 1.1 | | -26.1 | 0.021 | -7.1 | 0.045 | |
| | | | 3 | 0.9 | | -26.2 | 0.046 | -4.8 | 0.089 | |
| | | | 4 | 1.2 | | -26.1 | 0.008 | -5.5 | 0.04 | |
| | | | 5 | 1.3 | | -23.4 | 0.013 | -6.2 | 0.034 | |
| | | | 6 | 28 | | -24.0 | 0.06 | -10.1 | 0.08 | |
| 9510502 | 0.999 | 0.145 | 1 | 2.9 | | -19.6 | 0.012 | -7.1 | 0.037 | |
| | | | 2 | 1 | | -26.4 | 0.167 | -13.0 | 0.25 | |
| | | | 3 | | | | | | | |
| | | | 4 | 0.9 | | -23.9 | 0.038 | -12.4 | 0.1 | |
| | | | 5 | 0.9 | | -21.8 | 0.024 | -11.1 | 0.042 | |
| | | | 6 | | | -23.4 | 0.022 | -10.2 | 0.035 | |
| 9510503 | | | 1 | 2.88 | | -19.5 | 0.019 | -6.9 | 0.03 | |
| | | | 2 | 0.9 | | | | | | |
| | | | 3 | 0.8 | | -26.0 | 0.031 | -9.5 | 0.022 | |
| | | | 4 | 0.9 | | -25.6 | 0.05 | -11.3 | 0.141 | |
| | | | 5 | 1 | | -23.8 | 0.013 | -12.4 | 0.1 | |
| | | | 6 | | | | | | | |
| 2535Fe5101 | 0.837 | 0.131 | 1 | 1.4 | | -14.1 | 0.607 | -2.2 | 0.283 | |
| | | | 2 | 0.5 | | -14.1 | 0.041 | -4.6 | 0.078 | |
| | | | 3 | 0.4 | | | | | | |
| | | | 4 | 0.5 | | -12.2 | 0.071 | -3.9 | 0.15 | |
| | | | 5 | 0.5 | | -12.4 | 0.055 | -3.8 | 0.204 | |
| | | | 6 | | | | | | | |
| 2535Fe5102 | 1.07 | 0.165 | 1 | 2 | | | | | | |
| | | | 2 | 0.7 | | | | | | |
| | | | 3 | 0.8 | | -16.7 | 0.021 | -3.3 | 0.108 | |
| | | | 4 | 0.9 | | -14.4 | 0.368 | -1.6 | 0.084 | |
| | | | 5 | 1.0 | | | | | | |
| | | | 6 | | | -20.9 | 0.028 | -6.1 | 0.049 | |
| 2535Al201 | 1.039 | 0.12 | 1 | 24.5 | | -18.3 | 0.031 | -2.8 | 0.051 | |
| | | | 2 | 8.6 | | -21.2 | 0.047 | -5.1 | 0.035 | |
| | | | 3 | 7.1 | | -20.7 | 0.022 | -12.6 | 0.052 | |
| | | | 4 | 6.1 | | -20.9 | 0.04 | -5.4 | 0.089 | |
| | | | 5 | | | | | | | |
| | | | 6 | | | | | | | |
| 2535Al202 | 0.646 | | 1 | 19.5 | | -18.8 | 0.081 | 2.2 | 0.159 | |
| | | | 2 | 5.3 | | | | | | |
| | | | 3 | 4.3 | | -21.1 | 0.101 | -4.6 | 0.116 | |
| | | | 4 | 3.9 | | -21.3 | 0.081 | -11.1 | 0.112 | |
| | | | 5 | 57.2 | | -19.3 | 0.066 | -5.8 | 0.12 | |
| | | | 6 | 85.9 | | -19.2 | 0.063 | -10.6 | 0.098 | |

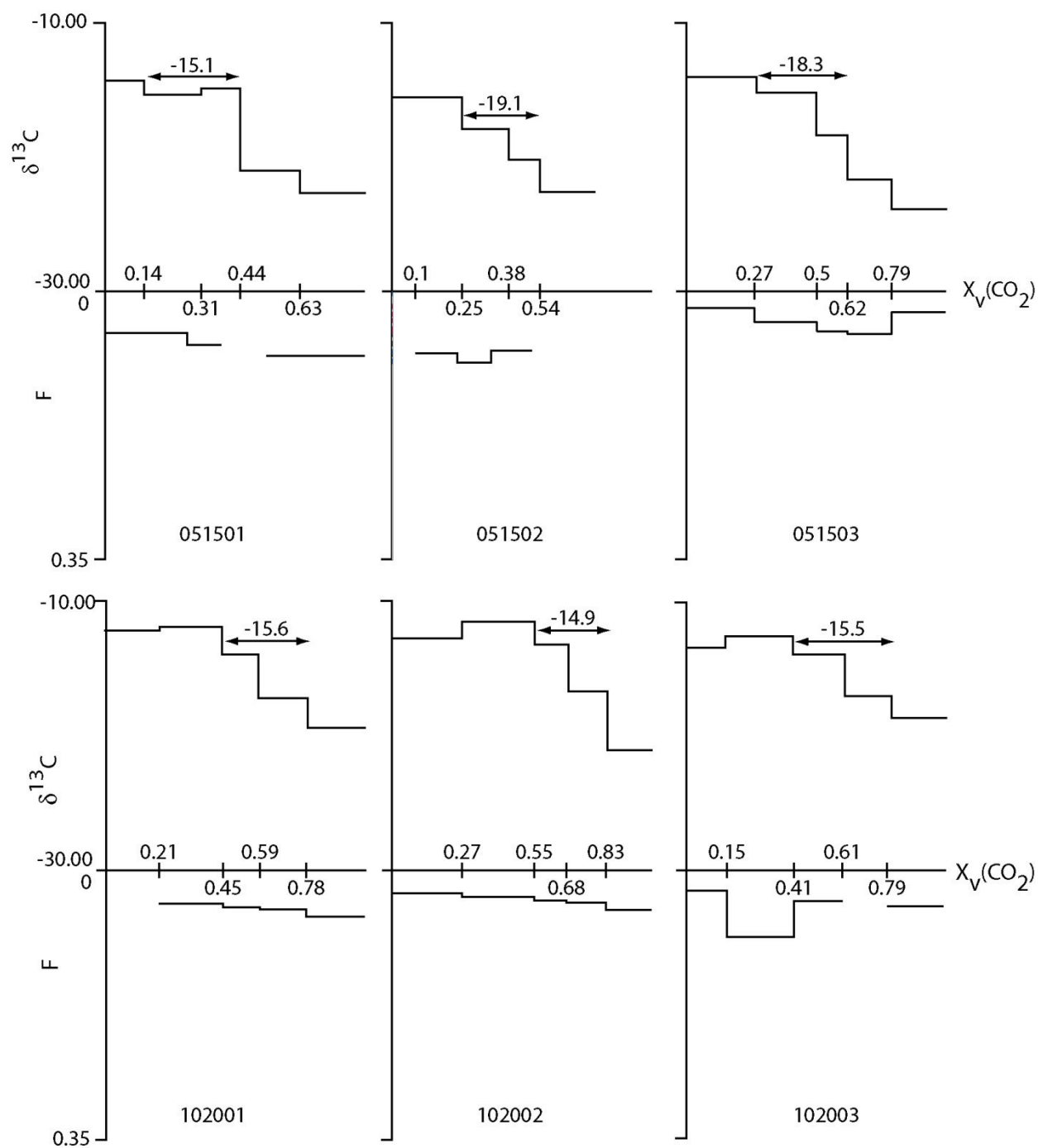


Figure B1. Dehydration/decarbonation steps for replicates of samples 0515 and 1020. $X_V(\text{CO}_2)$ is the fraction of the total CO_2 yield in a given step. Average plateau $\delta^{13}\text{C}$ values are labeled on arrows representing the plateau region.

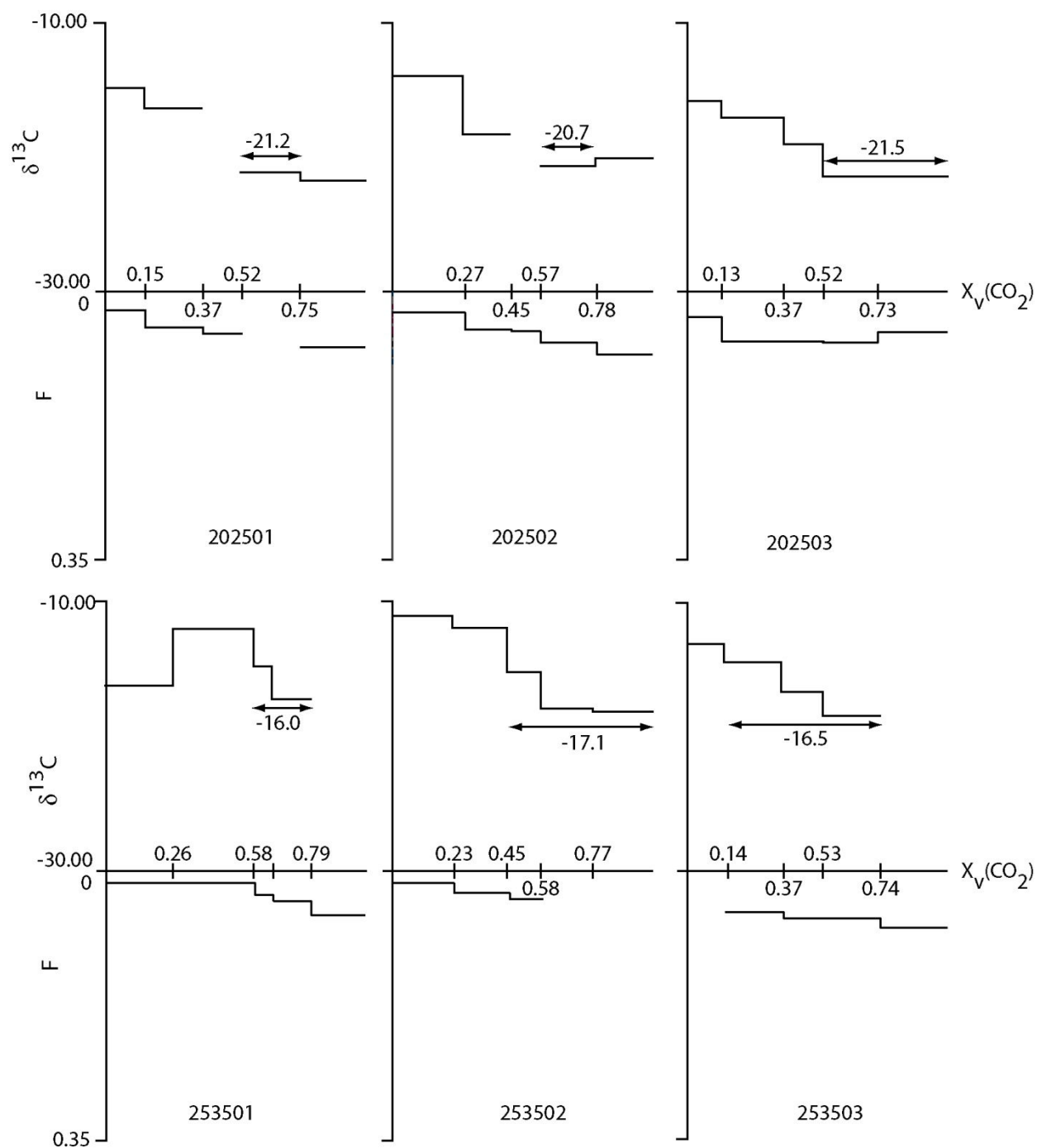


Figure B2. Dehydration/decarbonation steps for replicates of samples 2025 and 2535. $X_V(\text{CO}_2)$ is the fraction of the total CO_2 yield in a given step. Average plateau $\delta^{13}\text{C}$ values are labeled on arrows representing the plateau region.

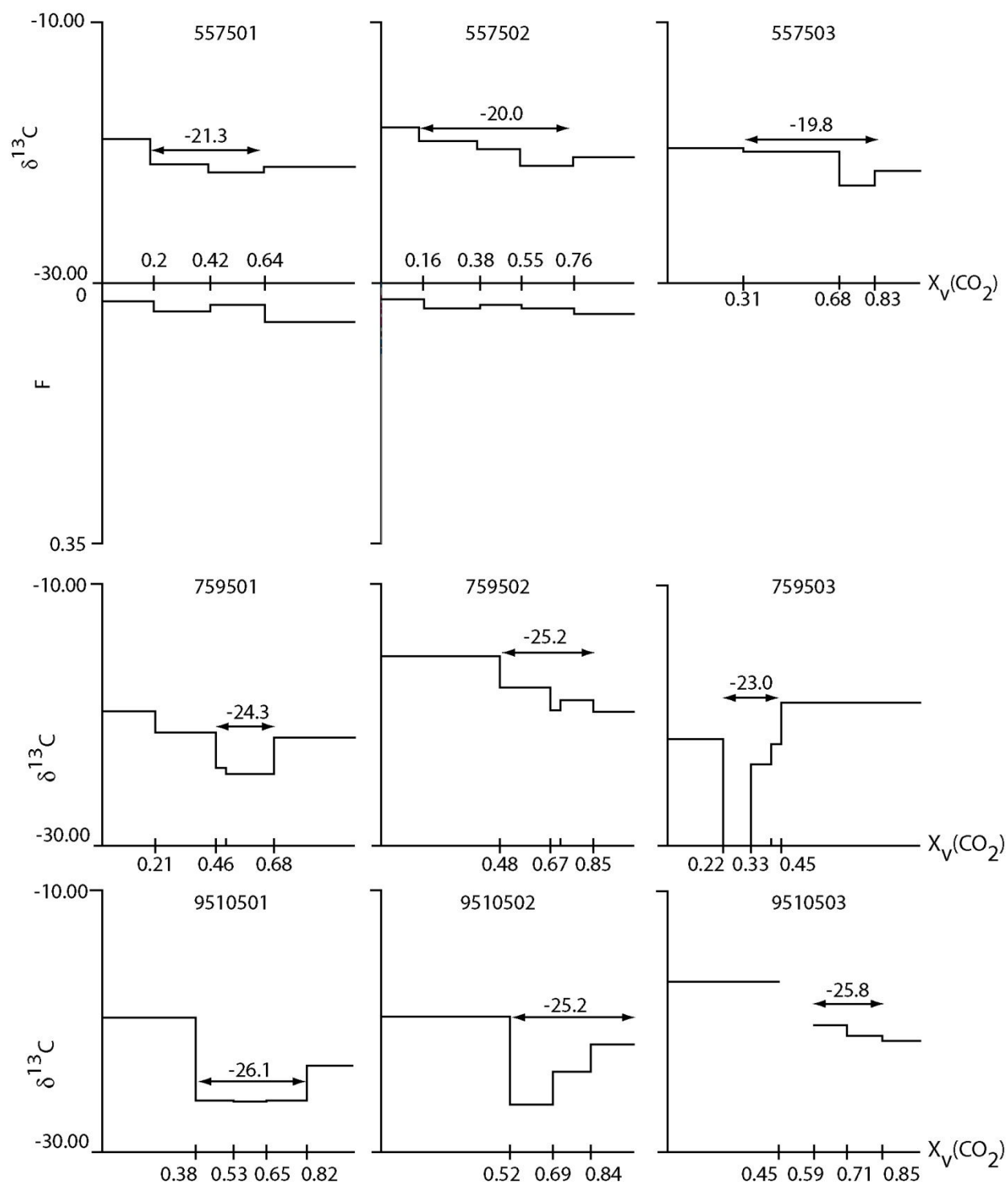


Figure B3. Dehydration/decarbonation steps for replicates of samples 5575, 7595, and 95105. $X_v(\text{CO}_2)$ is the fraction of the total CO_2 yield in a given step. Average plateau $\delta^{13}\text{C}$ values are labeled on arrows representing the plateau region.

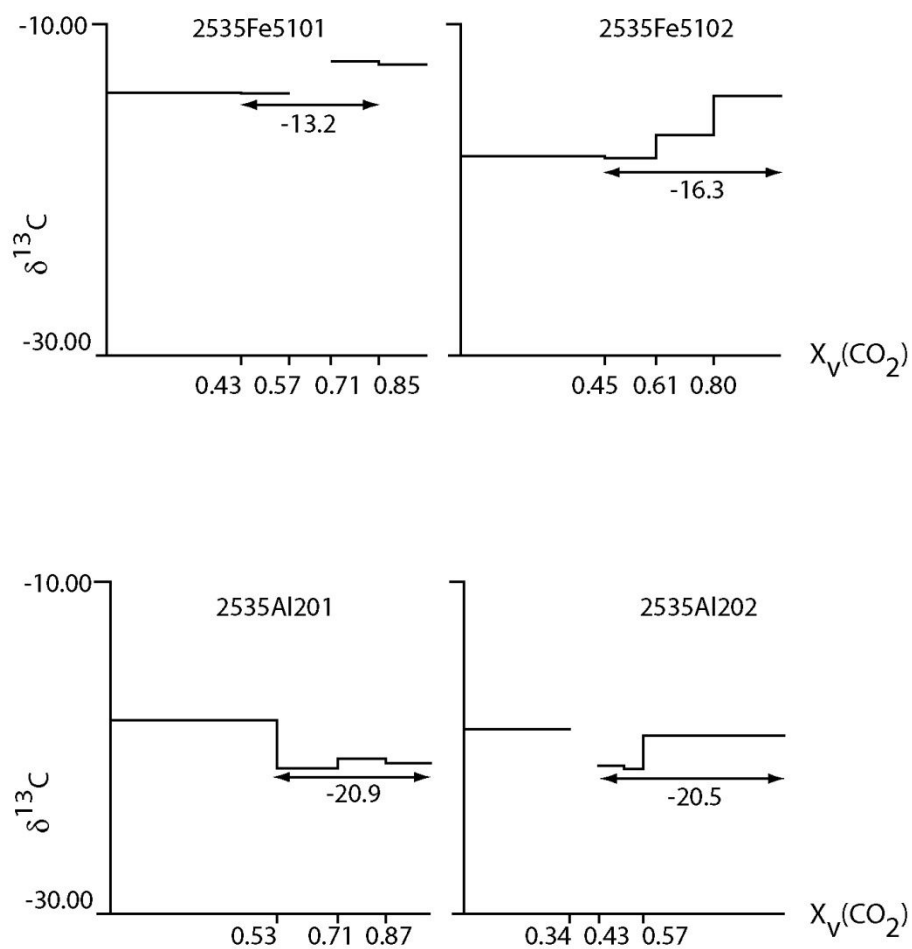


Figure B4. Dehydration/decarbonation steps for replicates of samples 2535Fe51 and 2535Al2. $X_v(\text{CO}_2)$ is the fraction of the total CO_2 yield in a given step. Average plateau $\delta^{13}\text{C}$ values are labeled on arrows representing the plateau region.